A drift chamber array for the measurement of electron trajectories

Comyn, M.

A DRIFT CHAMBER ARRAY FOR THE MEASUREMENT OF ELECTRON TRAJECTORIES

by

M. COMYN, B.Sc.

A thesis submitted to the University of Durham for the Degree of Doctor of Philosophy.

Being an account of the work carried out at the University of Durham during the period October 1974 to September 1977.

THIS THESIS IS DEDICATED TO

MY MOTHER AND MARGARET

ABSTRACT

This thesis describes an array of eight multi-cell drift chambers, of novel design, used in the (g-2) Muon Storage Ring at CERN. The array detected decay electrons traversing an inhomogeneous magnetic field ranging from 14.75 kG to 4 kG over the length of the chambers. Data analysis aimed to reconstruct the circulating muon beam profile and determine the decay electron energies. Results from the (g-2) experiment are outlined.

The development of drift chambers, the principle of operation and their future uses are discussed. The design considerations and operating parameters of the (g-2) chambers are explained. A gas mixture of argon-methane (90:10) was used in the chambers. The computerized data acquisition system developed at CERN is described in detail. It incorporated a new Drift Time Digitizer system.

The data were analysed to produce chamber drift velocity calibrations. Electric equipotential plots were derived to enable the computation of theoretical drift velocities. The existence of variable drift velocities throughout the drift spaces was revealed. Particles traversing the chambers near the cell boundaries were observed to produce recorded drift times at both adjacent sense wires. Analysis of the data in these dual detection regions produced better estimates of the drift velocities which were in good agreement with the theoretical values. An experimental scanning system is outlined which would provide accurate drift velocity calibrations in such complex fields.

The performance of the drift chamber array is evaluated and the principles of the track reconstruction outlined. The analysis produced underestimates of the radius of curvature of the circulating muons and the decay electron energies. It is demonstrated that low spatial resolutions due to inaccuracies in the drift velocity calibrations produced such errors. Improvements to the drift chamber design and operating parameters are suggested that would increase the attainable spatial resolution.

CONTENTS

CHAPTER 1

DRIFT CHAMBERS AND THEIR APPLICATION TO THE (g-2) EXPERIMENT

The drift chamber is a multiwire, gas filled, position sensitive detector. A particle traversing the chamber leaves a trail of primary ionization and the electrons are drifted towards a collecting, or sense, wire by the application of an electric field. A knowledge of the velocity and time of drift allows an accurate determination of the position of traversal of the particle. As such the drift chamber has become one of the most useful position sensing detectors available to experimentalists in the field of high energy nuclear physics today.

This thesis describes the development, data acquisition and analysis associated with an array of eight specialized drift chambers used to track electrons decaying from the Muon Storage Ring of the latest (g-2) experiment at CERN.

1.1 The Evolution of the Drift Chamber

Over the past few decades several classes of detectors have been developed for the detection of elementary particles in the fields of cosmic ray physics and nuclear physics, especially since the advent of particle accelerators. Many are gaseous detectors which may be broadly categorized in two classes; continuously sensitive, or primary detectors such as the proportional counter or Geiger-Muller tube, which are normally used in the counting mode, and triggerable, or secondary detectors such as streamer and spark chambers used to gain positional information. The secondary detectors have to be triggered using a primary detector. The distinction between primary

and secondary detectors is mainly due to the magnitude of the potential applied to the detector and thus the degree of charge amplification within the gaseous volume. If avalanching occurs close to the primary ionization and visible discharges occur, then continuous operation becomes impossible due to spurious breakdown.

In high energy nuclear physics there was a need for a detector that would allow accurate reconstruction of particle trajectories at rates much higher than those obtainable with bubble chambers or triggerable devices. Thus the detector had to be continuously sensitive and have high spatial resolution. In 1968 Charpak et al. at CERN[1] developed the multiwire proportional chamber (MWPC). It operated on the same principle as the single wire cylindrical proportional counter but had several parallel sense wires aligned in a plane equidistant between two plane cathodes as shown in figure 1.1. A typical sense wire spacing was 2 mm with a 5 mm gap to the electrodes. The sense wireswere typically 25 μm in diameter and the electrons from the primary ionization, caused by the traversal of the incident particle, were accelerated towards the sense wire which was maintained at earth potential or a positive voltage. As the field became greater towards the wire Townsend avalanching occurred in a controlled manner such that saturation did not occur. The pulse height detected on the sense wire was then proportional to the number of primary electrons. By careful choice of gas mixture and applied electric field a pulse would be detected on one wire only and the chamber resolution would be half the wire spacing. The minimum wire spacing appeared to be 1 mm, due to electrostatic repulsion between sense wires, so the resolution

of the MWPC was still less than that of a spark chamber, which with suitable readout methods could be capable of spatial resolutions in the order of $\pm$ 0.3 mm[2]. It was noted, however, that the time of arrival of the pulses on the sense wires was dependent upon the position of traversal of the incident particle. This property was investigated further and the drift chamber was evolved.[3,5].

The sense wire spacing was increased and the electrons drifted from their point of birth towards the sense wire, where Townsend avalanching occurred at close range. The velocity of the drift process was dependent upon the chamber gas and the applied electric field. Knowing the time of traversal of the incident particle using a scintillator, for example, the delay before the manifestation of a pulse on the sense wire could be used to calculate the drift distance and hence the initial position of the particle. A drift chamber can thus have a unit cell or a series of cells as shown in figure 1.2.

A full description of drift chambers and their theory of operation is given in Chapter 2 so it is sufficient at this stage merely to mention their general properties. With drift spaces up to 5 cm in length spatial resolutions of 100 μm and timing resolutions of 5 ns may be obtained in the absence of magnetic fields. Using electric field corrections drift chambers may be operated in magnetic fields with reduced resolution. They are continuously sensitive and may work at rates in excess of 10^5 pulses/wire/second. Apart from their increased spatial resolution over MWPC's, their main advantage is the reduction in number of channels of electronics required per unit chamber area. As an amplifier discriminator circuit is required for each sense wire the cost of large area MWPC's becomes prohibitive.

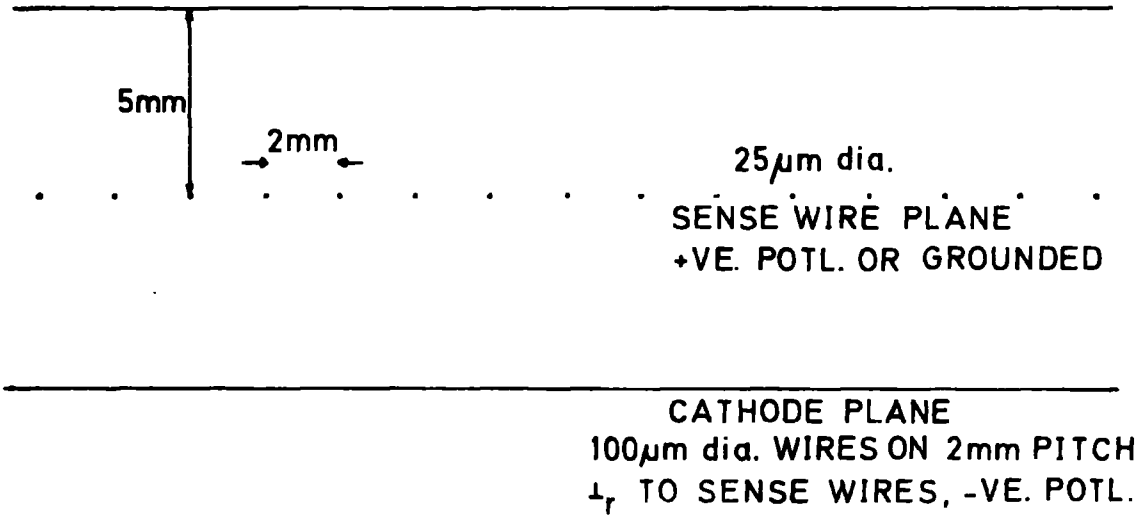

FIG. 1.1 : MWPC SHOWING TYPICAL PARAMETERS

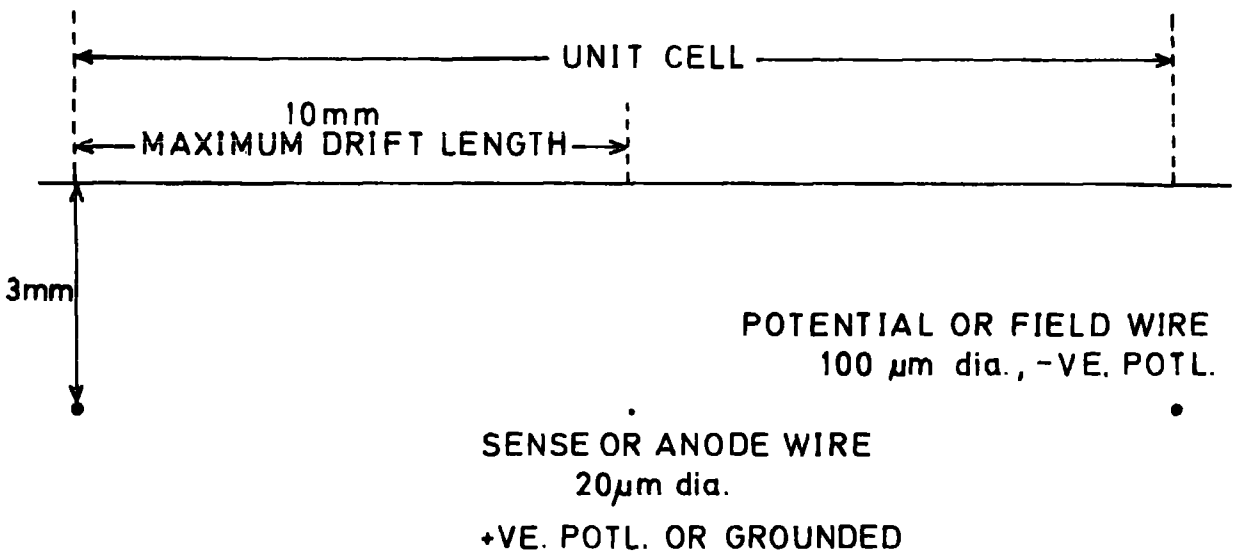

FIG. 1.2 : DRIFT CHAMBER SHOWING TYPICAL PARAMETERS

The chambers discussed in this thesis were designed to operate in the inhomogeneous fringe field of the (g-2) storage ring. Chamber design and testing commenced in 1973 following initial publication on drift chambers around 1970[3,4,5]. The array was one of the first to be designed to operate in a magnetic field, especially as regards the severe inhomogeneity present over the active chamber volume in the (g-2) experiment.

Complete discussion of drift chambers, and the (g-2) chambers in particular, is covered in the following chapters of this thesis. The remainder of this chapter deals with the (g-2) experiment and explains the reasons why a drift chamber array was required.

1.2 The (g-2) Experiments at CERN

The (g-2) experiment at CERN to which this thesis refers[6] was the third in a series to measure the anomalous magnetic moment of the muon to increased accuracy. Such a measurement is a critical test of the present state of the theory of Quantum Electrodynamics (QED). Dirac theory predicts that for a relativistic particle of spin $\frac{1}{2}$ interacting with an external field B, the magnetic moment should be equal to one Bohr magneton:

$$\vec{\mu} = - g \mu_0 \vec{s} \qquad (1.1)$$

where $\mu_0 = e\hbar/2m_0c$, m_0 referring to the rest mass of the muon.

$\vec{s}$ is the spin obtained from the three Pauli spin matrices.

The g-factor is equal to 2 for Dirac particles and hence the measured magnetic moment is the maximum expectation value of $\vec{\mu}$,

which is predicted to be μ_0. Due to radiative corrections the g values for the electron and muon have values slightly different from 2 and hence the anomaly "a" is introduced:

$$\mu = -2(1+a)\mu_0\vec{s} \qquad (1.2)$$

Thus $$a \equiv (g-2)/2 \qquad (1.3)$$

giving the experiments their characteristic name "g-2".

As described in section 1.2.2 the spin vector of the muon rotates faster than its momentum vector in the presence of a magnetic field. The frequency of this precession offers a direct method of calculating the anomaly.

The first experiment was performed on the CERN Synchro-Cyclotron during the period 1958-61[7,8,9,10] observing muon decays at rest. The final experimental value reduced the anomaly from 15% uncertainty to 0.4% by observing nearly one million stopped muons.

$$a_\mu^{(exp)} = (1162 \pm 5) \times 10^{-6}$$

whereas at the time $a_\mu^{(theory)} = 1165 \times 10^{-6}$

The second experiment was performed on the CERN Proton-Synchrotron during 1964-68[11,12,13] using a storage ring of 5m central orbit diameter and a field of 1.711T. The stored muons had a momentum of 1.28 ± 0.2 GeV/c giving a γ of about 12. Combining data for positive and negative muons decaying in flight, the latter providing the majority of the data, the experimental result was:

$$a_\mu^{(exp)} = (116616 \pm 31) \times 10^{-8}$$

equivalent to an uncertainty of 270 parts per million (ppm) of which 215 were due to random errors, the majority attributable to an uncertainty in the mean radius of the muon sample. By that time the theoretical value had been computed to greater accuracy:

$$a_{\mu}^{(\text{theory})} = (1165897 \pm 8) \times 10^{-9}$$

giving $a_{\mu}^{(\text{exp})} - a_{\mu}^{(\text{theory})} = +(28 \pm 31) \times 10^{-8}$ i.e. a positive difference of 0.9 standard deviations.

1.2.1 Motivation for the Third (g-2) Experiment

By 1969 the theoretical value of a_{μ} had been lowered to $(116564 \pm 1) \times 10^{-8}$ making the experimental result of the second experiment 1.7 standard deviations higher than the best theoretical limit.[6b] Whilst the discrepancy could have been due to undiscovered systematic errors, it could also be attributed to the first sign of a departure from QED theory or hitherto unknown couplings of the muon which could explain its mass difference with the electron. Hence a more accurate (g-2) experiment was required in order to remove or confirm the deviation. The level of accuracy aimed for in the new experiment was to be 10-20 ppm.

During the intervening period before the new experiment became operational it could be expected that the computed theoretical value would be improved upon.

Many lessons were learnt from the second experiment and the main contributory factors to the errors could be removed or lessened.[14,15] In particular a greater knowledge of the mean radial position of the

muon population, and hence the mean magnetic field seen by the ensemble was necessary. To accomplish this it was proposed to replace the radial magnetic field focusing of the second experiment by an extremely well defined and homogeneous magnetic field and electrostatic quadrupole focusing in the vertical direction. As described in the section below a "magic" value could be ascribed to the energy of the stored muons which would allow the electric field to have no effect on the precession of the muon spin vector. This would apply exactly for the central momentum of the muon ensemble with only small corrections necessary for muons describing other radii. This energy corresponded to a γ of 29.3 and a momentum of 3.098 GeV/c with a homogeneous field of 1.475T. Such a method of containment of the circulating beam would also reduce instabilities and hence fewer muons would be lost from the storage region.

Another major disadvantage of the second experiment was the method of injection. Protons from a fast ejection channel were impinged upon a target next to the storage vessel producing pions which subsequently decayed into muons. Of these a small proportion had the correct momentum and angle to be stored. However a large non-rotating and rotating background of protons, pions and electrons existed at early times which confused the analysis. Not only was the analysis of the precession frequency masked but, more importantly, also the fast rotation analysis. This followed the rotation time of the injected bunch of muons in order to determine their mean radius. A 25% loss of muons, between the time when the muon radius was determined and the time interval when the precession frequency was calculated, raised the possibility of a change in the mean radius

of the ensemble which could not be resolved and provided a large error. Also the large initial background paralysed the counters at early times.

In the new experiment a momentum selected pion beam was to be injected directly into the ring with a higher acceptance. This method would be cleaner and store a greater number of muons with better longitudinal polarization. Hence data at early times would be cleaner and the precession asymmetry would have a greater amplitude. As the energy of the stored muons was greater the relativistic time dilation also increased and hence the muons could be stored for longer. As the number of (g-2) cycles per muon lifetime depended upon the value of γB the analysis could be extended to longer times and hence the accuracy of the experiment was increased. In all the new experiment improved the data taking rate by a factor of 24 per unit time, per injected bunch over the second experiment.

Not only was the anomalous magnetic moment of positive and negative muons capable of being measured experimentally to greater accuracy than ever before, but also the lifetime of the muons in flight. Confirmation of Einstein's Clock Paradox was another result obtainable from the data. A subsidiary experiment would determine an upper limit to the muon electric dipole moment (EDM).

Therefore apart from a more accurate check on the state of the art of QED theory the new (g-2) experiment would provide excellent tests of relativity theory.

1.2.2. Brief Theory of (g-2) of the Muon and Analysis of the Experimental Data.

The anomalous magnetic moment of the muon may be represented as the sum of three terms:

$$a_\mu = a^{QED} + a^{strong} + a^{weak} \qquad (1.4)$$

Discussion of the theory behind the three values is beyond the scope of this thesis but is reviewed extensively elsewhere.[16,17,18,19,20]

The QED contribution is derived from Feynmann graphs, up to the tenth order at present. All the sixth order graphs, of which there are seventy-two, have been calculated by several groups, although some still contain numerical computer integration errors. The eighth order contributions have only been roughly estimated.[21] The QED term is given by a power series in α, the fine structure constant:

$$a^{QED} = C_2\left(\frac{\alpha}{\pi}\right) + C_4\left(\frac{\alpha}{\pi}\right)^2 + C_6\left(\frac{\alpha}{\pi}\right)^3 + C_8\left(\frac{\alpha}{\pi}\right)^4 + \ldots \quad (1.5)$$

where $\alpha^{-1} = 137.03604(11)$ is taken as the most accurate value available.[22]

The latest estimates of the coefficients give[23]:

$$a^{QED} = 0.5\left(\frac{\alpha}{\pi}\right) + 0.76578\left(\frac{\alpha}{\pi}\right)^2 + 22.93\left(\frac{\alpha}{\pi}\right)^3 + (111\pm 8)\left(\frac{\alpha}{\pi}\right)^4 + (420\pm 30)\left(\frac{\alpha}{\pi}\right)^5 \quad (1.6)$$

The hadronic contribution, a^{strong}, comes from vacuum polarization and a^{weak} is derived from Weinberg's theory of weak interactions.

The latest estimates give:

$$a_\mu \text{ (QED)} = (11658518 \pm 24) \times 10^{-10}$$

$$a_\mu \text{ (strong)} = (667 \pm 94) \times 10^{-10}$$

$$a_\mu \text{(weak)} = (2 \pm 2) \times 10^{-9}$$

yielding

$$a_\mu \text{(theory)} = (1165921 \pm 10) \times 10^{-9}$$

An observable consequence of the muon's anomalous magnetic moment is that, when in a magnetic field, its spin vector rotates faster than its momentum vector. The angular frequency of this precession is given by:

$$\vec{\omega}_a = - \frac{e}{mc} aB \qquad (1.7)$$

which allows a direct method of measuring the anomaly.

However, as already explained, a homogeneous magnetic field with vertical electric focusing was employed, so the precession frequency was shifted due to the electric field. Assuming that the muon moved transversely to $\vec{B}$ and $\vec{E}$ in the lab and that the muon had no electric dipole moment[8], the corrected precession frequency was[24]:

$$\vec{\omega}_a = - \frac{e}{mc} \left[a\vec{B} + \left(\frac{1}{\gamma^2 - 1} - a \right) \beta \times \vec{E} \right] \qquad (1.8)$$

It can be seen that by choosing $\gamma = (1 + \frac{1}{a})^{\frac{1}{2}}$ the E dependence vanished and the spin effective field once more became identically equal to B. For the muon $a^{-1} \simeq 858$ which led to the "magic" value for γ of 29.3 corresponding to a momentum for the muons of 3.094 GeV/c. The cancellation of the field applied only to muons with the central momentum, small corrections having to be made for those with slightly different orbits.

Selecting decay electrons with energies greater than 1.75 GeV in the lab ensured that they had decayed in the forward direction in the muon rest frame. As the electrons were emitted preferentially along the spin vector, and the muon sample was initially longitudinally polarized, it was possible to follow the polarization with time by recording decay electrons emerging on the inside of the ring, the count rate being modulated by the precession frequency given in equation (1.7). Figure 1.3 shows the final data from the (g-2) experiment, taken from reference 25, for electron decay energies above 1.75 GeV with the precession frequency detectable over 120 (g-2) cycles. The data were fitted by the maximum likelihood method to the function [25]

$$N(t) = N_0 \left[L(t) \exp(-t/\tau) \left\{ 1 - A \cos(\omega_a t + \phi) \right\} + B \right] \qquad (1.9)$$

describing an exponential decay with the muon time-dilated lifetime $\tau = \gamma \tau_0$, a symmetry A and phase ϕ of the modulation, and constant background B, which was very small. The function

$$L(t) = 1 + A_L \exp(-t/\tau_L) \qquad (1.10)$$

was included to make allowance for muon losses at early times and gain changes in the electronic counters. All eight parameters $N_0, \tau, A, \omega_a, \phi, B, A_L$ and τ_L were allowed to vary, optimization being derived using the program MINUIT[26].

Great care was taken to ensure that no faulty data affected the overall results. Having checked the fitting procedure using Monte Carlo methods the data was split into four energy bands and fitted independently. Further subgroups according to beam characteristics, counter position and the starting time of the fit

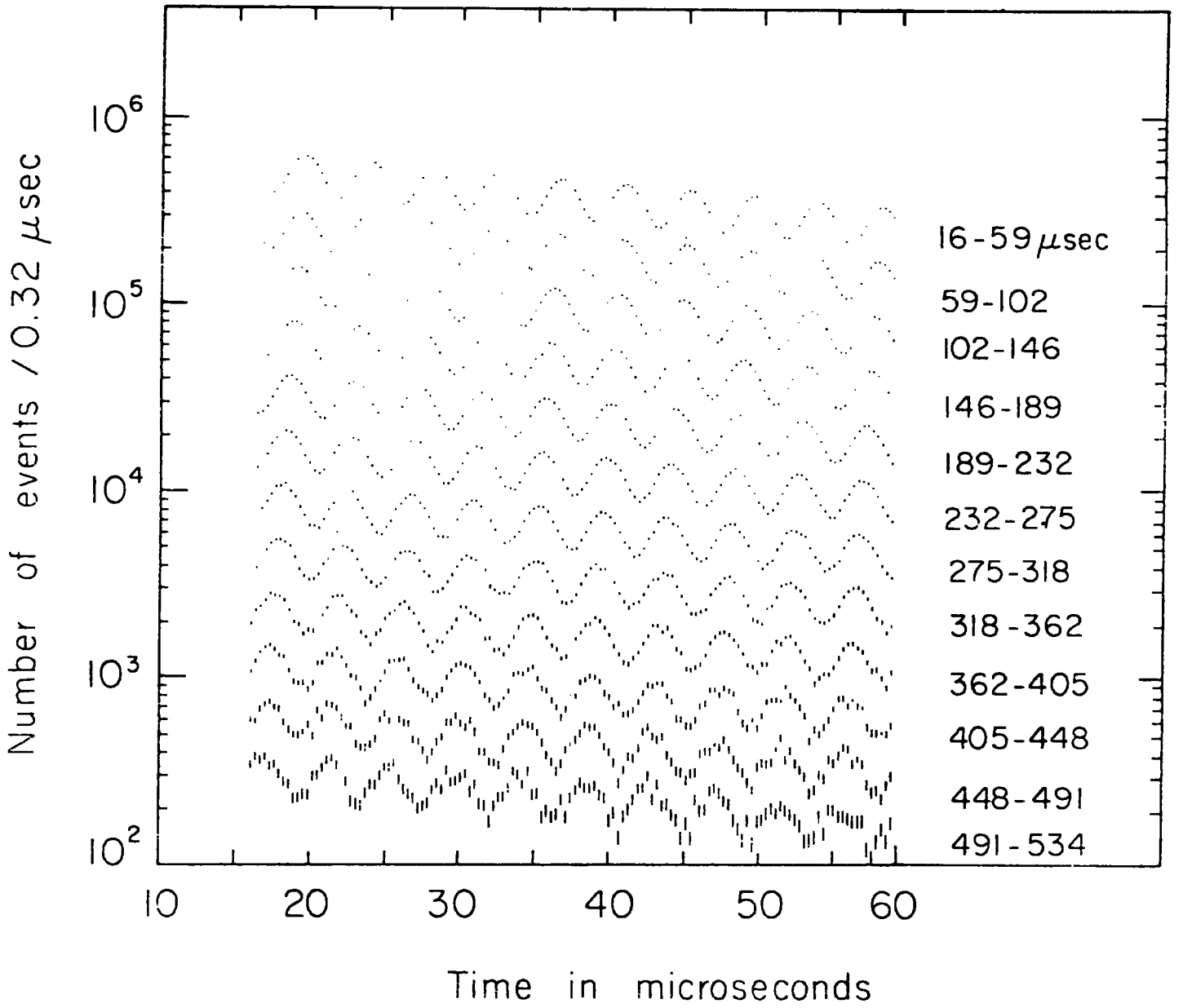

FIG. 1.3: FINAL (g-2) TIME DISTRIBUTION OF DECAY ELECTRONS

were studied to ensure that no systematic effects were present beyond the normal statistical fluctuations.

It could be shown[14] that the error in ω_a was roughly proportional to $(\tau A\sqrt{N})^{-1}$. For the ring τ, the time-dilated lifetime, was fixed. By raising the energy threshold of the detected decay electrons the asymmetry, A, was raised but N, the number of recorded muon decays, fell. An optimum threshold of 1.75 GeV maximized the value of $A\sqrt{N}$.

To derive the value of a_μ from ω_a required a knowledge of the value $(e/m_\mu c)\bar{B}$ as shown in equation (1.7), $\bar{B}$ being the mean field seen by the muon ensemble. This could be calculated by measuring the (g-2) homogeneous magnetic field in terms of the proton magnetic resonance frequency $\bar{\omega}_p$. By making the necessary corrections for the bulk diamagnetic effect of the cylindrical water sample of the NMR probe used, and the diamagnetic screening of the orbital electrons of a water molecule, the measured frequency could be corrected to that for free protons, $\bar{\omega}_p^o$[27].

From the Larmor frequency ω_L of the muon at rest

$$\omega_L = \frac{ge\bar{B}}{2mc} = (1+a)\frac{e\bar{B}}{mc} \qquad (1.11)$$

hence

$$\frac{e\bar{B}}{mc} = (1+a)^{-1}\frac{\omega_\mu^o}{\omega_p^o}\bar{\omega}_p^o \qquad (1.12)$$

The value of $\lambda = \omega_\mu/\omega_p^o$ was known very accurately from an independent experiment.[28] Hence combining equations (1.7) and (1.12) gave:

$$\frac{\overline{\omega}_p^o}{\omega_a} = \left(\frac{1+a}{a}\right)\frac{1}{\lambda} \qquad (1.13)$$

Leading to $$a = \frac{1}{R_f \lambda - 1} \qquad (1.14)$$ where $R_f = \frac{\overline{\omega}_p^o}{\omega_a}$

Hence the whole (g-2) experimental analysis revolved around the measurement of the ratio R_f. By using a master crystal oscillator for the measurement of the times of the electron decays and for the measurement and stabilization of the magnetic field, using nuclear magnetic resonance probes and magnetometers as described in the next section, any drift in the clock was nullified by use of the ratio of the two derived quantities.

1.2.3 The Experimental Layout

Figure 1.4 shows a general view of the (g-2) storage ring and figure 1.5 gives a detailed plan of the various parts of the ring and detection system.

One to four fast ejected bunches of protons were incident upon a Cu target producing pions which were momentum selected at 3.1 GeV/c $\pm$ 0.75%. About 10^6 pions were produced per 10^{11} protons incident upon the target, the negative polarity being slightly less intense but without a high proton contamination. An electrostatic pick-up in the proton beam gave the zero time reference for all (g-2) timing.

The pions were inflected into the storage region using an inflector,[29] in the form of a coaxial line, as shown in figure 1.6,

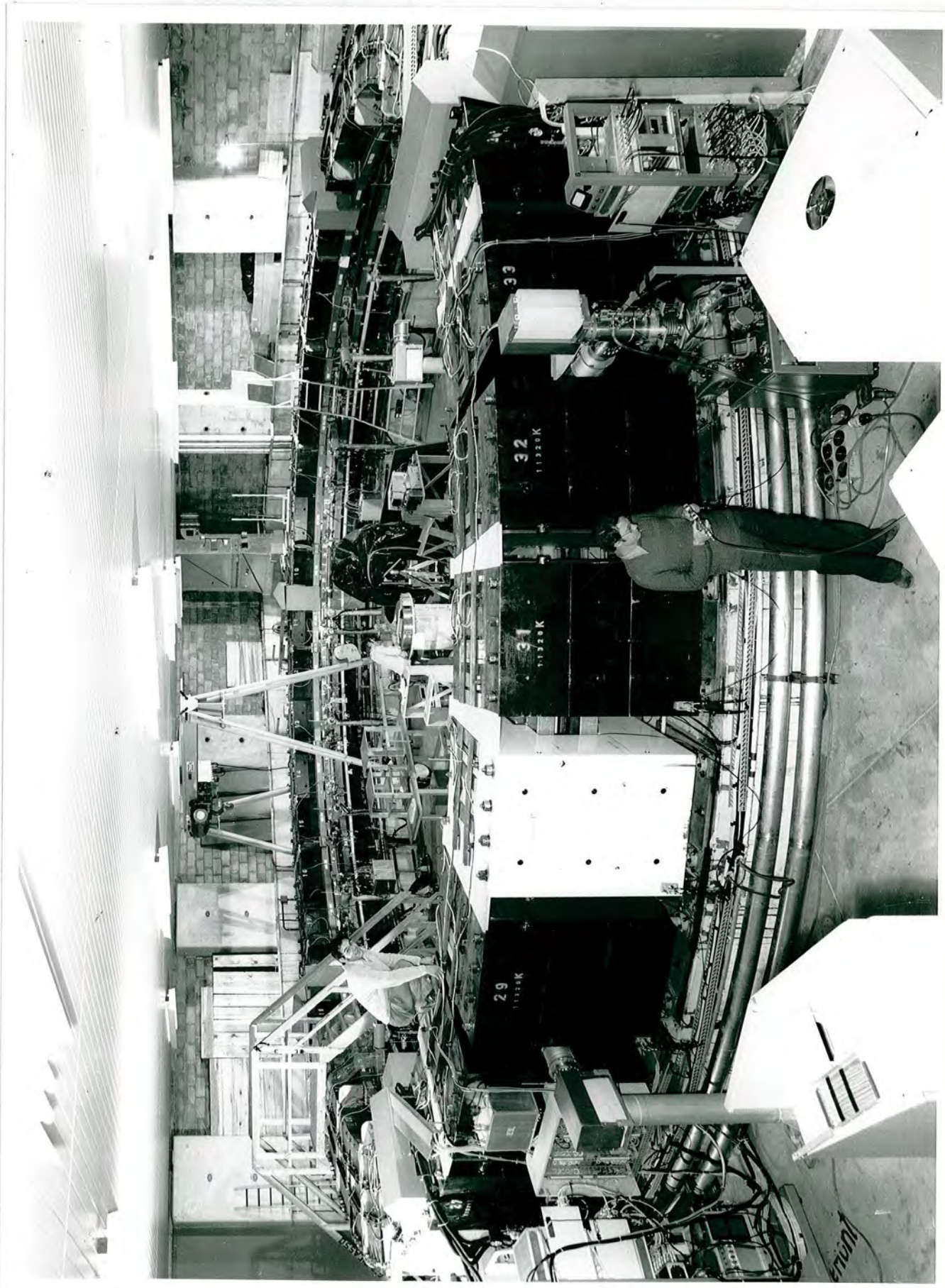

PHOTO CERN

FIG. 1.4: VIEW OF THE (g-2) MUON STORAGE RING

which was pulsed to cancel the local field of 1.475T. The trajectories of the pions were straightened, allowing them to travel about two-thirds of the way round the ring before being lost from the storage volume. At such momenta the pion lifetime is about 580ns; so as it took only 100 ns to move this far, about one tenth of the pions decayed into muons within the storage volume. Of these only two in a thousand had momenta and angles within the acceptance values of the ring. The decay modes for the two polarities were:

$$\pi^+ \rightarrow \mu^+ + \upsilon_\mu \qquad (1.15)$$

$$\pi^- \rightarrow \mu^- + \bar{\upsilon}_\mu \qquad (1.16)$$

By having pion momenta slightly above that of the central acceptance momenta of the stored muons the neutrinos were used to kick the muons into closed orbits. Accepting muons within about 1% of their maximum lab energy only, ensured that they were formed from forward pion decay and hence an initial longitudinal polarization of nearly 97% was possible. About two hundred muons were stored for each incident proton bunch and they initially occupied a distance of approximately 3m azimuthally.

The (g-2) storage ring was in the form of a regular polygon of 40 C-shaped bending magnets, the open side facing the ring centre.[30] The field of 1.475T was homogeneous over the storage volume which had a central radius of 7m about the ring centre and a useful cross-section of 8 cm in the vertical direction and 12 cm radially. The storage tank also contained the electrodes for the pulsed electrostatic focusing field.[31] It was built in ten sections, each spanning 36° in azimuth, but of these only eight contained electrodes. A field

free region existed over the inflector section of the ring with another such region on the opposite side, where the drift chamber array was located, to prevent closed orbit distortion. For the drift chamber section the normal 3 mm aluminium alloy inner wall was replaced by 0.8 mm titanium to reduce scattering and showering of the decay electrons. The tank was maintained at a vacuum in excess of 10^{-7} torr to prevent muon losses due to collisions with the residual gas molecules and to prevent breakdown on the application of the focusing field, potentials of typically 40 kV being applied throughout the storage period. Vacuum tank sections removed from the ring are shown in figure 1.7 with the thin-walled section nearest the floor.

The magnets were shimmed to provide such an accurate homogeneous field and each block was continuously monitored and stabilized at one point using a nuclear magnetic resonance (NMR) probe and two compensating coils wound around the yoke.[32] An accurate knowledge of the stability of the field was essential so 37 of the blocks had "plunging" probes attached to the vacuum tank. The NMR probes, multiplexed to eight automatic magnetometers, could be driven into the storage tank radially on the median plane, under computer control, and within ten minutes could measure over 400 points. Such measurements were performed at least twice a day during physics runs. Between runs the vacuum tank was removed and a mapping machine, shown in figure 1.8, employing 8 NMR probes attached to the same magnetometers, measured the field at over 250,000 mesh points, a complete scan taking 10 hours. By using a cycling method when switching on the magnets the field could be restored reproducibly

within the errors of the measuring system. Careful calibration of the NMR probes and corrections for the presence of the vacuum tank, inflector and probes during normal running conditions allowed the plunging probe measurements to be related directly to the overall field map. With strict monitoring of the stability of the 2 MW magnet power supply, cooling water temperature and ambient (g-2) experimental hall temperature, the average magnetic field experienced by the muon ensemble could be estimated to better than 3 ppm with an accurate knowledge of short-term and long-term stability.

The muons circulated the storage region with a rotation period of 147 ns. The precession period, given by $2\pi/\omega_a$, was 4.3 μs. By following the initial bunch, up to 40 μs into the detection period, fast rotation analysis yielded a mean radius of the muon ensemble accurate to $\pm$ 1 mm. The decay modes for the muons in flight were:

$$\mu^+ \rightarrow e^+ + \bar{\upsilon}_\mu + \upsilon_e \qquad (1.17)$$

$$\mu^- \rightarrow e^- + \upsilon_\mu + \bar{\upsilon}_e \qquad (1.18)$$

By only accepting decay electrons above a certain energy in the lab ensured that they decayed in the forward direction in the muon rest frame.[20] As the electrons generally have lower momentum than the muon, they decay on the inside of the ring. Of the two hundred stored muons only about thirty produced electrons above the energy threshold. These were detected using twenty energy measuring shower detectors, in the form of lead plastic scintillator sandwiches[29], shown in figure 1.9, distributed around the ring. For each decay

electron the time of decay, pulse height (in five bins) and counter number were recorded using a Digitron system[33,34] interfaced with a PDP11/20 computer through CAMAC. Each shower counter pulse was fanned-out six ways to yield a timing channel and five energy levels. The timing channel was input to a Time Quantizer, to place the times in the nearest 10 ns time-bin, before input to one of five Digitrons covering the twenty detectors and a sixth handling all counters to study the queueing losses at high rates.[25] The arrival times of the decay electrons were measured relative to the proton pick-up pulse with a resolution better than 10 ns over the 650 μs detection period. The Digitron Controller used the same 100 MHz master clock as employed by the NMR magnetometers. The entire system was rigourously checked on-line and off-line for timing errors and queueing losses.[35,36]

A seventh Digitron handled pulses from the five muon electric dipole moment (EDM) counters.[37] These were twin thin scintillator counters designed to cover an active area similar to the shower counters as shown in figure 1.9. The two arms were mounted vertically above each other to cover the upper and lower areas of the magnet pole gap, thus being referred to as "up" and "down" counters. They were used to search for a vertical component to the precession frequency which would be caused if an EDM existed. Thus the two scintillators labelled the decay electron as being above or below the median plane. This did not correspond to an upward - or downward - going electron as not all of the muons decayed from the median plane. Corrections were made using a Monte Carlo simulation. The twin scintillators, of equal efficiency, were adjusted vertically to give equal numbers of counts in the "up" and "down" counters. This ensured that the split

between them corresponded to the centre of the stored muon population, which was not necessarily half way between the pole pieces due to a small radial component of the magnetic field displacing the median plane.

The shower counters suffered gain changes throughout the detection period due to the high flux of particles at injection saturating the photomultipliers.[38] The effect was minimized by blanking the dynode chains for the first few microseconds of the cycle. The gain function was measured using a system of light-emitting diodes (LED's), attached to the shower counters. A fixed pattern of pulses were applied to the counters, using the LED's, along with normal beam injection. Analysis of the responses throughout the detection period showed that the counters closest to the inflector had the steepest gain curves and they were thus removed from the overall (g-2) analysis.[39]

A detailed study was made of the muon losses and proton contamination of the π^+ injection, the beam being unseparated. With the negative polarity the anti-proton background was negligeable. The muon detector consisted of four scintillator counters, each preceded by two-radiation-length lead absorbers. The muons could be discriminated from electrons on the basis of pulse height and a small five-gap optical spark chamber which confirmed their straight trajectories.[39]

A method of electric scraping was devised, using the electrostatic quadrupoles, to remove the muons in orbits closest to the storage region extremities at early times. By moving the

ensemble downwards and sideways, with the vertical and horizontal fields, the muons with the largest betatron oscillations in the horizontal plane could be removed by inserting aperture stops. The scraping voltages were applied for the first few microseconds and then the muon ensemble was allowed to return adiabatically to the centre of the storage region, with those muons most likely to be lost removed.

Employing the above experimental methods, along with exhaustive calibrations and checks for systematic errors, the errors in the analysis could be limited to purely statistical fluctuations. Other small order corrections due to betatron oscillations[40] and pitch corrections[41] had to be included in the overall results.

1.3 The Need for a Drift Chamber Array

As described in the preceding sections, an important parameter that had to be determined accurately for the (g-2) analysis was the mean magnetic field experienced by the muon ensemble during the storage period. Thus not only did the magnetic field have to be known precisely over the entire storage volume but also the distribution of the muon radii. Using fast rotation analysis, described in the following section, the mean radius of the muon sample could be determined to $\pm$ 1 mm using data taken during the first 40 μs of the (g-2) storage period. An independent check of this value could be achieved by using an array of drift

chambers to track the decay electrons back into the storage region to their positions of birth. It was hoped that the drift chamber array would yield results for the muon distribution to a greater accuracy than that obtainable from fast rotation analysis. Also the drift chamber array would be able to detect decay electrons throughout the entire 650 μs detection period and thus be able to determine if there was any shift in the distribution with time - an effect which the fast rotation analysis would be unable to detect.

From momentum analysis of the decay electrons an independent calibration of the energy resolution of the shower counters would be possible.

Knowing the arrival times of the decay electrons would enable a time distribution to be constructed, which would show the structure of the (g-2) precession frequency, and thus confirm that the (g-2) data was due to decay electrons only and did not have a contribution from lost muons.

Additional use of three MWPC's,[42] which are not described in detail in this thesis, within the array of eight drift chambers would yield vertical co-ordinate information. This would confirm whether the decay electrons were travelling horizontally and if they had decayed from the median plane of the storage region.

Figure 1.10 shows the location of the drift chamber array in the thin-walled field-free vacuum tank section immediately across the ring from the inflector and upstream of the EDM counter and shower counter C10. Positioning the drift chamber array in this

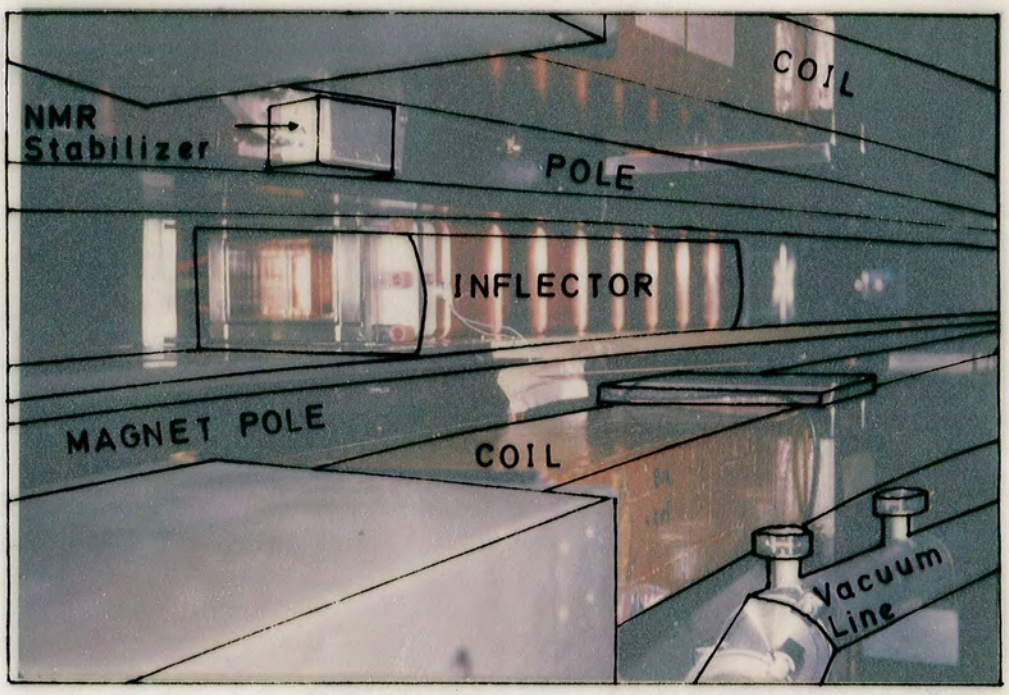

FIG. 1.6: THE INFLECTOR

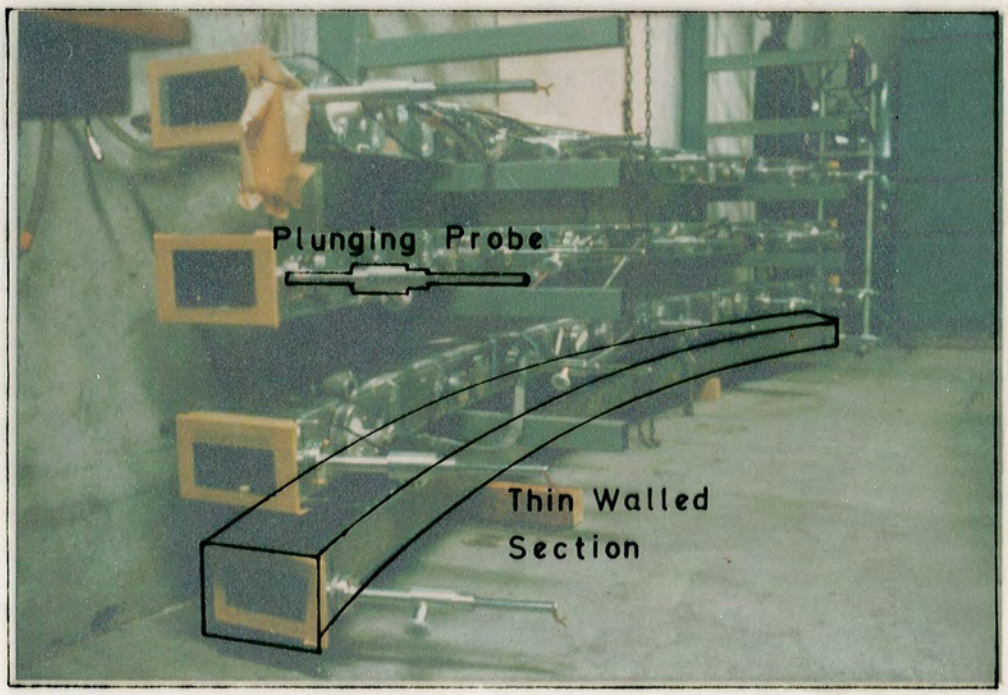

FIG. 1.7: VACUUM TANK SECTIONS

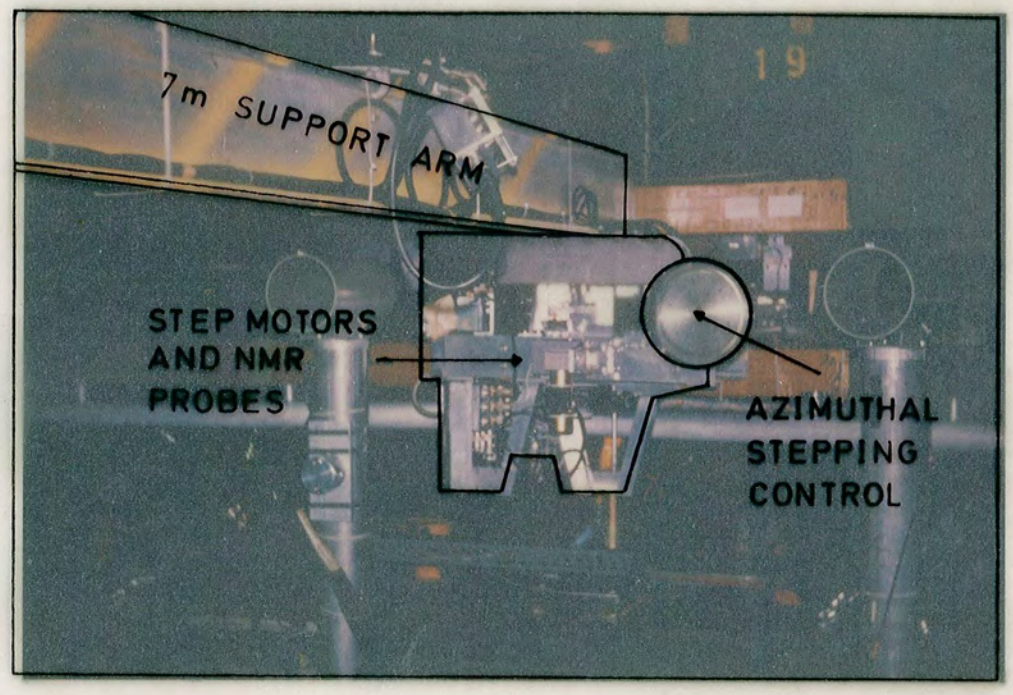

FIG. 1.8 : FIELD MAPPING MACHINE

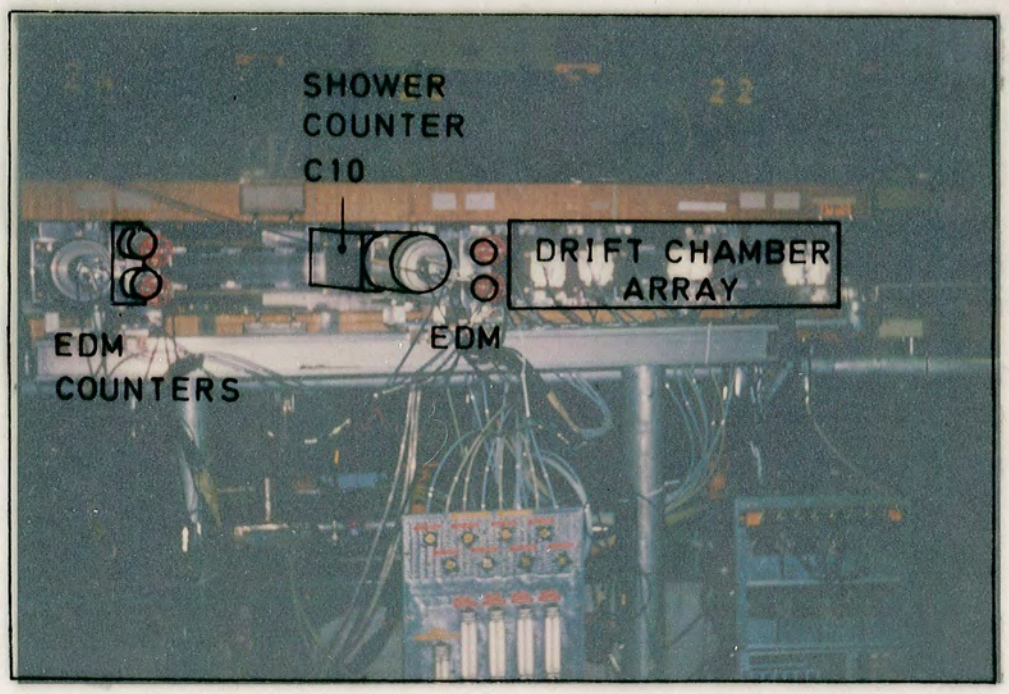

FIG. 1.9 : SHOWER AND EDM COUNTERS

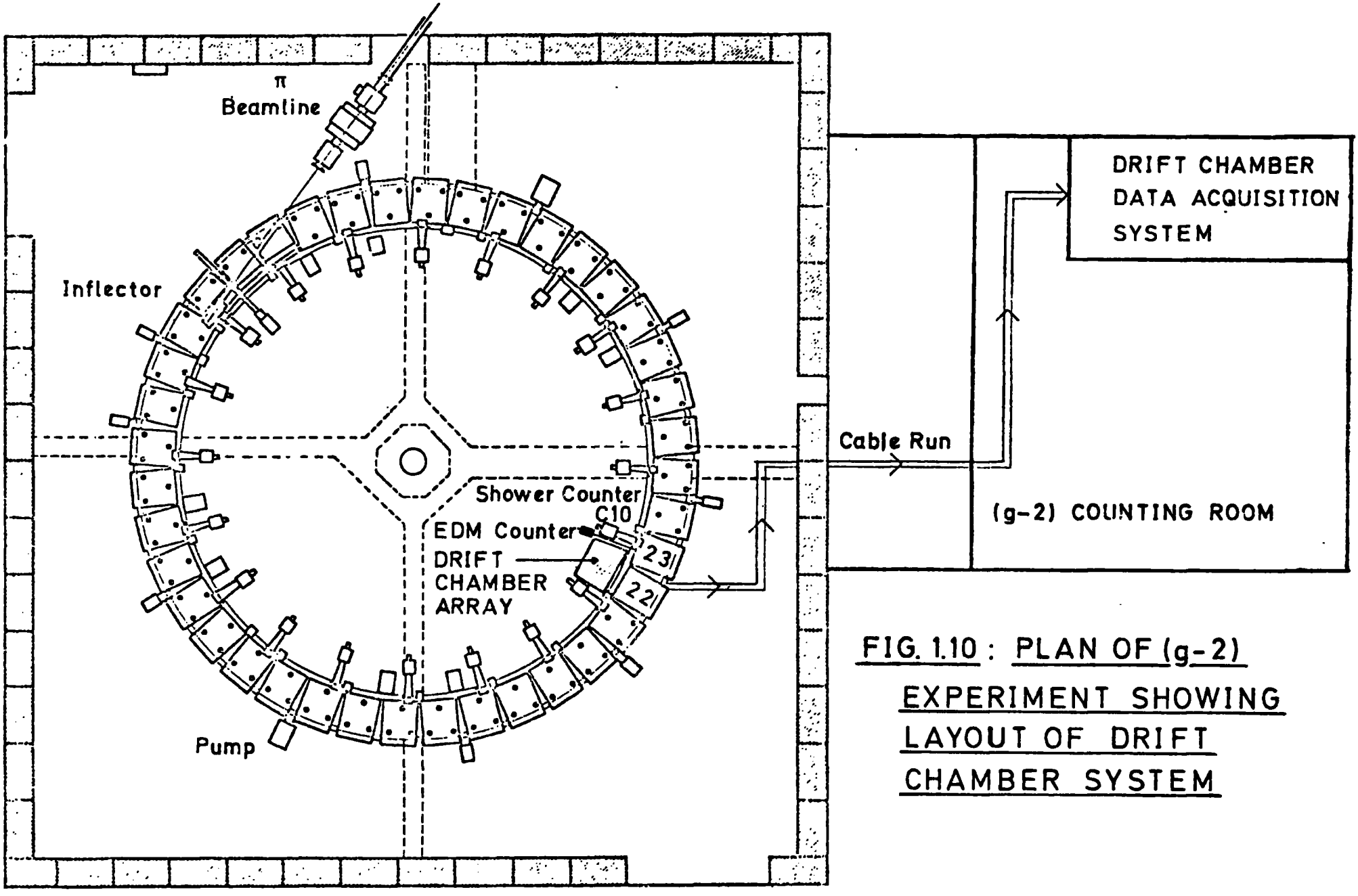

FIG. 1.10 : PLAN OF (g-2) EXPERIMENT SHOWING LAYOUT OF DRIFT CHAMBER SYSTEM

section of the ring prevented distortion of the decay electron tracks by the pulsed electrostatic focusing field and also reduced showering of the decay electrons on their passage through the vacuum tank wall.

Drift chambers were used in preference to MWPC's or spark chambers due to their inherently better spatial resolution and low cost of construction and associated electronics. Initial work on the use of drift chambers in homogeneous magnetic fields in the region of 1.5T[43] suggested that a spatial resolution of 200 μm was attainable with correct field compensation, as described in Chapter 2. It was expected that the inhomogeneous (g-2) fringe field would slightly worsen this value. However, using MWPC's with a sense wire spacing of 2 mm would yield a resolution of 1 mm and spark chambers could be expected to have resolutions of the same order,[2] especially considering that the chambers were required to be as narrow as possible in order to detect several points on a track over a short distance in azimuth. However spark chambers are not continuously sensitive and would have to be triggered using shower counter C10.

Initial simulations of track reconstructions[44] using arrays of various geometries and an approximation to a homogeneous fringe field, extending 20 cm radially inwards from the centre of the storage volume, indicated the errors for various resolutions.

Using MWPC's with 2 mm wire spacing, and a resolution of 1 mm, and assuming four points on the track over 60 cm in azimuth, indicated that the error in the determination of the muon radius would range from 3 mm at 750 MeV/c momentum through 10 mm at

1500 MeV/c to 48 mm at 2500 MeV/c. By halving the wire spacing to 1 mm, and increasing the resolution to 0.5 mm, the corresponding errors in the muon radii were halved. Thus, assuming a maximum resolution of 200 μm for the drift chambers, the errors could be reduced to 0.8 mm, 2.5 mm and 12 mm respectively by extrapolation of the trend in improvement of determination. Addition of further points to the trajectory would reduce the error further. However for lower momentum decay electrons the acceptance of the array, due to geometrical considerations of its length in azimuth and the chambers only extending 14 cm inwards from the vacuum tank wall, would prevent more than five points being detected.

Thus drift chambers were the obvious choice of detector to obtain such an accuracy despite the increased difficulties associated with operating themin inhomogeneous magnetic fields. The exact geometrical layout of the drift chamber array and the relevant design considerations are discussed in Chapter 3.

1.3.1. Fast Rotation Analysis

The injected bunch of muons was initially spread over about 3 m in azimuth or 10 ns in time as opposed to the revolution time around the ring of 147 ns. Hence at early times the counting rate was modulated at the rotation frequency of the bunch. However as the muons were spread across phase-space there was a distribution in radii and the muons on the inside of the ring took a shorter time to revolve than those on the outside, as shown in figure 1.11. The muons on the outside of the ring had to travel an extra distance of

$2\pi r$ per turn, neglecting betatron oscillations, and therefore the bunch widened and eventually overlapped itself. A least squares fit to the time intervals between peaks, T_{1-3} in Figure 1.11, enabled the mean of the momentum distribution to be calculated, and a study of the broadening of the bunch structure, W_{1-4}, allowed a calculation of the radial distribution of the bunch.[13]

Comparison was made with a Monte Carlo orbit tracking program to obtain the correction for the previously assumed ideal phase-space distribution. In fact analysis of data up to 40 μs into the (g-2) detection period revealed a distribution due to uniform filling of the available phase space shifted radially outwards by 2 mm and narrowed by about two percent by the closed orbit distortion in the electrode-free sections.[45] A section of the data is shown in figure 1.12.

1.4 Results from the (g-2) Experiment

The final results from the latest (g-2) experiment represent the analysis of 140 million muon decays. The time distribution of the decay electrons has been displayed in figure 1.3.

The final results for the muon anomalies, after taking account of all correction terms,[25] are:

$$a_{\mu^+} = 1165910(12) \times 10^{-9} \qquad (10 \text{ ppm})$$

$$a_{\mu^-} = 1165936(12) \times 10^{-9} \qquad (10 \text{ ppm})$$

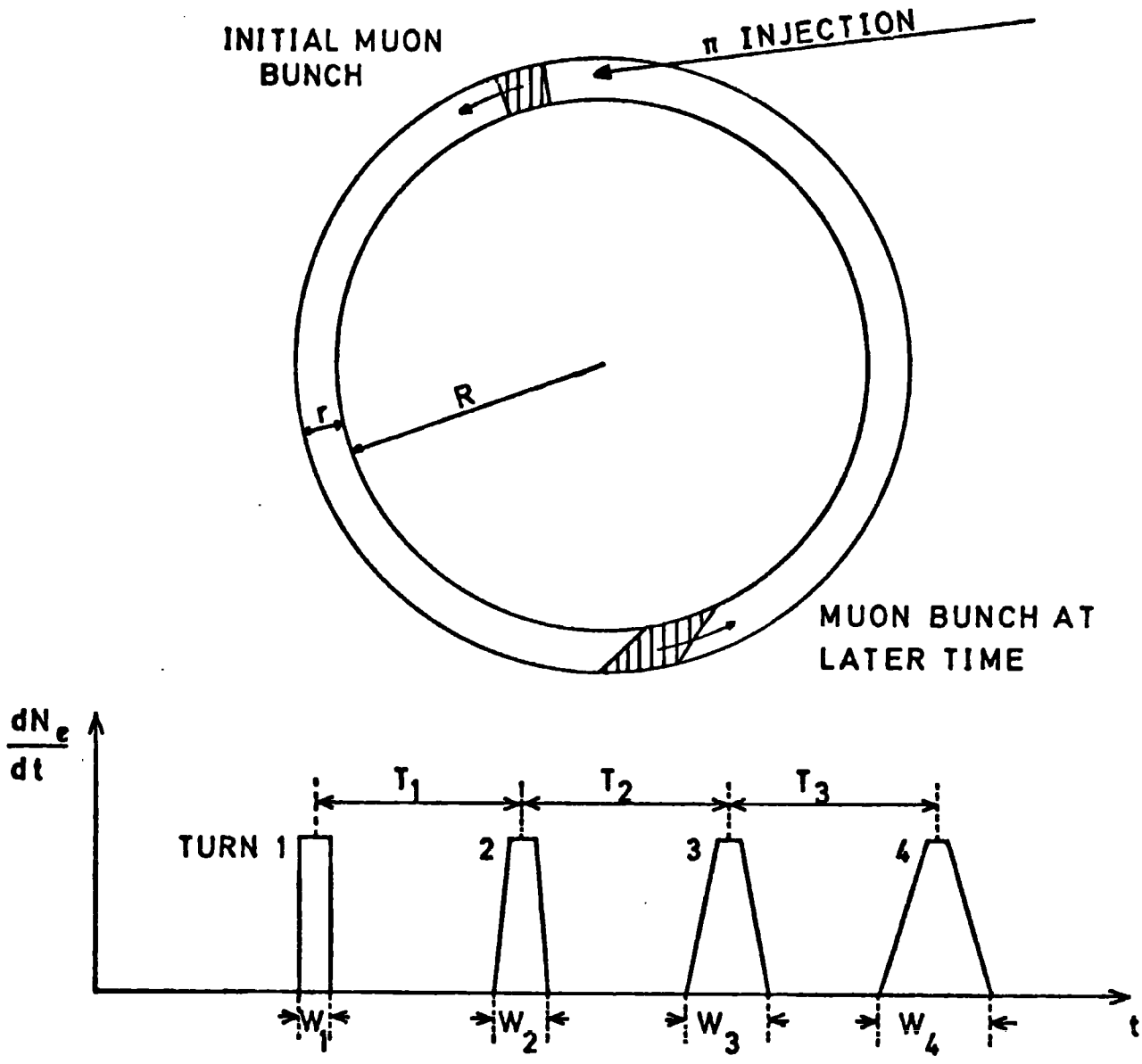

FIG. 1.11 : FAST ROTATION ANALYSIS SHOWING DEVELOPMENT OF MUON BUNCH

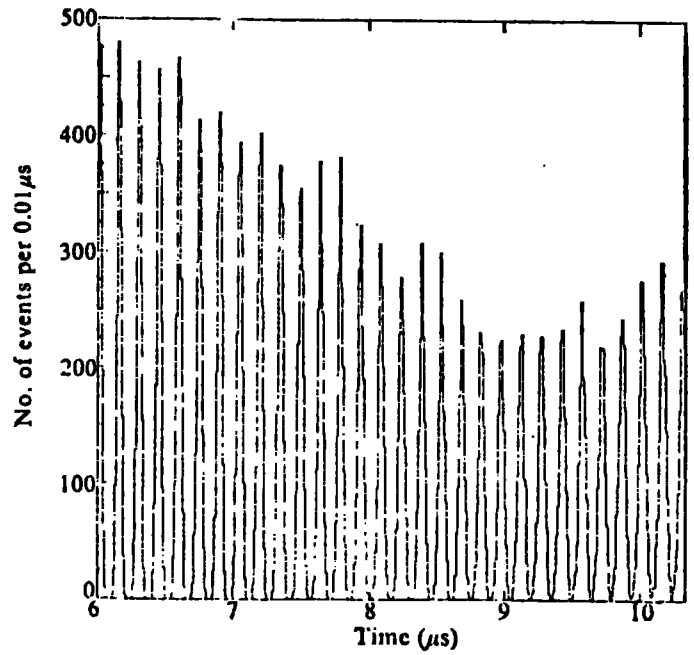

FIG. 1.12 : (g-2) FAST ROTATION DATA

giving an overall weighted mean of

$$a_\mu = 1165922(9) \times 10^{-9} \qquad (8 \text{ ppm})$$

Compared with the latest theoretical value of

$$a_\mu^{(\text{theory})} = 1165921(10) \times 10^{-9} \qquad (9 \text{ ppm})$$

Hence the agreement with QED theory is remarkable and the muon appears to behave as predicted with no indication of a coupling to an unknown force. Hence the mass difference between the muon and electron of $m_\mu / m_e = 206.84$ remains as one of the mysteries of nature.

The difference between the g-factors for positive and negative muons yields:

$$(g_{\mu^-} - g_{\mu^+}) / g = 0.026 \pm 0.017 \text{ ppm}$$

which represents the most accurate check of the CPT theorem applied to muons.

Calculations of the relativistic lifetimes, τ, of the positive and negative muons[39] using the fitting equation (1.9) for a γ of 29.327(4) and the corresponding lifetime at rest, τ_o, given by $\tau = \gamma\tau_o$ are:

$$\tau^+ = 64.419(58)\ \mu s \qquad \tau_o^+ = 2.1966(20)\ \mu s$$

$$\tau^- = 64.368(29)\ \mu s \qquad \tau_o^- = 2.1948(10)\ \mu s$$

giving a weighted average of

$$\tau_{\mu^+ + \mu^-} = 64.378(26)\ \mu s \qquad \tau^o_{\mu^+ + \mu^-} = 2.1952(9)\ \mu s$$

The most accurate value for τ_o^+ [46] to date is 2.19711(8) μs. Hence the fractional difference between the (g-2) value derived from $\tau_o^+ = \tau^+ / \sqrt{\gamma}$ and the most accurate value is 2×10^{-3}, at the 95% confidence level, and represents the most accurate test of relativistic time dilation to date.

For negative muons the most accurate value of τ_o^- was [47] 2.198(2) μs so the (g-2) value, assuming the correctness of special relativity, is the most precise value to date.

Comparing this value with the high-precision value of τ_o^+, the fractional difference gives:

$$(\tau_o^- - \tau_o^+) / \tau_o^+ = -0.00105(46)$$

or at the 95% confidence level the difference is in the range -0.002 to -0.00013. This limit, which should vanish by CPT invariance of the weak interaction, is comparable to the best direct measurement[47] of τ_o^- / τ_o^+.

The muon revolving around the (g-2) ring has a transverse acceleration of about 10^{18}g and may be considered as the moving clock in the so called "twin or clock paradox",[48,49] the stationary clock being the muon decaying at rest. The 0.1% precision in the time dilation factor at a transverse acceleration of 10^{18}g is the most accurate test to date.

It has been suggested that special relativity breaks down at small distances and Redei has calculated a correction for the muon lifetime in flight[39]:

$$\tau = \gamma \tau_o \left[1 + (2.5 \times 10^{24} \gamma^2 b^2) \right] \qquad (1.19)$$

where b is in centimetres. From the (g-2) value of τ^+ the limit on b at the 95% confidence level is

$$b \leq 9.6 \times 10^{-16} \text{ cm}$$

which puts an upper limit on the granularity of space-time.[49]

The independent EDM experiment[37] sought to measure the muon's electric dipole moment. The existence of such a moment would alter the precession frequency of the muon so that equation (1.8) becomes:

$$\vec{\omega} = -\frac{e}{mc}\left\{ a\vec{B} + \left(\frac{1}{\gamma^2 - 1} - a\right)\vec{\beta} \times \vec{E} + \frac{f}{2}\left(\vec{E} + \vec{\beta} \times \vec{B}\right)\right\} \quad (1.20)$$

where the dipole moment is defined in analogy with the magnetic moment as:

$$D \equiv (f/2)(e\hbar/2mc) \quad (1.21)$$

As the electric field was small compared to the magnetic field, and the "magic" value of γ was used, the precession frequency became:

$$\vec{\omega} = \vec{\omega}_a + \vec{\omega}_{edm} = -\frac{e}{mc}\left(a\vec{B} + \frac{f}{2}\vec{\beta} \times \vec{B}\right) \quad (1.22)$$

This would cause the plane of the spin precession to tilt and the (g-2) precession frequency would appear to increase. The EDM contribution would introduce a vertical component which would constitute the directly observable effect seen by studying the number of decay electrons travelling upwards and downwards from the muon decay. Results calculated from 11.4 million decay electrons yielded the values:

$$D_{\mu^+} = (8.6 \pm 4.5) \times 10^{-19} \text{ e.cm}$$

$$D_{\mu^-} = (0.8 \pm 4.3) \times 10^{-19} \text{ e.cm}$$

Assuming the CPT theorem for muons the combined value was:

$$D_{\mu} = (3.7 \pm 3.4) \times 10^{-19} \text{ e.cm}$$

One standard deviation errors being quoted.

At 95% confidence $|D_\mu| \leq 1.05 \times 10^{-18}$ e.cm which represents a factor of 27 improvement over the previous best direct measurement realised in the first (g-2) experiment at CERN[8].

By assigning to the EDM contribution the entire deviation of the experimental value of ω_a from theory, in the latest (g-2) experiment, would yield an upper limit of $|D_\mu| \leq 0.74 \times 10^{-18}$ e.cm at 95% confidence which is comparable to the above result.

Hence apart from measuring the anomalous magnetic moment of the muon to the highest accuracy to date, and thus confirming QED theory related to the muon, the latest (g-2) experiment has provided stringent tests of special relativity and the CPT theorem relating to muons, plus a new upper limit to the EDM of muons.

REFERENCES

1) Charpak, G., Bouclier, R., Bressani, T., Favier, J., Zupancic, C.,
Nucl. Instr. Meth. 62 (1968) 235

2) See for example the review in:
Rice-Evans, P.,
Spark, Streamer, Proportional and Drift Chambers, (Richelieu Press) 1974 Chap. 3

3) Bressani, T., Charpak, G., Rahm, D., Zupancic, C.,
Track Localization by means of a Drift Chamber, Proc. Internat. Seminar on Filmless Spark and Streamer Chambers, Dubna, 1969 (JINR, Dubna, 1969) p. 275

4) Charpak, G., Rahm, D., Steiner, H.,
Nucl. Instr. Meth. 80 (1970) 13

5) Walenta, A. H., Heintze, J., Schurlein, B.,
Nucl. Instr. Meth. 92 (1971) 373

6) a) Bailey, J. M., Combley, F. H., Hattersley, P.M.,
Proposal to Measure the Anomalous Magnetic Moment of the Muon at a Level of 10-20 ppm
Daresbury Lab Selection Committee
DNPL/SCP 77 1972

b) Bailey, J. M., Farley, F. J. M., Jostlein, H., Petrucci, G., Wickens, F.,
CERN Electronics Experiments Committee
PH I/COM-69/20 19th May 1969

7) Charpak, G., Farley, F. J. M., Garwin, R. L., Muller, T., Sens, J. C., Telegdi, V. L., Zichichi, A.,
Phys. Rev. Letters 6 (1961) 128

8) Charpak, G., Farley, F. J. M., Garwin, R. L., Muller, T., Sens, J. C., Zichichi, A.,
Nuovo Cimento 22 (1961) 1043

9) Charpak, G., Farley, F. J. M., Garwin, R. L., Muller, T., Sens, J. C., Zichichi, A.,
Phys. Letters 1 (1962) 16

10) Charpak, G., Farley, F. J. M., Garwin, R. L., Muller, T., Sens, J. C., Zichichi, A.,
Nuovo Cimento 37 (1965) 1241

11) Farley, F. J. M., Bailey, J. M., Brown, R. C. A., Giesch, M., Jostlein, H., van der Meer, S., Picasso, E., Tannenbaum, M.,
Nuovo Cimento 45 (1966) 281

12) Bailey, J. M., Bartl, W., von Bochmann, G., Brown, R. C. A., Farley, F. J. M., Jostlein, H., Picasso, E., Williams, R. W.,
Phys. Letters 28B (1968) 287

13) Bailey, J. M., Bartl, W., von Bochmann, G., Brown, R. C. A., Farley, F. J. M., Giesch, M., Jostlein, H., van der Meer, S., Picasso, E., Williams, R. W.,
Nuovo Cimento 9A (1972) 369

14) Bailey, J. M., Picasso, E.,
Progr. in Nucl. Phys. 12(I) (1970) 43

15) Combley, F. H., Picasso, E.,
Phys. Reports 14C (1974) 1

16) Lautrup, B. E., Peterman, A., de Rafael, E.,
Phys. Reports 3C (1972) 193

17) Rich, A., Wesley, J. C.,
Rev. Mod. Phys. 44 (1972) 250

18) Farley, F. J. M.,
Contemp. Phys. 16 (1975) 413

19) Calmet, J., Narison, S., Perrottet, M., de Rafael, E.,
Rev. Mod. Phys. 49 (1977) 21

20) Combley, F. H.,
1975, Proc. 7th Internat. Symposium on Lepton and Photon Interactions at High Energies, Stanford, 1975 (ed. W.T.Kirk) (Stanford Univ., Stanford) p. 913

21) Calmet, J., Peterman, A.,
Phys. Letters 56B (1975) 383

22) Cohen, E. R., Taylor, B. N.,
Journal of Physical and Chemical Reference Data 2 (1973) 663

23) Field, J. H.,
Proc. EPS Internat. Conf. on High-Energy Physics, Palermo, 1975
(Editrice Compositori, Bologna, 1976) p. 247

24) Bargmann, V., Michel, L., Telegdi, V. L.,
Phys. Rev. Letters 2 (1959) 435

25) Bailey, J. M., Borer, K., Combley, F., Drumm, H., Farley, F. J. M., Field, J. H., Flegel, W., Hattersley, P. M., Krienen, F., Lange, F., Picasso, E., von Euden, W.,
Phys. Letters 68B (1977) 191

26) James, F., Roos, M.,
MINUIT Comp. Phys. Comm. 10 (1975) 343
and CERN Computer Centre Long Write-Ups
D506, D516 20/6/74

27) Borer, K., Lange, F.,
Nucl. Instr. Meth. 143 (1977) 219

28) Crowe, K. M., Hague, J. F., Rothberg, J. E., Schenck, A., Williams, D. L., Williams, R. W., Young, K. K.,
Phys. Rev. D5 (1972) 2145

29) Bailey, J. M., Bassompierre, G., Borer, K., Combley, F., Hattersley, P., Lebee, G., Petrucci, G., Picasso, E., Pizer, H. I., Runolfsson, O., Tinguely, R.,
CERN NP Internal Report 70-13

30) Borer, K., Drumm, H., Eck, C., Petrucci, G., Runolfsson, O.,
Proc. 5th Internat. Conf. on Magnet Technology, Rome, 1975 (Lab. Naz., CNEN, Rome, 1975) p. 133

31) Flegel, W., Krienen, F.,
Nucl. Instr. Meth. 113 (1973) 549

32) Borer, K.,
Nucl. Instr. Meth. 143 (1977) 203

33) Pizer, H. I.,
CERN NP Electronics Development I Report 72-1

34) Pizer, H. I., van Koningsveld, L., Verweij, H.,
CERN EP Internal Report 76-17

35) Pizer, H. I.,
Nucl. Instr. Meth. 123 (1975) 461

36) Field, J. H., Lange, F., von Ruden, W.,
Nucl. Instr. Meth. 143 (1977) 227

37) Bailey, J. M., Borer, K., Combley, F., Drumm, H., Farley, F. J. M.,
Field, J. H., Flegel, W., Hattersley, P. M., Krienen, F.
Lange, F., Picasso, E., von Ruden, W.,
CERN Preprint 6/7/77 Submitted to
Journal of Physics G (Nuclear Physics)

38) Farley, F. J. M., Carter, B. S.,
Nucl. Instr. Meth. 28 (1964) 279

39) Bailey, J. M., Borer, K., Combley, F., Drumm, H., Krienen, F.,
Lange, F., Picasso, E., von Ruden, W., Farley, F. J. M.,
Field, J. H., Flegel, W., Hattersley, P. M.,
Nature 268 (1977) 301

40) Field, J. H., Fiorentini, G.,
Nuovo Cimento 21A (1974) 297

41) Farley, F. J. M.,
Phys. Letters 42B (1972) 66

42) Cunningham, R. A., Taylor, D. G., Walker, R. P.,
Daresbury Laboratory Preprint
DL/P 274 (Instrumentation) May 1977
submitted to Nucl. Instr. Meth.

43) Charpak, G., Sauli, F., Duinker, W.,
Nucl. Instr. Meth. 108 (1973) 413

44) Field, J. H.,
(g-2) Group Internal Note 5/12/72

45) Bailey, J. M., Borer, K., Combley, F., Drumm, H., Eck, C., Farley, F. J. M., Field, J. H., Flegel, W., Hattersley, P. M., Krienen, F., Lange, F., Petrucci, G. Picasso, E., Pizer, H. I., Runolfsson, O., Williams, R. W., Wojcicki, S.,
Phys. Letters 55B (1975) 420

46) Balandin, M. P., Crebenyuk, V. M., Zinov, V. G., Konin, A. D., Ponomarev, A. N.,
Soviet Phys. JETP 40 (1974) 811

47) Meyer, S. L., et al.,
Phys. Rev. 132 (1963) 2693

48) Farley, F. J. M., Bailey, J. M., Picasso, E.,
Nature 217 (1968) 17

49) Wilkie, T.,
Nature 268 (1977) 295

CHAPTER 2

THE DRIFT CHAMBER PRINCIPLE

2.1 Introduction

This chapter describes the various constructional philosophies of drift chambers in use today and the factors determining the accuracy of their operation. The processes occurring within the gaseous volume are outlined and a comparison of the commonly used gas mixtures is made. Factors governing the positional accuracy and efficiency of the chambers are discussed. The use of drift chambers in a magnetic field, as in the case of the (g-2) chambers, is covered with regard to operating techniques and expected results. Methods of combating the inherent left/right ambiguity are described. Finally a brief review is made of present and future uses of drift chambers as well as hybrid derivations designed for specific tasks.

2.2 Drift Chamber Design

The positional information is derived from a knowledge of the drift time and the drift velocity. The drift time is defined as the delay between the time of traversal of the particle, normally provided by a scintillator, and the manifestation of a pulse on the sense wire. The drift velocity is primarily dependent upon the gas mixture and the electric field applied to the gaseous volume.

Three basic design philosophies have been used in drift chamber construction since their inception. The main difference between them lies in the homogeneity of the electric field produced over the chamber and hence determines the characteristic spatial resolution and space-time relationship across the detection region. The maximum length of the drift space depends upon the type of construction.

The first type, reported by Walenta et al.[1] in 1971 and developed by the Heidelberg group, was a direct extension from the MWPC with the sense wire spacing increased to 1 cm. As shown in figure 2.1, field wires were placed alternately between the sense wires to maintain a high electric field across the cell. Typical chamber parameters are also displayed. The field wires were either maintained at the cathode voltage or at a negative potential with respect to it.[2] However the field was still inhomogeneous, as shown, causing non-linearity of the space-time relationship due to varying drift velocities across the cell and the paths taken by the electron swarms following the field lines. One solution was to use non-linear clocks to determine the drift distance.[3,4] By careful choice of the cathode spacing, applied field and gas mixture this method afforded an attractive mode of construction for large area chambers.[5] By either using strips of almost the inter-cathode gap width instead of field wires,[6,7] or large diameter sense wires[8] (100 μm instead of 20 μm), the electric field could be made more homogeneous throughout the

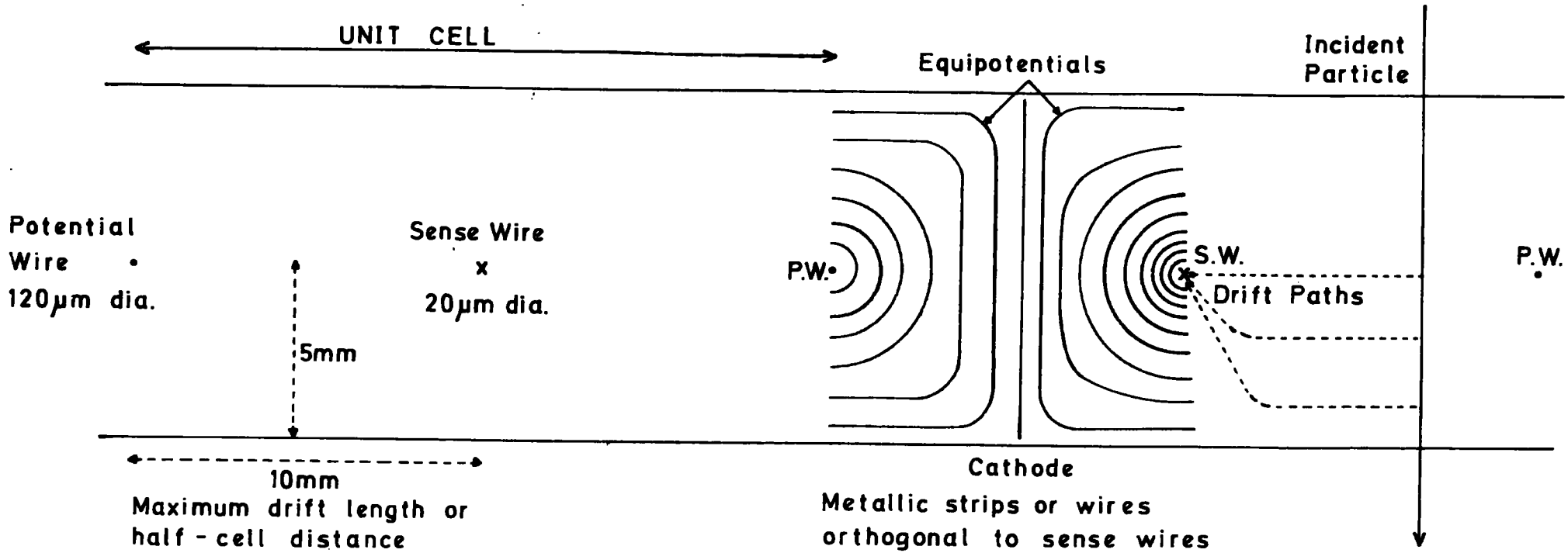

POTENTIALS

	i	ii
S.W.	0	+ve
Cathode	-ve	0 or -ve
P.W.	=cathode or more -ve	

FIG. 2.1 : MULTI-CELL DRIFT CHAMBER OF THE WALENTA TYPE

chamber volume. Spatial resolutions of up to 0.2 mm have been achieved and such chambers also operated in magnetic fields[9] without the need for field compensation due to the cylindrical nature of the electric field. However the cathode spacing must be comparable to the half-cell length, i.e. sense wire to field wire distance, so only short drift lengths may be used if close chamber packing is required.

The second type of chamber was developed at Saclay,[10] after initial work at CERN[11], and had the advantage of a completely homogeneous drift field as shown in figure 2.2. Drift lengths of up to 1 m proved feasible but involved the use of extremely high potentials. The electron swarms drifted in a unique direction towards a single sense wire. As the diffusion of the swarm is proportional to the drift distance, as shown later in this chapter, the resolution varied from 0.6 mm for a 10 cm drift length to 1.6 mm over 50 cm. For many applications such resolutions suffice and the method is cheap due to the low number of channels of electronics used per unit area.

The third mode of construction was developed at CERN by Charpak et al.[12] and is often called the adjustable field drift chamber (AFDC). The (g-2) chambers are of this type. Figure 2.3 shows the application of the graduated field and typical equipotentials in a half-cell. Although more difficult to construct, this type of chamber offers a much higher intrinsic spatial resolution, 60-100 μm being attainable in the absence of a magnetic field.[13,14,15] The cathode wires are mounted parallel

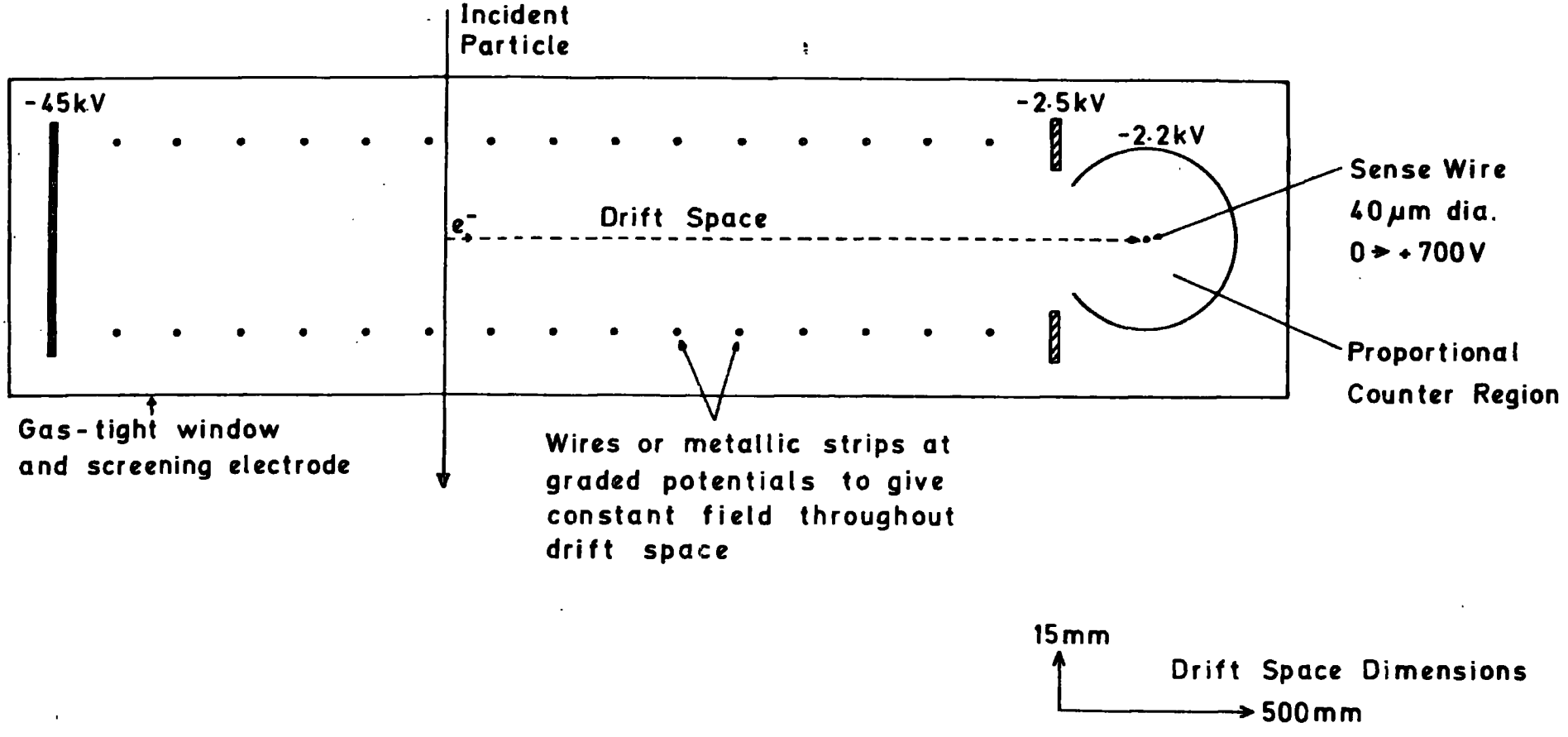

FIG. 2.2 : SINGLE-CELL DRIFT CHAMBER OF THE SACLAY TYPE SHOWING TYPICAL OPERATING PARAMETERS

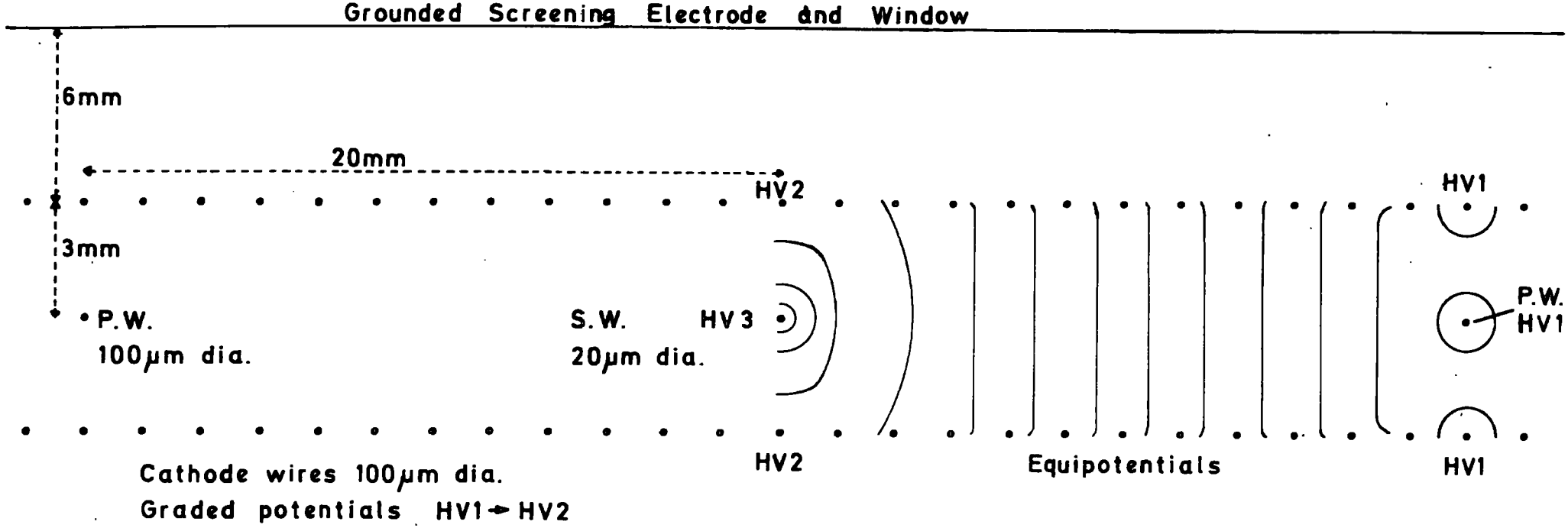

POTENTIALS	i	or	ii	
HV1	-ve		-ve	|HV1| > |HV2|
HV2	-ve		0	
HV3	0		+ve	

FIG. 2.3 : MULTI-CELL DRIFT CHAMBER OF THE ADJUSTABLE FIELD (CHARPAK) TYPE SHOWING TYPICAL PARAMETERS

to the sense wires and the graduated potentials produced using a voltage divider network, the maximum potential being applied to the field wires and the two neighbouring cathode wires. Either one supply may be used, as in the (g-2) drift chamber case, with the sense wires grounded and all cathode wires at negative potentials, or two supplies may be used to provide the drift field and a positive potential on the sense wire independently. The two supply system offers greater flexibility when studying chamber parameters such as the drift field and the acceleration field around the sense wire.

Chamber design is very dependent upon the specific application and type. The frames of chambers with wire cathode planes have to be strong as the wires are mounted under tension to prevent sagging and electrostatic repulsion. The frame also has to be light to enable easy manoeuvrability and, in some applications, to present the least density of absorber possible to the incident particles. Commonly used materials which fulfil these requirements are perspex and G10 - glass-fibre epoxy-resin. The chamber volume is made gas-tight using thin windows of melinex. In applications where the absorbtion length is not critical the cathode planes may be etched on printed circuit boards, which also serve as the chamber windows. This option is especially attractive for large chambers as rigid frames are no longer required. In all chambers the sense wires have to be of small diameter, typically 20 μm, and are accurately attached to connection boards on the chamber frame. As their positions have to be known precisely complex surveying

techniques are required in large arrays and overall chamber rigidity is important. Due to the attainable spatial resolutions of the chambers the overall mechanical tolerances of all components must be high. This applies not only to the positional accuracy of the sense wires but also to the inter-cathode gap which determines the electric field around the sense wire. The chamber frame must also support all electrical connections and provide means of flushing the chamber gas continuously.

A more detailed discussion of chamber design is given in Chapter 3 where the construction of the (g-2) chambers is explained.

2.3 Electron Processes in Drift Chambers

Having discussed the general design features of drift chambers and the methods of producing the electric fields it is pertinent at this stage to describe the electron processes occurring within the gaseous volume. Various processes occur from the time a particle traverses the chamber, leaving a trail of primary ionization, to the stage when the resultant electron swarms have drifted towards the sense wire, entered the avalanche region and formed a pulse on the wire. A diagrammatic representation of the processes is given in figure 2.4.

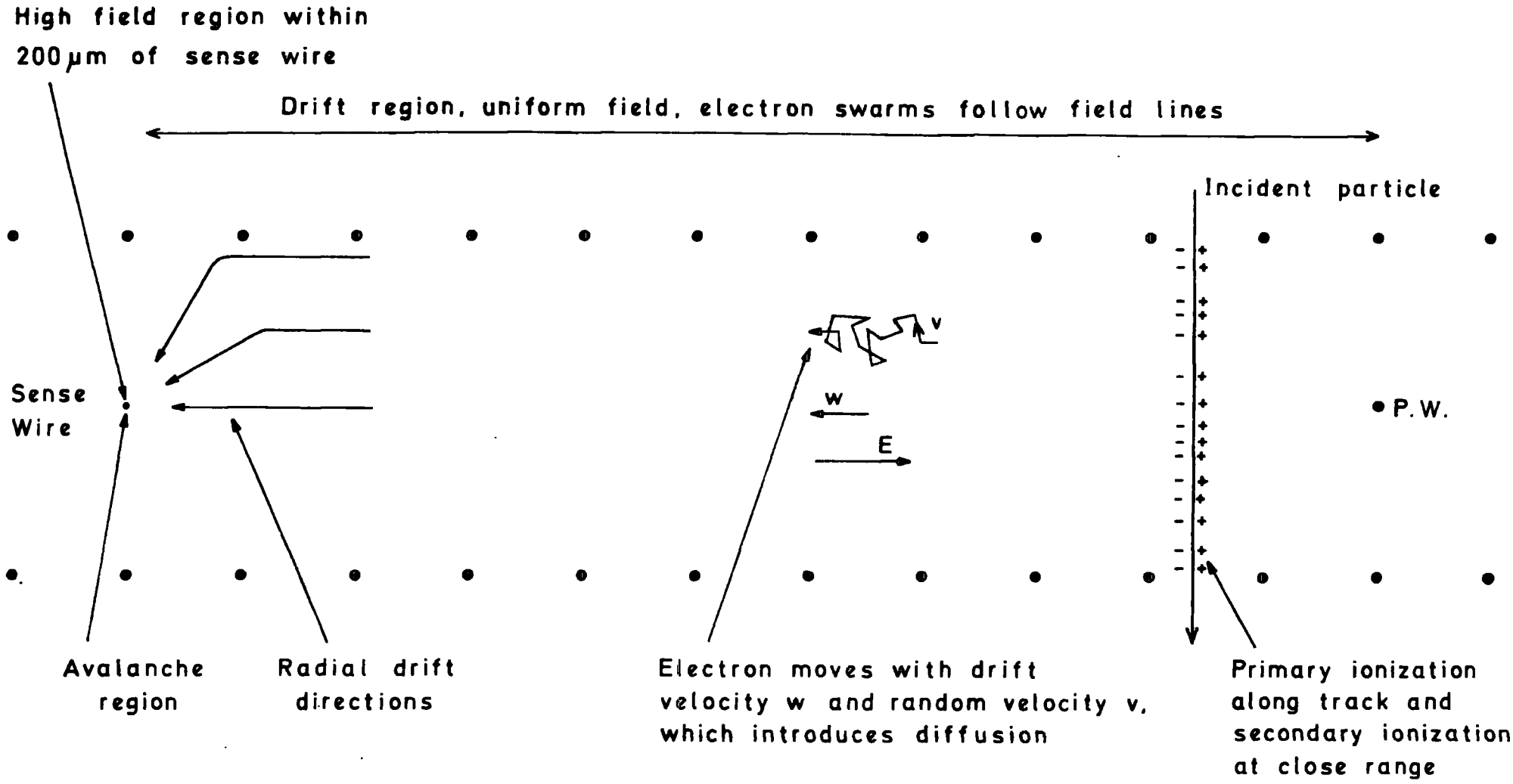

FIG. 2.4 : ELECTRON PROCESSES IN A DRIFT CHAMBER

2.3.1 Primary Ionization

The particle traversing the chamber liberates primary ion pairs along its path predominantly by inelastic Coulomb collisions. At the electron energies concerned in the (g-2) experiment, 1 - 3 GeV, the energy loss is on the flat part of the dE/dx curve and is thus constant. For the Ar 90%/CH_4 10% mixture used in the (g-2) chambers a relativistic electron typically deposits 2 keV per cm.[16] The primary electrons have typical energies of 70 eV, which is close to the maximum ionization cross-section of the gas, and a mean free path for ionizing collisions of about 1 μm. Hence the range of the electrons will be only a few microns as they quickly lose energy through elastic and excitation collisions as well as liberating two or three secondary electrons by further ionization before being stopped. Thus about 90 ion pairs/cm are formed in the gas. The distribution of the total energy of the primary electrons is of the Landau form which has a long tail at high energies. This is due to the formation of δ- electrons at short distances with high energy transfer. However even for δ-rays of 6 keV energy their range is less than 150 μm. By limiting the width of the chamber the probability of δ-ray formation is lessened and the initial track width is small. Once resolutions of better than 50 μm are attempted, however, the range of the primary electrons becomes an important factor and may, indeed, be the decisive limiting factor of attainable drift chamber resolution.

2.3.2. The Drift Process and Diffusion

The processes governing the drifting of the free electrons towards the sense wire are dependent upon the electric field and the gas mixture. This section deals only with electrons drifting in an electric field, the contributions associated with the additional presence of a magnetic field are dealt with in section 2.4.

If no electric field is present the free electrons quickly assume a characteristic thermal energy by elastic collisions with the gas molecules. This is given by the Maxwell formula $^3/_2$ kT corresponding to about 0.03 eV at room temperature and a velocity of 10^7 cm/s. If an electric field is applied the electrons maintain a random velocity, v, but also exhibit a small drift velocity, w, along the field direction. This is typically in the range 10^5 to 10^7 cm/s. The random velocity introduces a diffusion term which describes the uncertainty in position of a single electron or the deviation from the centroid of a swarm of electrons. Exhaustive studies have been made in the past regarding drift velocities in gases[17] but these mainly dealt with pure gases and not the mixtures normally associated with wire chamber operation. Recent studies by Palladino and Sadoulet[16,18] have extended the classical theories of electrons in gases to such mixtures and also considered the effects of operating in a magnetic field.

The free electron is continuously accelerated by the electric field, E, and reaches a stable drift velocity in about 10^{-11} s. The mean drift velocity in the direction of the sense wire plane

may be defined as:

$$w = \langle v_x \rangle = \iiint v_x \, F(\vec{r}, \vec{v}, t) \, d\vec{v} \qquad (2.1)$$

where $F(\vec{r}, \vec{v}, t)$ is the velocity distribution of the electrons at the point $\vec{r}$ at time t. In the presence of external fields F does not necessarily refer to a Maxwellian distribution.

The mobility is defined as:

$$\mu = w / E \qquad (2.2)$$

which is dependent upon the pressure and temperature, parameters which are normally constant for drift chambers. Unfortunately, however, μ is also a function of E, as is w, so the concept of mobility must be used with caution.

A swarm of electrons moving in a field E with drift velocity w travel a distance $x = wt$ in a time t with an associated longitudinal and lateral deviation due to diffusion. The diffusion coefficient, D, may be defined as the ratio between the net number of particles flowing through unit area per second, J, and the density gradient of the diffusing particles, ∇N to give Fick's Law of Diffusion:

$$J = - D \nabla N \qquad (2.3)$$

Alternatively, Townsend[17] expressed it in terms of the mean of the collision distance and velocity:

$$D = \langle l \, v \rangle / 3 \qquad (2.4)$$

It may be shown[16] that the rms of the dispersion of the electrons in one dimension is given by:

$$\sigma_x = \sqrt{\frac{2Dx}{W}} = \sqrt{\frac{2Dx}{\mu E}} = \sqrt{\frac{2\varepsilon_k x}{eE}} \qquad (2.5)$$

where $\varepsilon_k = eD/\mu \qquad (2.6)$

is known as the characteristic energy which is related to the electron temperature, T_e, and may be determined experimentally. Because of the ratio of the electron and molecular masses kinetic energy is not normally lost in elastic collisions due to momentum conservation. Thus in electric fields electrons have temperatures higher than the gas temperature given, in the usual notation, by:

$$^3/_2\ kT_e = \tfrac{1}{2}\ m_e\ v^2 \qquad (2.7)$$

A rigourous mathematical approach given by Palladino and Sadoulet[16] derived a formula for the drift velocity from the equations of motion. They used the thermal velocity, v, and the mean free path for electron collisions with gas molecules, l. Assuming that the differential cross-section for electron-molecule scattering was isotropic and allowing for non-constant collision frequencies with rise in energy yielded:

$$w = \frac{2eE}{3m}\left\langle\frac{l}{v}\right\rangle + \frac{eE}{3m}\left\langle\frac{dl}{dv}\right\rangle \qquad (2.8)$$

Assuming constant collision frequencies this expression naively becomes:

$$w = \frac{eE}{m}\left\langle\frac{l}{v}\right\rangle \qquad (2.9)$$

where the averaging is over the energy distribution of the electrons. Introducing a constant, C, for the type of distribution used gives:

$$w = C\ \frac{eE}{m}\frac{l}{v} \qquad (2.10)$$

Combining equations (2.2), (2.4), (2.7) and (2.9) leads to the relationship

$$D / \mu = kT_e / e \qquad (2.11)$$

which, by comparing with equation (2.6), shows the relationship between characteristic energy and electron temperature.

The Maxwellian distribution assumes that only elastic collisions occur and that the cross-section is proportional to v^{-1}. A better approximation is found to be the Druyvestian distribution which also assumes elastic collisions but a cross-section independent of v.

Attempts to theoretically simulate the relationships between drift velocity and diffusion with increasing electric field are complicated by the dependence of the characteristic energy with field, through w and D, as shown in figure 2.5 taken from reference 16 for theoretical and experimental results. Also experimental cross-section data for common drift chamber gas mixtures are either sparse or non-existent so approximations have to be made. Figure 2.6 shows the dependence of the cross-section for momentum transfer with electron energy, $\epsilon = \frac{1}{2} m_e v^2$, for argon taken from reference 16. The fractional energy loss per collision and mean free path are dependent upon the electron energy through power law relationships. For a constant cross-section the drift velocity increases with field as shown in equation 2.10. As seen in figure 2.6, towards the Ramsauer dip at 0.3 eV the cross-section falls and ϵ_k and w rise rapidly. For higher energies the cross-section rises and ϵ_k and w are almost constant. This continues until the tail of the energy distribution passes the excitation potential of 11.5 eV. At this stage the energy loss increases and w rises sharply and ϵ_k levels off.

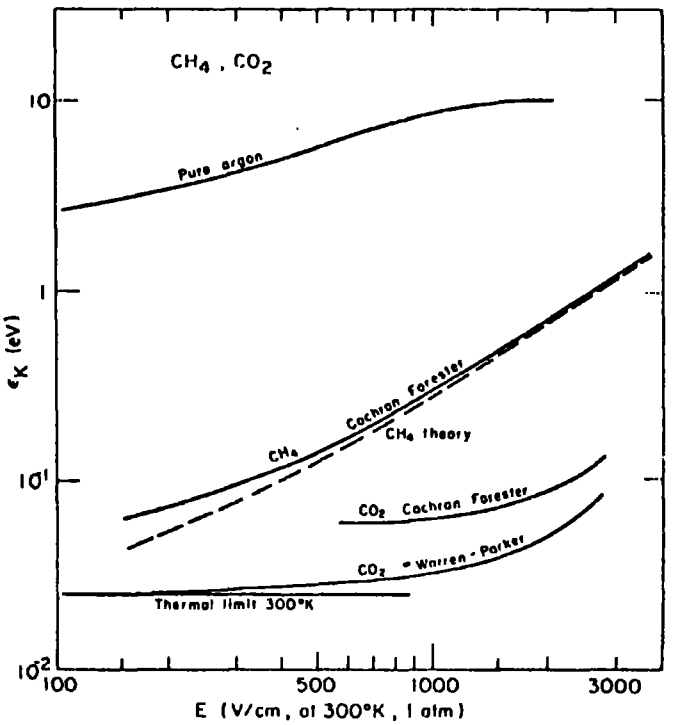

FIG. 2.5 : CHARACTERISTIC ENERGY, ϵ_k, VERSUS FIELD, E

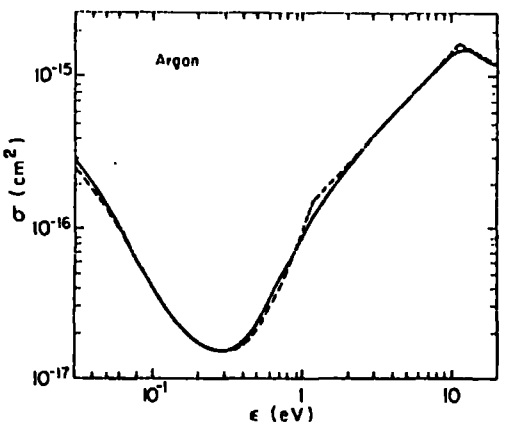

DOTTED LINE REPRESENTS FIT USED BY PALLADINO AND SADOULET IN COMPUTER SIMULATIONS

FIG. 2.6 : MOMENTUM TRANSFER CROSS-SECTIONS FOR ELECTRONS IN ARGON

The addition of small amounts of organic gases partially fills the Ramsauer dip and also introduces vibrational and rotational energies which are important factors. The drift velocity levels off at lower energies, the organic gas effectively cooling the electrons, and produces the observed relationship between drift velocity and field. The addition of available vibrational and rotational energies explains the saturation of the drift velocity at high fields. The relative behaviour of noble gas mixtures containing various concentrations of added organic gas may be explained in terms of the degree of filling of the Ramsauer dip.

Palladino and Sadoulet have developed the theories of other workers to produce numerical methods,[16,18] using Boltzmann transport equations and theoretical or experimental cross-sections, to derive models for the variation of drift velocity and diffusion with field. Their results for some common drift chamber gases are shown in figures 2.7 and 2.8, the values for argon agreeing well with experiment over five orders of magnitude of field.

2.3.3 The Avalanche Region

Having drifted from their primary and secondary ionization positions, the electrons experience very high fields at a distance of a few wire diameters from the sense wire. They attain high enough energies to cause further ionization and excitation of the gas molecules and successive ionizations form an avalanche. The electron multiplication may be described in terms of Townsend's

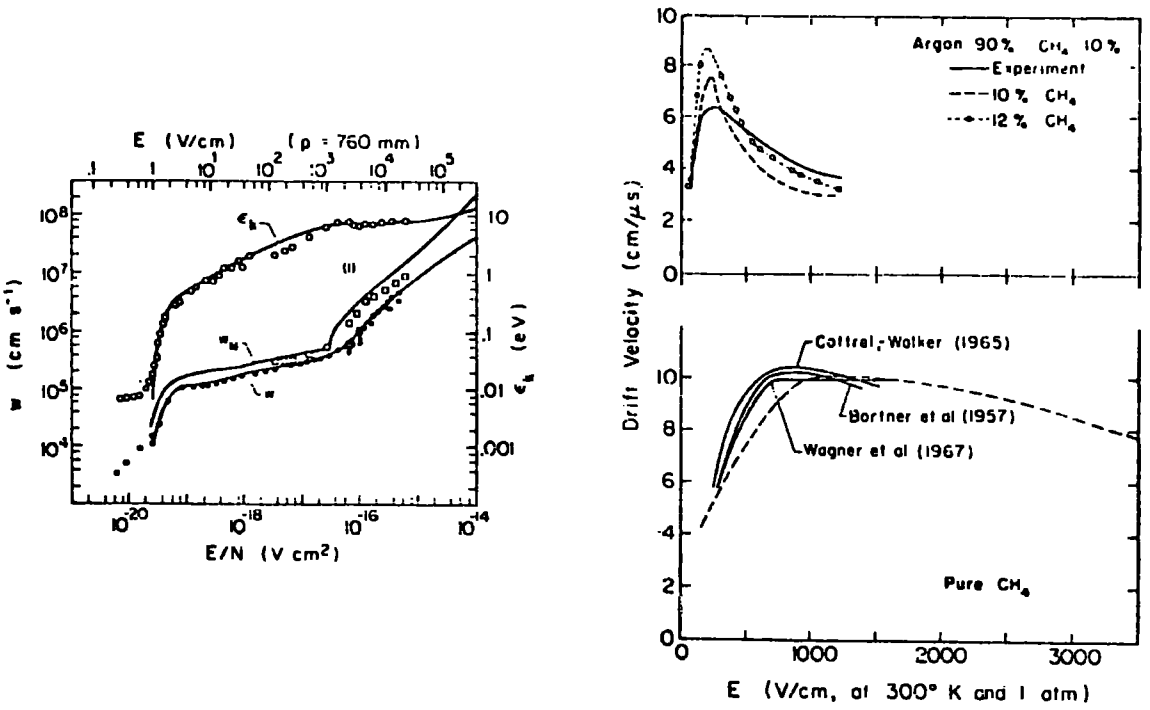

FIG. 2.7: COMPUTED DRIFT VELOCITIES AGAINST EXPERIMENTAL VALUES

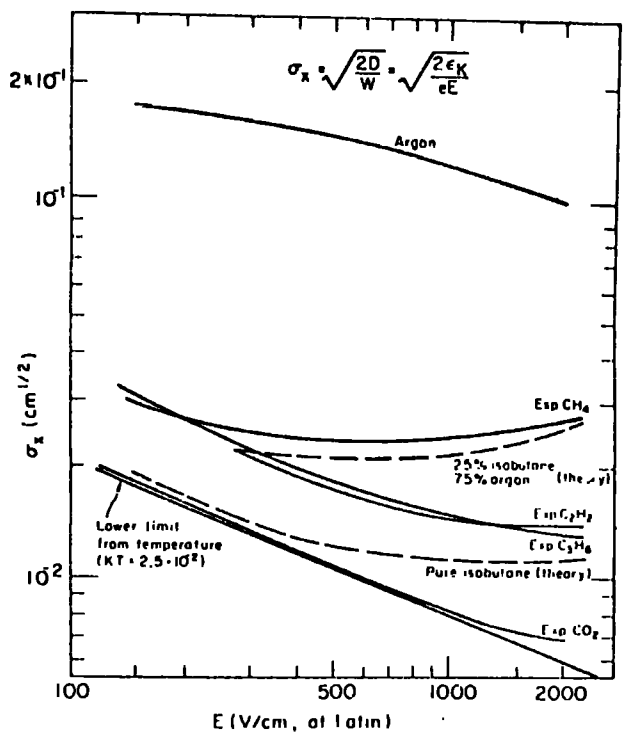

FIG. 2.8: COMPUTED AND EXPERIMENTAL VALUES FOR DISPERSION, σ_x, VERSUS FIELD, E

first coefficient, α, which defines the fractional increase in the number of electrons during a 1 cm movement in the direction of constant field E:

$$\frac{dn}{n} = \alpha dx \qquad (2.12)$$

The field around a sense wire is roughly cylindrical as far as the nearest cathode wire but is not constant, due to the $^1/r$ effect, and may be approximated to that in a proportional counter. For a sense wire radius r_1, sense wire to cathode spacing r_2 and cathode potential V, the field at distance x is given by[19]:

$$E(x) = V \,/\, x \ln (r_2 \,/\, r_1). \qquad (2.13)$$

Although Townsend's coefficient is valid for constant E, Palladino and Sadoulet have demonstrated[16] that it is still valid in an inhomogeneous field although equilibrium of the avalanche may not be achieved. The gain in the number of electrons in moving from x_0 to x_1 may be given as:

$$N_1 = N_0 \exp\left[\int_{x_0}^{x_1} \alpha (x)\, dx \right] \qquad (2.14)$$

where α is varying with E and thus x. It may be shown[19] that the amplification is typically of the order 10^6 and that the majority of the multiplication occurs within 100 μm of the sense wire.

The resultant pulse, seen across a resistor to earth, has a fast risetime of a few nanoseconds due to the electrons incident upon the wire. The majority of the pulse, which may last many microseconds, is due to the slower movement of the positive ions formed in the avalanche. These migrate down the entire potential towards the cathode wires.

The avalanche forms such a high density of positive ions around the sense wire that a space charge exists, over a length of a few hundred microns,[20] which lowers the effective field around the wire. A dead-space is produced on the sense wire at this point for several microseconds and limits the performance of drift chambers at high rates.

2.4 Operation of Drift Chambers in a Magnetic Field

It is often desirable to operate drift chambers in a magnetic field, as in spectrometers. Unfortunately the field direction is usually parallel to the sense wires and the Lorentz force tends to sweep the electrons from the chamber volume as shown in figure 2.9. Much of the early research[21] studied low fields where the deflection angle, θ, was small. For the electric fields encountered in drift chambers and magnetic fields of 1T the angle may be as large as 50°. Thus much of the data has been acquired experimentally as the cross-sections and transport coefficients are insufficiently known to produce theoretical predictions. It has been found by Charpak's group at CERN that a simple model proposed by Townsend predicted results in good agreement with those obtained using a specially designed chamber.[15] Writing the differential equations of motion of an electron moving in a gas with random velocities and crossed fields it is found, by suitable averaging over the velocity distributions, that:

$$w_0 = w\ (E,\ B = 0) = \frac{keE\tau}{m} \qquad (2.15)$$

$$w\ (E,\ B) = k\frac{E}{B}\ \frac{\omega\tau}{\sqrt{1 + \omega^2\tau^2}} \qquad (2.16)$$

and $\tan\ \theta\ (E,\ B) = \omega\tau \qquad (2.17)$

where $\tau = \tau\ (E,\ B)$ is the mean free time between collisions, a function of both E and B, and $\omega = eB/m$ the Larmor frequency of the electrons. The value of k depends upon the velocity distribution, 0.75 corresponding to a Maxwellian distribution[17c] was found to give good agreement with experimental results.[15] The above equations include modified drift velocity components that make allowance for the curving of the electron path in a magnetic field. Palladino and Sadoulet demonstrate[16] that this decreases the mean free path by a factor $(1 + \omega^2\tau^2)^{-1}$. Figure 2.10 presents the various drift velocity components discussed in this section.

Equations (2.16) and (2.17) are only valid at low fields as they are derived on the assumption of isotropic elastic collisions which do not occur when the electron energy, or collision cross-section, is a strong function of E. Making the crude assumption that $\tau\ (E,\ B) = \tau_0\ (E) = \tau\ (E,0)$ the equations may be re-written as:

$$w\ (E,\ B) = w_0(1 + \omega^2\tau^2)^{-\frac{1}{2}} = w_0\left[1 + \frac{Bw_0}{kE}\right]^{-\frac{1}{2}} \qquad (2.18)$$

$$\tan\ \theta = \omega\tau_0 = Bw_0/kE \qquad (2.19)$$

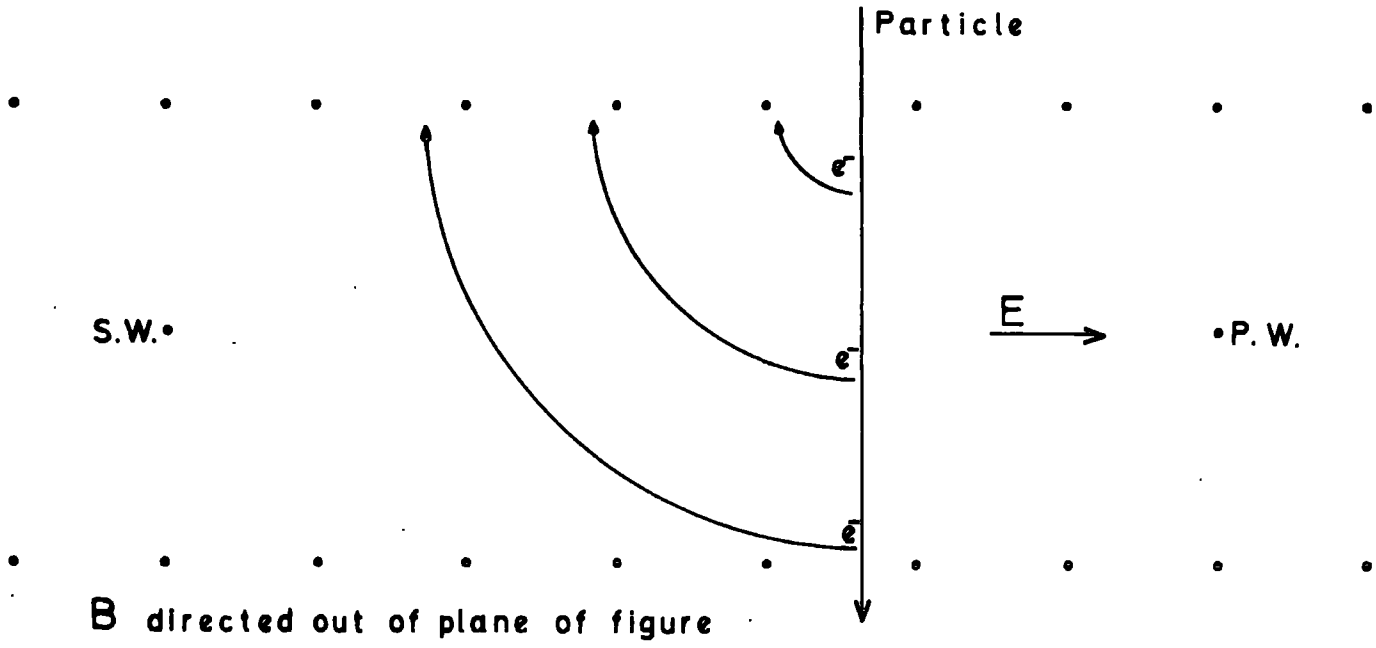

FIG. 2.9 : ACTION OF LORENTZ FORCE ON DRIFTING ELECTRONS

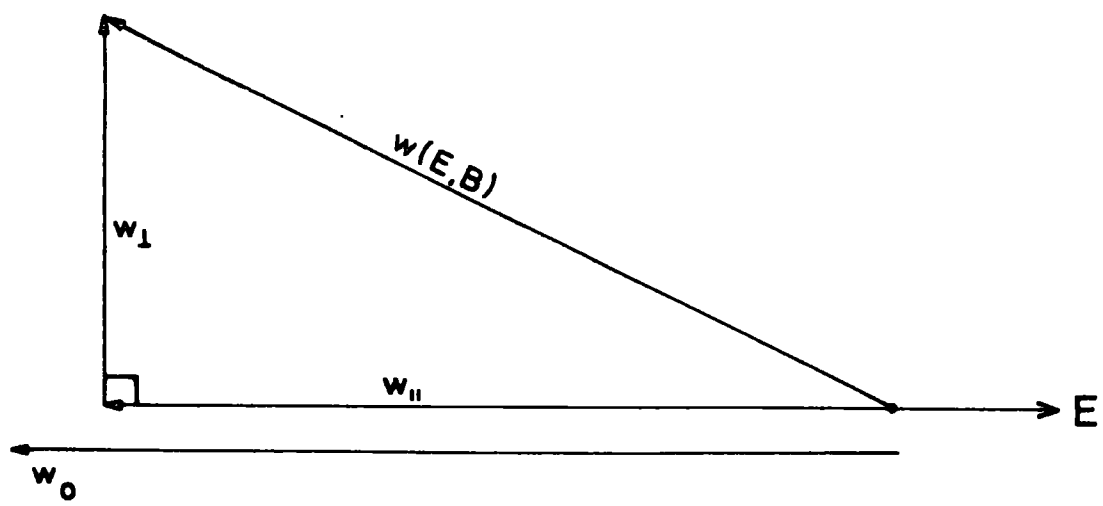

FIG. 2.10 : DRIFT VELOCITY COMPONENTS

Figure 2.11 shows the results obtained by Breskin et al.[15] indicating the good agreement between the theoretical values (solid line) and experiment, divergence occurring at higher fields. Combining equations (2.16) and (2.17) allows a correlation of drift velocity and deflection angle with field:

$$w\ (E,\ B) = k\frac{E}{B} \sin \Theta\ (E,\ B) \qquad (2.20)$$

Figure 2.12 from the same reference[15] shows the good agreement obtained with a special chamber, the theoretical values of w (E, B) being shown as a solid line.

The simple theory adequately describes the drift velocities at low fields but is incorrect at higher values where the drift velocity saturates for all magnetic fields as shown in figure 2.13 taken from the same reference.

Palladino and Sadoulet have derived a more rigourous theory[16,18] for drift velocities in magnetic fields. They used the concept of a magnetic drift velocity, w_m, defined by:

$$w_m = \frac{w_\perp}{w_{//}} \frac{E}{B} \qquad (2.21)$$

and thus $$\tan \Theta = w_m\ B/E \qquad (2.22)$$

Equating (2.19) and (2.22) reveals the relationship

$$w_m = w_o/k \qquad (2.23)$$

Figure 2.14 shows the good agreement of their theory with experimental data for w_m and w, due to Charpak et al., for argon isobutane mixtures.

The design of the adjustable field drift chamber allowed a novel solution to the problem of inefficiencies caused by the angle

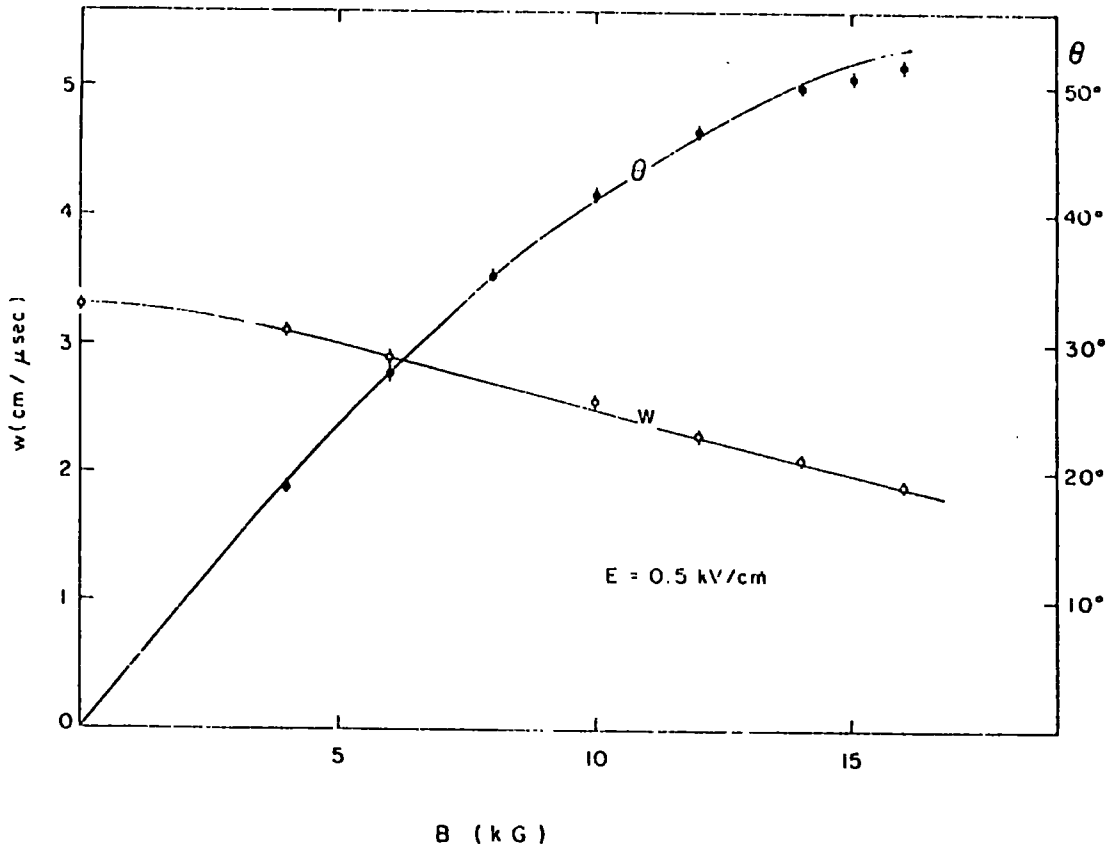

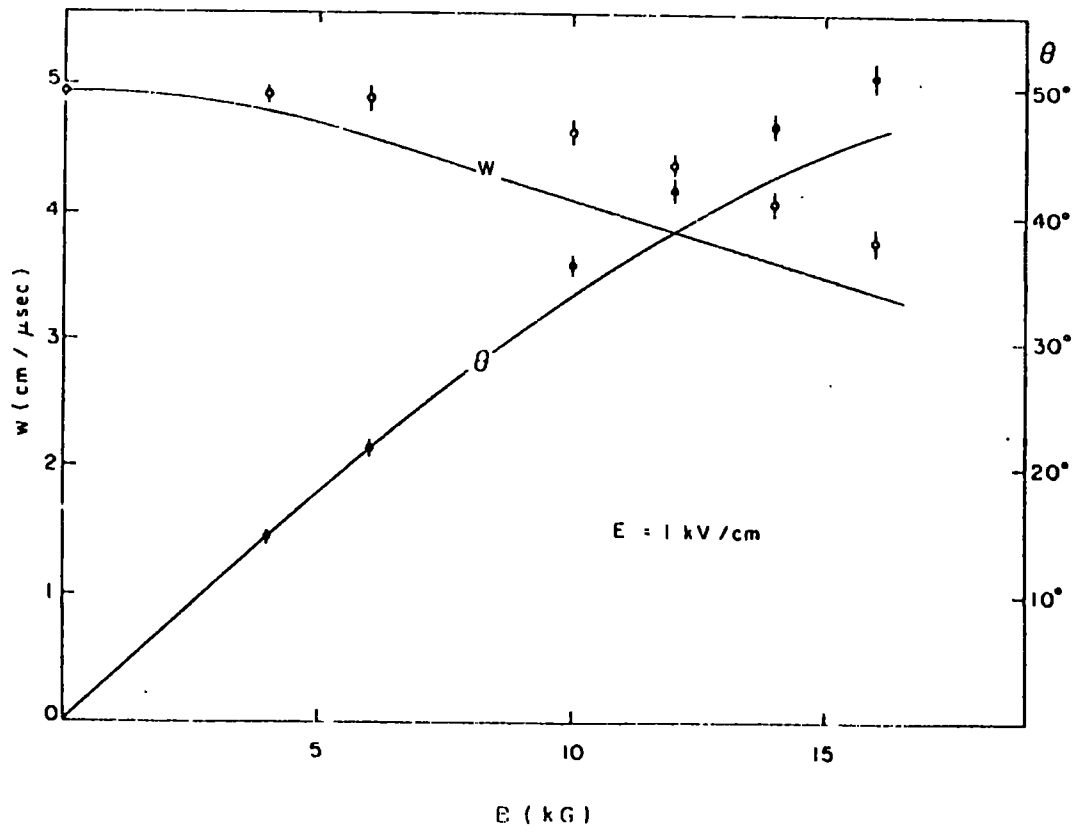

FIG. 2.11 : COMPARISON OF THEORETICAL AND EXPERIMENTAL VALUES FOR W & θ AGAINST B FOR TWO VALUES OF E

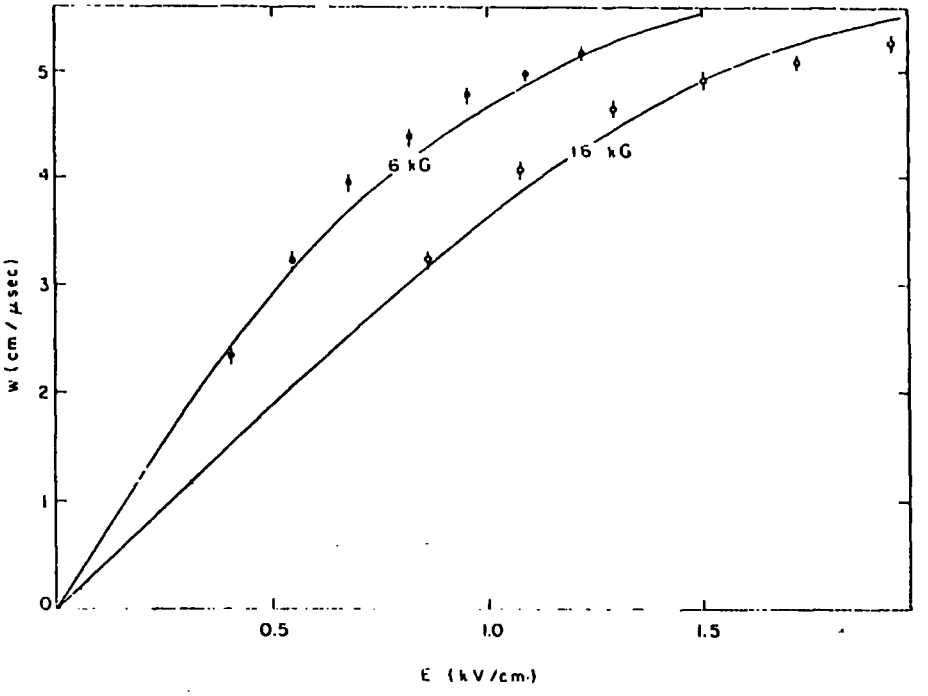

FIG. 2.12: COMPUTED AND EXPERIMENTAL VALUES OF TRUE DRIFT VELOCITY DERIVED FROM KNOWN VALUES OF ELECTRIC AND MAGNETIC FIELDS AND DRIFT ANGLE

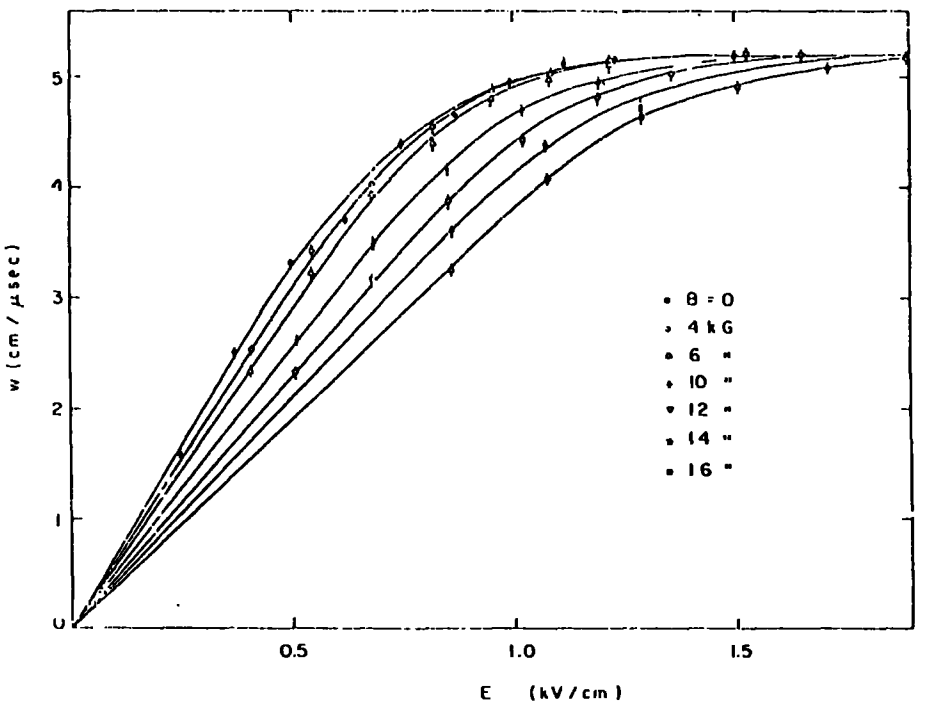

FIG. 2.13: SATURATION OF DRIFT VELOCITIES FOR ALL MAGNETIC FIELDS AT HIGH ELECTRIC FIELD VALUES

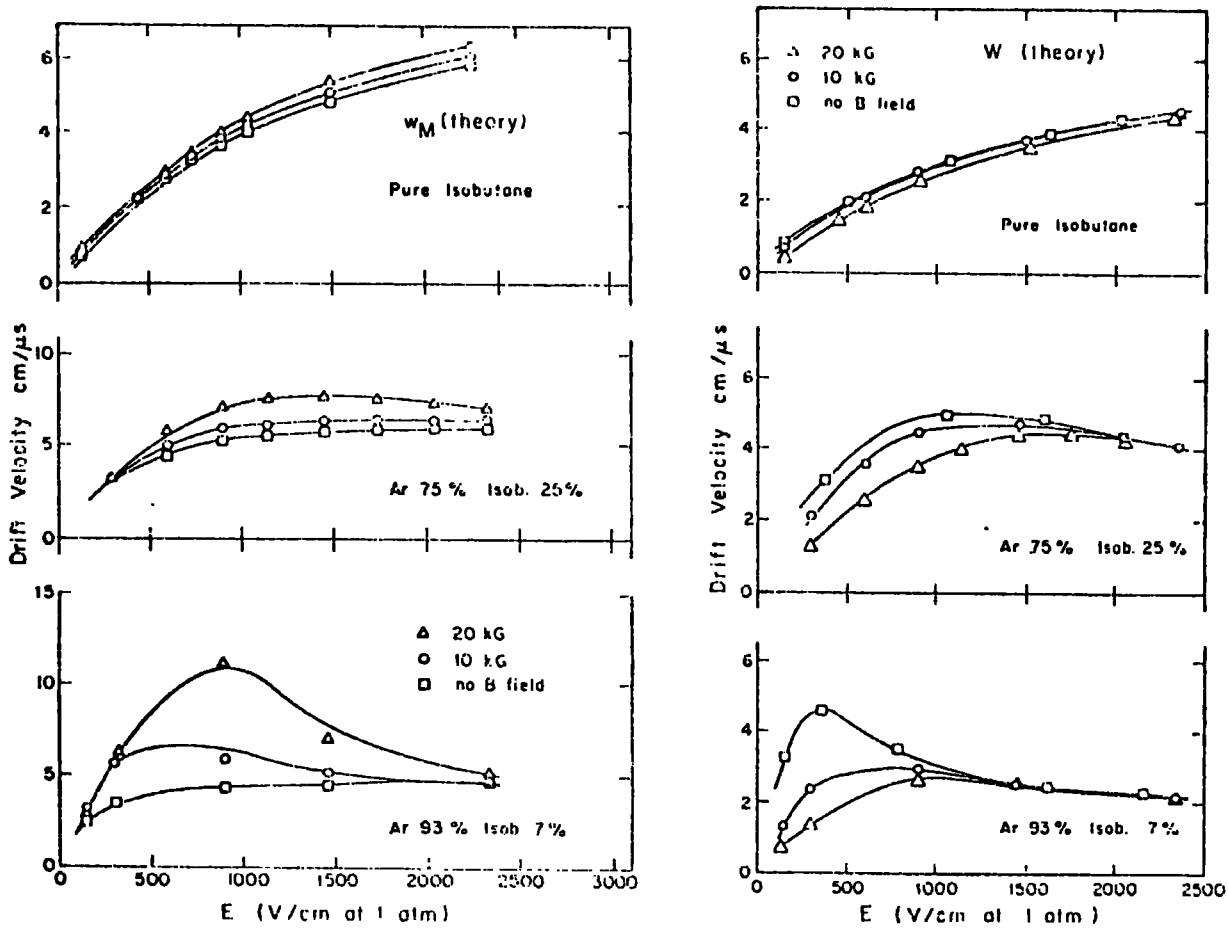

W_M and W versus B (Theory)

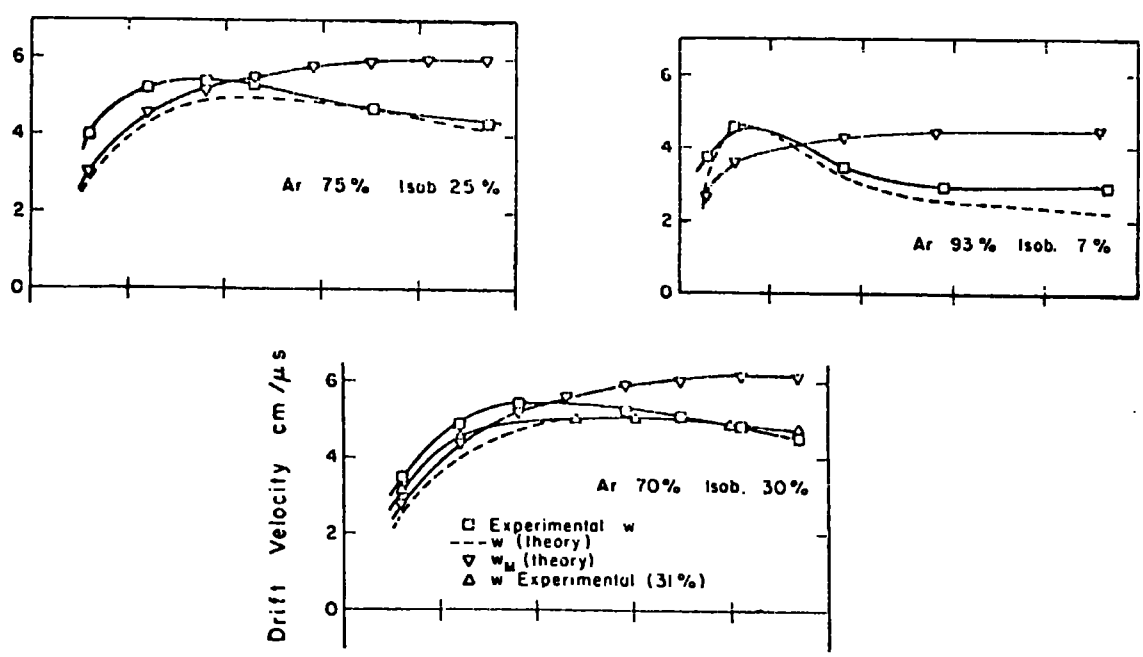

W_M and W at B = 0 (Experimental and Theory)

FIG. 2.14 : THEORETICAL VALUES OF W_M AND W DUE TO PALLADINO & SADOULET AGAINST EXPTL. VALUES DUE TO CHARPAK et al.

of drift, θ.[12] The electric drift field could be tilted by staggering the potentials applied to the cathode wires, as shown in figure 2.15. By correct compensation of the Lorentz force the drift velocity could be restored to the sense wire plane. However only discrete angles of tilt, γ, were possible corresponding to multiples of the wire spacing. Thus the compensation may not be exact, as shown in figure 2.16, the drift velocity in the sense wire plane, w_s, being given by:

$$w_s = w\ (E,\ B)\ \cos\ (\gamma - \theta) \qquad (2.24)$$

Knowing the value of B and using equations (2.22) and (2.23) a value of E is chosen and values of w_m and θ deduced. The nearest value of γ is used and if necessary the value of E altered to give exact compensation. It must be noted that the value of E used in all the above equations refers to the field at an angle γ to the sense wire plane, as shown in figure 2.16, which is constant regardless of the electron drift direction. In terms of E_0, the applied field in the sense wire plane, the field E is given by:

$$E = E_0 \ /\ \cos\gamma \qquad (2.25)$$

Although the field is constant over most of the chamber volume, it becomes radial around the sense wire. However as it is also higher the electrons tend to follow the field lines without influence from B. Avalanching occurs as in the non-tilted case but, due to the slanting, the potentials opposite the sense wire are higher and the resultant higher field gives different chamber characteristics. To reproduce the non-slanted characteristics the potentials may be adjusted accordingly.

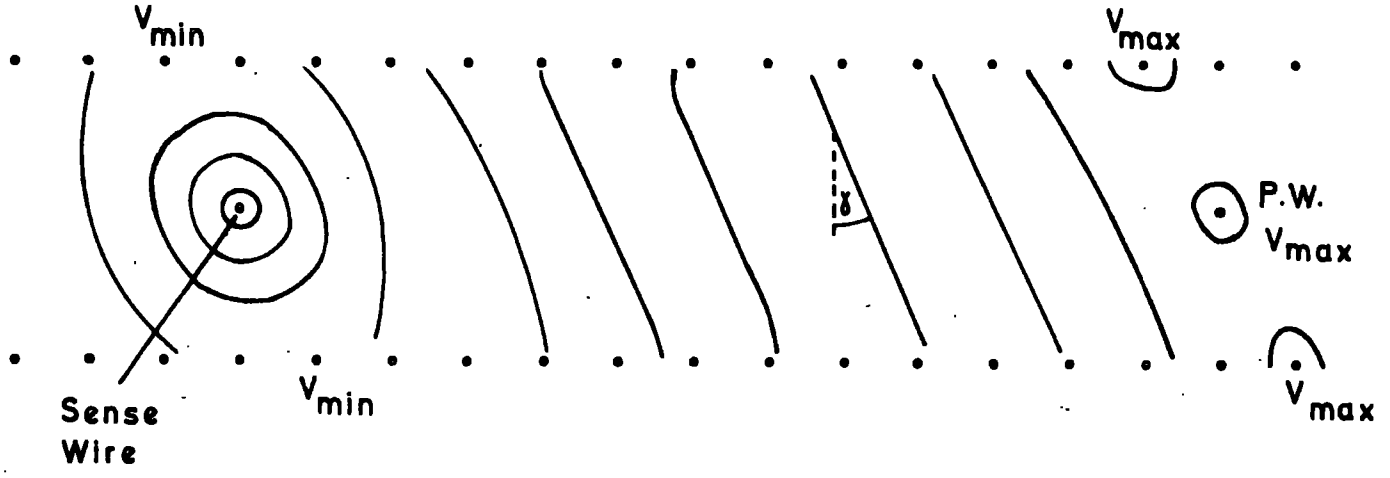

FIG. 2.15 : TILTING OF EQUIPOTENTIALS FOR MAGNETIC FIELD COMPENSATION

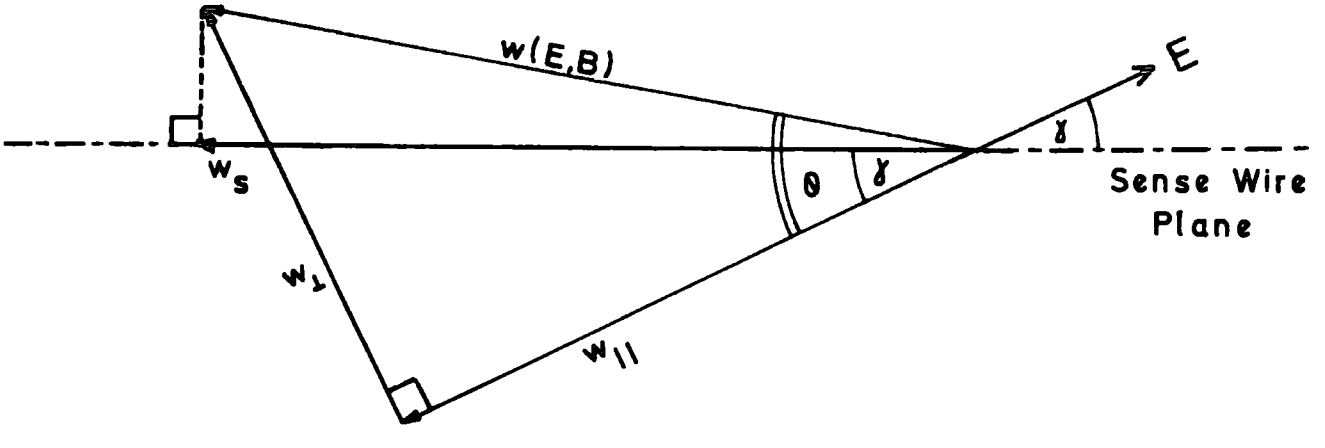

FIG. 2.16 : OBSERVED DRIFT VELOCITY WITH NON-EXACT FIELD COMPENSATION

Chambers operating in homogeneous magnetic fields up to 1.6T with exact field compensation and saturated drift velocities have achieved spatial resolutions of 100 - 200 μm, depending upon the drift length.[12,13,15] Exact calibrations and complex software corrections are necessary for inhomogeneous fields.[13]

2.5 Factors Determining the Choice of a Drift Chamber Gas Mixture

Several factors determine the choice of a specific gas mixture for a particular chamber.

As described in Chapter 4 the maximum timing resolution of the digitizing electronics is normally 2 ns due to cost considerations. Thus for short drift spaces the drift velocity of the gas must not be too high or the maximum realizable spatial resolution will correspond to a timing resolution in excess of 2 ns. Similarly the maximum digitizable drift time using commercial electronics is of the order of 1 μs so for long drift spaces the drift velocity of the gas must be high.

The degree of diffusion over the drift space is a major contributor to the overall accuracy of the chamber. From the expressions given in equation (2.5) for σ_x, the rms of the dispersion, it may be assumed that to lower its value the characteristic energy, ε_k, should be lowered and the field, E, raised. However figure 2.5 illustrates that the two parameters are not independent and figure 2.8 demonstrates the dramatic effect of the addition of a small amount of multi-atomic gas to argon. The effective temperature is lowered and hence also the diffusion. A lower limit to the cooling effect exists due to the ambient temperature of the gas.

A further requirement is that the gas should have an extended drift velocity saturation region at higher fields. Any small variation in the field over the drift space, due to the method of application of the field or constructional imperfections, would then have no effect on the linearity of the drift time/distance relationship.

In the case of chambers operating in a magnetic field, where the drift velocities and trajectories are modified, it is preferable to use a gas which minimizes the effects and has a saturated drift velocity at higher electric fields for all magnetic field values.

The temperature and pressure may vary in some applications so it is necessary that the saturation region also exhibits stability towards such variations. When using gas mixtures a small percentage change in the concentration of the constituents should preferably have no effect on the drift velocity.

Figure 2.17 shows drift velocity curves against field for a variety of commonly used chamber gases. The range of available saturated drift velocities suggests their specific application for long or short drift spaces.

2.6 Operational Considerations of Drift Chambers

In a drift chamber system four additional factors relevant to their operation have to be considered to allow a full understanding of their working and to achieve correct interpretation of the results.

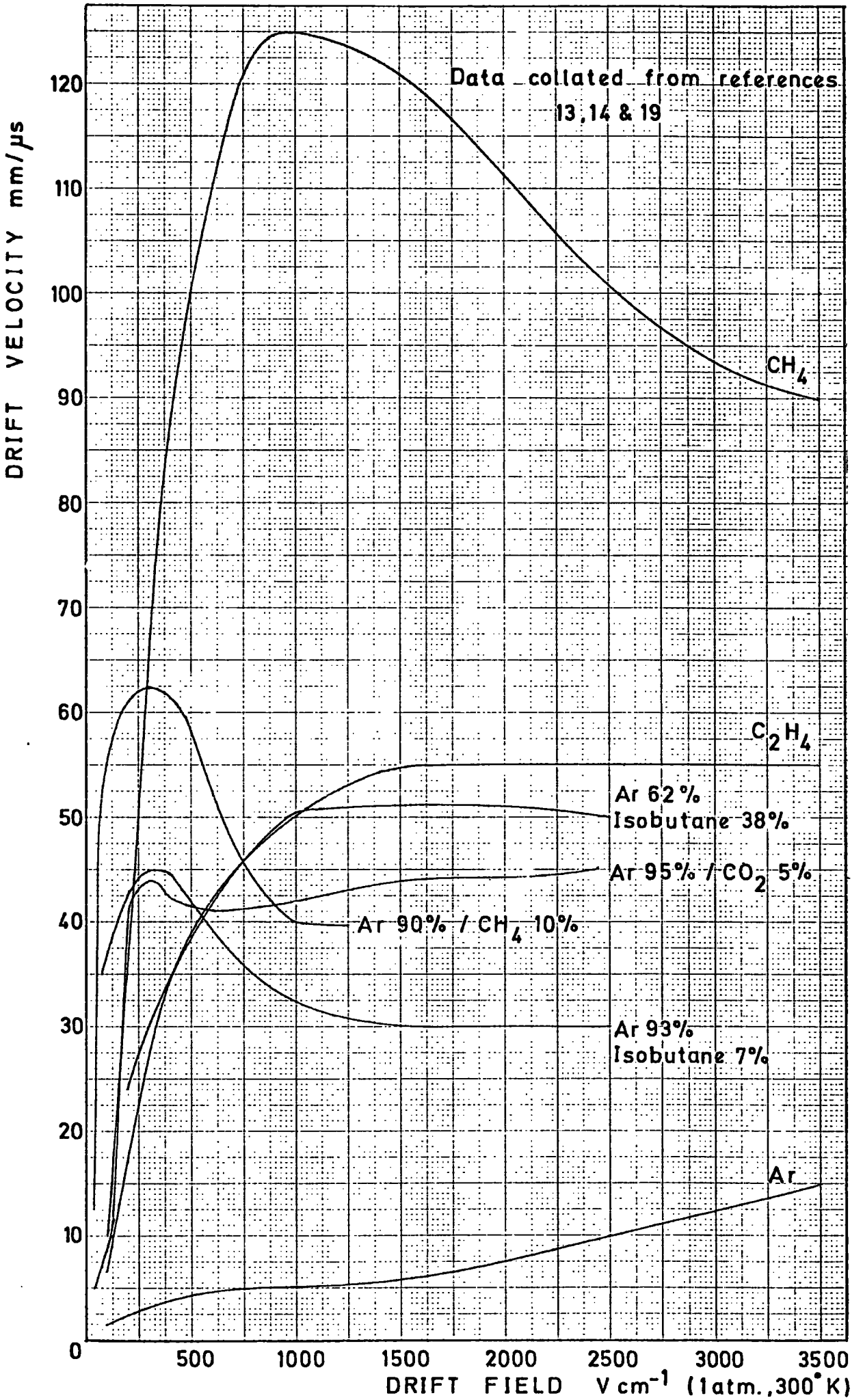

FIG. 2.17 : COMPARISON OF DRIFT VELOCITIES

2.6.1 Angled Tracks

The leading edge of the pulse detected on the sense wire represents the arrival of the avalanche formed by the primary electron created closest to the sense wire, distance x_1 in figure 2.18, and not necessarily the shortest distance to the track, x, due to the statistical nature of the formation of the primary ionization. If the electronic threshold for detection of the pulse is set low enough this minimum time will be recorded. If the particle is not incident orthogonally to the sense wire plane then the drift time recorded corresponds to the shortest distance from the track to the sense wire following the field lines, as shown in figure 2.19 taken from Breskin et al.[13] Simple geometrical models for predicting the drift length in the sense wire plane from the angle of incidence agree well with experimental results obtained by accurately scanning the chamber. Figure 2.20 shows the approximation used by Charpak et al. which assumed radial drift up to the sense wire/cathode spacing and then drift along the cathode plane itself. The equations deriving the intercept of the track on the sense wire plane, s, from an angle of incidence θ, drift time t, constant velocity w, and sense wire/cathode gap d, are:

$$s = wt / \cos\theta \qquad \text{for } 0 < t < g / w \sin\theta \qquad (2.26)$$

and

$$s = wt + \left(\frac{g}{\sin\theta}\right)\left(\frac{1}{\cos\theta} - 1\right) \qquad \text{for } t > g / w \sin\theta \qquad (2.27)$$

Results gained by Charpak et al.[13] show good agreement between experiment and the simple theory for the drift time/distance relationship as shown in figure 2.21 for the zero magnetic field case and

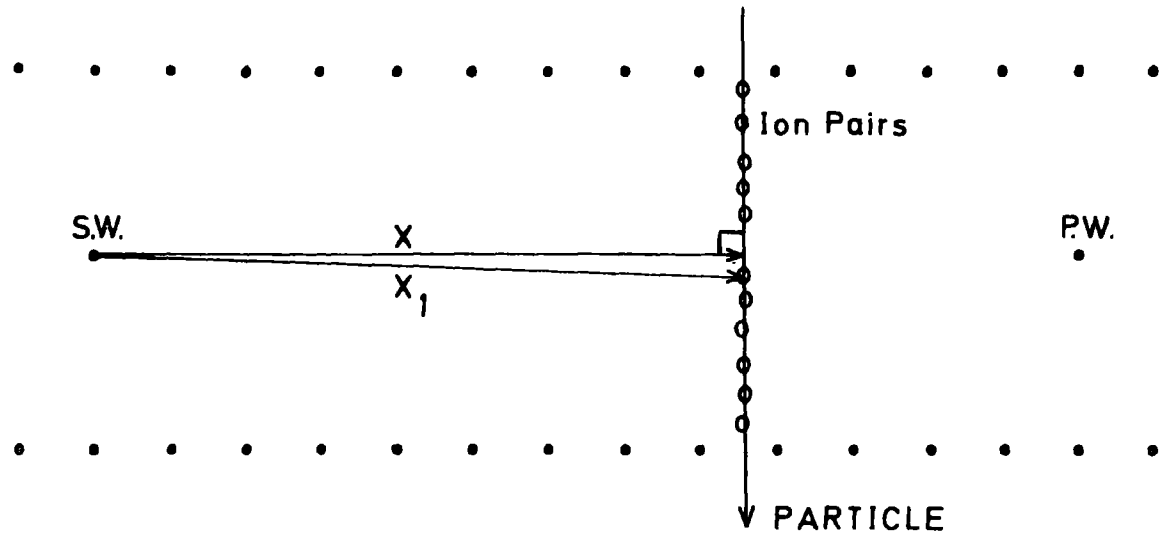

FIG. 2.18: DEMONSTRATION THAT DISTANCE FROM SENSE WIRE TO CLOSEST PRIMARY ELECTRON IS GREATER THAN THE PERPENDICULAR DISTANCE TO THE TRACK

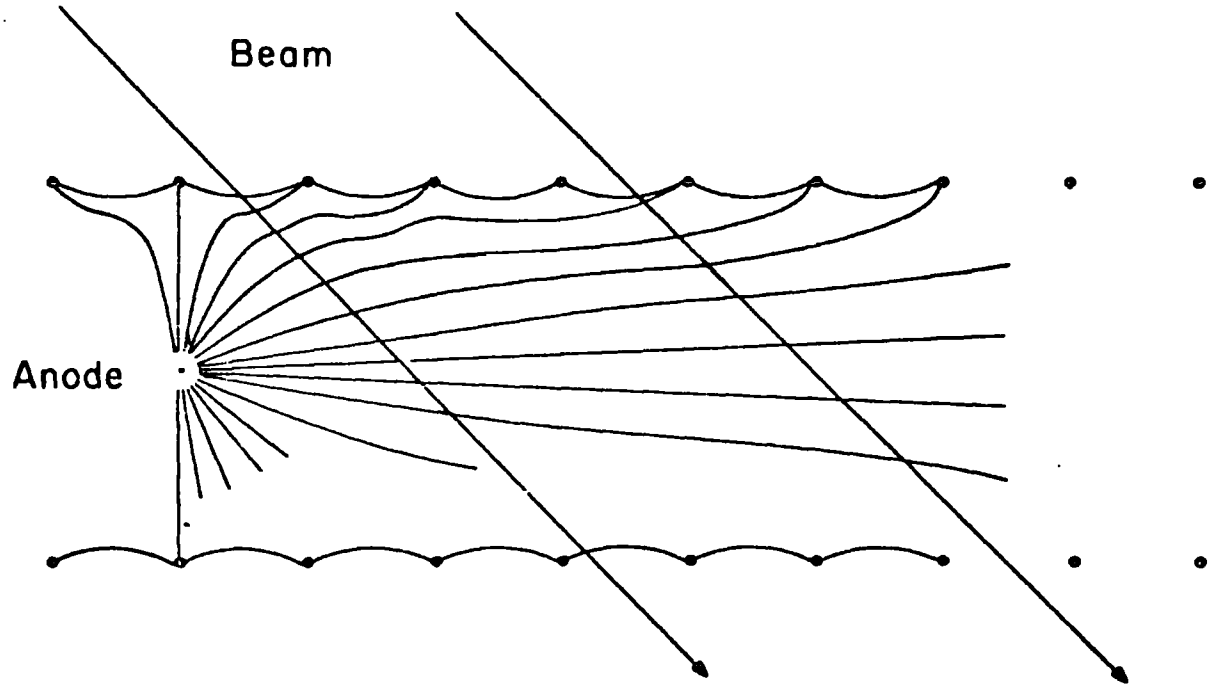

FIG. 2.19: TYPICAL FIELD LINES IN A CHAMBER INDICATING THE SHORTEST DRIFT DISTANCE FOR ELECTRON SWARMS CREATED BY ANGLED TRACKS

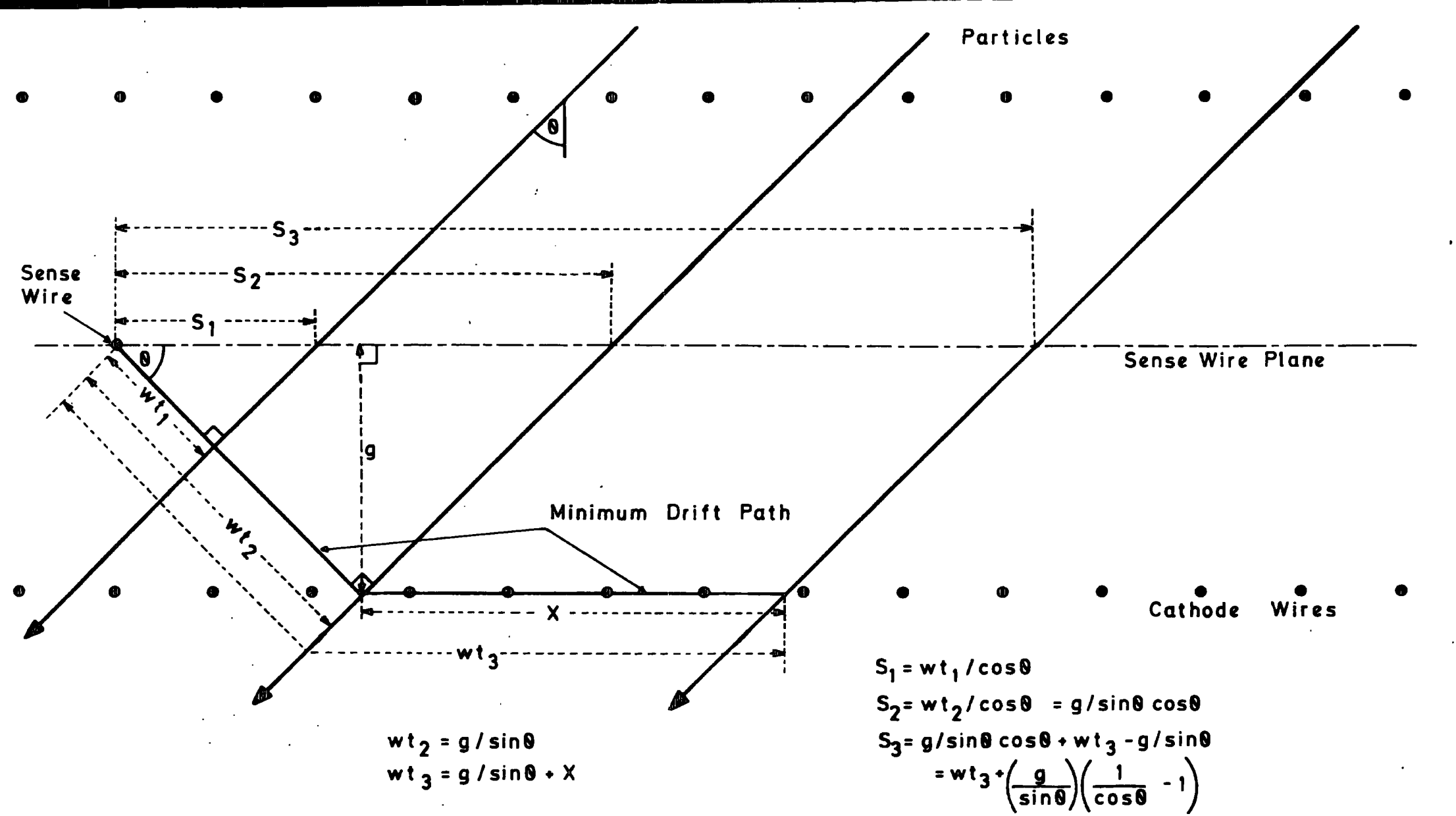

FIG. 2.20 : MODEL FOR DETERMINING THE INTERCEPTS OF ANGLED TRACKS ON THE SENSE WIRE PLANE FROM THE MINIMUM DRIFT TIMES

figure 2.22 for a field of 1T. In the latter case, with exact field compensation applied, the tracks were incident at $\pm$ 42° to the normal. The experimental points indicate that there was no difference in behaviour for tracks inclined in the same direction or opposite to the direction of field tilt.

At large incidence angles the electrons drifting close to the cathode plane are perturbed by the deformation of the field lines around the cathode wires and hence a modulation is caused[13] in the space-time relationship as shown in figure 2.23.

2.6.2 Reduction of Pulse Height around the Sense Wire

It has been noted by other workers[13,15] as well as during the study of the (g-2) drift chambers[22,23] that the pulse height measured on the sense wire is dependent not only upon the chamber operating voltage and particle energy but also the drift distance. Figure 2.24 shows results from the (g-2) chambers using a ^{90}Sr source and figure 2.25 results using a minimum ionizing beam, taken from reference 15. Similar lowerings of the pulse height are shown in both cases.

Several factors contribute to the effect. Most amplifier-discriminator circuits used for drift chamber readout have a differential function and thus the time development of the pulse is important. For particles traversing at long distances from the sense wire the primary electrons have approximately the same drift length and they reach the avalanche region at about the same time

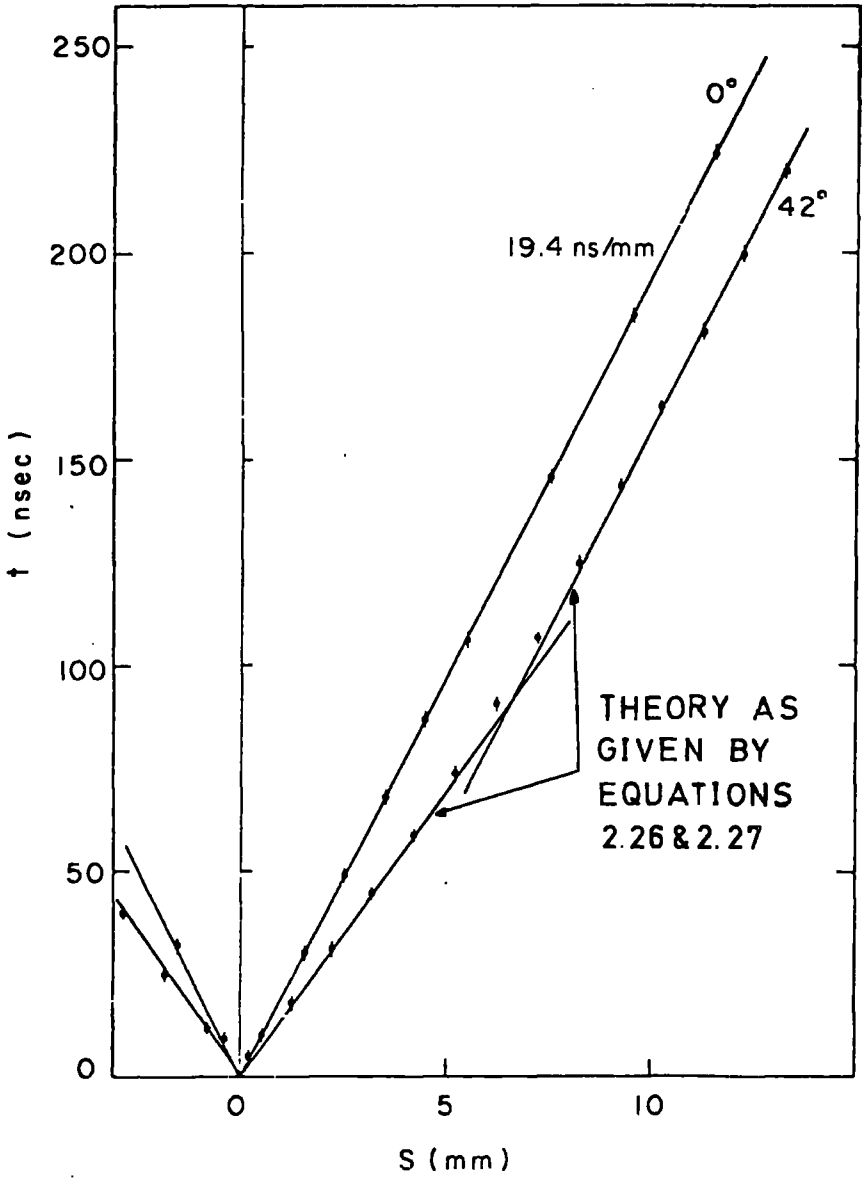

FIG. 2.21: SPACE-TIME RELATIONSHIPS WITH B=0 SHOWING THEORETICAL FIT FOR LARGE ANGLE TRACKS

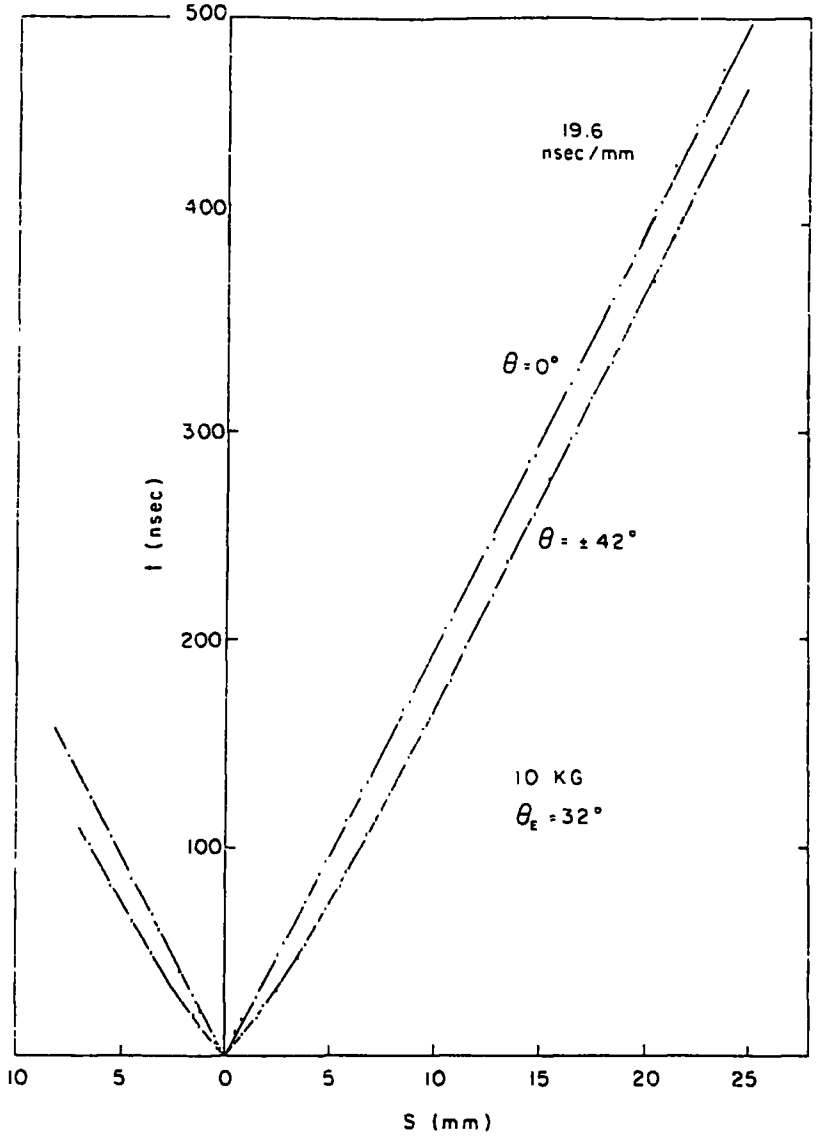

FIG. 2.22: SPACE-TIME RELATIONSHIPS WITH B = 1 TESLA AND CORRECT ELECTRIC FIELD COMPENSATION

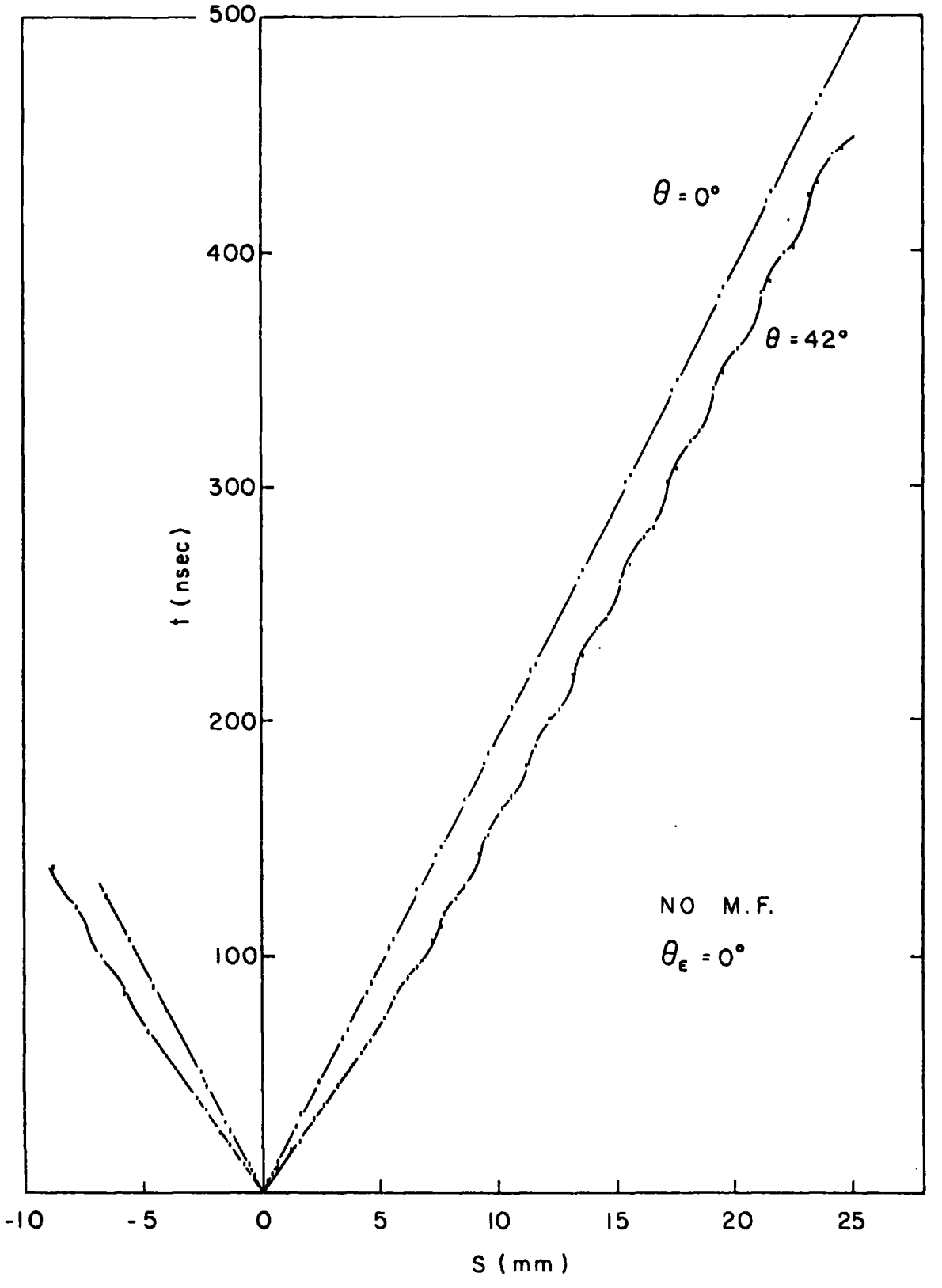

FIG. 2.23: SPACE-TIME RELATIONSHIP DERIVED BY ACCURATE SCANNING SHOWING MODULATION (EXAGGERATED) FOR LARGE ANGLE TRACKS (B = 0)

giving a large fast-rising pulse. However for particles traversing close to the sense wire the drift lengths range from zero to several millimetres and there is a greater time spread in the pulse formation and thus the overall pulse height is lower.

The above explanation would suggest that for the detection of X-rays where, for example, the 5.9 keV photoproduction event associated with an ^{55}Fe source has a space extension of only 150 μm,[24] no such lowering of the pulse height would occur. However, as shown in figure 2.26, Charpak et al.[15] found similar effects for ^{55}Fe and evidence that the applied field was the contributory factor rather than the time development of the pulse. It is inferred[15] that interaction between avalanches occurs at distances below 220 μm and thus charge magnification is lowered for particles traversing close to the sense wire. For longer drift distances diffusion causes the primary electrons to separate and the resultant avalanches interact to a lesser degree and form a larger pulse.

2.6.3 Rate Effects

When attempting to operate drift chambers with high incident particle fluxes similar space charge problems arise as observed in MWPC's.[20] A dead-space localized to about 200 μm on the sense wire, corresponding to the position of incidence of the avalanche, occurs due to a space charge of positive ions which modify the electric field and reduce the multiplication factor. The sense wire becomes insensitive over that length for maybe several tens of microseconds whilst the positive ions migrate from the sensitive region. An upper limit to the efficient detection rate of a drift chamber corresponds

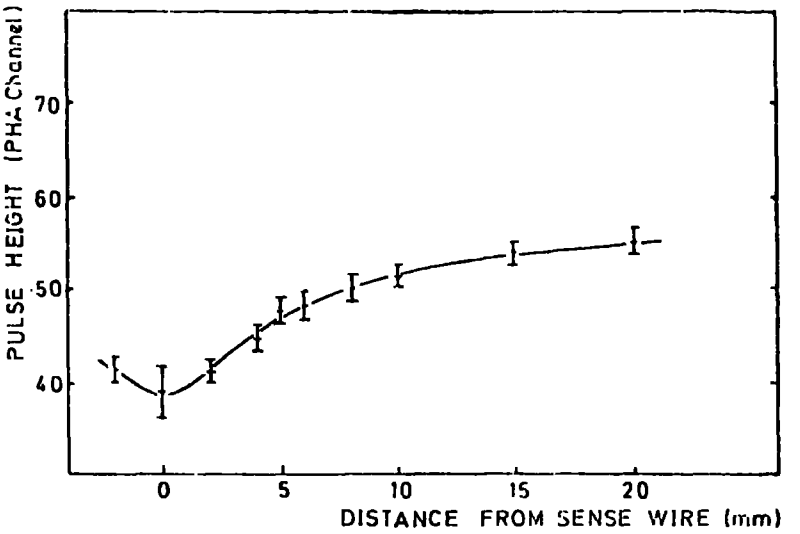

FIG. 2.24: LOWERING OF PULSE HEIGHT AROUND SENSE WIRE IN A PROTOTYPE (g-2) CHAMBER WITH A COLLIMATED Sr 90 SOURCE

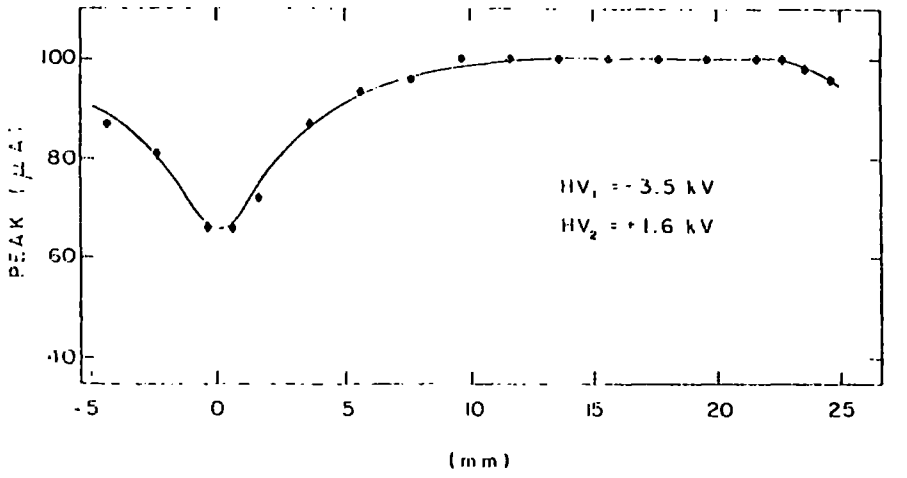

FIG. 2.25: LOWERING OF PULSE HEIGHT AROUND SENSE WIRE WITH MINIMUM IONIZING BEAM

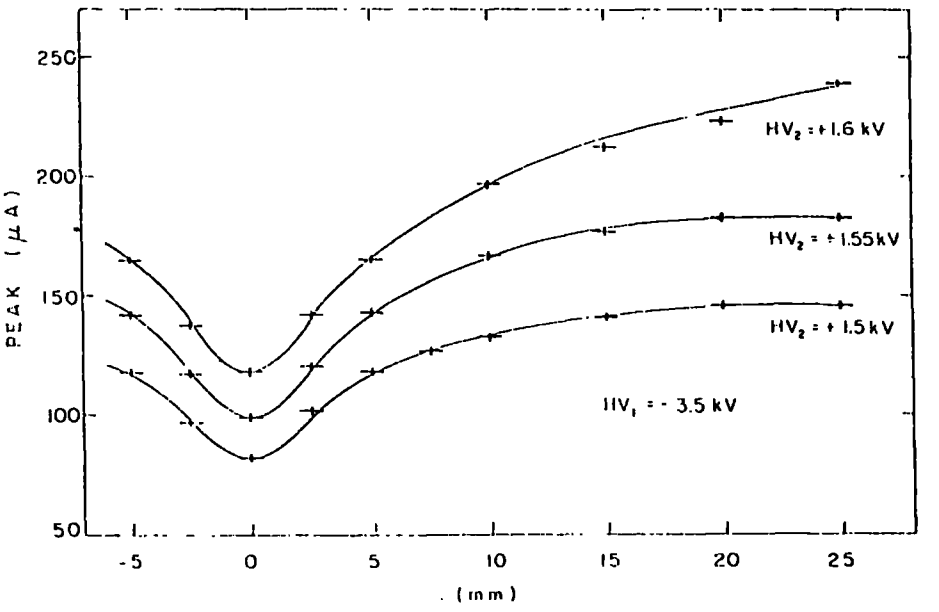

FIG. 2.26: LOWERING OF PULSE HEIGHT AROUND SENSE WIRE WITH COLLIMATED Fe 55 SOURCE

to an incident flux of 2×10^5 particles cm^{-2} s^{-1}. (13)

Apart from the space charge effect there is a limit to the minimum detectable separation of particles. This is due to the occupation time of the amplifier-discriminator circuit, which is normally a minimum of 50 ns. Assuming that the electronics is capable of handling multi-track events, the minimum resolvable separation is the drift distance covered in the occupation time.

Care has to be taken that the zero timing trigger refers to the traversal time of all the detected particles or erroneous drift times will result. The maximum repetition rate of the triggers is limited by the maximum drift time in a cell, often called the memory time.

Thus there is a limit on the frequency and density of the beam of particles incident upon a drift chamber if full efficiency is to guaranteed.

2.6.4. Solutions to the Left-Right Ambiguity

A fundamental problem in the analysis of drift chamber data is the ambiguity as to which side of the sense wire the particle passed. Referring to the drift space on either side of the sense wire, this is called the left-right ambiguity. Several solutions to the problem have been suggested, of which some are presented diagrammatically in figure 2.27.

The simplest solution was to stagger two chambers by a half-cell spacing, as suggested by Walenta et al.[3] and used successfully in large chamber arrays.[25] Summing the two drift times produced in the chambers by a traversing particle not only allowed a continuous

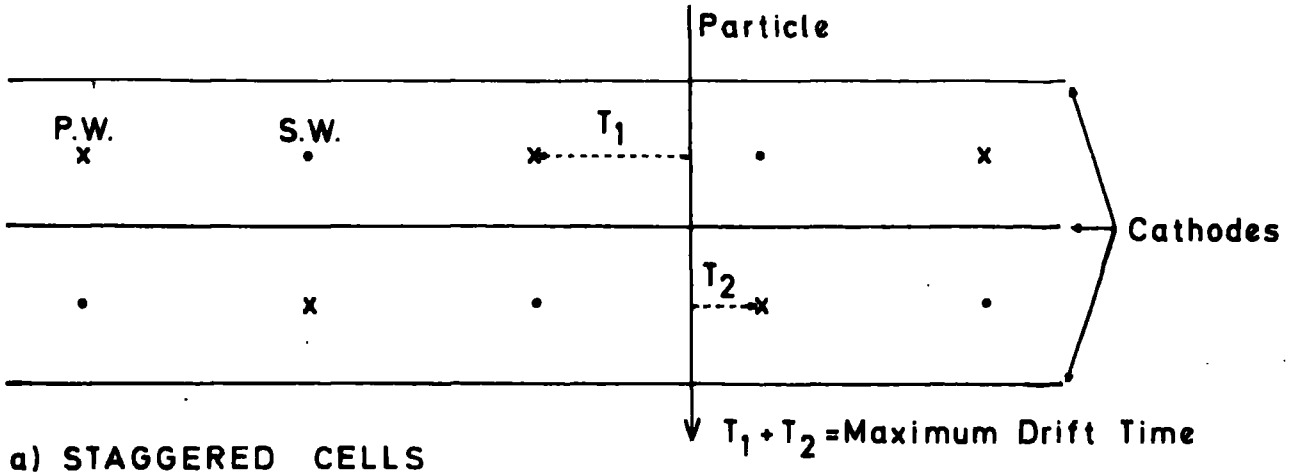

a) STAGGERED CELLS

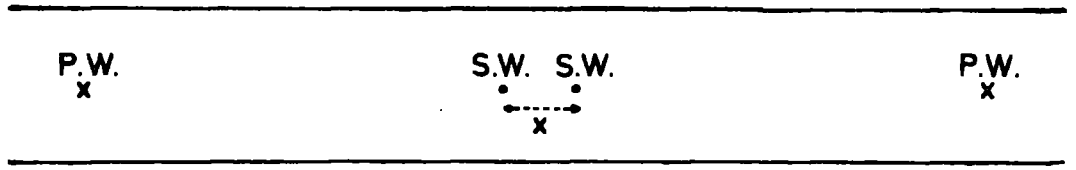

b) SENSE WIRE DOUBLET

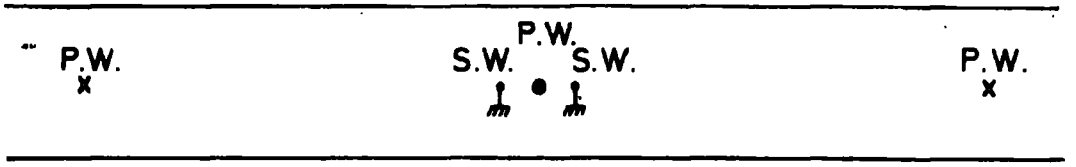

c) WIRE TRIPLET

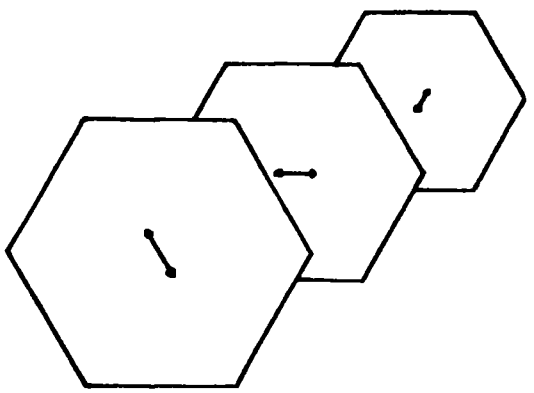

Arrows indicate sense wire directions

d) THREE CHAMBER ORIENTATIONS

FIG. 2.27 : SOLUTIONS TO THE LEFT-RIGHT AMBIGUITY

monitor of the maximum drift time, and thus the drift velocity, but also allowed immediate rejection of spurious hits giving an unambiguous track. Using three chambers with the middle one staggered by half a cell compared to the outer pair presented a novel solution whereby an independent zero timing trigger was no longer required.[12,14] The relative drift times between the chambers provided both the timing and the positional information.

These methods, however, only provided a solution to the ambiguity after computation which was costly in both time and money for large arrays. A more elegant solution would consist of a direct chamber signal indicating from which side of the cell the electrons had drifted.

The initial solution devised by Walenta et al.[1] consisted of a pair of 20 μm sense wires spaced by 1 mm with individual readout. A negative pulse was observed only on the sense wire closest the traversal of the particle. However for particles passing between the two sense wires, or close to them, some ambiguity still existed. Electrostatic repulsion problems were also encountered between the pair if the wires were long. This problem was overcome[2] by having a triplet of wires with a 100 μm diameter potential wire, at a negative potential, positioned between and 1 mm from a pair of grounded 20 μm diameter sense wires. The voltage on the potential wire was adjusted to provide stable equilibrium between the sense wire pair.

The original paper by Walenta[1] discussed the possibility of resolving the left-right ambiguity by observing the time difference between the induced positive pulses on the potential wires of a

Walenta-type chamber with a single sense wire. Recent work on the effect[26] has shown that the previously observed difference in arrival times was in fact due to different induced pulse heights. The latest research has shown that a larger induced pulse occurs on the potential wire closest the traversing particle than on the similar potential wire on the opposite side of the sense wire. Observation of the polarity of the difference signal between the potential wires permits an accurate solution of the ambiguity. This effect may be explained in terms of imaging of charges and the discovery[27] that at lower fields the avalanche is localized on the side of the sense wire closest to the traversing particle. This phenomenon was confirmed by observing that positive ions could only be collected on the potential wire located on the same side of the sense wire as the primary ionization. Only at higher fields did the avalanche begin to surround the wire and thus allow positive ions to drift along field lines towards the far potential wire. Such a solution of the ambiguity is valid for angled tracks and for traversals of particles close to the sense wire. For large drift spaces, field shaping electrodes close to the sense wire may be used as pick-up electrodes. It appears that such a method will become widely used in the near future.

A similar method suggested by Charpak and Sauli[28] involved the use of pairs of 20 μm diameter sense wires separated by 0.2 mm and spaced every 6 mm. The wires were only 25 cm long so no electrostatic problems were encountered. The wire pairs were electrically connected but it was found that the wire nearest the traversing particle had a negative pulse formed on it and the other an attenuated induced positive

pulse due to effective screening by the equipotentials and avalanching occurring only at very close range. Positive pulses were also induced on the two neighbouring pairs of wires, the pair nearest the traversing particle having a pulse height double that on the opposite pair. Using differential amplifiers a resolution of the ambiguity could be achieved. However due to the many wires and channels of electronics required this method has not found widespread favour.

Another approach developed by Charpak et al.,[13] similar to the sense wire doublet solution of Walenta but applicable to large chambers, used two 20 μm diameter sense wires separated by 100 μm with independent readout. The wires were joined by small droplets of epoxy every 50 mm over their 50 cm length to limit electrostatic repulsion and the ambiguous region between them so that the error was below the 50 μm spatial resolution of the chamber. A negative pulse was observed on the wire nearest the traversing particle and a positive pulse induced on the other, allowing solution of the ambiguity.

A common approach for large area drift chamber arrays employs three layers of multi-cell single sense wire chambers with the sense wire planes aligned at 60° in relation to each other.[5,29] The three wires hit for each incident particle define unambiguously its position in two dimensions and also its time of passage by combination of the drift times, removing the need for an independent timing trigger. Excellent timing and spatial resolution is achieved and any spurious hits may be rejected. Multi-track resolution is also possible at high rates using suitable electronics.

Using arrays of chambers, as in the (g-2) experiment, with large curvature of the particle track in a magnetic field allows removal of

the ambiguities through track reconstruction. However foreknowledge of several trajectory constraints is necessary and the computation is complex. Single sense wire cells may be used and the chambers need not be staggered but in many cases such a system would be undesirable and often impossible for resolution of multitrack events.

2.7 Summary of Factors Limiting the Spatial Resolution of Drift Chambers

Having described the principles of drift chamber operation it is useful at this stage to summarize the various contributions that limit the spatial resolution of a drift chamber. A detailed discussion of such contributions was given by Walenta during the early stages of drift chamber development.[2]

Several factors are associated with the primary deposition of electrons. The process is statistical in nature and the ionization occurs in clusters of one or several ion pairs. The drift time recorded corresponds to the distance drifted by the cluster with the shortest drift path, along the field lines, to the sense wire. This distance is normally greater than the shortest distance between the particle trajectory and the sense wire. Also the amplifier-discriminator system is set at a certain threshold which may not be the minimum possible. Therefore the timing derived from the sense wire pulse may not correspond to the arrival of the first electrons in the avalanche and time slewing may occur. This is especially so if there is a strong time dependence in avalanche formation, as for angled tracks or tracks traversing close to the sense wire, or if

the traversing particles deposit various amounts of energy and thus numbers of primary electrons giving variations in pulse height. Any δ -rays formed by the traversing particle may widen the initial track of primary ionization and worsen the resolution.

The effects of diffusion have been discussed, the degree depending mainly upon the drift distance and the electric field.

The presence of magnetic fields, especially parallel to the sense wires, distorts the trajectories of the drifting electrons, unless compensation is introduced, and thus the space-time relationships are altered. Particles not incident normally to the sense wire plane also introduce such effects.

If the applied electric drift field is not high enough the drift velocity may not be saturated and complicated non-linearity of the space-time relationship occurs if the field is not uniform. Corrections must be made either in the hardware or software.

The timing resolution of the digitizing electronics must be in excess of that required to achieve the maximum spatial resolution of the chamber to avoid the introduction of time jitter.

Drift velocity variations may occur with alterations of temperature, pressure and gas mixture concentrations. A method of constant drift velocity monitoring, such as the use of staggered cells, is beneficial.

Errors may be introduced by imprecise mechanical tolerances and lack of cleanliness. Examples are perturbations of the field due to non-uniform cathode gaps, dust particles or globules of solder on sense wires and incorrect alignment of sense and cathode wires. Chamber arrays must be accurately surveyed to determine exact sense wire positions.

The latter contributions may be minimized by careful design, construction and operation. However contributions due to gaseous processes are harder to remove and constitute the inherent limit to drift chamber resolution.

Figure 2.28 shows one of the most accurate sets of data published to date[30] with the overall resolution divided into three contributory processes. It must be noted, however, that such presentations of intrinsic accuracy in no way constitute the absolute accuracy of a chamber as the data are taken at discrete points in the chamber over short runs. No account of any non-linearity of the space-time correlation is included. To obtain an indication of the overall accuracy of the chamber both contributions must be known to equal precision.

2.8 Present and Future Uses of Drift Chambers

Drift chambers are now used for various applications in most high energy physics laboratories in the world. Early chambers, and those used for development, were normally quite small with an active area of only a few hundred square centimetres. However with the advent of higher energy accelerators, such as the 400 GeV SPS at CERN and Fermilab, much larger detector arrays are now required.

In many instances the maximum possible resolution is required, but for applications where resolution is not so critical and rates are low, drift chambers with long drift spaces are used in preference to MWPC's. Not only are fewer channels of electronics used per unit area but also electrostatic instability problems are not so great.

A neutrino experiment at Fermilab[5] used five chambers of the Walenta type with 5 cm drift lengths and an overall area of 13 m^2. Spatial resolutions of 0.35 mm were achieved. At CERN a current neutrino experiment[29] employs twenty hexagonal drift chambers built at Saclay totalling 720 m^2. The chambers have three sense wire planes aligned at 60° to each other to remove left-right ambiguities. A gas mixture of 70% Ar, 30% Isobutane plus methylal and field shaping of a Charpak type yields a maximum drift time of 600 ns over the 3 cm drift space. The 3,720 sense wires are up to 4 m long which introduces problems of signal attenuation due to the resistance of the wire. Digitization circuitry based on a 100 MHz clock provides spatial resolutions better than 1 mm.

Some chambers[31] designed for use on the forward spectrometer of the European Muon Collaboration at the CERN SPS will have active areas up to 4.5 x 9.6 m^2. They are of the adjustable field type and use self-supporting cathode planes of copper strips mounted on insulating epoxy material which is attached to the lightweight honeycomb material of the mainframe. The penetrating nature of the muons to be detected allows the use of such dense materials for chamber construction.

Chambers using printed circuit boards for cathode planes have been used for two projects at Durham. Test were performed[32] upon chambers of 52 x 52 cm^2 effective area built by International Research and Development Co. Ltd., for ESTEC to be used in balloon experiments to study cosmic gamma ray radiation. A smaller set of six chambers[33] with an active area of 13 x 13 cm^2 were built in Durham for use in conjunction with a flash-tube hodoscope at the Daresbury Laboratory Testbeam Facility. The chambers could be sandwiched closely together

with the sense wires orthogonally aligned in successive chambers by etching the cathode design mutually perpendicularly on opposite faces of the epoxy sheet. Field penetration between chambers was slight and the method allowed simple chamber construction. They were used to define the point of entry of positrons to the flash-tube chamber. The cells were staggered in alternate chambers, three chambers for each dimension, to remove ambiguities and resolutions of $\pm$ 0.3 mm were achieved for the 26 mm maximum drift lengths.

The use of three chambers with sense wire planes at different orientations to resolve the left-right ambiguity, reject spurious hits and gain two-dimensional co-ordinate information involves much computation. A more elegant solution would be to gain the two-dimensional information from a single chamber. For a chamber of the Walenta type, with cathode wires orthogonal to the sense wires, the localized avalanche on the sense wires could be located through the induced pulses on the cathode wires.[34] For adjustable field drift chambers however, where the sense and cathode wires are parallel, other methods must be used. Initial research used the method of "current division" on the sense wire.[12,35] By observing the current pulses propagated to each end of the sense wire, in direct ratio to the distances travelled, the position of the avalanche may be determined. The method is expensive electronically and the resolution is only of the order of 1 cm over 1 m of wire. A more accurate method[36] involves the use of a helical delay line which may either be placed in a sense wire triplet, as shown in figure 2.29, or positioned in the cathode plane. A pulse is induced on the delay line corresponding to the avalanche on the neighbouring sense wire and

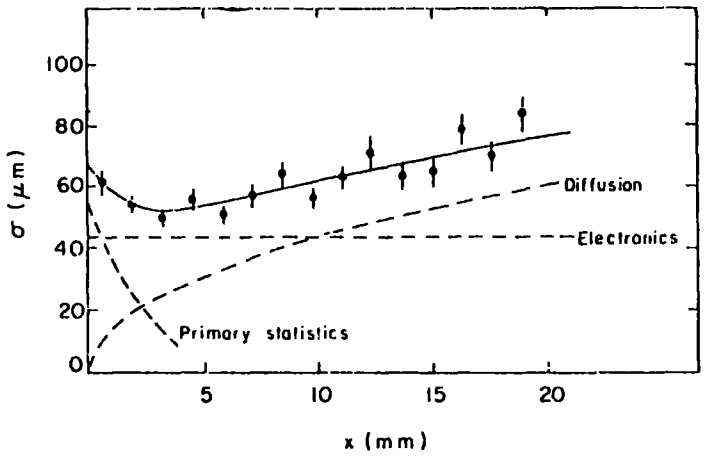

FIG. 2.28 : EXPERIMENTAL DATA DUE TO SAULI et al. SHOWING THE INTRINSIC ACCURACY OF A DRIFT CHAMBER AND INDICATING THE THREE CONTRIBUTORY PROCESSES

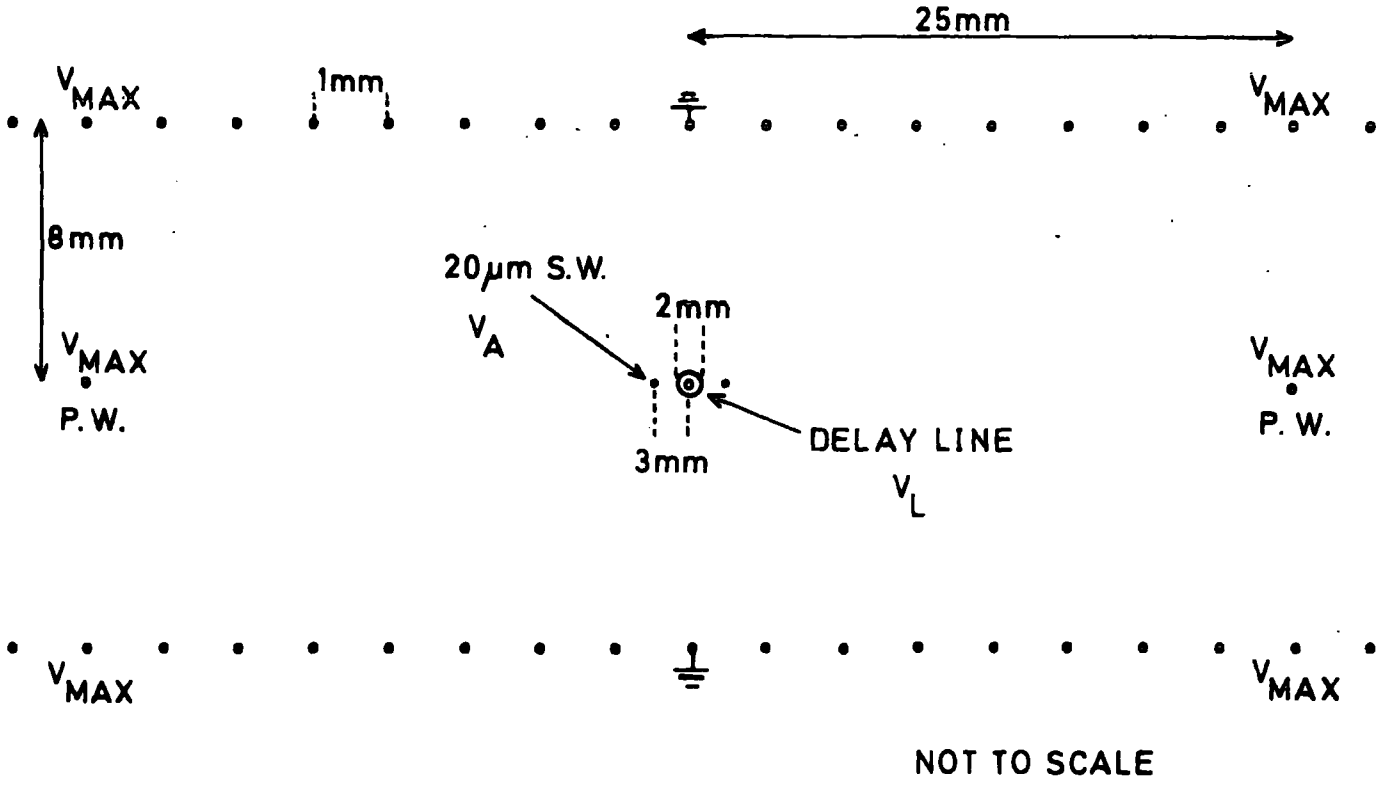

FIG. 2.29 : 2-DIMENSIONAL DRIFT CHAMBER

the difference in propagation delays to each end of the delay line determines the position of the avalanche. Resolutions of better than 3 mm over a 150 cm long sense wire have been achieved using a 2 mm diameter delay line[37] and 0.4 mm over 10 cm for a delay line wound on a 6 mm diameter ceramic cylinder.[38] Latest developments include the use of a thin strip printed circuit delay line[39] positioned orthogonally to the cathode plane between a sense wire doublet. This method has yielded a resolution of 1 mm for an ^{55}Fe source and 3 mm for a muon beam over a 30 cm sense wire. Future work on these methods should allow the resolution of the second dimension to approach the 100 μm attainable over the drift direction. As the chambers also use sense wire doublets the left-right ambiguity is successfully resolved throughout the chamber volume.

Drift chambers have been designed to operate at low pressures in order to track heavily ionizing particles. Using methylal vapour at 20 torr alpha particles were located to an accuracy of 1.5 mm.[40]

An application of the drift chamber principle called ISIS[41,42], shown in figure 2.30, uses a plane of 300 sense wires, similar to an MWPC, to detect electrons drifted over distances of up to 2 m. Positional accuracy of approximately 2 mm from the track and energy resolution from the pulse heights enables the chamber to distinguish between kaons, pions and protons from 5 GeV/c to 100 GeV/c momentum. Such a chamber represents the closest approach to a fully electronic track chamber.

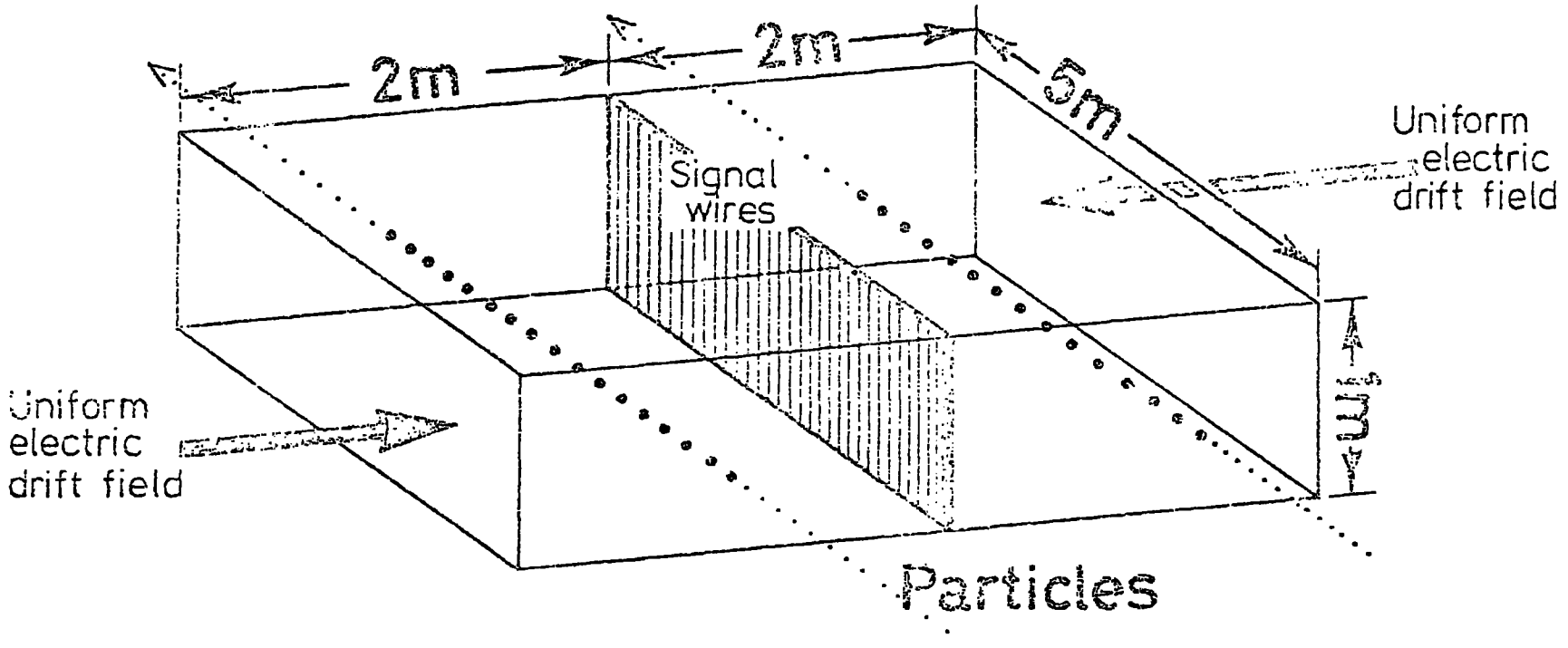

FIG. 2.30 : OUTLINE OF THE ISIS CHAMBER

Recent development of spherical drift chambers at CERN for X-ray imaging illustrate the wide range of applications of the drift chamber principle. They may be used in the study of X-ray diffraction patterns, pin-hole imaging and angular distributions of X-ray cascades in nuclear physics. The prototype chamber discussed in reference 43 is shown in figure 2.31. The chamber has an opening angle of 50° and a detection area of 10 x 10 cm^2, although a later chamber[44] has a 90° opening angle and a 50 x 50 cm^2 detection area. X-rays diffracted from the rotating crystal pass into the spherical drift region which has a radial field. This is achieved using two spherical electrodes, E_1 and E_2, and a resistive divider on the conical outer face of the chamber to provide potentials to conducting rings. As the X-ray trajectories are parallel to the drift field no loss of resolution occurs on capture. The resultant electrons are drifted through the field and then across a transfer region into a multiwire chamber with a 1 mm wire spacing. Two dimensional information is derived by the "centre of gravity of the avalanche" method[45] using the positive induced signals on the two cathode planes, which are perpendicular to each other. Using a gas mixture of argon 75%, isobutane 23%, methylal 2% accuracies of 0.5 mm have been achieved with 8 keV X-rays.[43] Using on-line computers these chambers may have future applications in medical physics and for X-ray crystallography study of rapid changes in crystalline structure which cannot be contemplated using conventional film techniques.

Another field of research at CERN involves the use of high density converters to detect γ-rays and neutrons.[45,46] The converters have

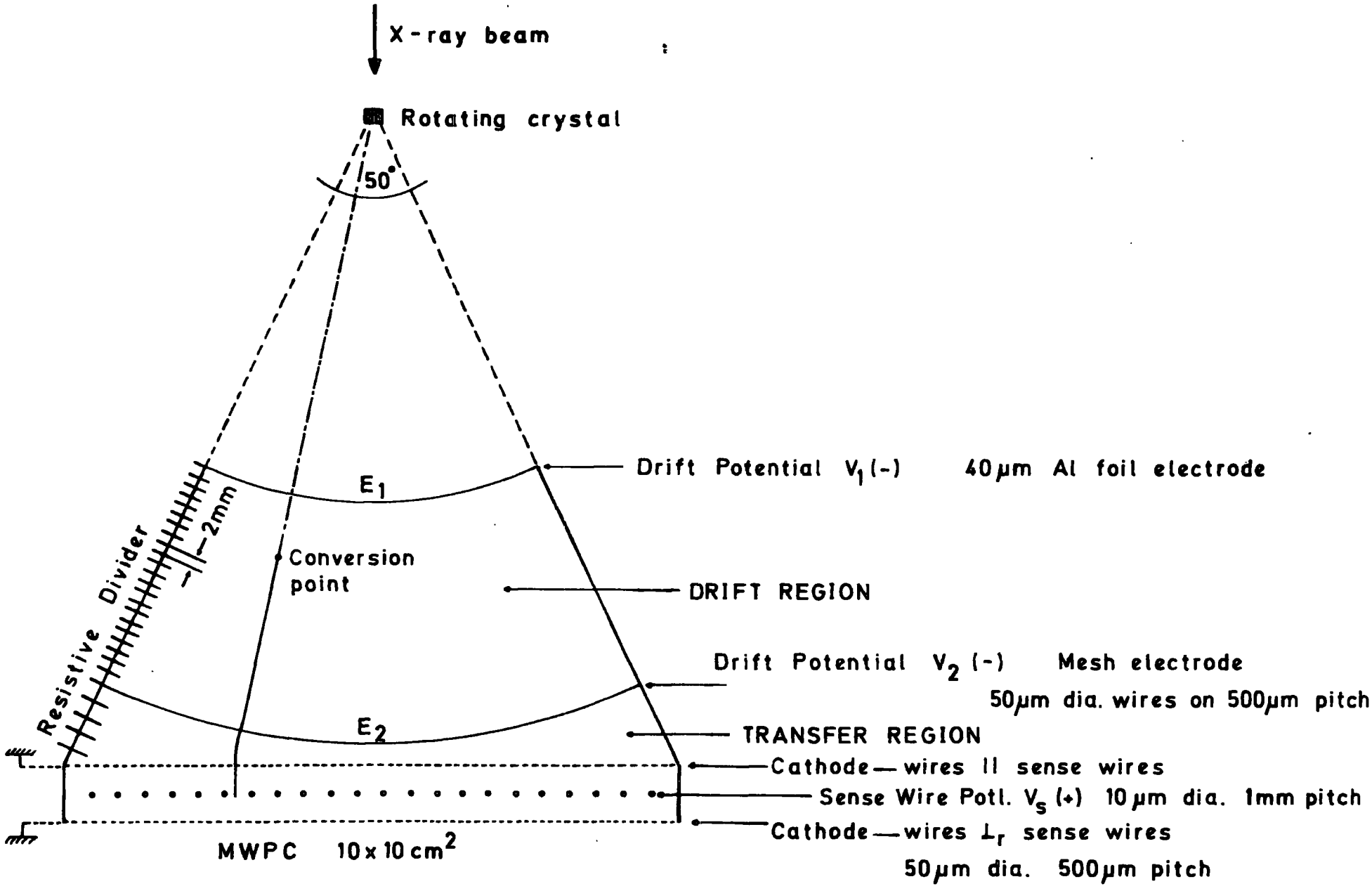

FIG. 2.31 : SCHEMATIC OF A SPHERICAL DRIFT CHAMBER

a uniform matrix of holes into which photoelectrons, formed by the conversion of the neutral particle in the solid, may escape. The converter is in the form of a stack of metal sheets and insulators to enable a field to be applied throughout its depth. The electrons escaping into the holes are drifted down into an MWPC as in the spherical drift chamber. Figure 2.32 demonstrates such a system. Much research is being undertaken, including in Durham,[47] to optimize the construction of the converter. Suitable choice of converter material and geometry allows the chambers to operate at various energies. Initial results indicate the possibility of detecting 0.66 MeV photons to a spatial accuracy of 1.3 mm fwhm with 5% efficiency, the latter being almost entirely due to the geometry of the converter.

Recent development of the scintillating drift chamber[48,49] following initial work by Policarpo et al.[50,51] has presented the possibility of constructing chambers capable of operating at rates greater than 3×10^6 particles mm^{-2} s^{-1}. The chamber shown in figure 2.33, taken from reference 49, relies upon the principle that primary electrons moving in an electric field with correct gaseous conditions produce light without charge amplification.[52] The primary scintillation caused by the traversing particle acts as the zero timing trigger and the drift time is measured by recording the incidence of a small pulse on the large diameter sense wire, typically 0.5 mm. Due to the low field around the sense wire charge amplification is low and space charge effects do not occur, allowing the chambers to be operated at high rates. With the correct combination of chamber gas and photomultiplier tube, and the self-triggering property of the chambers, neutral particles, X-rays,

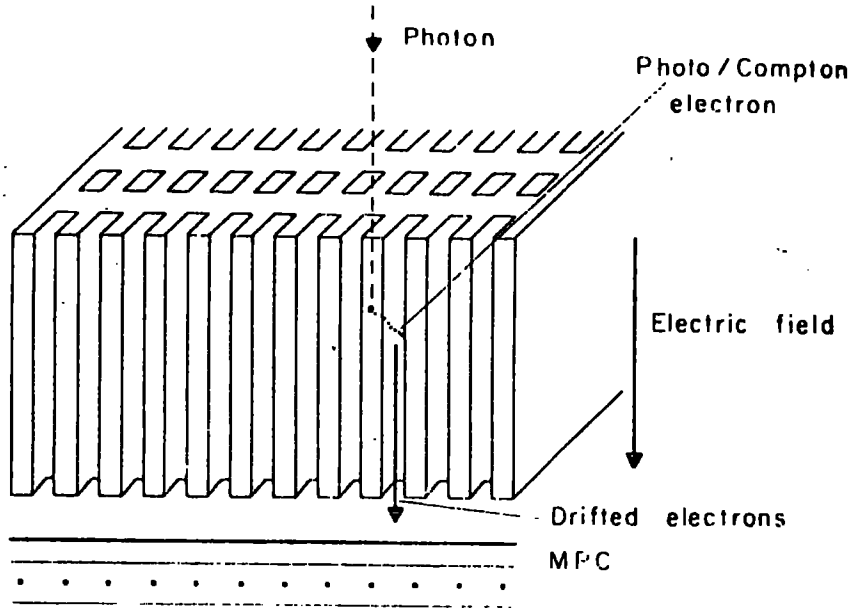

FIG. 2.32 : LAYOUT OF A HIGH-DENSITY DRIFT CHAMBER

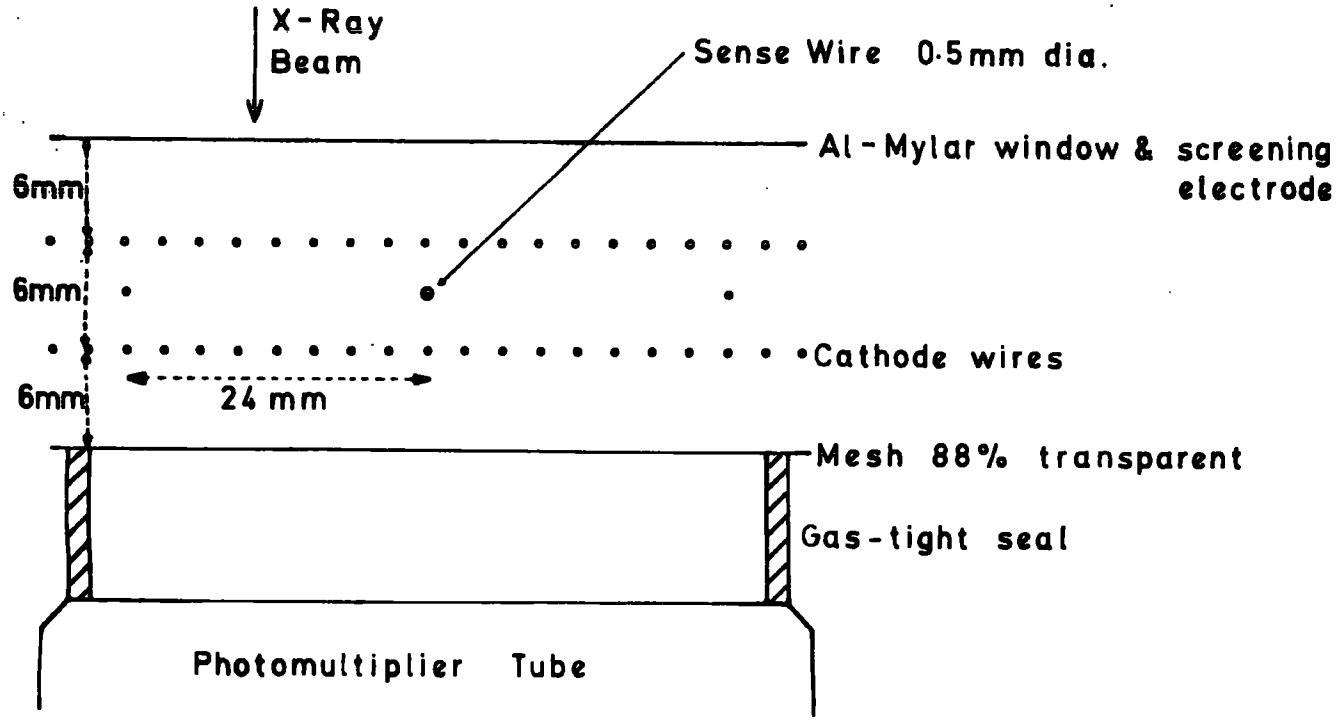

FIG. 2.33 : OUTLINE OF THE SCINTILLATING DRIFT CHAMBER

heavily and minimum ionizing particles may be detected. This extension of the drift chamber principle is receiving much attention at present, including at Durham where a high-rate X-ray detector for use at the new Daresbury Laboratory Synchrotron Radiation Facility is being developed.

2.9 Conclusions

It has been shown why drift chambers have become one of the most important classes of detector in the field of particle location today. Only for high rate and multiplicity applications are MWPC's still preferable in high energy physics due to the lower cost and inherently better spatial resolution of drift chambers. As indicated, the properties and modes of operation of drift chambers are well understood in terms of the classical theories of electrons in gases.

Recent developments concerning the increase of attainable spatial resolution and the ability to obtain unambiguous two dimensional read-out has served to increase the number of drift chamber applications. Hybrid chambers may also find applications in the fields of medical physics and X-ray crystallography.

Although the ultimate spatial resolution attainable is limited by basic gaseous processes there are several areas where drift chamber development is still far from complete. Current research is directed towards improving the spatial resolution in the second dimension along the sense wire, orthogonal to the drift direction, operation at high rates and extension to the detection of neutrals and heavily ionizing particles.

REFERENCES

1) Walenta, A. H., Heintze, J., Schurlein, B.,
Nucl. Instr. Meth. 92 (1971) 373

2) Walenta, A. H.,
Nucl. Instr. Meth. 111 (1973) 467

3) Heintze, J., Walenta, A. H.,
Nucl. Instr. Meth. 111 (1973) 461

4) Schurlein, B., Farr, W., Siebert, H. W., Walenta, A. H.,
Nucl. Instr. Meth. 114 (1974) 587

5) Cheng, D. C., Kozanecki, W. A., Piccioni, R. L., Rubbia, C., Suluk, L. R., Weedon, H. J., Whittaker, J.,
Nucl. Instr. Meth. 117 (1974) 157

6) Becker, U., Burger, J. D., Forber, R., Leong, J., Perasso, L.,
Nucl. Instr. Meth. 128 (1975) 593

7) Atac, M., Taylor, W. E.,
Nucl. Instr. Meth. 120 (1974) 147

8) Walenta, A. H.,
IEEE Trans. Nuclear Sci. NS-22 (1975) 251

9) Sadoulet, B., Litke, A.,
Nucl. Instr. Meth. 124 (1975) 349

10) Chaminade, R., Duchazeaubeneix, J. C., Laspalles, C., Saudinos, J.
Nucl. Instr. Meth. 111 (1973) 77

11) Bressani, T., Charpak, G., Rahm, D., Zupancic, C.,
Track Localization by means of a Drift Chamber, Proc. Internat. Seminar on Filmless Spark and Streamer Chambers, Dubna, 1969 (JINR, Dubna, 1969) p.275

12) Charpak, G., Sauli, F., Duinker, W.,
Nucl. Instr. Meth. 108 (1973) 413

13) Breskin, A., Charpak, G. Gabioud, B., Sauli, F., Traunter, N., Duinker, W., Schultz, G.,
Nucl. Instr. Meth. 119 (1974) 9

14) Charpak, G.,
Drift Chambers, Proc. ESRO Workshop, Frascati, 24-25 Oct 1974
(ESRO, c/o ESTEC, Noordwijk, Neth.), p. 109

15) Breskin, A., Charpak, G., Sauli, F., Atkinson, M., Schultz, G.,
Nucl. Instr. Meth. 124 (1975) 189

16) Palladino, V., Sadoulet, B.,
Lawrence Berkeley Laboratory Report
LBL - 3013 (1974)

17) See for example:
a) Townsend, J. S.,
Electricity in Gases, Claredon Press, Oxford (1915)
b) Huxley, L. G. H., Crompton, R. W.,
The Diffusion and Drift of Electrons in Gases
Wiley, New York (1974)
c) Loeb, L.,
Basic Processes of Gaseous Electronics,
University of California Press, 1961

18) Palladino, V., Sadoulet, B.,
Nucl. Instr. Meth. 128 (1975) 323

19) Sauli, F.,
Principles of Operation of Multiwire
Proportional and Drift Chambers
CERN 77-09 3rd May 1977

20) Makowski, B., Sadoulet, B.,
Space Charge Effects in Multiwire
Proportional Counters
CERN/D - Ph 2 PHYS 73-3

21) See for example:
a) Townsend, J. S.,
Electrons in Gases,
Hutchinson's Scientific Publications,
London, 1948
b) Huxley, L. H. G., Zaarou, A. A.,
Proc. Royal Soc. A196 (1949) 402

22) Browell, R.,
Ph.D. Thesis, University of Durham (1976)

23) Short, K. A.,
Ph.D. Thesis, University of Durham (1975)

24) Hough, J.,
Nucl. Instr. Meth. 105 (1972) 323

25) Cheng, D. C., Kozanecki, W. A., Piccioni, R. L., Rubbia, C.,
Sulak, L. R., Weedon, H. J., Whittaker, J. J.,
Proc. Int. Conf. on Instrumentation for
High Energy Physics, Frascati, 1973
(ed. S. Stipcich), (CNEN, Frascati, 1973),
p.268

26) Walenta, A. H.,
Left-Right Assignment in Drift Chambers
and MWPC's Using Induced Signals,
Brookhaven National Laboratory Internal Report,
BNL 23162, August 1977, sub. to Nucl. Instr. Meth.

27) Fisher, J., Okuno, H., Walenta, A. H.,
Spatial Distribution of the Avalanche in
Proportional Counters,
Brookhaven National Laboratory Internal Report,
BNL 23163, August 1977, sub. to Nucl. Instr. Meth.

28) Charpak, G., Sauli, F.,
Nucl. Instr. Meth. 107 (1973) 371

29) Marel, G., Bloch, P., Brehin, S., Devaux, B., Diamant-Berger, A. M.,
Leschevin, C., Maillard, J., Malbequi, Y., Martin, H., Patoux, A.,
Pelle, J., Plancoulaine, J., Tarte, G., Turlay, R.,
Nucl. Instr. Meth. 141 (1977) 43

30) Filatova, N. A., Nigmanov, T. S. Pugachevich, V. P., Riabtsov, V. D.,
Shafranov, M. D., Tsyganov, E. N., Uralsky, D. V.,
Vodopianov, A. S., Sauli, F., Atac, M.,
Nucl. Instr. Meth. 143 (1977) 17

31) Connell, K. A., Cunningham, R. A., Edwards, M., Gabathuler, E.,
Norton, P. R., Walker, R. P.,
Nucl. Instr. Meth. 144 (1977) 453

32) Breare, J. M., Meyer-Berkhout, U.,
Durham University Internal Report
NI - 76 - 23

33) Hedge, A. R., Humrich, A.,
Durham University Internal Report
NI - 77 - 12

34) Walenta, A. H.,
Two-dimensional read-out of Drift Chambers
Proc. 16th Int. Conf. on High-Energy Physics,
Batavia, 1972, (Chicago, August 1972)

35) Foeth, H., Hammarstrom, R., Rubbia, C.,
Nucl. Instr. Meth. 109 (1973) 512

36) Charpak, G., Sauli, F., Santiard, J. C.,
CERN NP Internal Report 73-16 2/10/73

37) Breskin, A., Charpak, G., Sauli, F., Santiard, J. C.,
Nucl. Instr. Meth. 119 (1974) 1

38) Breskin, A., Charpak, G., Sauli, F.,
Nucl. Instr. Meth. 125 (1975) 321

39) Atac, M., Bosshard, R., Erhan, S., Schlein, P.,
Nucl. Instr. Meth. 140 (1977) 461

40) Breskin, A., Charpak, G., Sauli, F.,
Nucl. Instr. Meth. 119 (1974) 7

41) Allison, W. W. M., Brooks, C. B., Cobb, J. H., Bunch, J. N.,
Lloyd, J. L., Fleming, R. W.,
Oxford University Nucl. Phys. Lab. Report
17-74 (1974)

42) Mulvey, J. H.,
Proc. Int. Conf. on Instrumentation for
High Energy Physics, Frascati, 1973
(ed S. Stipcich), (CNEN, Frascati, 1973),
p.259

43) Charpak, G., Hajduk, Z., Jeavons, A., Kahn, R., Stubbs, R.,
Nucl. Instr. Meth. 122 (1974) 307

44) Charpak, G., Demierre, C., Kahn, R., Santiard, J. C., Sauli, F.,
Nucl. Instr. Meth. 141 (1977) 449

45) Jeavons, A. P., Charpak, G., Stubbs, R. J.,
Nucl. Instr. Meth. 124 (1975) 491

46) Jeavons, A. P., Cate, C.,
IEEE Trans. Nuclear Sci. NS-23 (1976) 640

47) Ariyaratne, T. R.,
Durham University Internal Report
NI - 77 - 7

48) Charpak, G., Majewski, S., Sauli, F.,
Nucl. Instr. Meth. 126 (1975) 381

49) Charpak, G., Majewski, S., Sauli, F.,
1975 Nucl. Science Symp., San Francisco,
19-21 Nov. 1975,
IEEE Trans. Nuclear Sci. NS-23 (1976) 202

50) Conde, C. A. N., Policarpo, A. J. P.,
Nucl. Instr. Meth. 53 (1967) 7

51) Policarpo, A. J. P., Alves, M. A. F., Salete, M., Leite, S. C. P.,
Nucl. Instr. Meth. 128 (1975) 49

52) Policarpo, A. J. P., Alves, M. A. F., dos Santo, M. C. M.,
Carvalho, M. J. T.,
Nucl. Instr. Meth. 102 (1972) 337

CHAPTER 3

THE (g-2) DRIFT CHAMBERS

3.1 Introduction

The (g-2) drift chambers were not only novel with respect to their intended use in the highly inhomogeneous fringe field of the Muon Storage Ring but also in their method of construction. The chambers had to be mounted between the pole pieces of the (g-2) magnets and present the maximum possible active area to the decaying electrons and also the least possible mass of absorber. A special curved end section had to be developed to match the profile of the vacuum storage vessel.

This chapter summarizes the design considerations and the choice of operating parameters for the chambers. Much of the initial work was performed by previous members of the Nuclear Instrumentation Group at Durham, the author assisting in the latter stages of design and the overall commissioning of the production chambers.

3.2 Design Considerations and Methods of Construction

The magnet aperture and the final chamber dimensions are shown in figure 3.1. This illustrates the basic requirements; the total active area to be comparable to that of the shower counter, which was to act as a timing trigger, and the minimum possible dimensions for the upper and lower support members. Not only did the curved end have to be thin to reduce scattering of the electrons but it also

ALL DIMENSIONS IN mm

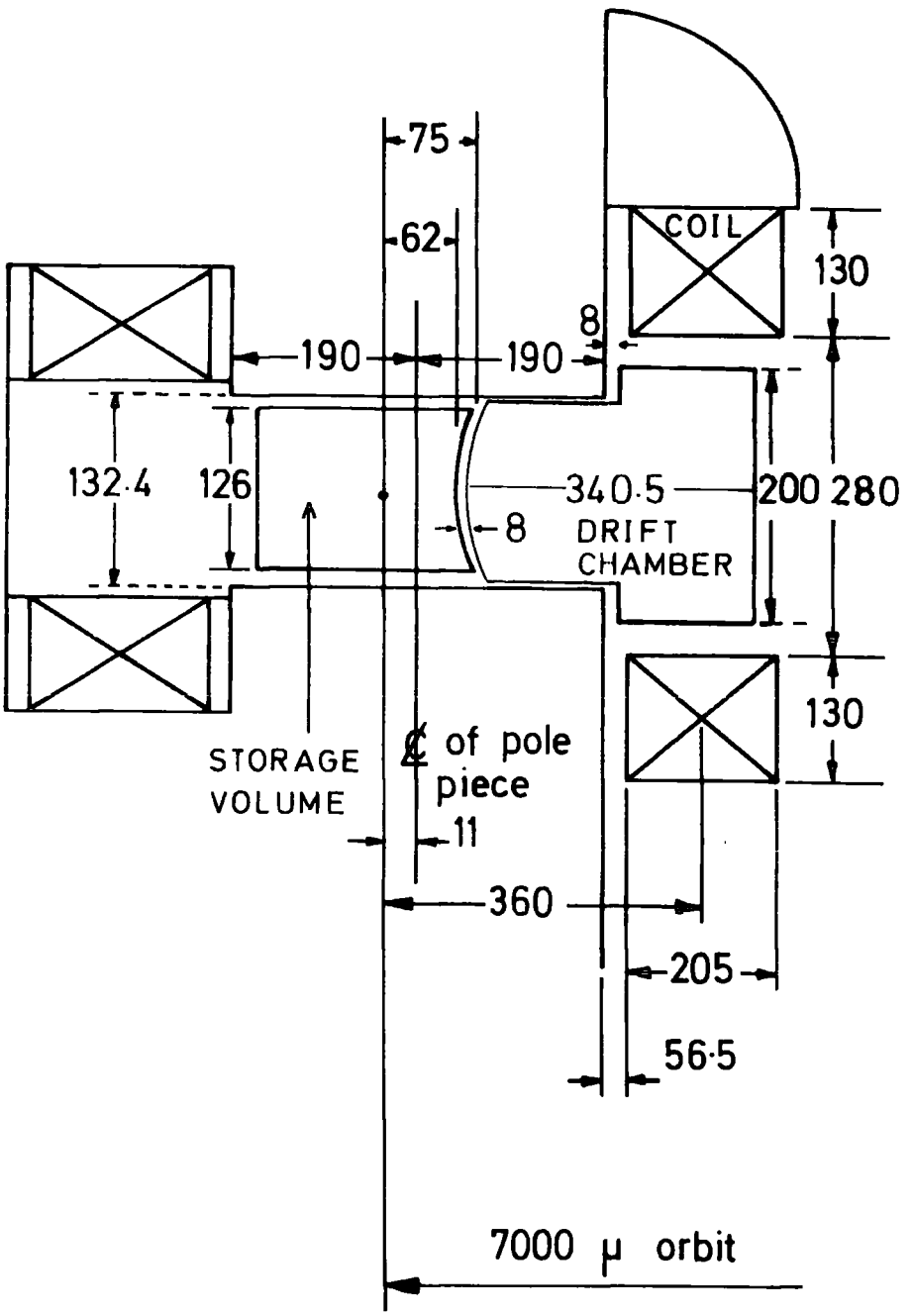

FIG. 3.1 : DIMENSIONS OF MAGNET APERTURE AND DRIFT CHAMBER

had to have the smallest possible cross-sectional area to allow detection of electrons as close to the storage volume as possible. The chambers were to be of the adjustable field type which implied that two planes of field shaping wires had to be wound on the frame. The use of printed circuit board to act as both window and electrode was not common at the time the chambers were designed, late 1973, and in any case an array of eight chambers would have presented too much material to the electrons. Thus the chambers had to incorporate two field shaping planes plus the sense wire plane and use thin melinex windows. It was also evident that the curved end section would provide little rigidity to the overall structure and that the upper and lower members would have to support the wire planes, attached under tension. Therefore a unique method of chamber design had to be devised as a traditional rigid square frame was not allowed in the (g-2) application. Figure 3.2 shows the proposed geometrical arrangement of the array. As the decay electrons would be between 1 and 3 GeV in energy a considerable range of curvatures had to be catered for. A prerequisite was that at least three and preferably four points were detected on each track. As they also had to be detected by the shower counter, the active volume of which extended about 25 cm radially inwards from the storage tank, it was obvious that the lower energy electrons would travel only a short distance in azimuth before being deflected too far towards the centre of the ring to be detected. Hence it was necessary to have as close a spacing as possible between the four drift chambers closest to the shower counter to provide sufficient points on the trajectories. On the other hand

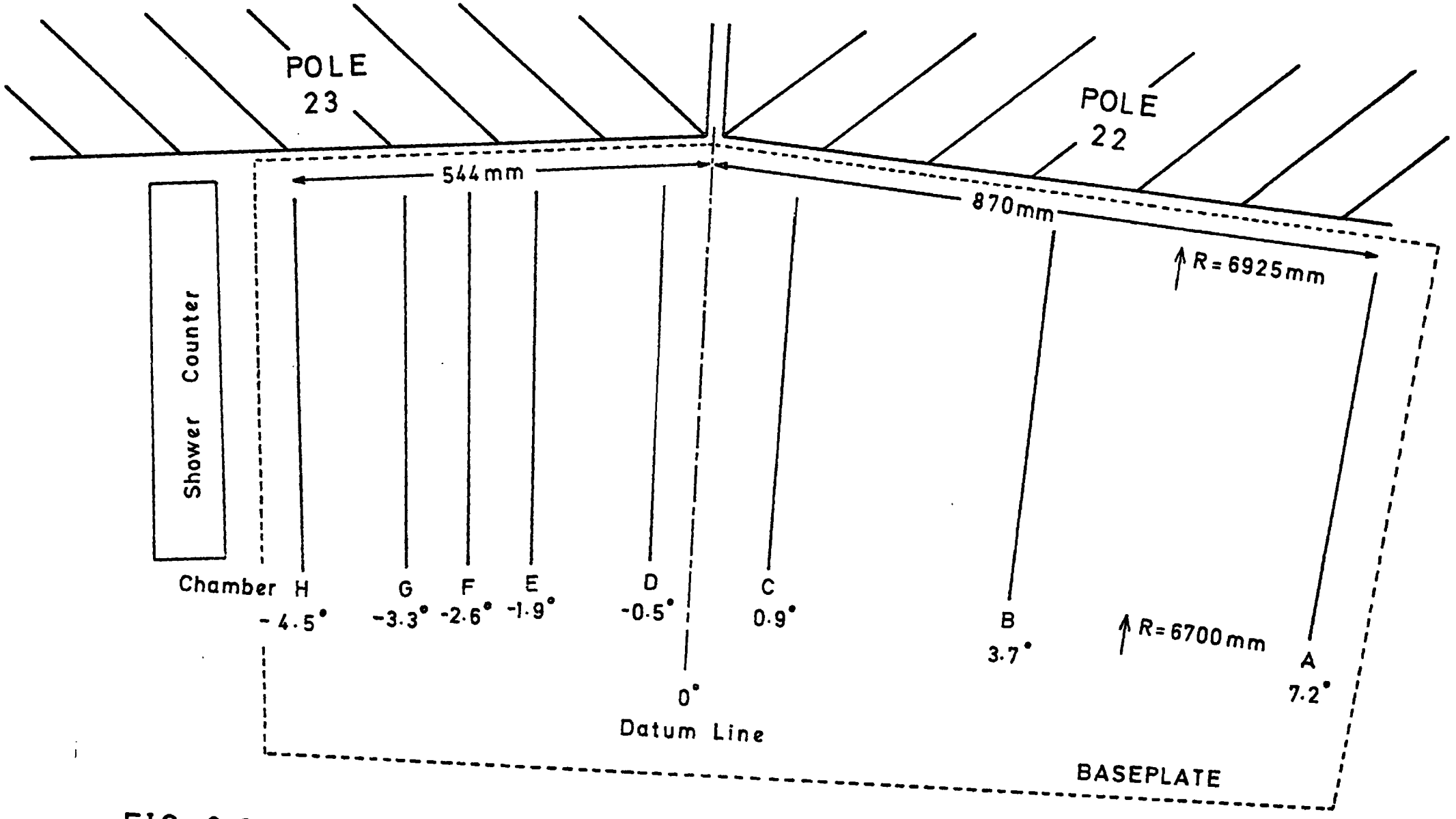

FIG. 3.2 : GEOMETRICAL LAYOUT OF DRIFT CHAMBER ARRAY

for the higher energy electrons, which were deflected much less, it was necessary to cover a large distance in azimuth in order that a reasonable sagitta on the track was produced to enable accurate tracking back into the storage volume to deduce the birth position. Therefore the width of each chamber had to be the minimum practicable to allow close packing near the shower counter, but at the same time the overall array had to extend one and a half magnet blocks in azimuth to accommodate the full range of energies to be detected.

3.2.1 The Chamber Body

A complete description of the design and construction methods is given elsewhere,[1,2] a brief summary only being given in the following sections. The chamber body is shown schematically in figure 3.3. The main frame had to be as rigid as possible to allow accurate mounting in a cradle which was positioned on the baseplate in the (g-2) ring. Also it was preferable to extend this main section along the side members as far as possible to increase their strength, as they had to support the wire planes without deflection. Thus the main member was constructed from 37 mm thick laminated glass-fibre epoxy-resin (G10) and extended along the side members so that when in position in the ring the faces almost touched the magnet poles.

The upper and lower side members were constructed from glass, which has a high Young's modulus. The lower member had a slot cut in it to allow passage of the gas mixture from an entry port in the main body to the curved end where it entered the chamber volume. Exit was via a port on the top of the main body, thus ensuring complete flushing of the chamber volume.

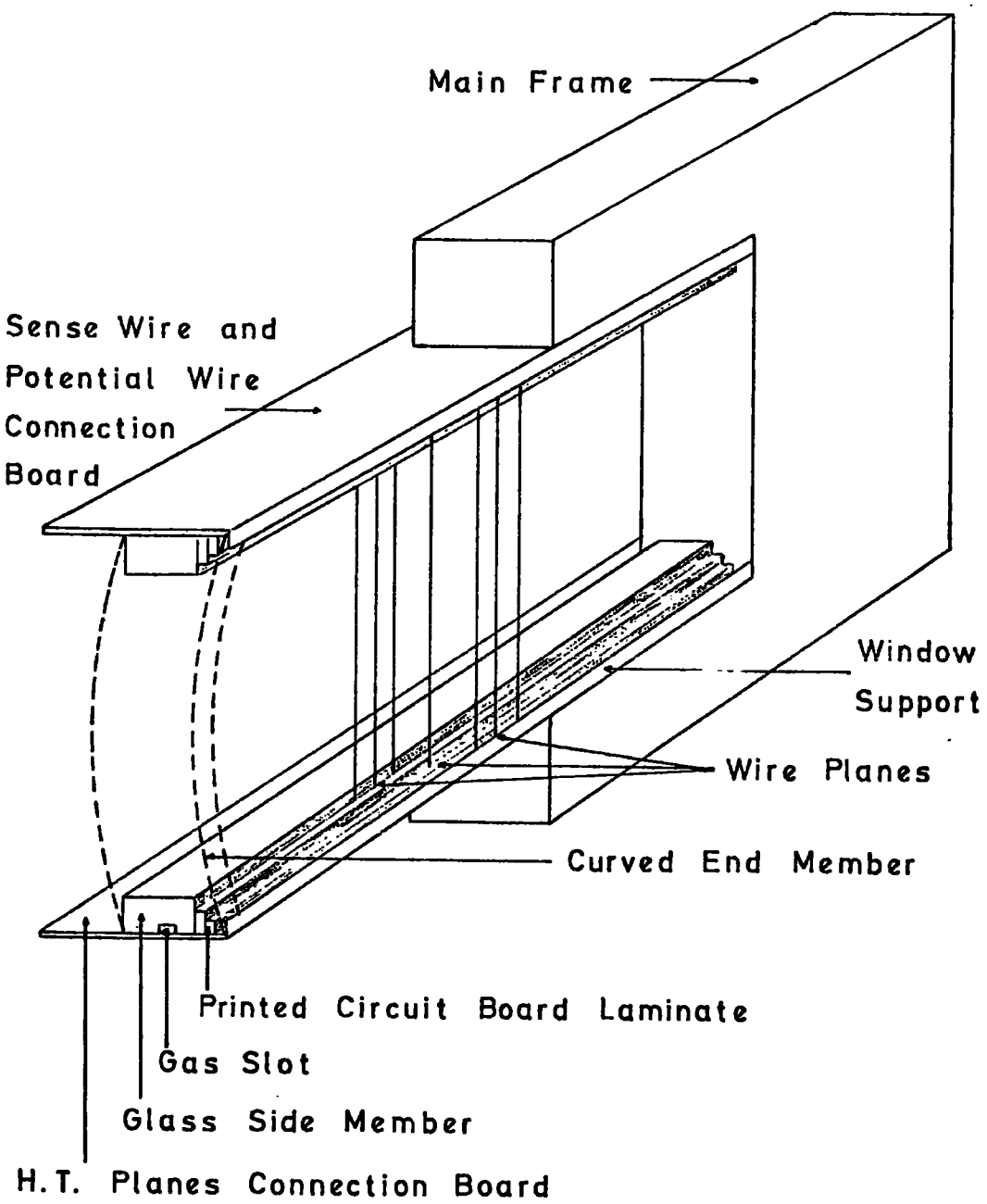

FIG. 3.3 : SCHEMATIC OF CHAMBER CONSTRUCTION

The curved end section was made from 0.5 mm G10 sheet bent to the correct curvature and adhered under tension to the side members. Various Araldite adhesives were used for the chamber construction.

The chamber therefore gained all its rigidity from the main and side members, and hardly any from the curved end. Important chamber dimensions are shown in figure 3.4, all machining being accurate to at least 125 μm with emphasis placed upon the parallelity of the side members and main member to ensure verticality of the sense wires.

3.2.2. Wire Planes and Electrical Connections

Figure 3.5 illustrates the mode of assembly of a system of printed circuit boards designed to allow internal mounting of the wire planes with connection to external boards for application of the applied potentials and readout of the sense wire signals. The internal and external sets of boards were mutually perpendicular, solder connections being made between the two. The laminate structure was bonded in Araldite to ensure that the inter-plane gaps were kept constant at 3.2 mm. The H.T. plane connection boards were at the bottom of the chamber and the sense wire/potential wire board at the top, all facing upstream.

The chamber was divided into eight cells of 28 mm from potential wire to potential wire, giving a drift length of 14 mm, with a variation in geometry for the curved end cell, as shown in figure 3.6 demonstrating a unit cell. The 120 μm diameter copper beryllium H.T. wires were wound on a 2 mm pitch. They were attached to the connection boards, using low temperature solder, under a tension of 50 g.

ALL DIMENSIONS IN mm
SIDE VIEW OF DOWNSTREAM FACE

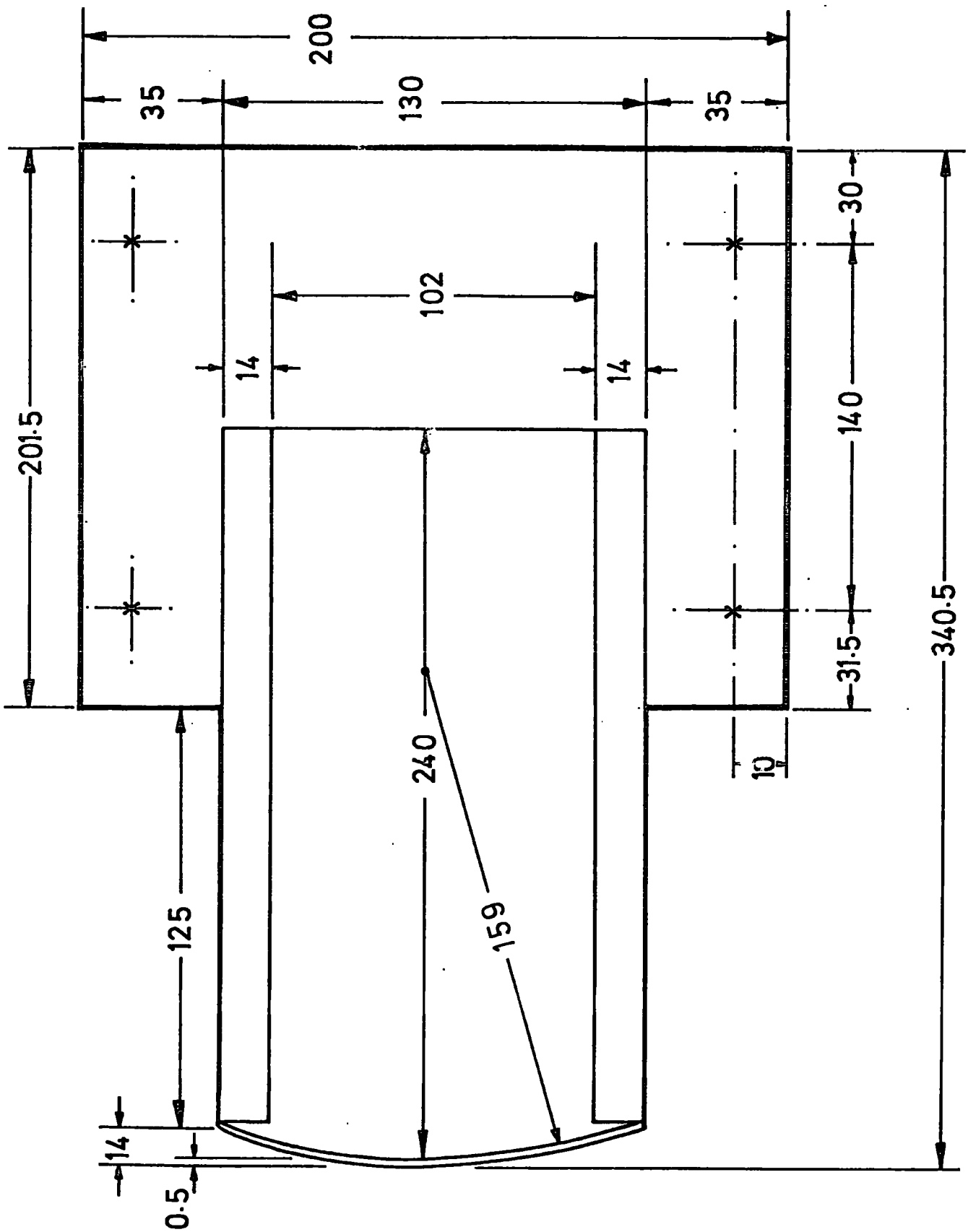

FIG. 3.4 : PRINCIPLE CHAMBER DIMENSIONS

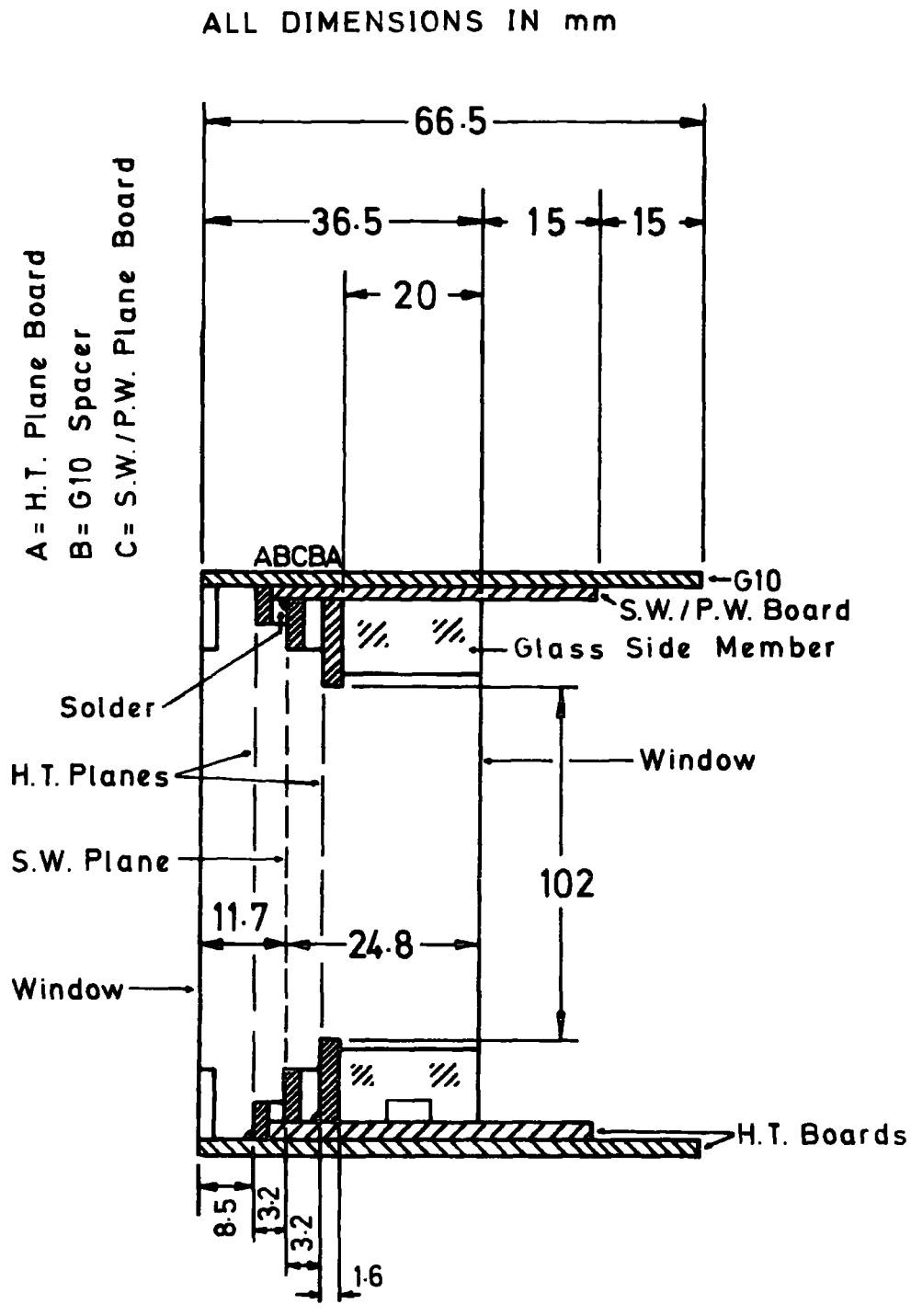

FIG. 3.5 : ASSEMBLY OF WIRE PLANES

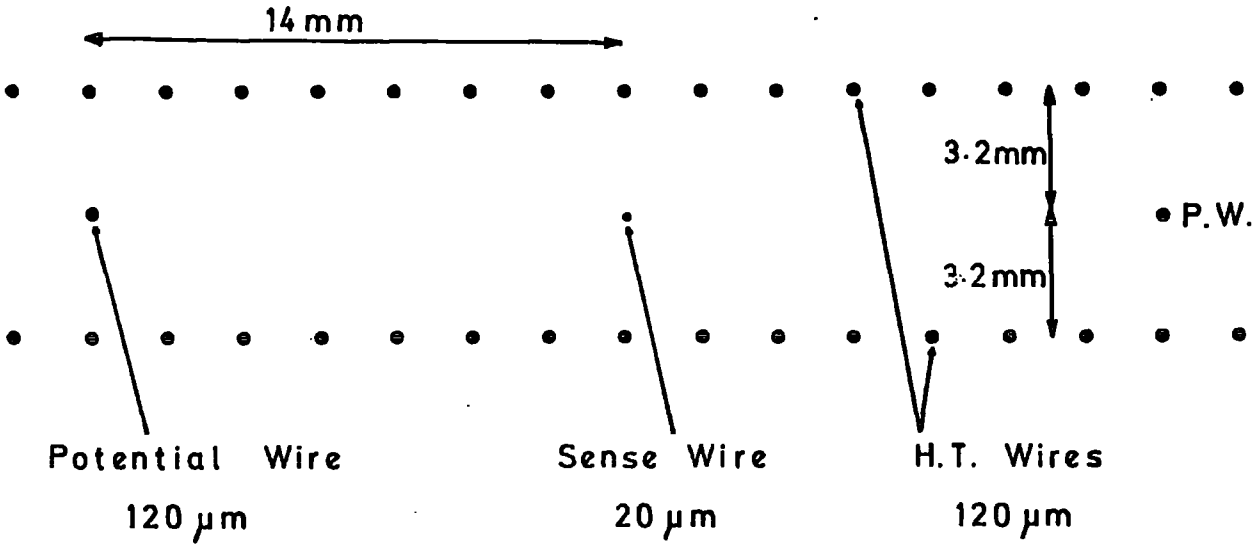

PLAN VIEW

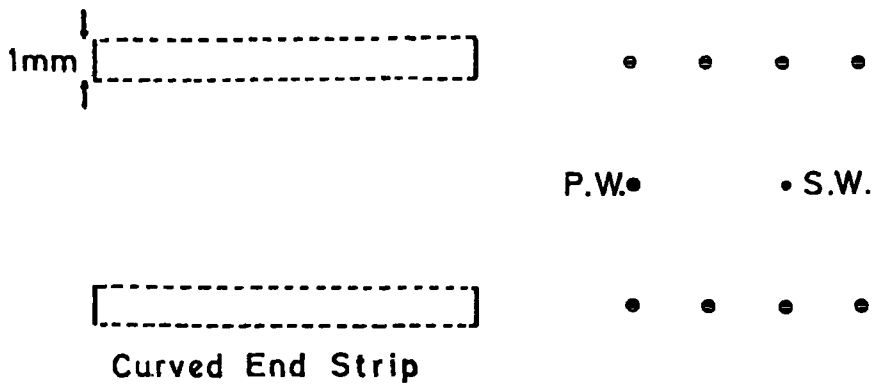

PLAN VIEW

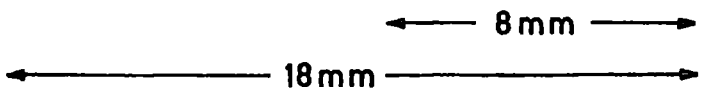

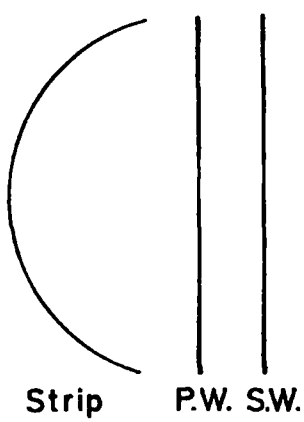

SIDE VIEW

(Not to scale)

FIG. 3.6 : NORMAL UNIT CELL & CURVED END CELL

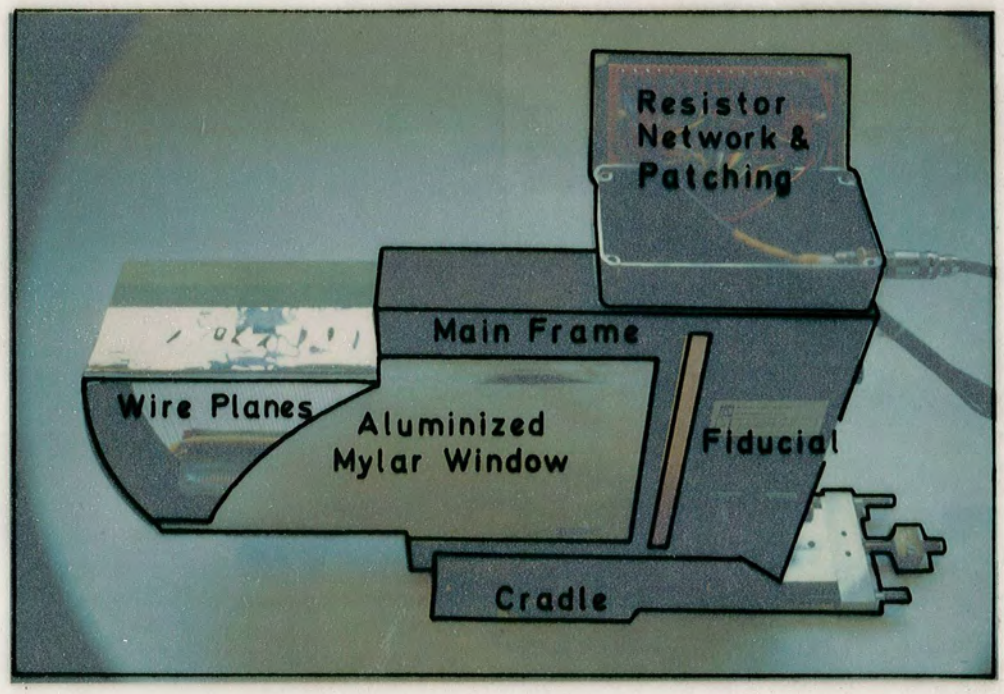

FIG. 3.7 : DOWNSTREAM VIEW OF g-2 CHAMBER

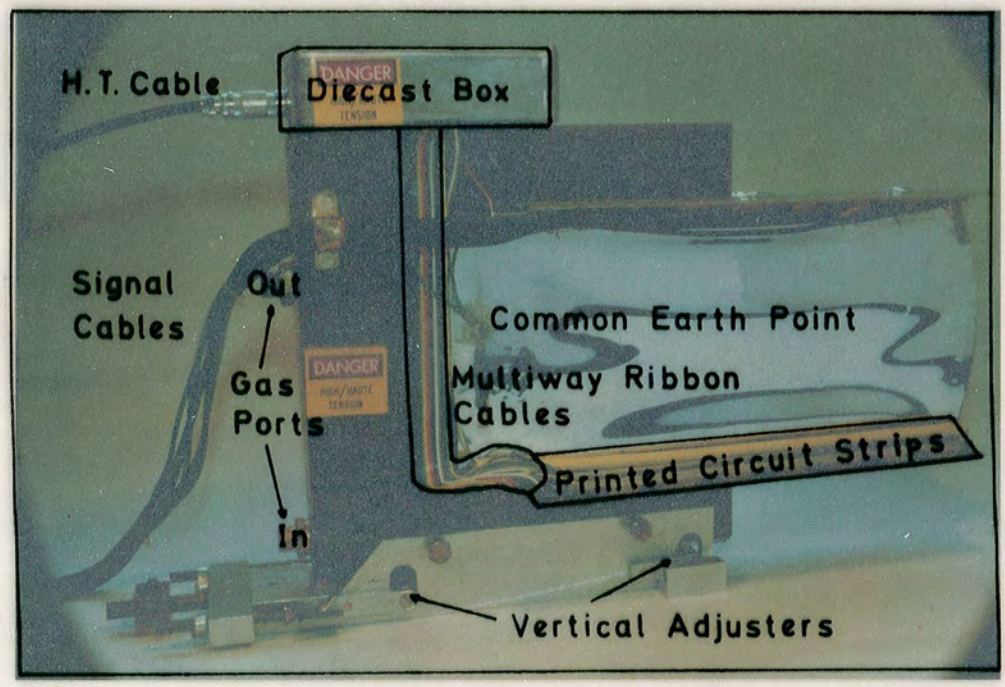

FIG. 3.8 : UPSTREAM VIEW OF g-2 CHAMBER

Positioning of the wires by eye to correspond to the middle of the copper strips on the connecting board proved to be sufficiently accurate. The 20 μm diameter gold plated tungsten sense wires were attached under 30 g tension. They were aligned parallel to a fiducial line, mounted vertically on the downstream face of the main chamber member, to an accuracy of 100 μm by a method of trial and error. The alternately spaced potential wires were of the same type as the H.T. wires and also mounted under 50 g tension, their positioning being done by eye to the centre of the copper strip. Figure 3.5 demonstrates that the step structure of the connection boards allowed easy replacement and cleaning of wires from the downstream side, as also shown in figure 3.7 which shows a photograph of the downstream side of the chamber. Part of the aluminized mylar window is removed to reveal the wire planes and the fiducial strip can be seen on the main body, aligned with a fiducial line on the chamber cradle.

Figure 3.8 shows a view of the upstream side of the chamber. The 8 ns miniature Lemo sense wire signal cables are seen running from the upper connection board. The H.T. connections to the two wire planes were via specially prepared printed circuit strips which connected identical wires in each cell, fourteen strips being required for both the upstream and downstream H.T. planes. Correct potentials were applied to each strip via multiway ribbon cables running to the voltage divider resistor network housed in a diecast box mounted on top of the chamber spine, as shown in more detail in figure 3.7. A rigourous colour coding was employed for patching between the ribbons and the relevant points on the voltage divider to provide the correct field gradient in the chambers. This was vital as the direction of electric field tilt, needed to compensate for the (g-2) magnetic field,

had to be reversed when the (g-2) experiment ran with stored muons of the opposite polarity, and hence reversed the magnetic field direction parallel to the sense wires. In figure 3.8 wires can also be seen leading to the potential wires on the upper connection board and to the curved end section which had two 1 mm copper strips adhered to the inner surface, coincident with the H.T. planes, to provide the field in this region.

Although this hard wiring method was laborious when altering the patching from the resistor network to the multiway ribbons during field reversal, it proved to be the most reliable considering the potentials involved and the space limitations for mounting the network. No commercial connectors were available to simplify the reversal procedure and also satisfy the electrical and physical requirements.

Allowing for the active chamber volume and the necessary width of the external connection boards, the minimum practicable width of the chambers was 67 mm.

The chamber windows were of 120 μm mylar, aluminized on the outer surface and attached to the chamber frame using 3 M "Twinstick" adhesive strip. This was the minimum window thickness that gave a reliable gastight seal. The method of attachment allowed easy removal for chamber repair and inspection. The whole of the chamber active volume was enclosed by the aluminized mylar to provide screening, particularly from the Suisse Romande television transmitter near CERN which caused severe interference problems with unscreened chambers.[2] The windows, earth braiding of the sense wire signal cables and the grounded end of the resistor network were all joined at a common point on the chamber.

Throughout the construction of the chambers only non-magnetic materials were used to prevent distortion of the (g-2) magnetic field and also to prevent stress upon the chambers.

The eight production chambers described above were built by the International Research and Development Co. Ltd. (I.R.D.) under close supervision from the University of Durham following the initial development of a small test chamber and a series of prototype chambers at Durham.

3.3. Application of the Electric Field

The final version of the voltage distribution network is described in Chapter 4, but for all tests of the prototype and production chambers a similar design of resistor network was used. As the (g-2) chambers were of the adjustable field type the graded drift field and acceleration field around the sense wire had to be produced using a voltage divider network. A single stablized high voltage supply was used and the resistor network altered to study the effects of various acceleration and drift fields. The sense wires were grounded through the pre-amplifier 50Ω input resistors and hence alleviated the need for decoupling circuits. Varying the voltage across the resistor network necessarily altered both the drift field and acceleration field, which was due to the potential on the H.T. wire opposite the sense wire. This system was not so versatile as a two supply arrangement due to the lack of independence of the two fields, but was easier to operate. Figure 3.9 shows the

general layout of the resistor network with the eight negative potentials from V_{max} to V_{min} required with the (g-2) cell geometry. The resistance to earth, R_E, and the applied voltage determined the value of V_{min} and the applied voltage alone determined the drift field with a particular network. To obtain various drift fields with the same value for V_{min} the value of R_E had to be altered as the applied voltage was changed. The drift field was defined as $(V_{max} - V_{min}) / 1.4$ V cm^{-1} which applied over most of the drift region except in the immediate vicinity of the sense wire. The high field around the sense wire penetrated further into the drift region for lower drift fields. For slanted field applications the same potentials were used but displaced the required number of wire spacings, the two H.T. planes being supplied independently. Note that in this case V_{min} is no longer opposite the sense wire and the accelerating voltage is increased.

3.4 Choice of Gas Mixture

At the time of the prototype chamber development little published data existed on drift velocities in suitable gas mixtures. Therefore studies were made in Durham,[2,3,4] using a test chamber and a Time to Amplitude Converter/Pulse Height Analyser system, to determine the drift velocities of a variety of gas mixtures in order to chose a suitable chamber gas. The main requirement was a drift velocity compatible with the 14 mm drift length to yield a maximum drift time of around 500 ns. Thus an attainable spatial resolution in excess of 100 μm, assuming 2 ns timing resolution, would be possible using commercial electronics.

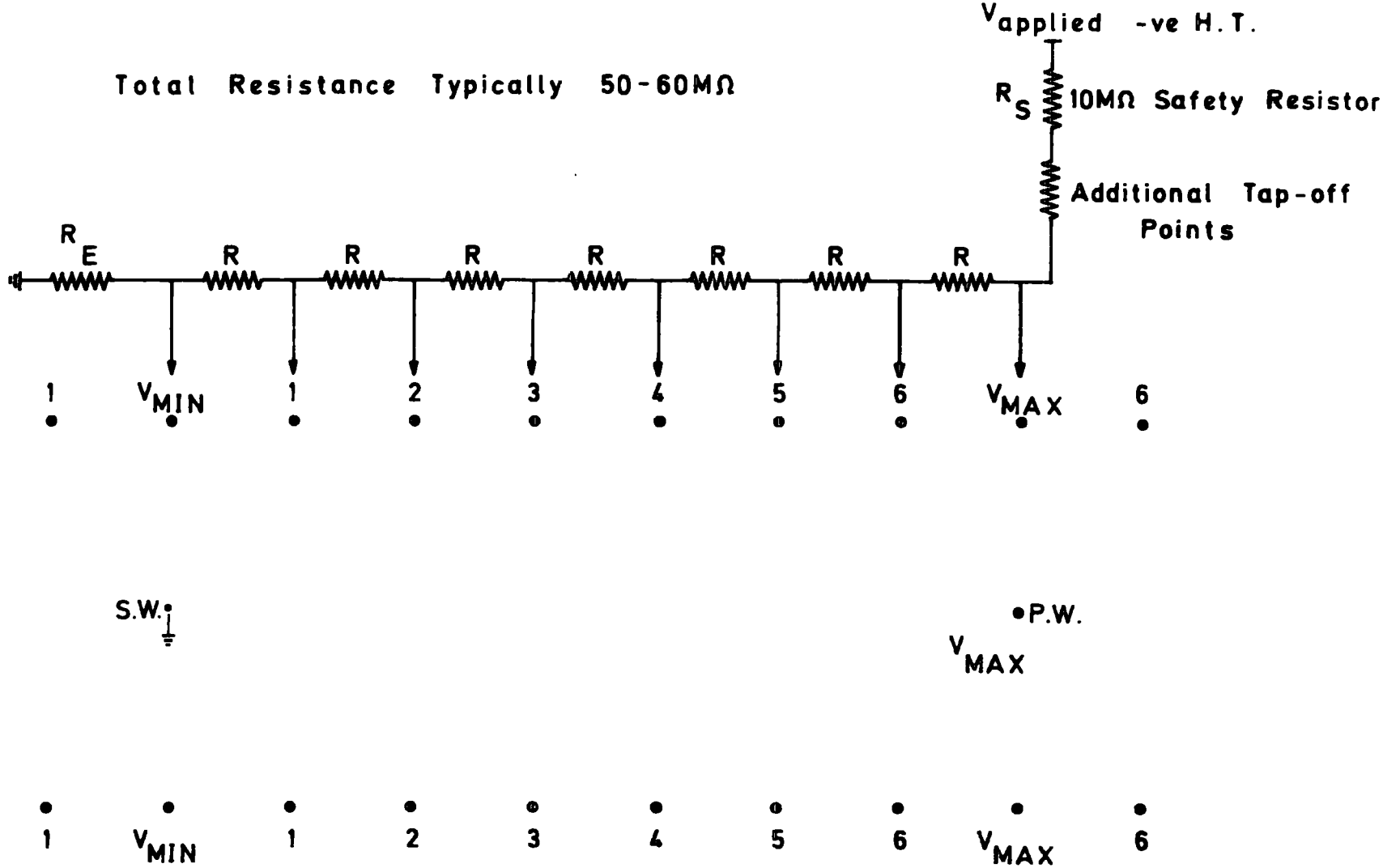

FIG. 3.9 : RESISTOR NETWORK AND VOLTAGE DISTRIBUTION IN UNIT CELL

Also the mixture had to display low diffusion characteristics and a saturated operation region where variations in electric and magnetic field or gas concentration would have a negligeable effect upon the drift velocity.

A collimated ^{90}Sr source was used with a scintillator-photo-multiplier system as the timing trigger. The beam of β-particles, of up to 2.27 MeV energy, was spread due to the geometry of the collimating slit and by multiple Coulomb scattering in air and the chamber windows. Hence spatial resolutions of only $\pm$ 0.7 mm were attainable which masked any diffusion effects but did provide a guide to the drift velocities of various mixtures.

Several methods were used by Browell and Short to determine the drift velocities. The whole cell was accurately scanned to provide the drift time/distance relationship from which the drift velocity could be obtained. However the method was laborious if repeated several times for each mixture so the source was positioned over the potential wire and the maximum drift time cut-off observed to derive the drift velocity. A novel method was devised for measuring the time to drift over 1 cm in the chamber.[2] When the collimated source was positioned over the fifth H.T. wire from the sense wire and the drift time spectrum displayed, a dip was observed in the peak corresponding to a "shadow" cast by the H.T. wire. Accurate measurement of the distance between the H.T. wire and sense wire and calibration of the P.H.A. allowed a quick direct measurement of the drift velocity with each mixture. It must be noted, however, that the value obtained did not allow for any alteration in drift velocity across the cell but did act as a direct comparison between mixtures. A simple gas mixing system

was developed to regulate the concentrations of argon, methane, isobutane and carbon dioxide using Rotameters.

The following results were obtained by Browell and Short[4] in advance of the majority of publications on chamber gas drift velocity curves. In all cases the error in drift velocity measurements is of the order of $\pm$ 1 mm μs^{-1}.

Figure 3.10 shows the results obtained for Ar/CH_4 mixtures demonstrating the variation with field and percentage methane content. Almost complete saturation in drift velocity occurred for fields above 600 V cm^{-1}. Drift velocities were low for low methane concentrations and appeared suitable for the (g-2) application. However for concentrations less than 3% spontaneous breakdown occurred at most operating voltages.

Figure 3.11 refers to argon/isobutane mixtures which possessed higher drift velocities and moderate saturation at higher fields, the curves being steadily rising functions of field. Comparison is made with the curve obtained by Charpak et al.[5] which is of lower value. This may be attributed to the measuring technique used in Durham.

The argon/isobutane/methane curves shown in figure 3.12 exhibit a mixture of the properties of the above two mixtures as would be expected. The methane content at low fields kept the drift velocity high and reduced it at high fields. The isobutane content raised the velocity steadily with field.

Figure 3.13 compares several of the mixtures to indicate the wide range of drift velocities available.

Despite the imprecise spatial resolution obtainable with the system it was found, by observing the full width half maximum (FWHM) of the drift time distribution, that measurable diffusion effects appeared to be

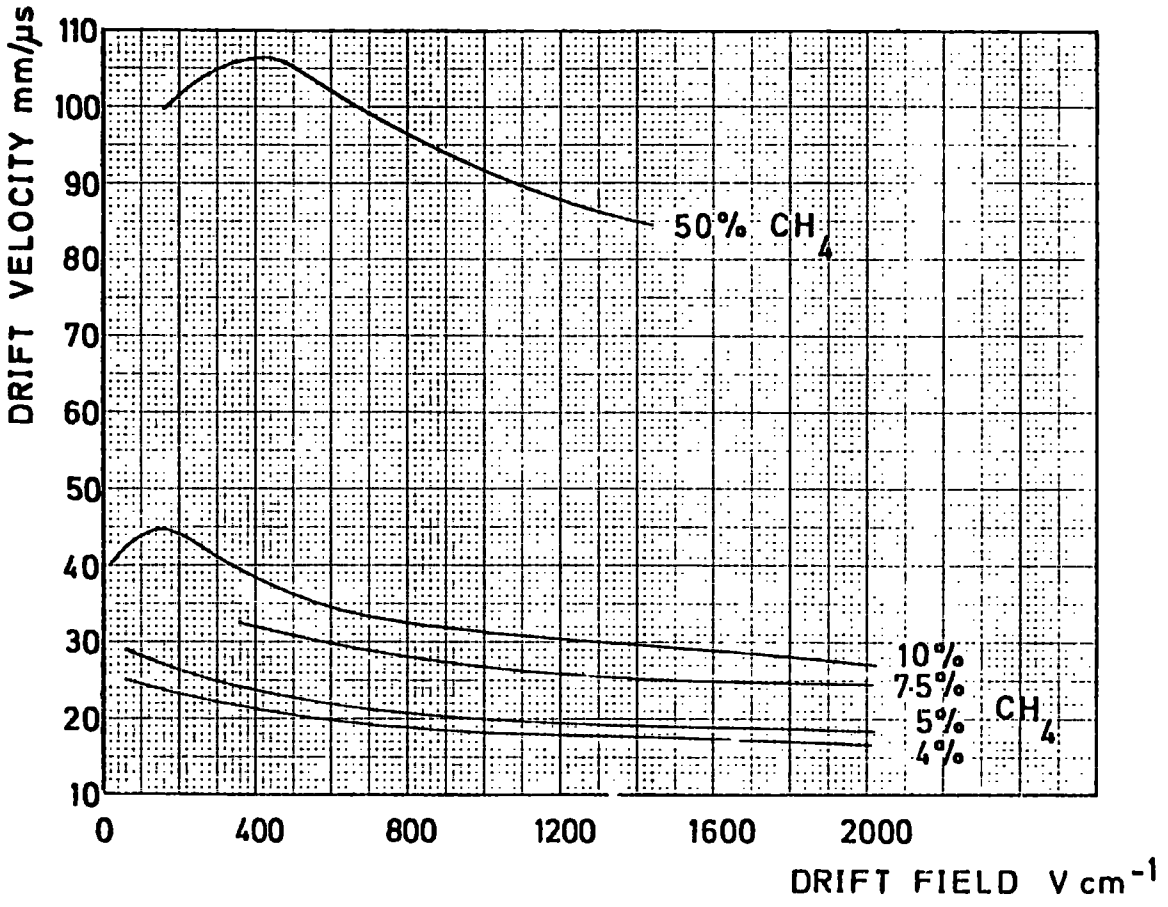

FIG. 3.10 : EXPERIMENTAL DRIFT VELOCITIES FOR ARGON-METHANE MIXTURES

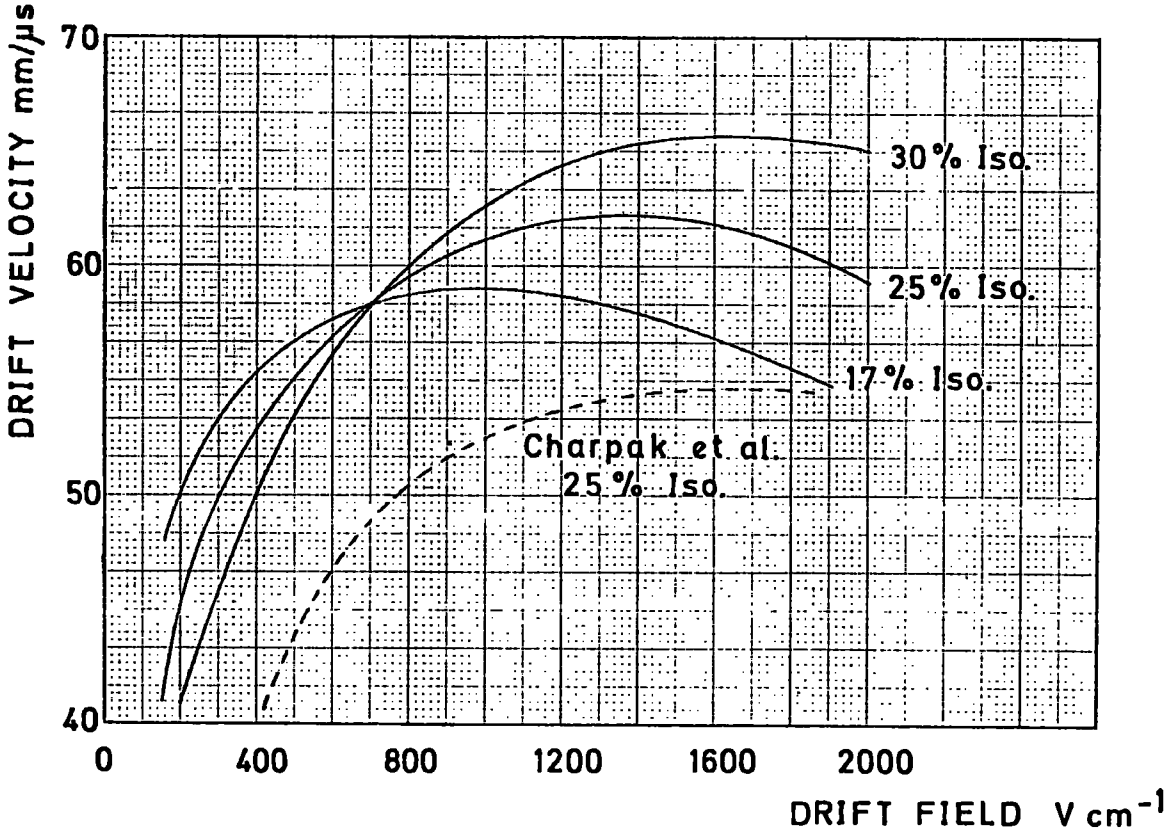

FIG. 3.11 : EXPERIMENTAL DRIFT VELOCITIES FOR ARGON-ISOBUTANE MIXTURES

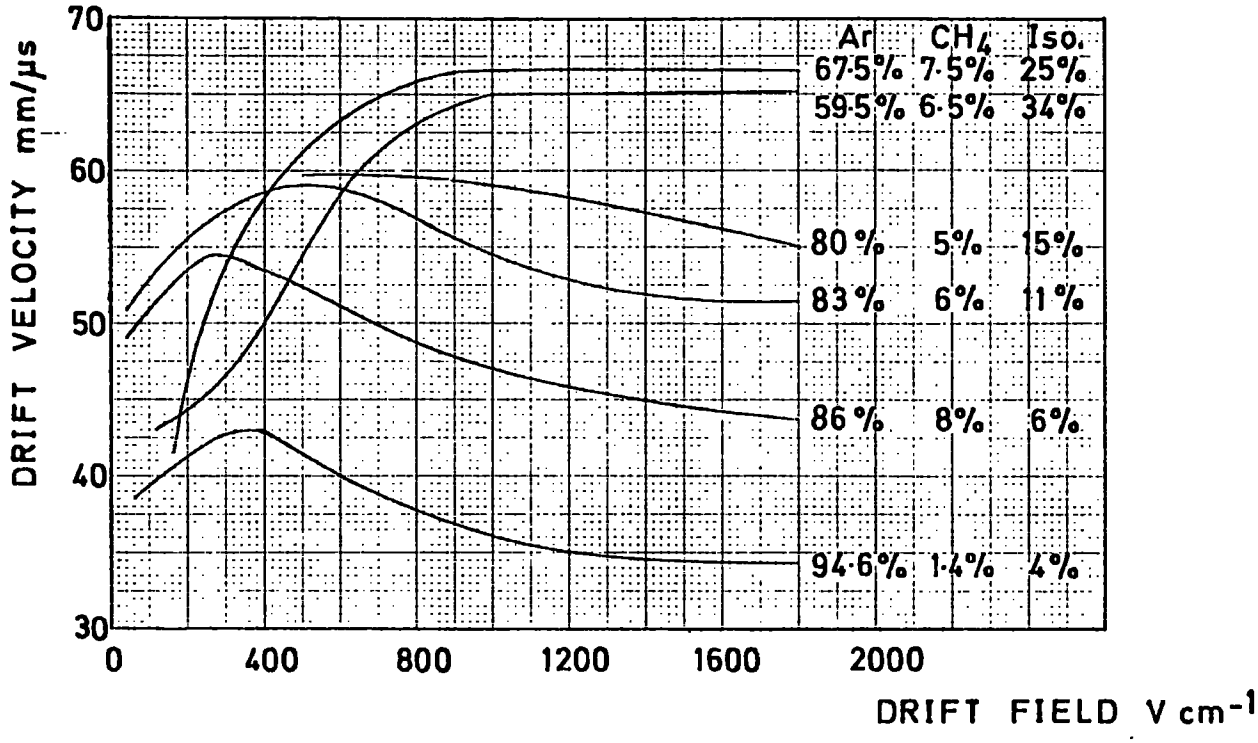

FIG. 3.12 : EXPERIMENTAL DRIFT VELOCITIES FOR ARGON-METHANE-ISOBUTANE MIXTURES

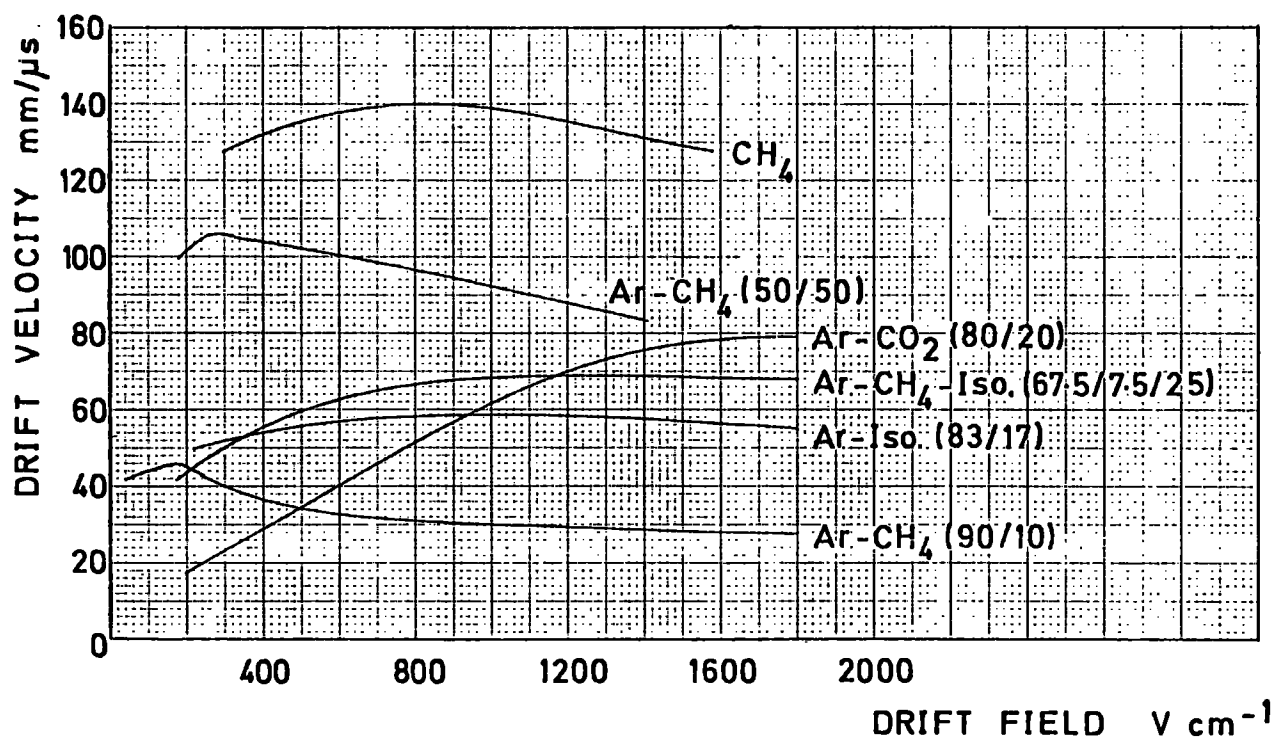

FIG. 3.13 : COMPARISON OF DRIFT VELOCITIES FOR VARIOUS MIXTURES

present for mixtures containing isobutane. The effect varied with percentage isobutane content and drift distance, but no such variations were observable with an Ar 90%/CH_4 10% mixture.

Considering all the mixtures tested it appeared that the argon methane mixtures were the most suitable with respect to their low drift velocities, wide operating region and small variations with methane concentration plus lack of measurable diffusion. As Ar 90%/CH_4 10% was obtainable as an accurate standard mix at low cost, and therefore did not require a complex mixing system, its use became attractive as the chambers would have to be tested at Durham University, Daresbury Laboratory and CERN with subsequent transportation of equipment. It was also a safer gas to use than those containing isobutane. More exotic mixtures, such as the "magic gas" favoured by Charpak's group[6] of Ar 67.2%/Isobutane 30.3% plus 2.5% methylal, have been used successfully in drift chambers but the simplicity of the Ar 90%/CH_4 10% mixture commended itself as the final choice for the (g-2) chambers.

It must be noted that all the above tests were performed using a prototype chamber in the absence of a magnetic field and with no electric field slant. In the final application the slanting of the electric field would increase the effective field in the chamber and hopefully ensure operation in the saturated drift velocity region.

3.5 Choice of Field Compensation Mechanism

Several designs were studied in an attempt to obtain the best electric field compensation mechanism for use in the (g-2) magnetic fringe field. As noted in the previous section a drift field of at

least 600 V cm^{-1} was necessary to ensure a saturated drift velocity in Ar 90%/CH_4 10%. Tests with prototype chambers had shown that the potential on the H.T. wire opposite the sense wire had to be at least 1.3 kV to guarantee high detection efficiencies.[2] Magnetic field data taken whilst the (g-2) C-magnets were under test before installation in the Muon Storage Ring were used in the computation of the compensation parameters. Figure 3.14 shows the radial median plane magnetic fields, in terms of the homogeneous field value of 14.745 kG, measured at the magnet block centre and the junction of two magnet blocks. The azimuthal variation of the radial field is shown and the profiles of a (g-2) drift chamber and the magnet block at the two azimuthal positions are indicated. The experimental drift velocity data displayed in figure 3.10 were also used in the calculations.

Knowledge of the above parameters allowed three compensation mechanisms to be considered. The first involved computing the potentials required on each H.T. wire in the chamber to exactly compensate for the inhomogeneous fringe field. Such an approach was impracticable due to the large number of H.T. connections that would have been necessary on the external connection boards in the limited space available, and also because of the resulting complexity of the voltage divider network. The second method, which was thoroughly tested with prototype chambers and a 7.5 kG magnet at the Daresbury Laboratory Test Beam and in the (g-2) field at CERN,[2] had three different field tilts down the length of the chamber. The tilting was performed by staggering the H.T. wire potentials on opposite sides of the sense wire plane by the required number of 2 mm wire-spacings. The two cells nearest the vacuum tank had a three wire-spacing tilt, the

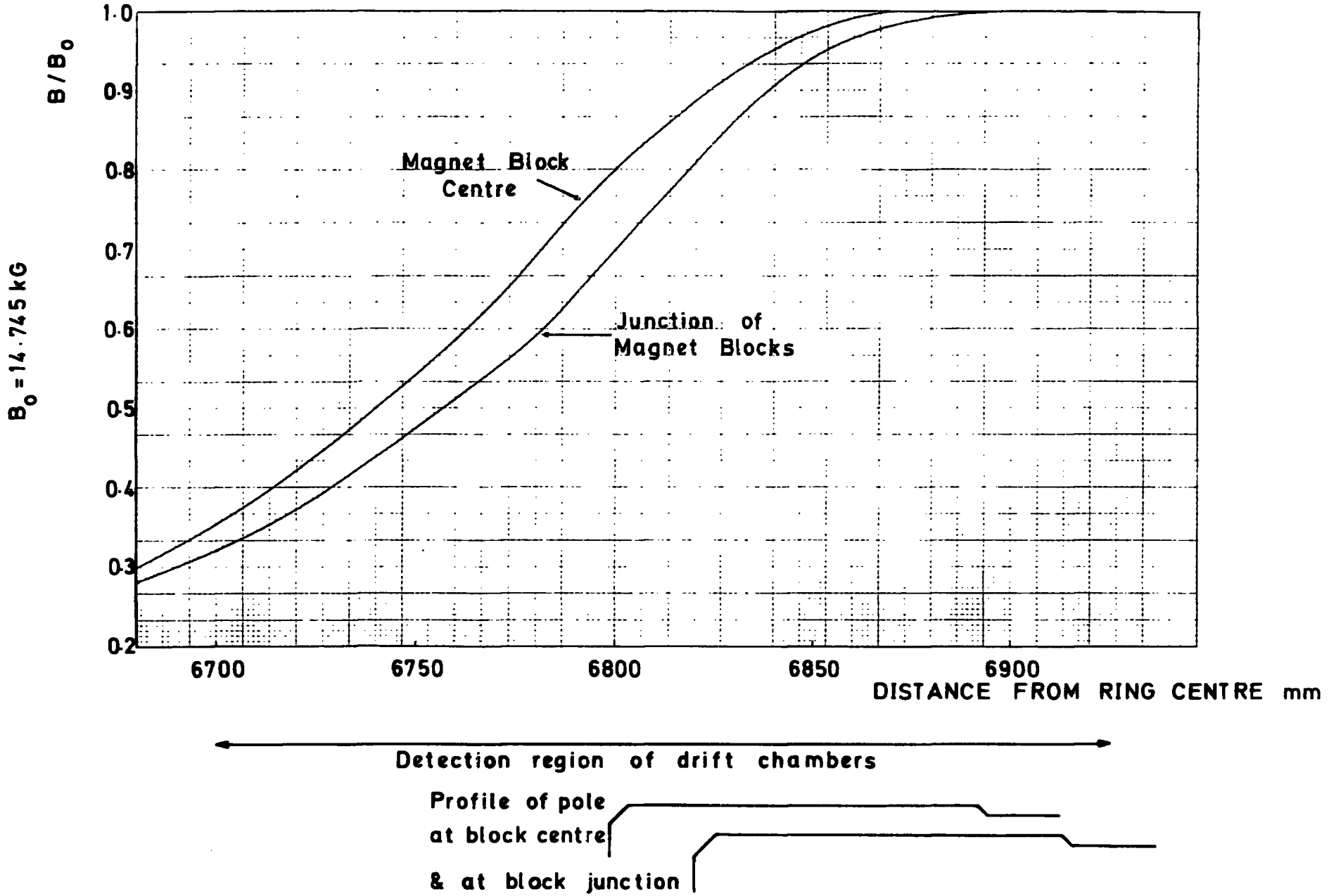

FIG. 3.14 : AZIMUTHAL VARIATION OF MEDIAN PLANE RADIAL MAGNETIC FIELD

next three cells a two wire-spacing tilt and the three cells closest the centre of the ring a one wire-spacing tilt. This method probably provided the most accurate compensation throughout the chamber. However uncertainty in the behaviour of the drift velocities at the discontinuities of tilt value, in the potential wire region, led to its replacement by thethird and final mechanism.

Using the known radial magnetic field values at the magnet block centre, an assumed electric field of $E_0 = 600$ V cm^{-1} in the sense wire plane and the experimental drift velocities, Short computed[2] the radial variation of drift angle, θ, along the chamber in 1 mm steps using equation (2.19) and k = 0.75 corresponding to a Maxwellian velocity distribution. The calculations were performed for 2, 3 and 4 wire-spacing slants, with corresponding values of tilt angle, γ, and absolute electric field, E, defined by equation (2.25). The values of θ obtained led to an evaluation of the modified drift velocity in the gas, w(E, B), as given by equation (2.16) and a knowledge of the corresponding values of $(\gamma - \theta)$ allowed the drift velocity parallel to the sense wire plane, w_s, to be calculated from equation (2.24). Figures 3.15 and 3.16 show the values obtained by Short for $(\gamma - \theta)$ and w_s exhibited radially from the vacuum tank wall towards the centre of the ring. It was obvious that the three wire-spacing tilt values offered the best compensation mechanism throughout the chamber volume with constant values of both parameters for the three most important cells closest to the vacuum tank. The observed drift velocity decreased in the higher magnetic fields close to the vacuum tank as expected. The variation in drift velocity throughout the chamber was small because in the lower magnetic fields towards the ring centre, where w(E, B) increased, the

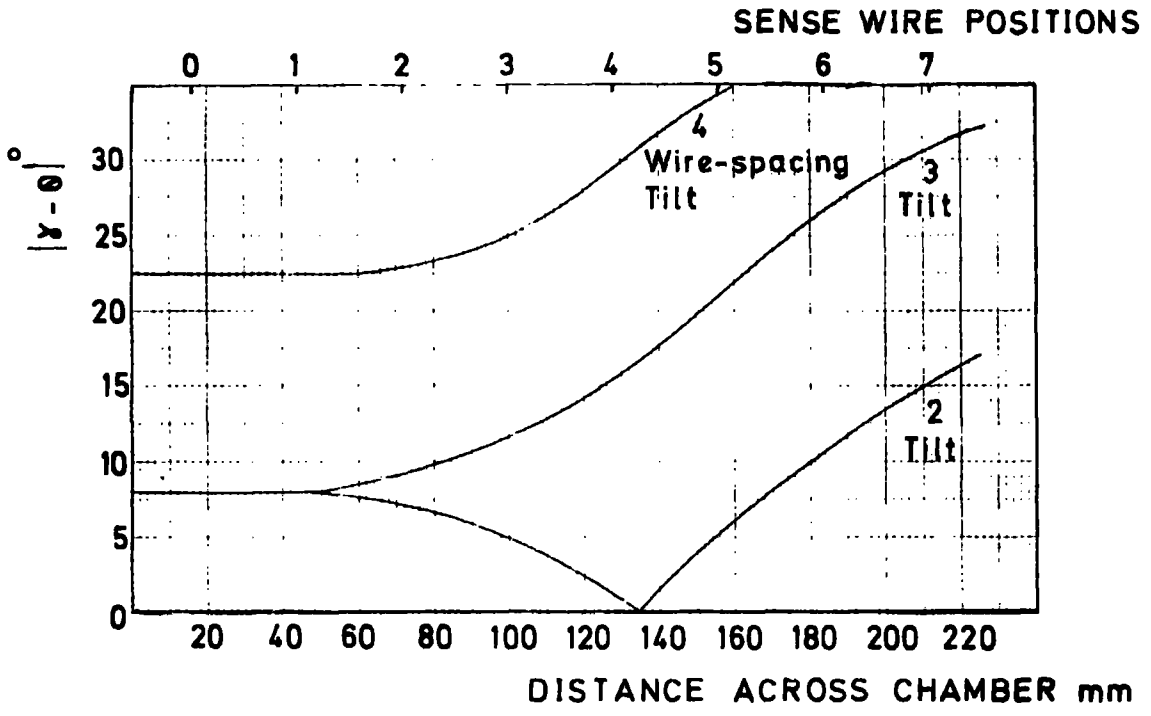

FIG. 3.15 : THEORETICAL DIFFERENCES BETWEEN DRIFT ANGLE AND ELECTRIC FIELD TILT ANGLE $|\gamma - \theta|^\circ$ ACROSS CHAMBER FOR DIFFERENT TILTS (DUE TO SHORT)

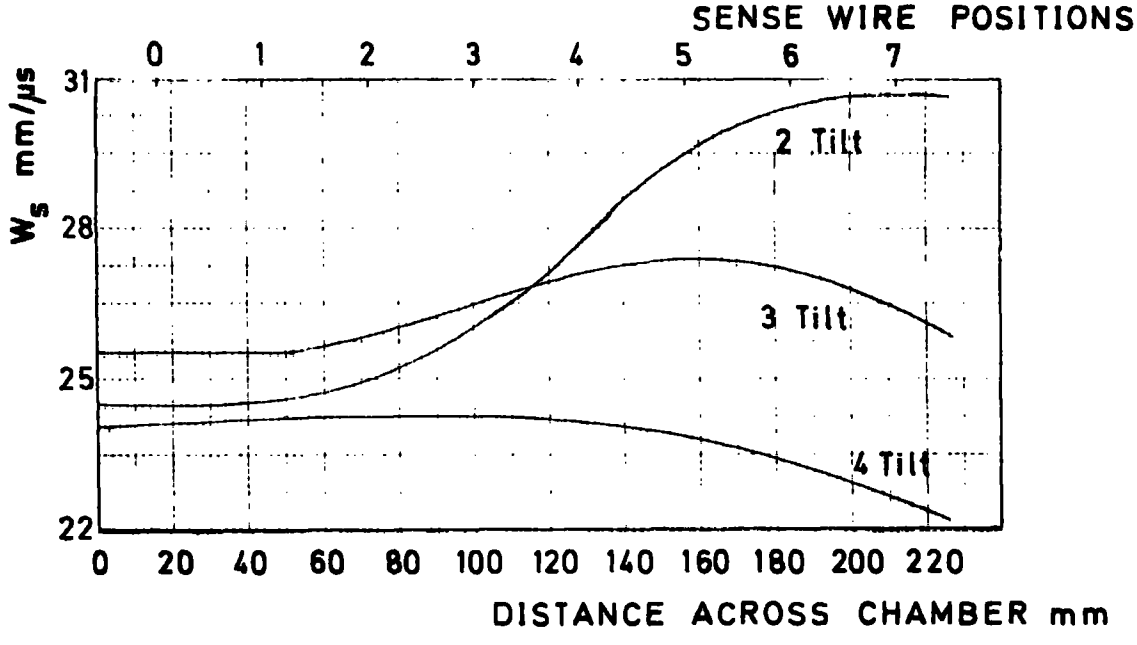

FIG. 3.16 : THEORETICAL VALUES OF THE OBSERVED DRIFT VELOCITY ACROSS THE CHAMBER (DUE TO SHORT)

electric field compensation became worse. Hence the electron swarms drifted at larger angles to the sense wire plane and the cosine function caused w_s to remain low. The values of w_s indicated that the maximum drift times would be of the order of 500 ns and thus would fall in the range of commercial digitizing electronics. Hence the voltage distribution network was designed to provide the necessary wire potentials to form a field in the sense wire plane of 600 V cm^{-1}.

Several points must be noted about the above model. The value of E_0 was computed from the wire potentials as $(V_{max} - V_{min}) / 1.4$ V cm^{-1}, as described in section 3.3, which in no way represented the true field throughout the chamber volume, especially once the tilting mechanism was applied. Also the calculations used an inter-cathode gap of 6 mm rather than the 6.4 mm chamber specification value. This led to high values of γ and $(\gamma - \theta)$. The value of k = 0.75 was used as other workers[7] found that a Maxwellian velocity distribution accurately described their experimental results. However studies performed by Browell[3] using small drift chambers of similar cell design and operating parameters to the (g-2) chambers suggested a value of k as low as 0.25. The experimental drift velocity data due to Short and Browell were used as little other published data existed. Also the method of field calculation used in its derivation was identical to that used to compute the compensation mechanism. Electric field simulations performed by a numerical relaxation method yielded similar drift fields along the majority of the drift space to that derived by the approximate method.[2]

Therefore the compensation mechanism was modelled on the most accurate data available at the time.

3.6 Initial Evaluation of the Production (g-2) Drift Chambers

After initial mechanical inspection of the chambers the sense wire positions were measured with respect to the chamber fiducials using a travelling microscope. All sense wires had to be parallel to within 50 μm to ensure their verticality when the chambers were mounted in the (g-2) ring. The chambers were cleaned and then clear mylar windows attached using Twinstick. Once the gastight properties of the chambers had been confirmed and the Ar 90%/CH_4 10% mixture had been flushed through for several hours, the drift field was applied and all chamber potentials checked using an electrostatic voltmeter. The chambers were tested for breakdown and an ^{55}Fe or ^{90}Sr source used to produce the chamber pulses. Initially severe breakdown problems were encountered and space charge effects noted on the curved end electrode strips. Thorough cleaning of the chambers to remove any dust and solder particles from the sense wires and removal of any spikes of wire showing through the solder connections greatly enhanced the chamber performance. The use of corona dope on any remaining points causing continuous breakdown eradicated the problem. The chambers operated better having had continuous flushing for several days and the potentials applied for long periods.

However the chambers were still found to break down at lower applied potentials than the prototypes. Measurement of the cathode/sense wire plane gaps along the length of a chamber revealed that instead of being constant at 3.2 mm they in fact varied by up to $\pm$ 0.4 mm from the specified value. Figure 3.17 indicates the variation in plane gaps measured across a typical chamber at the top and bottom of each sense wire. The discrepancies were caused by the method of manufacturing the laminated connection board assemblies and were irrevocable. Therefore

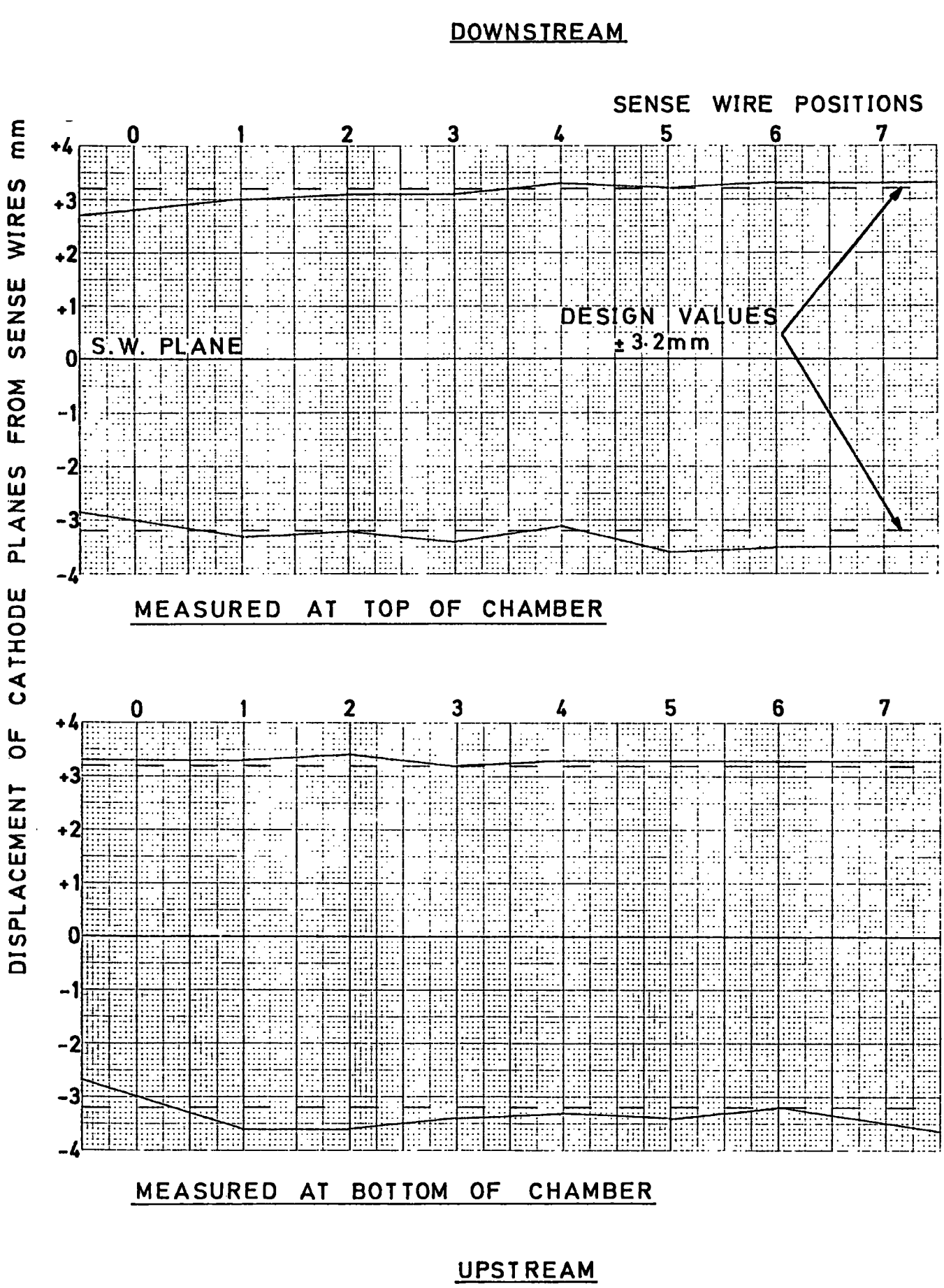

FIG. 3.17 : VARIATION IN SENSE WIRE - CATHODE PLANE GAPS ALONG A CHAMBER

the potentials had to be modified around the sense wires to lower the field. Of course the situation was exacerbated when the three wire-spacing field tilt was applied. With reference to figure 3.9, $V_{min + 1}$ would have been opposite the sense wire on one cathode plane and $V_{min + 2}$ on the other. In the final compensation mechanism V_{min} = 1360 V with 120 V increments up to V_{max} = 2200 V giving a drift field of E_0 = 600 V cm^{-1}. The voltage divider network had to be modified so that the four lowest potentials became 1360, 1430, 1550 and 1730 volts respectively. These values lowered the field around the sense wires sufficiently to almost eradicate spontaneous breakdown.

Pulse heights of 25 mV into 50Ω were measured with a ^{90}Sr source placed close to a chamber. However the efficient operating plateau of the chambers was very narrow. An applied voltage of 2.9 kV was required across the resistor network to produce a drift field of 600 V cm^{-1} in the sense wire plane. An increase of more than 100 V in the applied voltage caused spontaneous breakdown to begin in many cells. Hence it was impossible to operate the chambers at higher field values with the field compensation mechanism in operation.

It was obviously impossible to repeat all the tests performed on the prototype chambers for each of the production chambers. However extensive tests were carried out at the Daresbury Laboratory Test Beam by Short and the author[2] with an operating system very similar to the TDC system used at CERN, which is discussed in Chapter 4. All tests were performed in the absence of a magnetic field and hence no field compensation was applied. A drift field of 600 V cm^{-1} was used. Four chambers were used in several geometrical arrangements in order to evaluate their performance. Clear mylar windows were used for ease of

inspection and thus the earth planes formed by the aluminized windows that were fitted later did not exist. Efficiencies of 99.5% were obtained using a stringent scintillator telescope system and positrons in the range 1–4 GeV. Linear drift time - distance relationships were confirmed in the cells and by staggering alternate chambers by a half-cell spacing constant drift velocities were observed on summing the four drift times associated with a straight track. Analysis of the data from the four chambers indicated an attainable spatial resolution of 150 $\pm$ 50 μm (standard deviation) for the normal cells and 300 $\pm$ 50 μm for the curved end cell. The results were obtained from a least squares fit to a straight line for the four chamber hit co-ordinates.

The successful operation of the chambers in the absence of a magnetic field, with reasonable spatial resolution, indicated that they would provide accurate data in the (g-2) environment so long as the field compensation mechanism was correct.

3.7 Mounting of the (g-2) Drift Chambers in the Muon Storage Ring

As spatial resolutions of the order of 200 μm were anticipated from the drift chambers it was necessary to design a mounting system that could be re-locatable to such an accuracy.

Figure 3.2 indicated the baseplate that was accurately positioned in the region of magnet blocks 22 and 23. A complete guide to the method of determining the chamber sense wire positions is detailed elsewhere,[8] an outline to the series of measurements required is given here. The baseplate was mounted horizontally on tubular supports with the aid of locating dowels which fitted into reamed holes in the magnet blocks. Measurements of the vertical height of the ring centre face of the baseplate and feeler gauge measurements of the gap between the baseplate

and magnet blocks confirmed its correct positioning. The 0° datum line corresponding to the radial junction of magnet blocks 22 and 23 was checked by viewing three 4 mm pins that could be fitted in holes reamed at intervals along the datum line. All datum lines scribed on the baseplate and holes reamed in it were performed on an accurate drilling table.

The drift chambers were mounted vertically in assigned cradles, as shown in figure 3.7. The cradles in turn were mounted on the baseplate, the centre lines of chambers A - G and the upstream face of chamber H being radial. The chamber and cradle fiducials were aligned and the cradle accurately positioned on the baseplate with the aid of a spacer which had two 4 mm pins positioned 114.95 mm apart centre to centre. One end of the spacer was positioned in a hole reamed in the baseplate at a nominal radius of 6452 mm from the ring centre and on the chamber centre lines. The other end fitted easily into a hole reamed in the centre line of the cradle, approximately 90 mm from the cradle fiducial, after appropriate manipulation of the radial adjustment screw. The cradle was then locked in position and the verticality of the chamber fiducial re-checked using an accurate spirit level. Any necessary alterations were performed using the two adjustment screws on the cradle. The curved end member of the chamber was now positioned approximately 15 mm from the vacuum tank.

Figure 3.18 shows the set of measurements required to determine the exact radial sense wire positions. An accurate rod and micrometer system was used to measure the distance from the ring centre to the ring centre face of the reamed hole in the baseplate - indicated by 6425 + Z mm in figure 3.18. The spacer distance was known and the distances Y

between the cradle fiducials and ring centre side of the reamed hole were measured with vernier calipers. The distance F between the chamber fiducial and sense wire "7" and the other sense wire displacements had already been determined. Hence addition of all the measurements produced the radial sense wire positions. A maximum error of 0.3 mm was quoted for the series of measurements.

A small correction had to be made, as indicated by figure 3.19, to compensate for the chambers being mounted radially along the centre line or upstream face rather than the sense wire plane. Hence the distances measured above referred to R by the nomenclature of figure 3.19. Calculation of the values of $\Delta\theta$ allowed the corresponding R' values to be derived.

Knowledge of the mounting angles θ allowed the sense wire angles θ' to be calculated and hence a cartesian co-ordinate system could be derived with the 0^{o} datum line as one axis and the ring centre as the origin of the co-ordinates. Such a system was used in the data analysis.

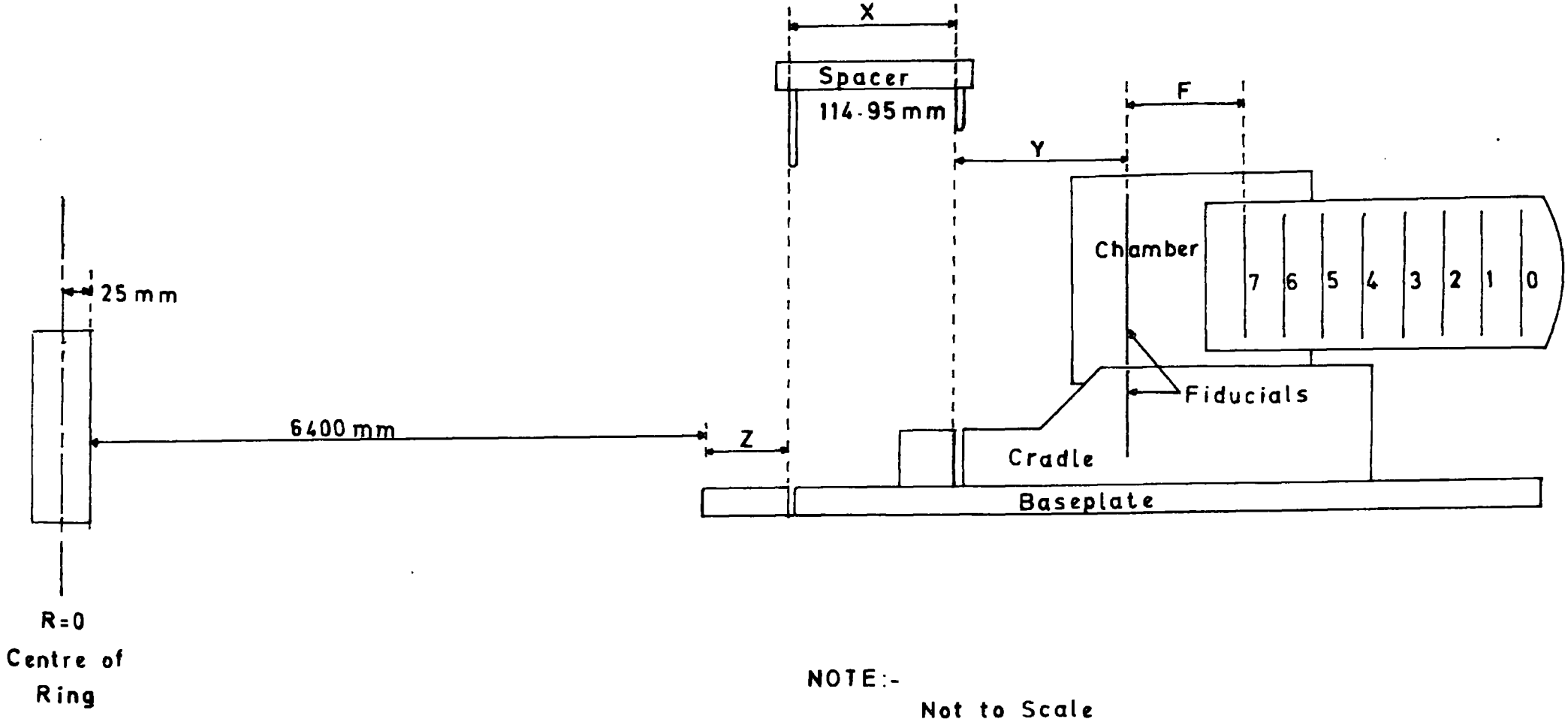

NOTE:-
Not to Scale

FIG. 3.18 : MEASUREMENTS TO DETERMINE RADIAL SENSE WIRE POSITIONS

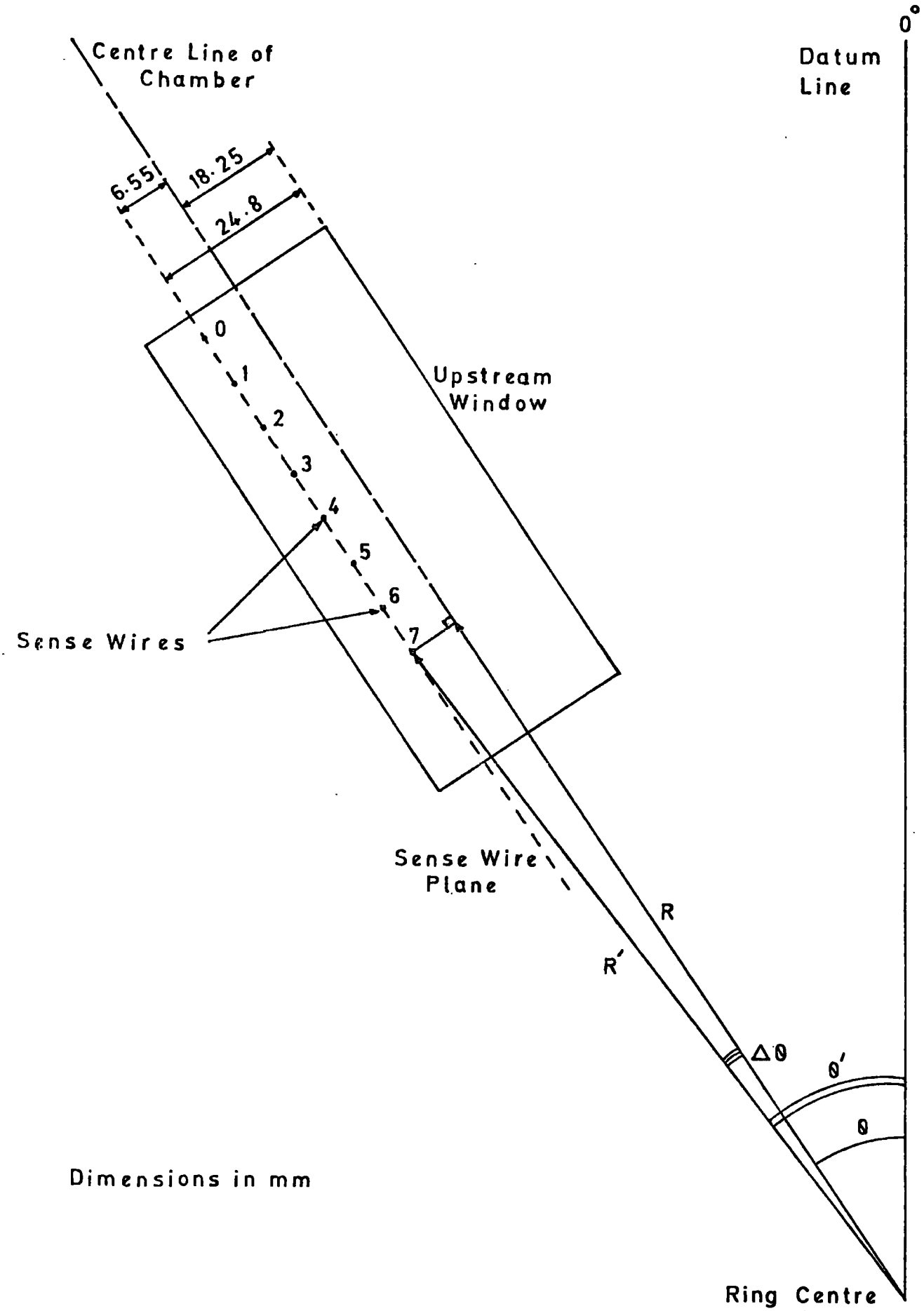

FIG. 3.19 : CORRECTION FOR NON-RADIAL MOUNTING OF SENSE WIRE PLANE

REFERENCES

1) Breare, J. M., Browell, R., Short, K. A., Webster, J.,
Durham University Internal Report NI 74 - 7

2) Short, K. A.,
Ph. D. Thesis University of Durham 1975

3) Browell, R.,
Ph. D. Thesis University of Durham 1976

4) Browell, R., Short, K. A.,
Durham University Internal Report NI 74 - 3

5) Charpak, G.,
Proc. Int. Conf. on Instrumentation for High-Energy Physics,
Dubna, Sept. 1970, p. 227

6) Breskin, A., Charpak, G., Gabioud, B., Sauli, F., Trautner, N., Duinker, W., Schultz, G.,
Nucl. Instr. Meth. 119 (1974) 9

7) Breskin, A., Charpak, G., Sauli, F., Atkinson, M., Schultz, G.,
Nucl. Instr. Meth. 124 (1975) 189

8) Comyn, M., Hedge, A.R.,
Durham University Internal Report NI 76 - 18

CHAPTER FOUR

THE EXPERIMENTAL SYSTEMS USED FOR DATA ACQUISITION

4.1 Introduction

The experimental system required to operate the (g-2) drift chamber array had several independent component parts which covered the operation of the chambers themselves and the processing of the signals from the sense wires. As described in Chapter 3 the eight drift chambers were accurately mounted in cradles upon a baseplate positioned in the region of magnet blocks 22 and 23 of the forty magnet (g-2) storage ring. Immediately downstream of the last drift chamber were an EDM counter - electric dipole moment - and the (g-2) shower counter C10,[1] a lead plastic scintillator sandwich detector, which was used as the timing trigger. As shown in figure 4.1 three MWPC's[2] were also part of the system, to give vertical co-ordinate information, but these were not operated in the total system and hence are not discussed in this thesis.

The pulse, due to the passage of an electron, in counter C10, was used as the trigger for the timing and the times of arrival of the pulses at the relevant sense wires, corresponding to the drift chamber cells through which the electron passed, were digitized relative to this.

This chapter describes the various parts of the system in detail and explains the various logic systems in use during the development of the system. The merits of the DTD CAMAC modules - Drift Time Digitizers - over the TDC modules - Time to Digital Converters - are discussed in relation to the (g-2) drift chamber array. Many aspects in the development of the data acquisition system for this array are

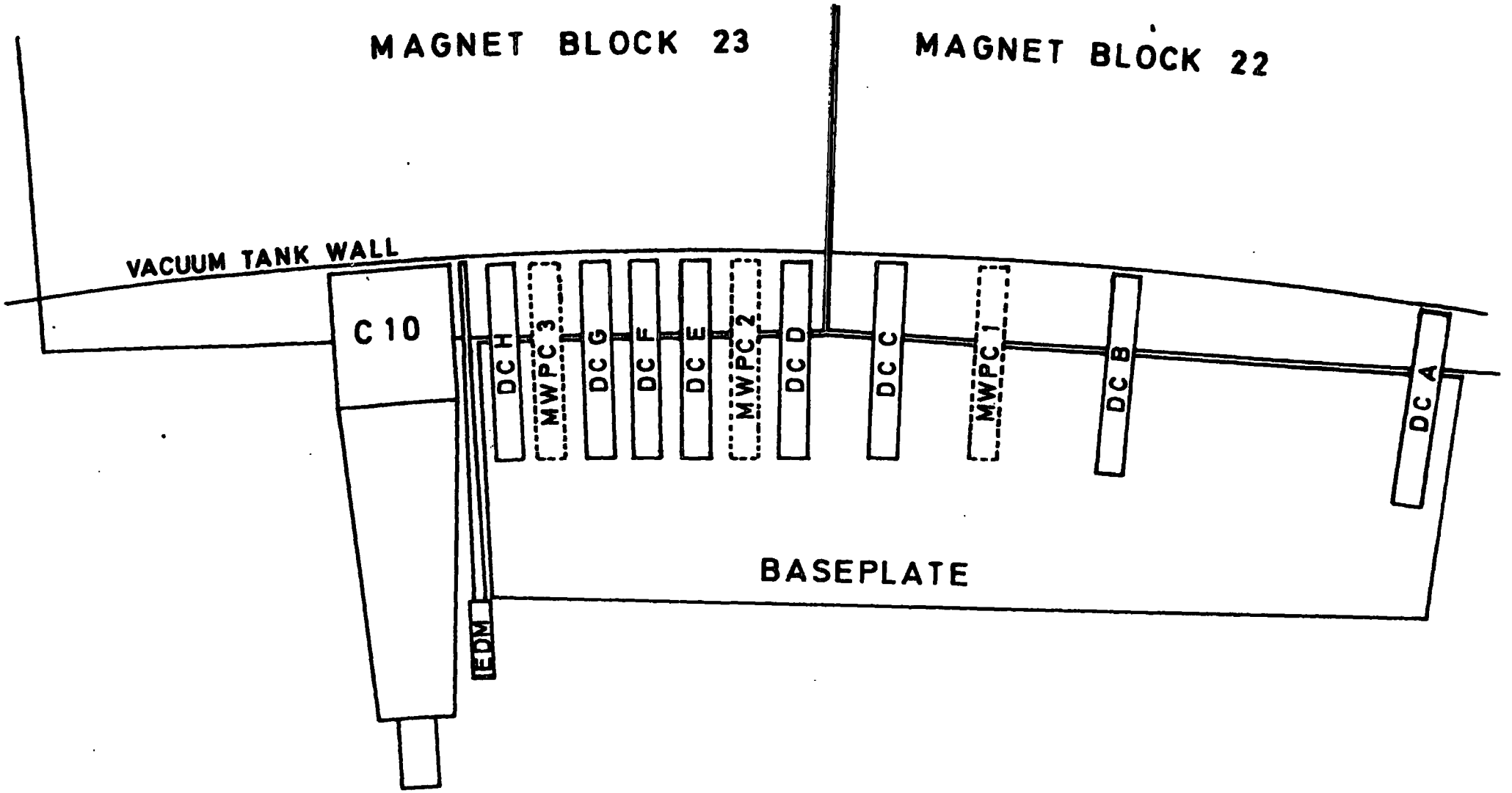

FIG 4.1 : CHAMBER AND COUNTER LAYOUT

relevant to the application of drift chambers in other experimental detection systems so the details are discussed fully.

4.2 The Overall System

The overall system is presented in the form of a block diagram in figure 4.2 which also shows the location of the various components.

The eight drift chambers had independent gas and H.T. supplies to allow individual demounting without affecting the overall system. Each chamber had eight pre-amplifiers associated with it and these are shown mounted in screened boxes in a rack immediately below the baseplate, alongside the gas monitoring rack, in figure 4.3.

Cables were run from the ring to the counting room through an underfloor tunnel and conduits. There were sixty-four 50Ω cables for the amplified sense wire signals running to a patch-panel in the counting room, eight H.T. cables from the distribution box after the Brandenburg power supply in the counting room to the H.T. distribution boxes mounted on the drift chamber frames, and also several spare cables for use with the gas monitoring alarm and checking of the system.

The C10 counter signal was routed via the shortest physical path as it had to be processed in the electronics, introducing further delays, and still arrive before the minimum delayed sense wire signal, so as to prevent a dead time occuring in the drift time digitization. This was particularly important when the TDC systems were being used, as will be explained in section 4.3.1.

In the counting room, shown in figure 4.4, all sense wire signal discrimination and system timing was performed using NIM modular electronics and the drift times digitized using TDC or DTD CAMAC modules.

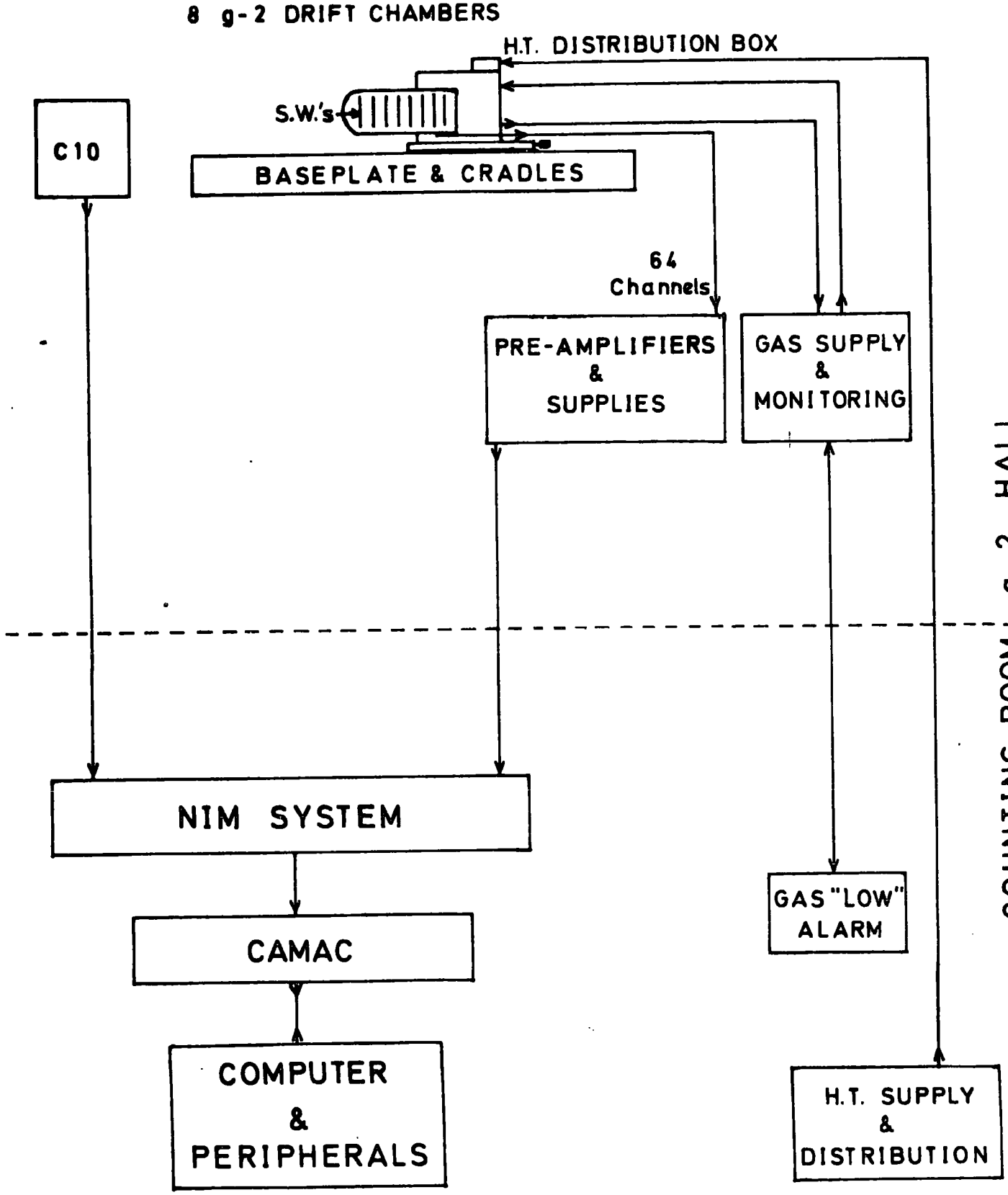

FIG 4.2 : BLOCK DIAGRAM OF g-2 D.C. SYSTEM

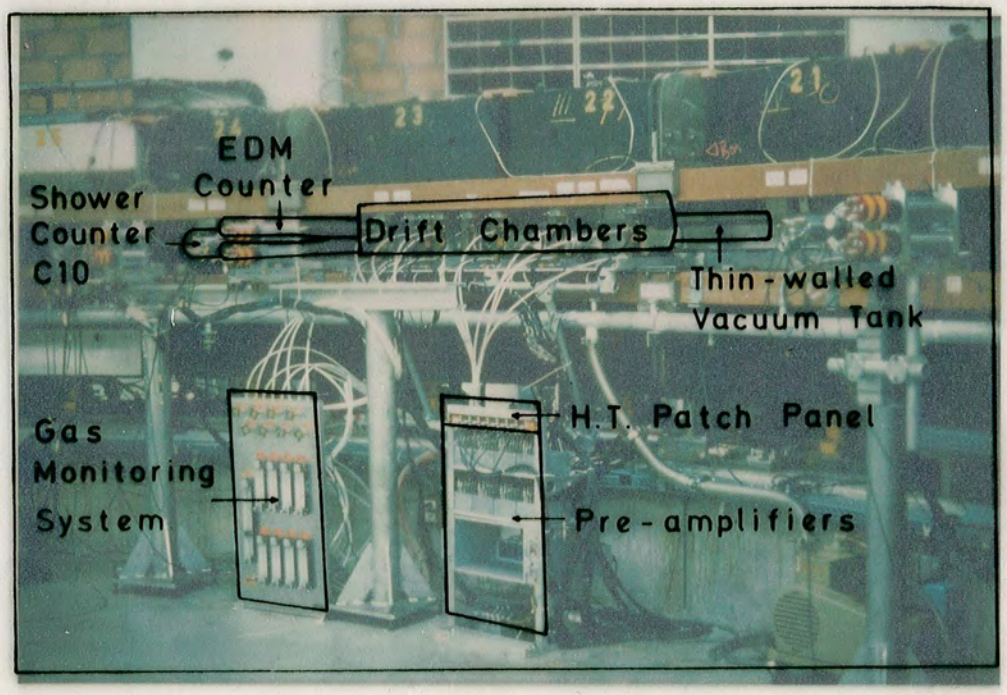

FIG. 4.3 : DRIFT CHAMBER ARRAY

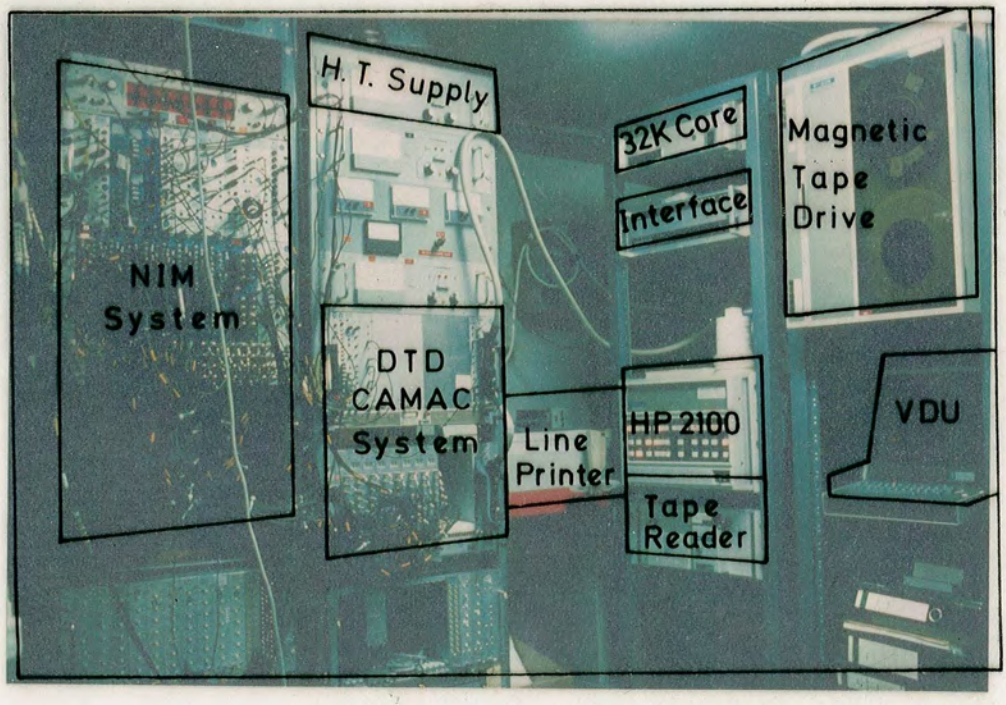

FIG. 4.4 : DATA ACQUISITION SYSTEM

The drift times and certain other items of data were interfaced with the Hewlett Packard 2100 mini-computer through CAMAC using software written in ASSEMBLER. The data was blocked and read on to magnetic tape, with rudimentary on-line low priority analysis, for future off-line analysis on the CDC 7600 computer at CERN or the IBM 370/168 at NUMAC (Durham).

As two totally different timing philosophies were used, relating to the TDC's and DTD's, the logic systems will be considered independently.

4.2.1. The Gas Supply System

The layout of the gas supply system is shown in figure 4.5. The requirements of the system for the (g-2) chambers were a steady flow rate with no surges, which would easily have damaged the seal on the thin melinex windows, and the ability to operate over long periods with no attention but with the provision of an alarm to indicate when the input flow fell below a safe minimum.

A premixed Ar 90%/CH_4 10% mixture was used which alleviated the need for a complex gas mixing system. A reducing head on the gas cylinder and an anti-surge valve controlled the gas flow through the nylon input line which passed to the monitoring panel in the ring. A Flowstat valve controlled the input flow which was monitored on a Rotameter calibrated up to 500cc /minute. A light sensitive cell attached to the glass Rotameter column activated the gas alarm when the float passed through the light beam and tripped a reed switch. The reset was in the ring which ensured that the gas flow was checked before resetting. The cell was positioned so that the alarm sounded

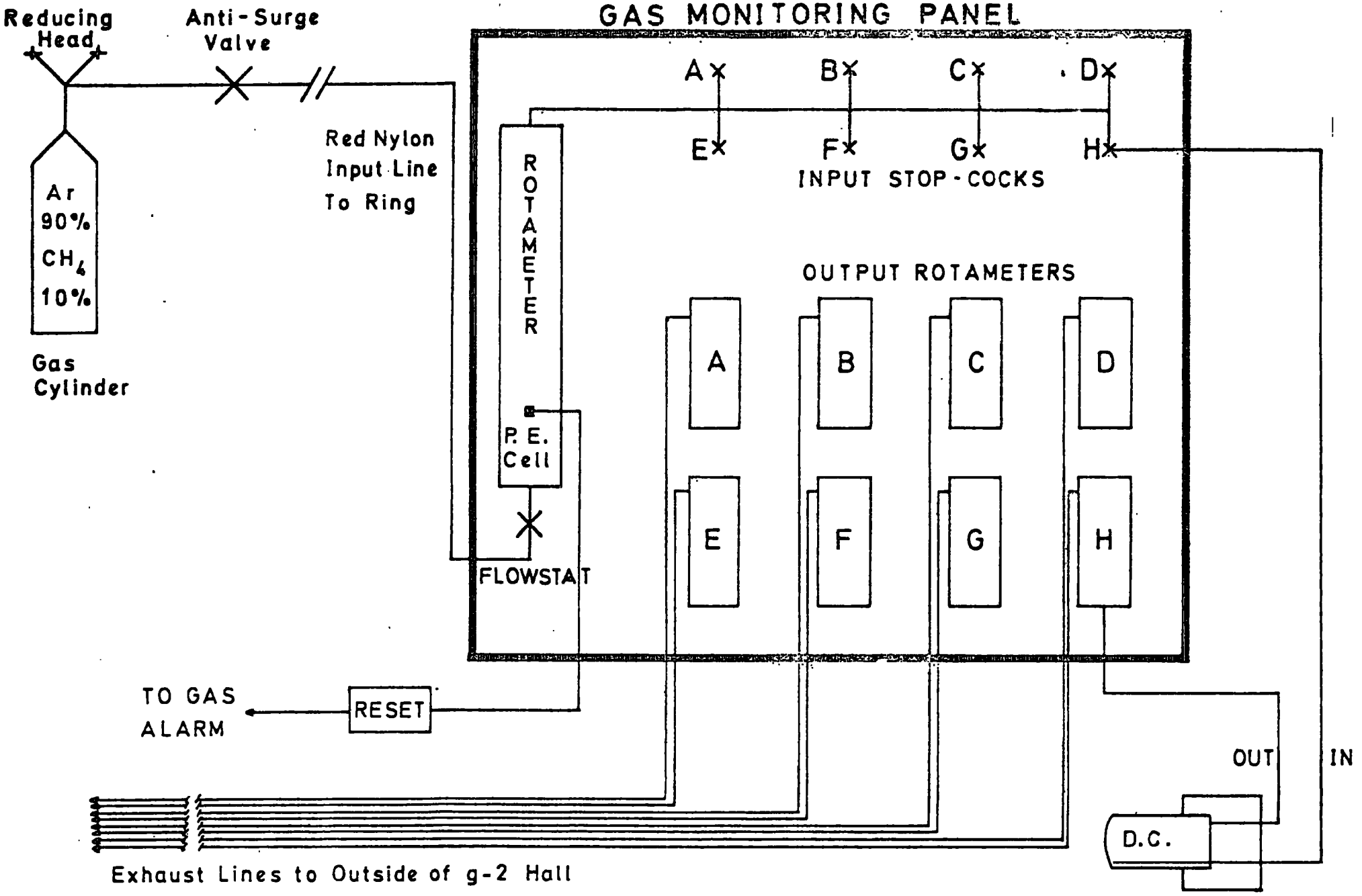

FIG 4.5 : GAS SUPPLY SYSTEM

when the input flow fell below 160cc/minute, i.e. 20cc/minute input to each of the eight chambers. The chambers were supplied in parallel but each could be individually isolated by means of a stop-cock. The outputs from each chamber were individually monitored on Rotameters with a maximum calibrated flowrate of 100cc/minute - 40cc/minute was a typical operating value. The eight exhaust lines passed to the outside of the experimental hall to prevent build-up of inflammable methane gas.

Periodic monitoring was performed and the alarm system proved to be adequate. The system continued to function satisfactorily even if a chamber developed a slight leak. The flow in a chamber was from the base at the curved end to the top at the spine end, thus ensuring a continuous flushing of the active area.

4.2.2. H.T. Distribution

A layout of the H.T. distribution system is given in figure 4.6. Immediately after the output from the Brandenburg regulated H.T. supply a fan was made through eight 10 MΩ safety resistors to limit the current in the cables passing to the ring. A safety lock was installed on the Brandenburg supply to ensure that the power was switched off whilst working in the ring.

A separate length of H.T. cable ran from a patch panel on the pre-amplifier rack to the H.T. distribution box on the drift chambers for ease of removal and also to ensure that the minimum pressure was exerted upon the chambers to prevent accidental movement.

As described in Chapter 3 the H.T. distribution network was contained within a small diecast box mounted on top of the chamber spine. Inside the resistor network was mounted on a sheet of veroboard and the chamber potentials were patched from the relevant points to the

two multiway ribbons supplying the upstream and downstream rails. A stringent colour coding was used as the network had to be completely altered for operation with positive or negative muons. Although this method was extremely tedious it was considered the most reliable within the volume allowed. No 32-way edge connectors small enough, or capable of standing off the potentials, were commercially available to simplify the procedure. The respective potentials for operation with positive and negative muon polarities are shown in figures 4.7a and 4.7b.

During the final checking of the chambers before a run all the potentials on the rails were checked using a 5kV electrostatic voltmeter to ensure that no shorting occurred either in the divider box or between the rails.

4.2.3. The Pre-amplifiers

The pre-amplifiers were of a low input impedance type with discrete transistors designed by H. Verweij at CERN[3] specifically for negative drift chamber pulse amplification. They had an input impedance of 20Ω and a voltage gain of 500 with a rise and fall time of about 5.5 ns. As will be described in section 4.3.2 they were slightly modified when the DTD system was introduced.

The amplifiers were built in Durham and throughout the experiment were used in preference to octal NIM module versions later introduced at CERN. They proved to be extremely reliable and withstood severe mechanical stress and electrical overload. The sixty-four pre-amplifiers were powered, through a distribution system designed and built in Durham,

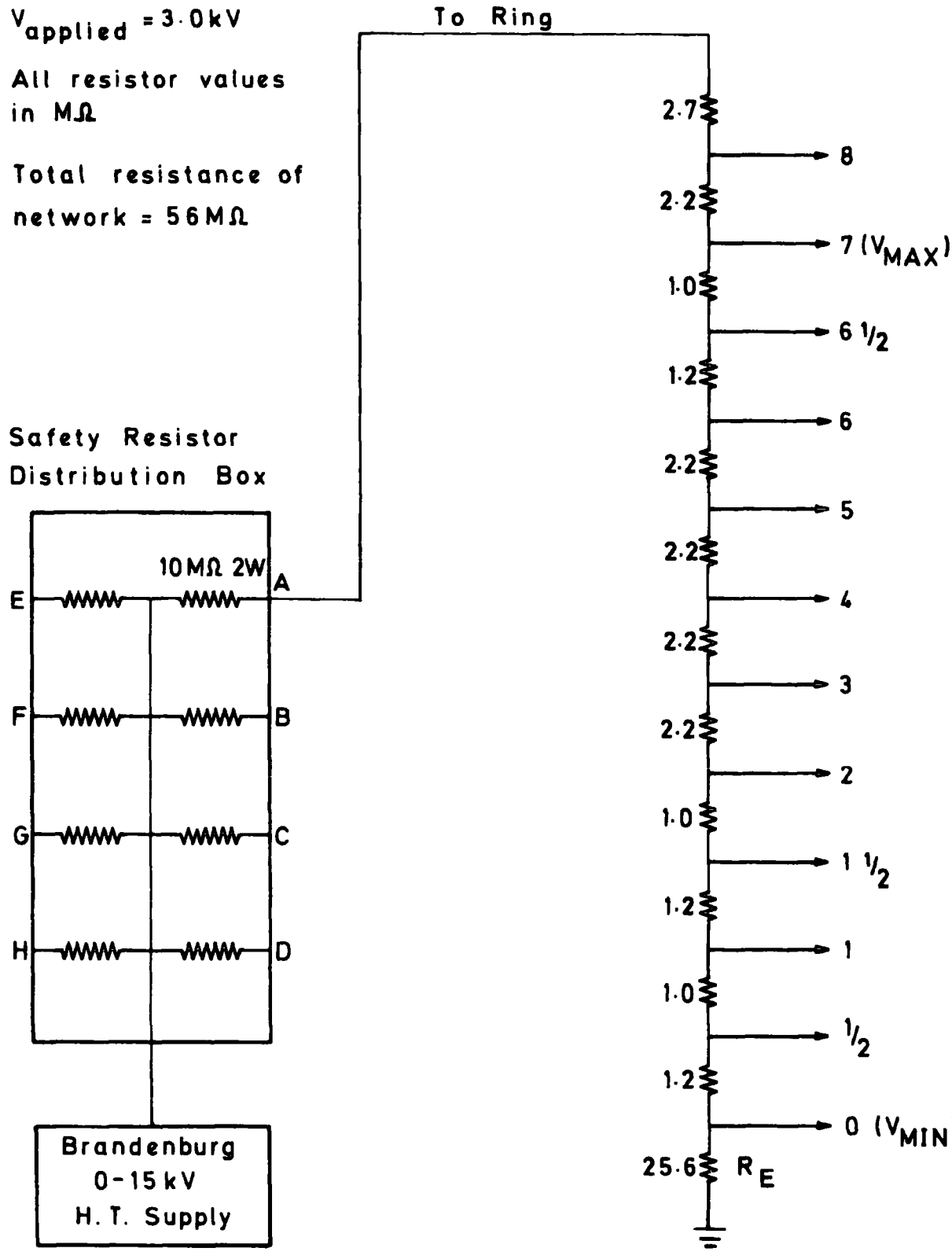

FIG. 4.6 : H.T. DISTRIBUTION SYSTEM

DOWNSTREAM

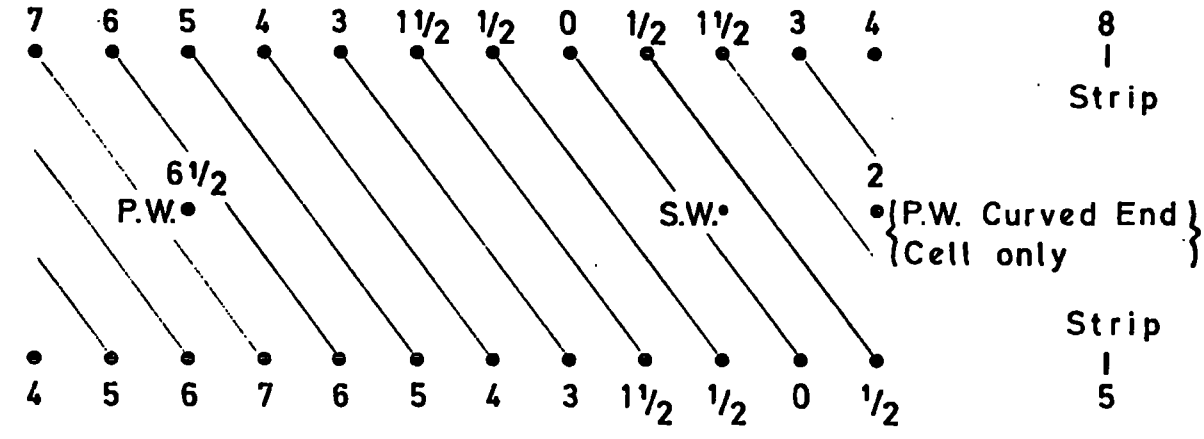

A μ^+ polarity

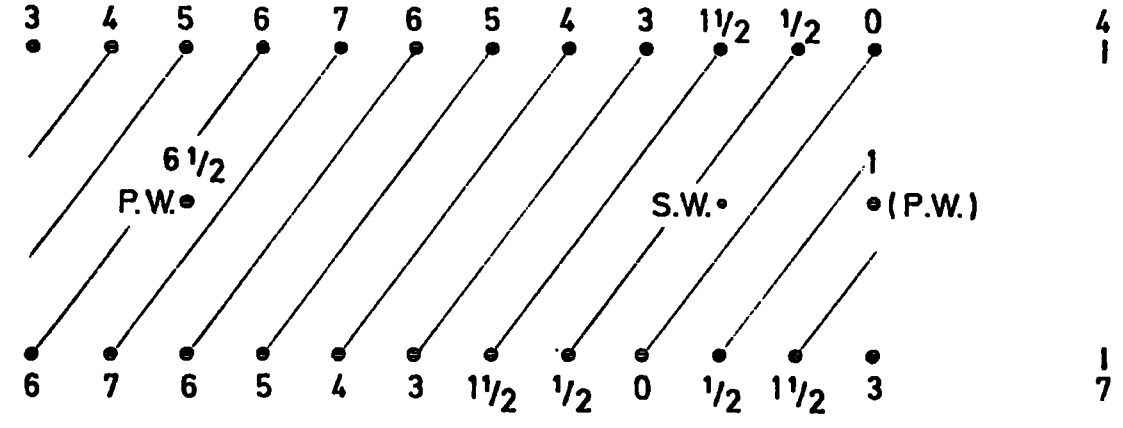

B μ^- polarity

UPSTREAM

POTENTIALS :-

8 = 2314 V	7 = 2196 V	$6\frac{1}{2}$ = 2143 V	6 = 2079 V
5 = 1961 V	4 = 1843 V	3 = 1725 V	2 = 1607 V
$1\frac{1}{2}$ = 1554 V	1 = 1489 V	$\frac{1}{2}$ = 1436 V	0 = 1371 V

S.W.'s = 0 V

FIG. 4.7 : CHAMBER WIRE POTENTIALS

from a NIM bin power supply sited in a rack immediately below the baseplate. The pre-amplifiers had to be positioned as close to the chambers as possible so that signal attenuation and distortion did not occur, sense wire outputs being typically 2 mV into 50Ω. 16 ns cables from the sense wires to the pre-amplifier inputs proved to be the minimum possible, due to physical considerations. The need for remote sensing of the current being drawn on the three power rails was not considered essential after perfect reliability using independent L.T. supplies during development at the Daresbury Laboratory and CERN.

4.3 The Data Acquisition System

The main requirement of the data acquisition system, apart from processing additional items of data such as the energy level of the decay electron and the time into the (g-2) cycle at which the event occurred, was to digitize the drift times in the cells of the drift chambers. In order to do that accurately the zero time at which the decay electron traversed the chambers had to be known, and for that purpose the shower counter C10 was used as a trigger. The signals from the sense wires had also to be discriminated and shaped and then the times between the C10 trigger and sense wire signals digitized. Account had to be taken of the delay between the arrival of the C10 trigger and the minimum possible drift time pulse, i.e. zero drift length, which was caused by inequalities in the physical delays of the system and had to be corrected for in the software.

Taking the maximum drift length in the (g-2) chambers of 14 mm, a possible resolution of 100 μm and a predicted maximum drift time in the order of 500 ns implied a timing resolution of 3.5 ns. Considering other drift chambers with longer drift spaces and greater drift velocities implied an optimum timing resolution, without introducing undue cost, of 2 ns. [4,5]. Two types of CAMAC module digitizers were available that would perform to such an accuracy. The first type - TDC's - will be discussed in section 4.4. They were used during the testing of the prototype and production chambers at the Daresbury Laboratory and during the initial runs at CERN. Several limitations were apparent and therefore the DTD system was introduced, as will be explained in section 4.5. With timing resolutions required to such an accuracy fast electronics and low discrimination levels of sense wire pulses were essential to reduce time slewing.

A block diagram of the data acquisition system is given in figure 4.8. The sense wire and C10 pulses were processed in the NIM logic and the drift times digitized in CAMAC, through which they were interfaced with the HP 2100 computer and associated 32K core. This was done either directly using a dedicated crate controller, in the case of the one crate TDC system, or through a Borer interface in the case of the two crate DTD system. Operating under an acquisition program written in ASSEMBLER the data was blocked and written on to magnetic tape. Display of data or programs on the V.D.U. was performed using the CERN version of Hewlett Packard BASIC called BAMBI, [6,7,8] in either an on-line or off-line mode. A paper tape reader and punch and a lineprinter allowed software development and loading of the operating system.

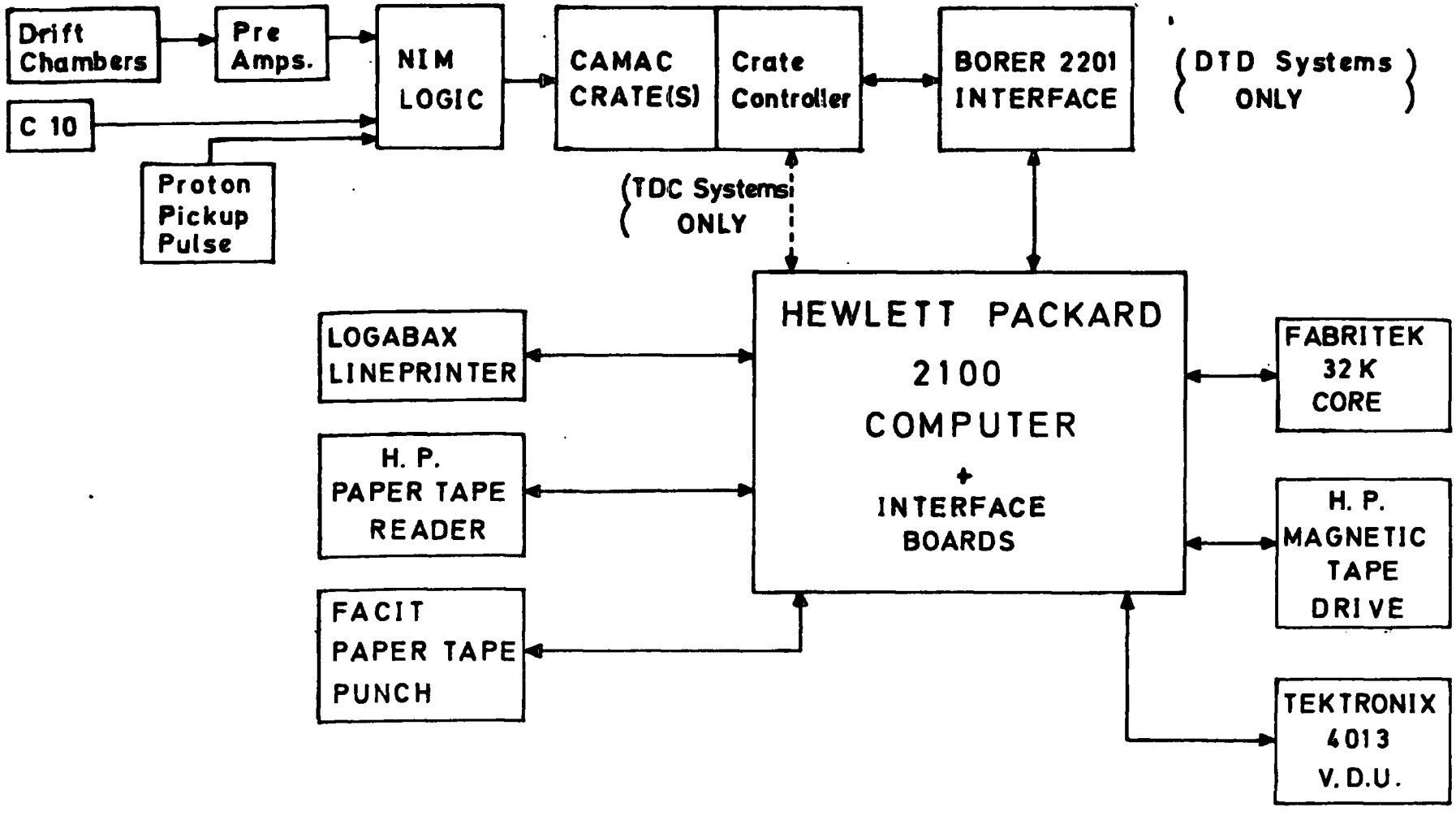

FIG 4.8: BLOCK DIAGRAM OF ELECTRONICS & COMPUTER

4.3.1. The NIM Logic

The essential tasks of the NIM logic were fivefold:-

i) Signals were accepted from the main (g-2) fast electronics corresponding to energy bins for the electrons detected in shower counter C10, which had a resolution of $\pm$ 250 MeV. The counter signal was fanned-out five ways and attenuated by various amounts and discriminated, thus giving signals if the energy was greater than the preset levels. The levels were labelled T10, A, B, C, and D roughly corresponding to energies greater than 500, 900, 1800, 2200 and 2800 MeV respectively. T10 could thus be used to indicate that a particle had been detected and used as a strobe for the other levels. A particle with energy greater than 2200 MeV but less than 2800 MeV would thus have bits T10, A, B and C associated with it.

ii) The second task was to attenuate the C10 pulse and discriminate at the - 50 mV level in order to only detect decay electrons with energies greater than 900 MeV and thus ensure that they had decayed in the forward direction in the muon rest frame.

The gain of the P.M. tube on the shower counter altered with varying beam conditions.[9] Also the applied B.T. was altered on occasions in connection with experiments on the EDM counter immediately upstream, so that only electrons with energies greater than 3000 MeV fell into energy bin D. Thus the attenuation had to be checked before each run to ensure that only particles above 900 MeV were accepted. To achieve this a program was written in BAMBI to calculate the energies of one hundred events from their respective energy bins. The attenuation was increased until no events occurred with only level T10 triggering as demonstrated in figure 4.9.

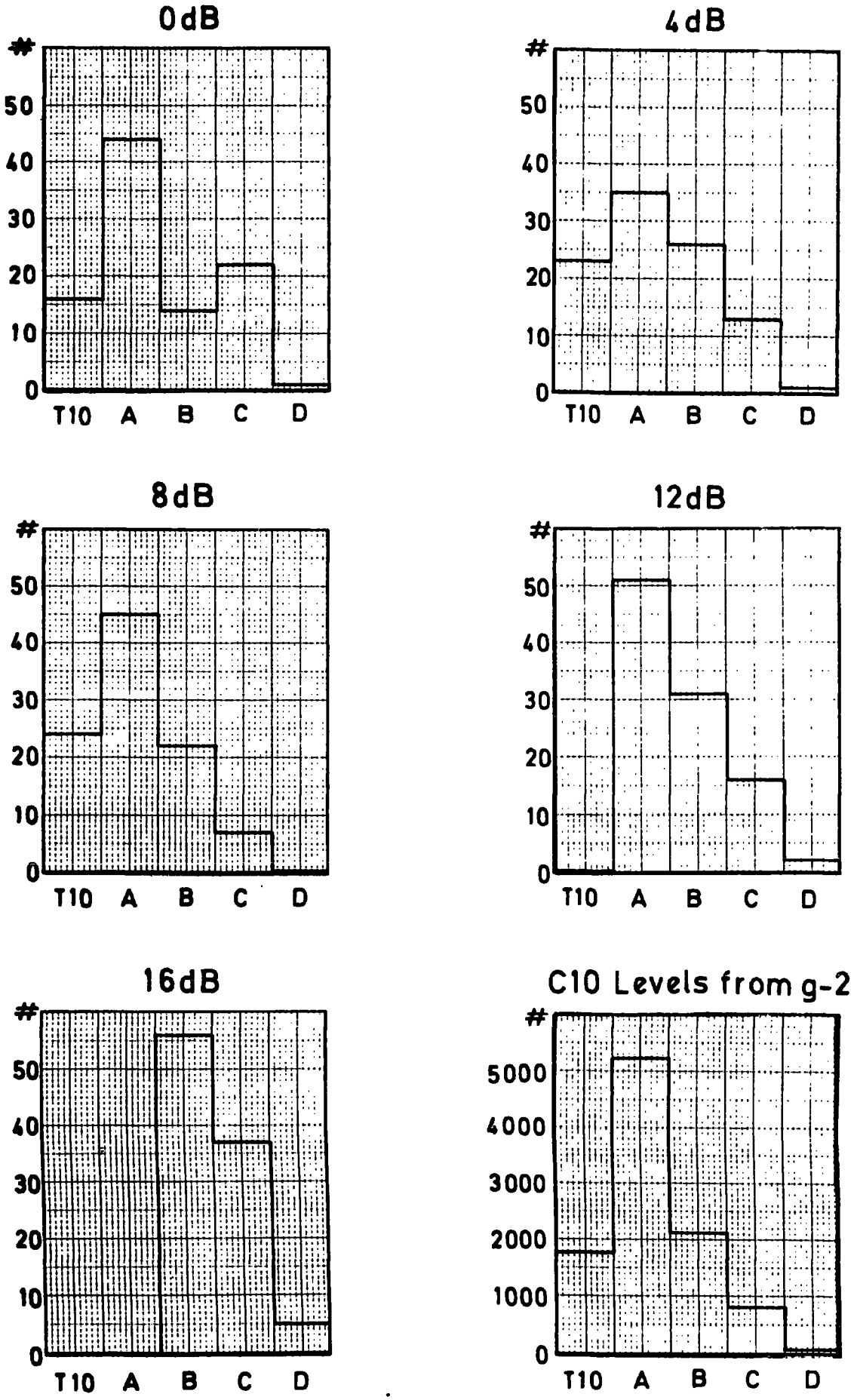

FIG 4.9 : DISTRIBUTION OF DECAY ELECTRON ENERGY LEVELS FOR VARIOUS VALUES OF C10 ATTENUATION

The valid C10 pulses were then used as the timing reference for digitization if the event occurred during the timing gate described below.

iii) The third function was to form a timing gate with reference to the proton pick-up pulse, which immediately preceded the pion injection into the (g-2) storage ring. This was used in coincidence with the processed C10 pulse to select a detectable particle.

Here it may be noted that the drift chambers had a dead time of approximately 50 μs after the injection of the polarized pion beam into the (g-2) storage ring. This was due to the enormous number of pions and secondaries passing through the chambers during injection, which was known as the "initial flash". The drift chamber array was immediately opposite the injection section of the ring which exacerbated the problem. A crude estimate yielded 10^5 particles passing through each chamber at that stage. Hence as the avalanches occurred around the sense wires the number of ion pairs in the chamber could exceed 10^{10}. It was thought that space charge effects around the sense and potential wires plus slow charge leakage from the mylar windows, which were only aluminized on the outer surface, caused the chamber inefficiency at early times after injection. Such effects when operating with high particle fluxes had been noted by other workers, as stated in Chapter 2.

When operating with negative polarity muons the injection was cleaner[9] and the chambers were able to detect tracks up to 10 μs earlier than with the positive polarity. During one run with negative muons only one PS pulse was injected into the ring instead of the normal two and analysis of the occurrence times of candidate events showed that the array only detected a few tracks between 30 and 50 μs and only became fully efficient thereafter.

As the electronics was only capable of storing one event per (g-2) cycle the gate was normally opened at between 50 and 100 μs into the cycle and extended until 500 μs. As the number of decay electrons fell exponentially with time the number detected after 500 μs was negligeable and in any case pick-up from the electrostatic focusing field electrodes occurred beyond 650 μs.

iv) Fourthly the sense wire signals had to be discriminated and shaped for input to the TDC's or DTD's. Due to high background noise in the chambers the level was set to - 100 mV which, assuming a linear voltage gain for the pre-amplifiers of x500, corresponded to 500 μV into 50Ω from the sense wires. This necessarily introduced unwanted time jitter as a much lower discrimination level would have been desirable, but it was the best compromise solution.

v) Finally the rest of the NIM logic served as a series of fan-outs for various signals to the CAMAC modules and will be discussed further in the following sections.

For the DTD system only the C10 pulse had to be delayed to act as a common stop for the DTD Controller. Also EDM information was introduced as will be discussed in section 4.5.

4.4 The TDC System

The TDC system will be described in order to demonstrate the development of the system and the advantages of the DTD system. It must be noted, however, that the majority of the analysis, to be discussed in Chapters 5 and 6, was performed on the DTD data due to its greater accuracy.

The TDC NIM logic system is presented in figure 4.10 with the

CAMAC system in figure 4.11 and on overall block diagram in figure 4.12.

As previously discussed the energy levels A, B, C and D were strobed with a shaped T10 pulse to give an indication of the decay electron energy. Those levels in coincidence were input to a Pattern B unit in CAMAC which presented a binary word on the dataway during readout. A coincidence between an attenuated and discriminated C10 pulse and the timing gate indicated a valid event and was fanned-out, using dual limiters, to perform several functions.

Eight Le Croy quad TDC's type 2226A and four octal TDC's type 2228 were used. Twelve of the coincidence fan-outs were required to provide front panel common "start" signals. The Octal TDC's also required artificial common stop signals because in the event of no stops occurring, i.e. no relevant sense wires hit, no Q response or LAM was generated and the acquisition program saw an empty CAMAC slot rather than eight locations. As the analysis program relied upon sixty-four channels of data being present this option caused fatal software errors, so two timing units and dual fan-outs were used to produce the artificial stops after the required delays. The quad TDC's had no such option and merely recorded overflow values. All TDC's had a maximum digitization time of 512 ns except for two octal units adjusted to 1 μs full range.

The other two fanned-out coincidences were used as an input to channel 1 of the Status "A" register, to give an external command to the crate controller to read and clear the crate, and as a "set" to a Cable Timed Shaper acting in bistable mode. A second pulse from the end marker of the timing gate produced the reset and the resulting output pulses were used as gates for the Pattern B unit and a micro-scaler. The latter recorded a 10 Mhz pulse train over the duration of the gate so that by knowing the time of the end of the timing gate

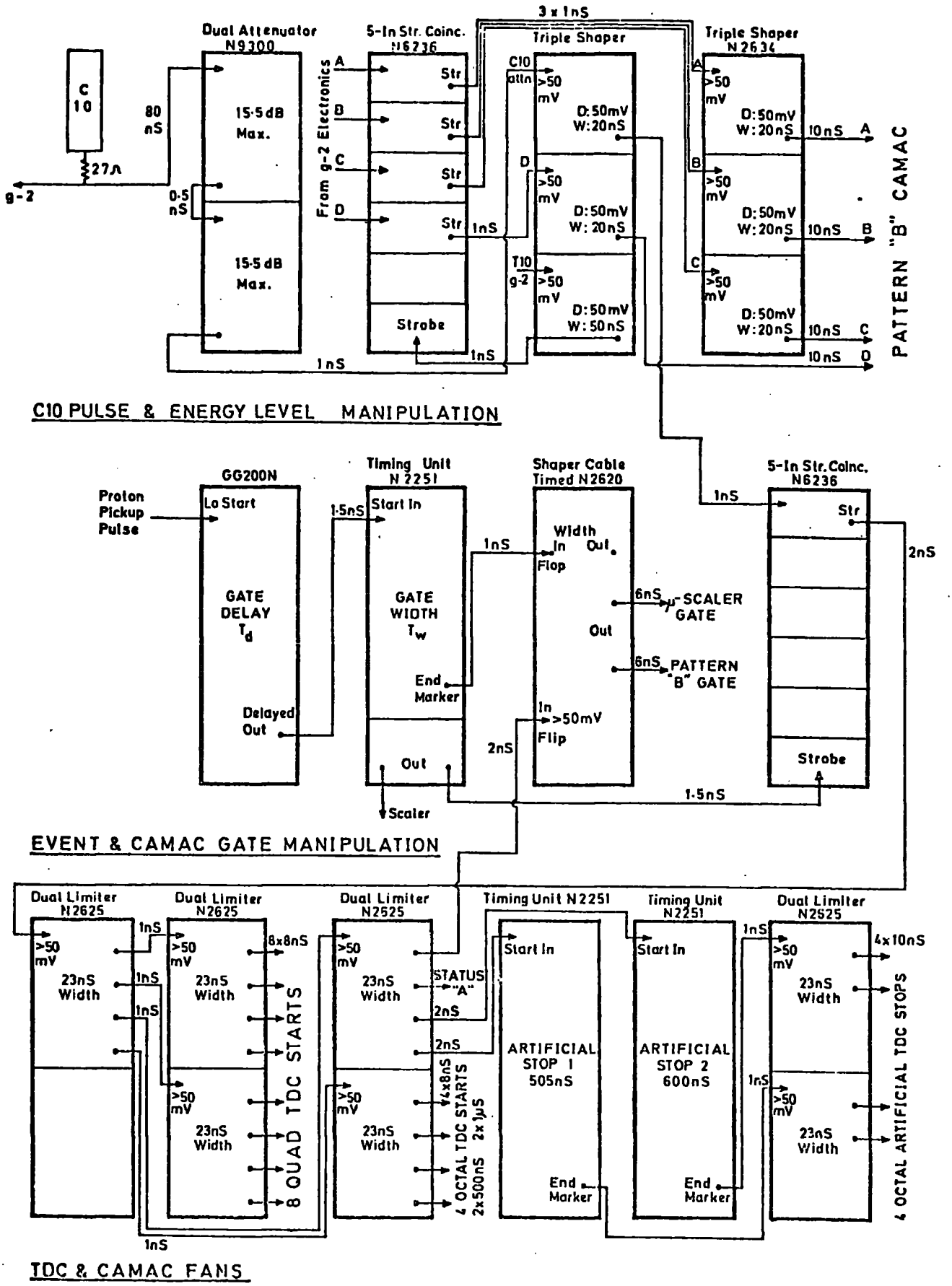

FIG. 4.10 : THE TDC NIM SYSTEM

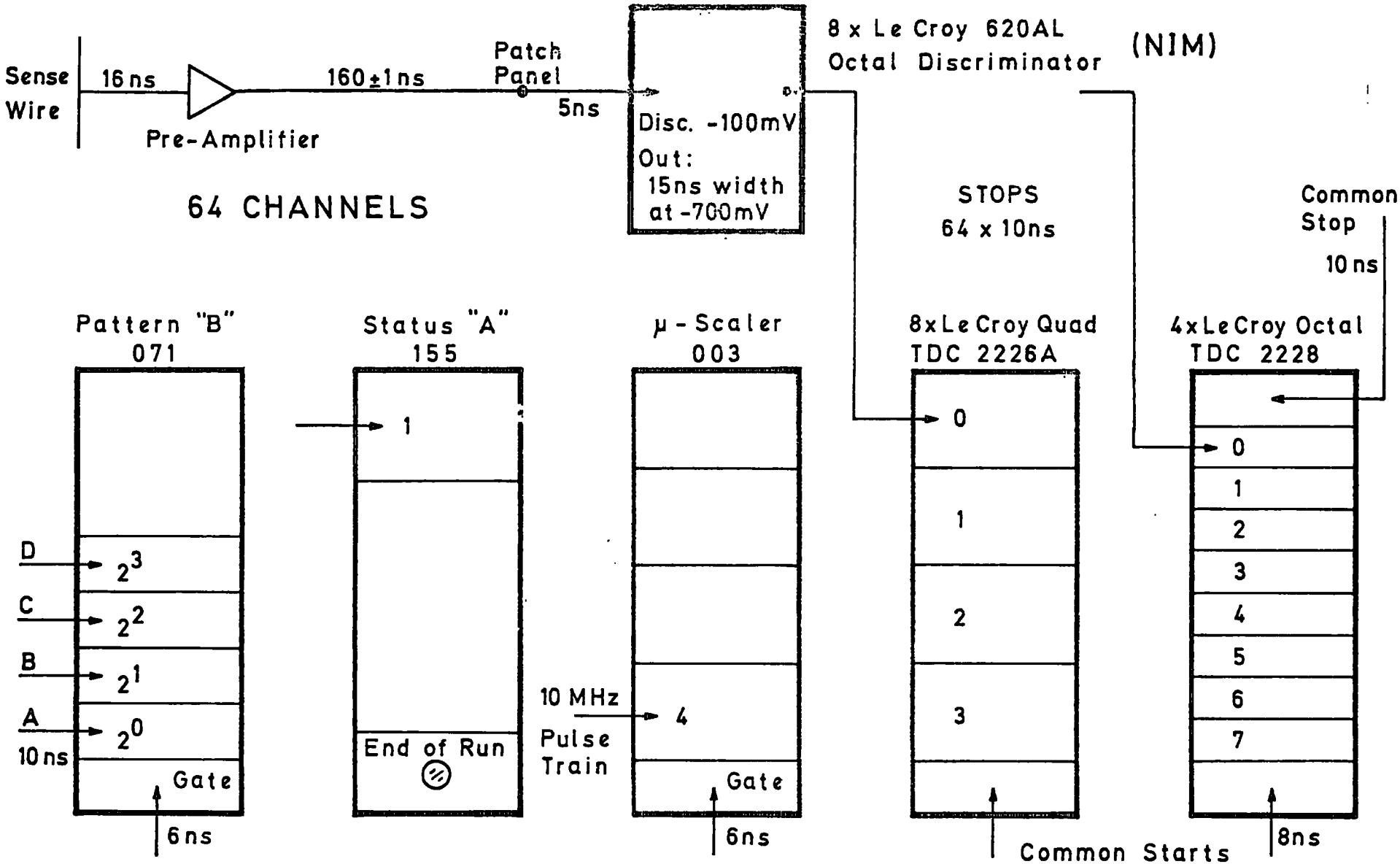

FIG. 4.11 : TDC CAMAC SYSTEM

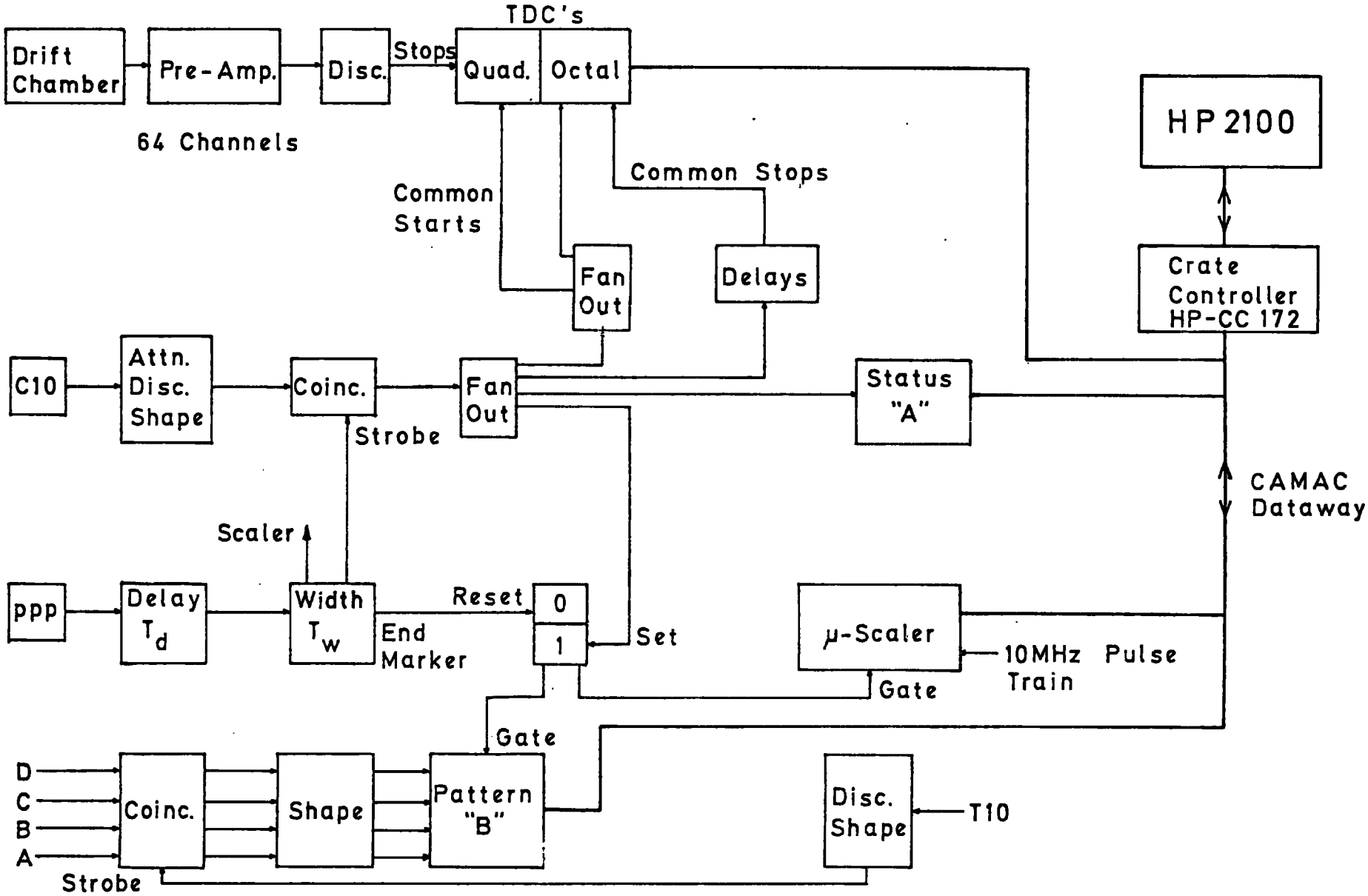

FIG. 4.12 : BLOCK DIAGRAM OF TDC BASED DATA ACQUISITION SYSTEM

the occurrence time of the decay electron could be computed using the inverse timing information.

A scaler was attached to an output from the timing gate to record the number of $(g-2)$ cycles during a run. A decay electron was not necessarily detected every cycle so this acted as a guide to the efficiency of the system.

The amplified sense wire pulses were discriminated at the - 100 mV level and the Le Croy octal 620AL discriminator units adjusted to give an output pulse of 15 ns width at the NIM level for input to the TDC stops.

Termination of a run was accomplished by pressing a button on the Status "A" register or a switch on the computer.

By making use of the pulsing system for the LED's, which were used in the main $(g-2)$ experiment to measure the gain of the shower counters,[9] a system was devised to measure the difference in arrival times at the TDC's of the "start" and "stop" signals. The stop signal corresponded to a zero drift length and by careful matching of delays, to represent the original system, the difference could be displayed on a calibrated oscilloscope. Allowing 5 ns for the traversal of light down the scintillator in the shower counter to the position of the LED, just in front of the photomultiplier window, the C10 starts were found to arrive 40 ± 4 ns before the sense wire stops. Hence there was no dead time in the digitization range and this value had to be deducted from all drift times in the software. This value agreed well with the theoretical figure calculated from the cable and photomultiplier delays plus propogation delays of the NIM modules.

4.4.1. Calibration of the TDC's

Time to digital conversion was accomplished in two stages with the Le Croy units. A capacitor was charged up by a constant current source initiated by the common "start" signal and terminated by the "stop" signal - each channel being independent. Hence the total charge on a capacitor was an analogue representation of the time interval. The charge was then removed at a constant rate whilst a 20 MHz oscillator, in the case of the octal units, was gated into a scaler, thus producing a digital output.

Each channel had to be calibrated to measure the offset at zero delay and the slope of the calibration curve. A program was written in BAMBI to record the delays set on twenty-four channels at a time using a pulse generator and a series of fan-outs in NIM and delays produced using delay boxes. Ten recordings were made at each 8 ns step throughout the time range of the TDC's.

Figure 4.13 shows a typical channel's calibration against true linearity and figure 4.14 demonstrates the different deviations from linearity throughout the four independent channels of a quad TDC. The curves show the extreme non-linearity of certain channels, up to 12 ns change in deviation over full-range, and the vast variation between the channels in a module. This was due to the design philosophy of the TDC modules which had independent charging and discharging current generators and capacitors for each channel. It must also be noted that TDC calibrations tended to drift with time.

To use TDC data accurately in analysis programs a least squares fit would have to have been made to the data and software corrections made accordingly.

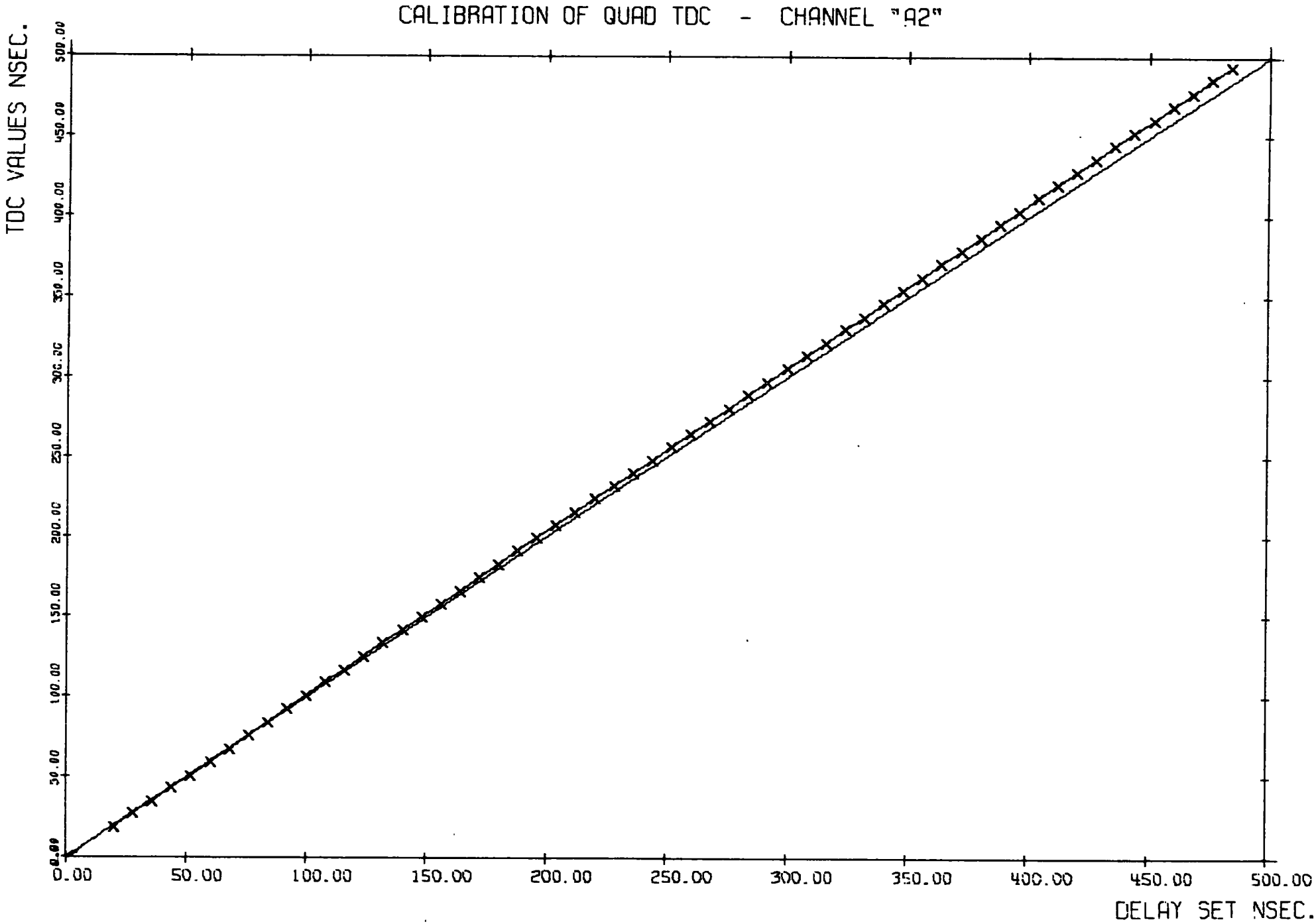

FIG. 4.13: TYPICAL CALIBRATION CURVE OF A TDC CHANNEL

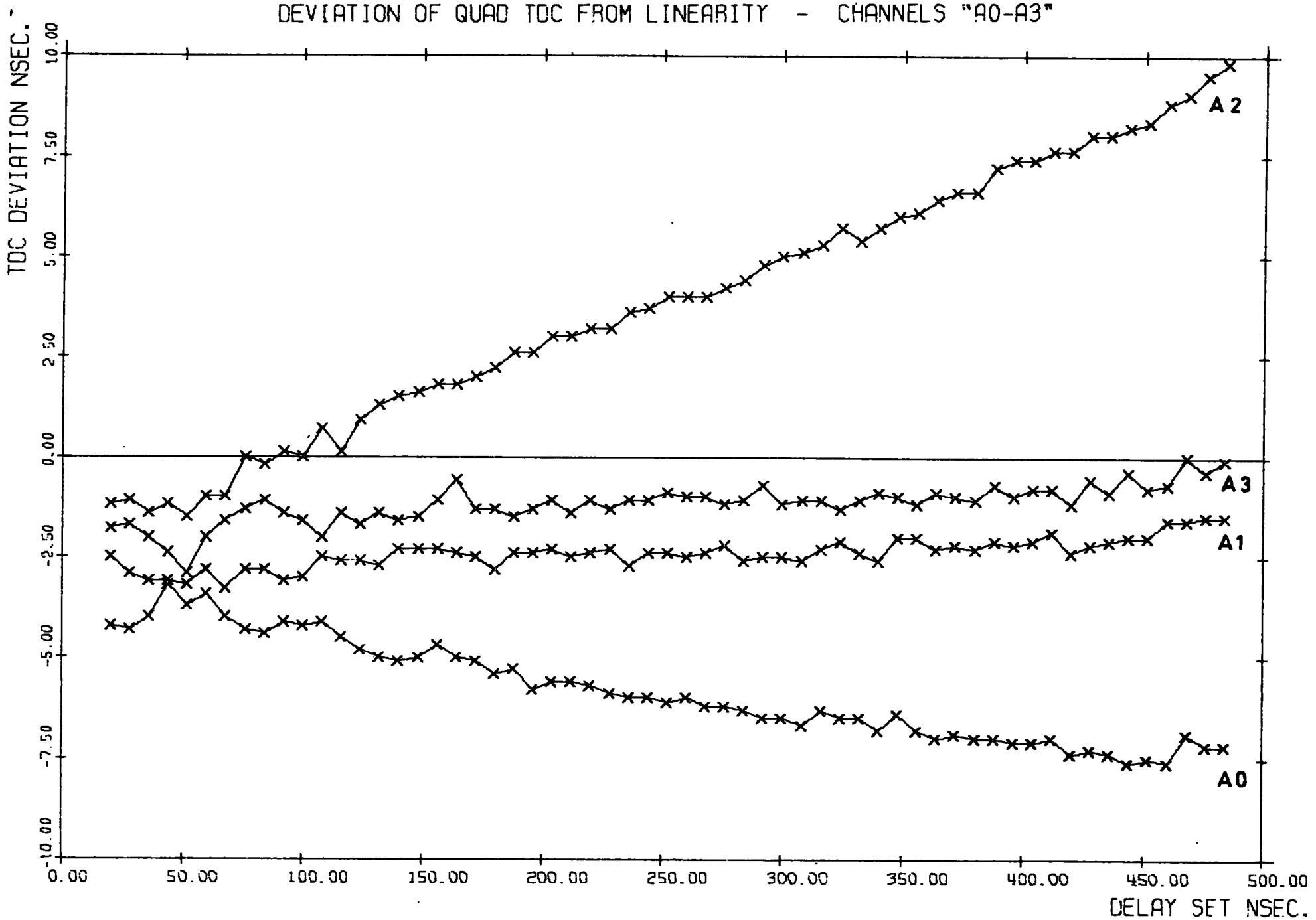

FIG. 4.14: TYPICAL DEVIATIONS OF A QUAD TDC FROM LINEARITY

4.4.2. Limitations of the TDC System

The most serious limitation of the TDC's was that they only had a one hit capability in each cell. Hence if a double or multiple hit occurred in a cell and the hit not connected with a correct track had the shorter drift time, then the track would appear to be perfect even though incorrect data were recorded. In the (g-2) experiment, where the decay electrons were detectable up to 500 μs after injection it would have been feasible in many cases to detect two tracks per cycle, especially if the drift chambers had been efficient from say 10 μs. However the TDC's had a digitization time of 50 μs (due to the 20 Mhz oscillator scaling in 500 ps bins) which when added to the CAMAC cycling time required to read and clear the crate made the proposition untenable over the allowed 400 μs timing gate.

The amount of software correction required for calibration of the drift times was also unwieldly, especially if on-line analysis had been attempted.

As far as the data acquisition system was concerned, several faults were noted. The Pattern B gate for acceptance of energy level signals was open from the receipt of the correct C10 pulse until the end of the timing gate. Hence if any later decay electrons were of higher energy than the particle detected, then the corresponding higher energy levels would be recorded in association with the lower energy track. A narrower gate and a veto were added in the DTD system.

The use of the Triple Shaper units for C10 and energy level signal shaping, as shown in figure 4.1C, was not totally satisfactory as they tended to produce double or triple outputs at lower discrimination levels or output widths, so they were replaced in the DTD system.

4.5 The DTD System

The (g-2) drift chamber array was one of the first experiments to use the CERN designed Drift Time Digitizer system. The mode of operation of the DTD's has been discussed in detail elsewhere[10,11] but briefly an octal double width CAMAC DTD 164[12] was allotted to each chamber and each sense wire was connected to an independent channel. The DTD's themselves were controlled by a DTD Controller Type 211[13], also a double width CAMAC unit. An inverse timing method was used whereby the sense wire signals acted as "starts" and a delayed C10 pulse was used as a common "stop".

The DTD system achieved a multi-track timing resolution of 2 ns by using a 125 Mhz crystal oscillator to produce the clock pulses in the Controller, giving an 8 ns resolution. An interpolator was used in each DTD timing channel to measure the delay between the arrival of the "start" pulse and the next positive going edge of the clock pulse, to 2 ns resolution. Another interpolator in the Controller measured the delay between the arrival of the "stop" pulse and the next positive going edge of the clock pulse also to 2 ns resolution. Using this system allowed the use of standard circuitry rather than the more expensive electronics that would have been necessarily associated with a 500 Mhz clock and would thus have defeated one of the main benefits of drift chambers over MWPC's - the cost of readout electronics per unit area.

A software CAMAC command started the output of the 125 Mhz clock from the Controller which was fanned-out by a type N4189 Fast Fanout[14] to the clock inputs of the DTD modules. The "enable" output was also fanned-out to the DTD's to allow them to accept "start" signals and

begin scaling the clock pulses. There were four timing channels per module, which were used in turn, and any number of wires were allowed to have hits at the same time, hence a possible maximum of thirty-two hits could be recorded in one module. Some restrictions applied to the incidence of the hits; starts occurring within 2 ns after the previous one were recorded as having occurred at the same time, starts occurring between 2 ns and 4 ns after the previous one were recorded as having occurred at the same time and at a time 2 ns later, while starts occurring more than 4 ns after the previous one were resolved and recorded as a separate time. Thus software corrections had to be made in the case of events occurring after 2 to 4 ns to allocate the later time as the true drift time. When the Controller received the common "stop" signal the interpolator measured the delay to the next positive going edge of the clock pulse and the clock was stopped. The "stop" output from the Controller was set and fanned-out to the DTD's 50 ns later which enabled them to be read.

On readout the modules presented a 16 bit binary word for each hit on the CAMAC dataway. The four most significant bits referred to the station number, set by front panel decade switches to 0 - 7 for chambers A - H respectively. The next three bits referred to the channel, and thus wire, number 0 - 7. The remaining nine bits gave the drift time, including vernier, in 2 ns bins. The three bit stop vernier, read from the Controller, had to be subtracted from this value in the software.

Spurious starts occurring before the true particle arrival time caused the time measuring channel to start digitizing. To overcome this problem the time measuring channel and associated wire register were reset when the two most significant scaler bits reached "1". Thus the maximum digitization time available was 768 ns.

4.5.1. The DTD NIM System

The final version of the DTD NIM logic is shown in figure 4.15 along with the CAMAC system in figure 4.16 and a block diagram in figure 4.17.

The NIM logic was radically different from the TDC system both because the DTD's used an inverse timing method and because the time slewing of the previous system was too great, as discussed below.

The C10 pulse was not only attenuated and discriminated to provide energy resolution but also, more importantly, gave a timing reference for the drift time digitization. C10 pulses were artificially produced using a pulse generator, bipolar amplifier and attenuator to cover the expected range of - 140 mV, for firing level T10, to - 500 mV, to fire level D. By independently altering the attenuation of the resulting pulse from 0 to 16 dB before discrimination at - 50 mV, as performed during the runs, time slewing of up to 6 ns occurred, which was unacceptable. The time slewing was measured by displaying on an oscilloscope the difference in arrival times of the artificially produced C10 pulses and sense wire pulses derived from the same source. With a fixed sense wire signal

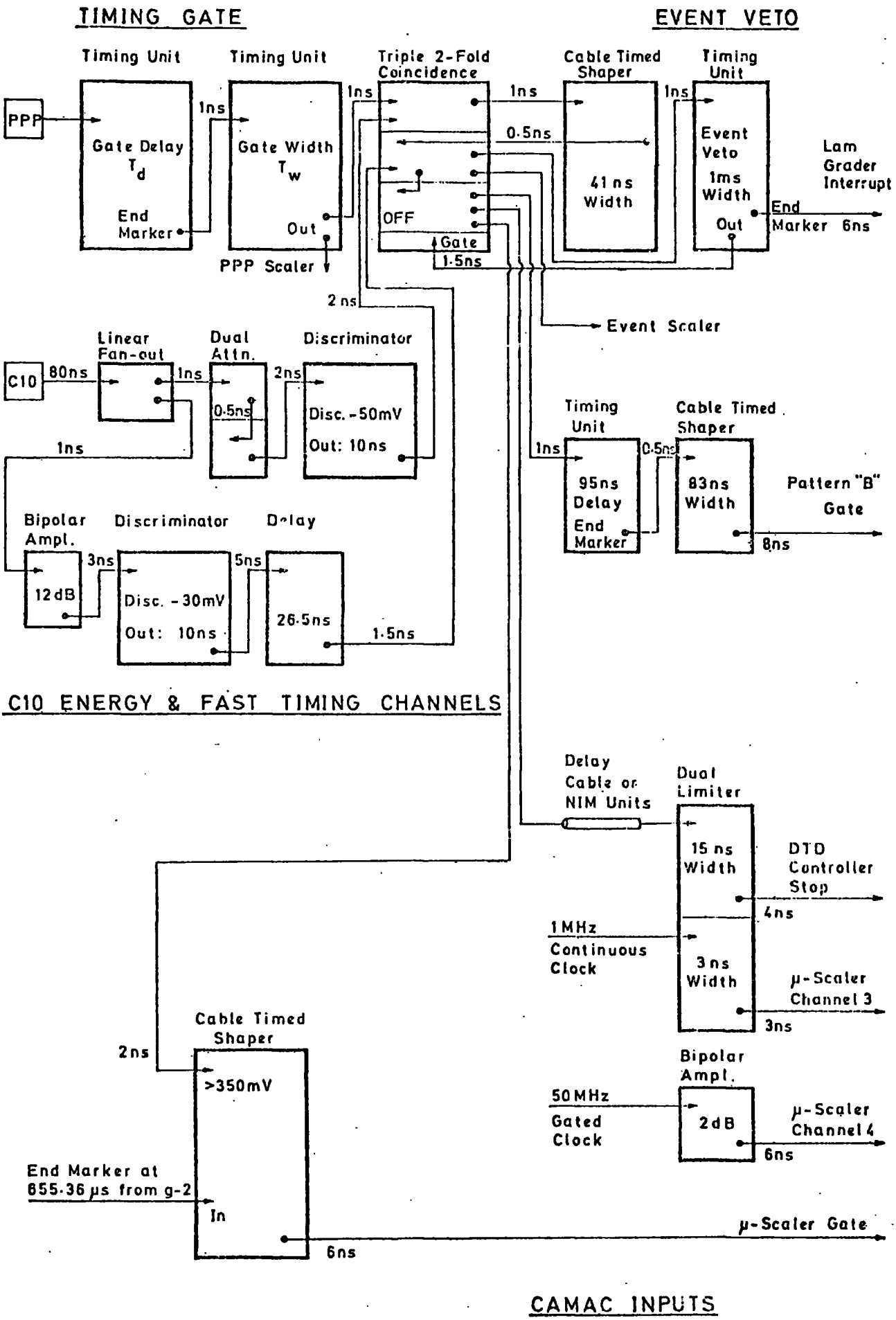

FIG. 4.15 : DTD NIM SYSTEM

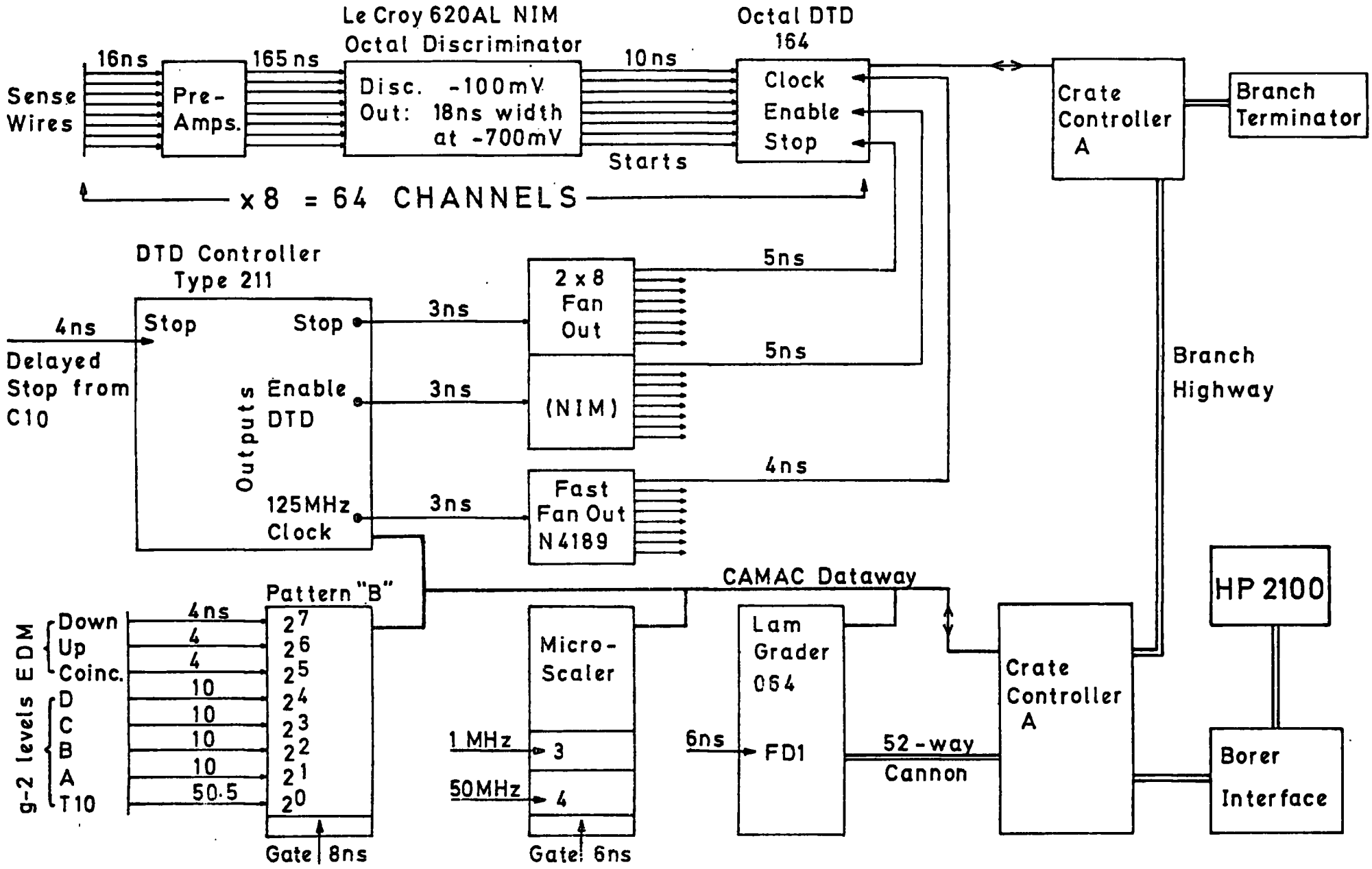

FIG. 4.16 : DTD CAMAC SYSTEM

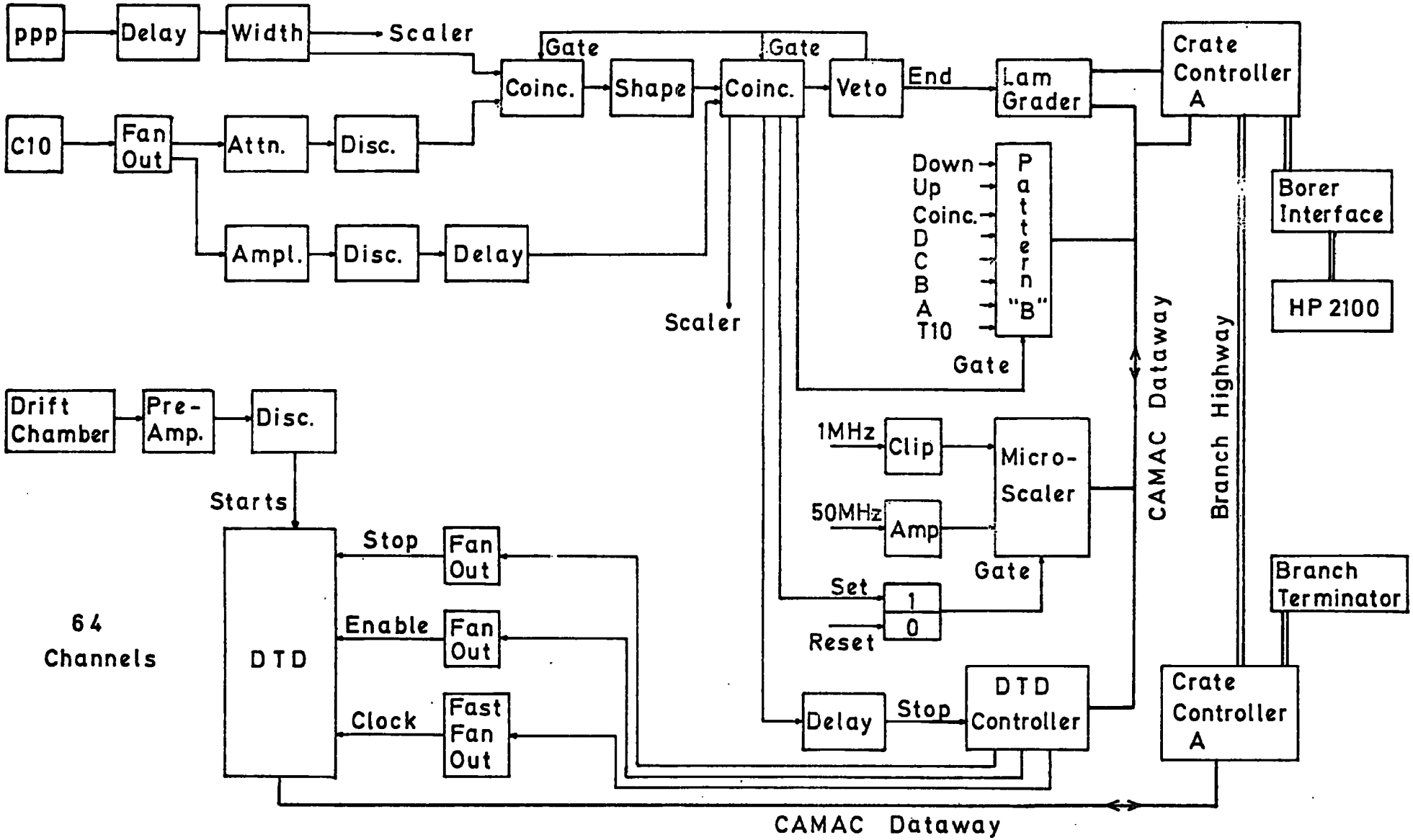

FIG. 4.17 : BLOCK DIAGRAM OF DTD BASED DATA ACQUISITION SYSTEM

the C10 pulse height and C10 attenuation were altered independently. For input pulse heights to the pre-amplifier ranging from 3 to 13.5 mV, i.e. the expected range, the delays in arrival times for various C10 settings agreed to within $\pm$ 1 ns and the time slewing was identical for all values. This indicated that the enforced high discrimination level of - 100 mV for the amplified drift chamber pulses produced less time jitter than that due to the method of attenuation of the C10 pulse. Results are displayed in figure 4.18 for C10 pulse heights corresponding to decay electron energies which just "fire" levels B, C and D. The time slewing is shown against various values of C10 attenuation for three separate sense wire pulse heights.

By fanning-out the C10 pulse into a fast timing channel and a"pulse height analysis" channel the time slewing was reduced to less than 2 ns which was considered acceptable. The "fast timing" channel was amplified by 12 dB and discriminated at - 30 mV, to reduce time jitter, and then delayed to match the other channel. The "pulse height analysis" channel was attenuated and discriminated at - 50 mV, as with the TDC system, and put in coincidence with the event timing gate as before. However the coincidence was now gated by a veto pulse so that only one particle could be detected per (g-2) cycle. This coincidence was shaped to have 40 ns width for input to a coincidence with the "fast timing" channel to ensure that the timing signal corresponded to a decay electron of correct energy. This second coincidence was also gated by the veto pulse to ensure the detection of only one particle per cycle.

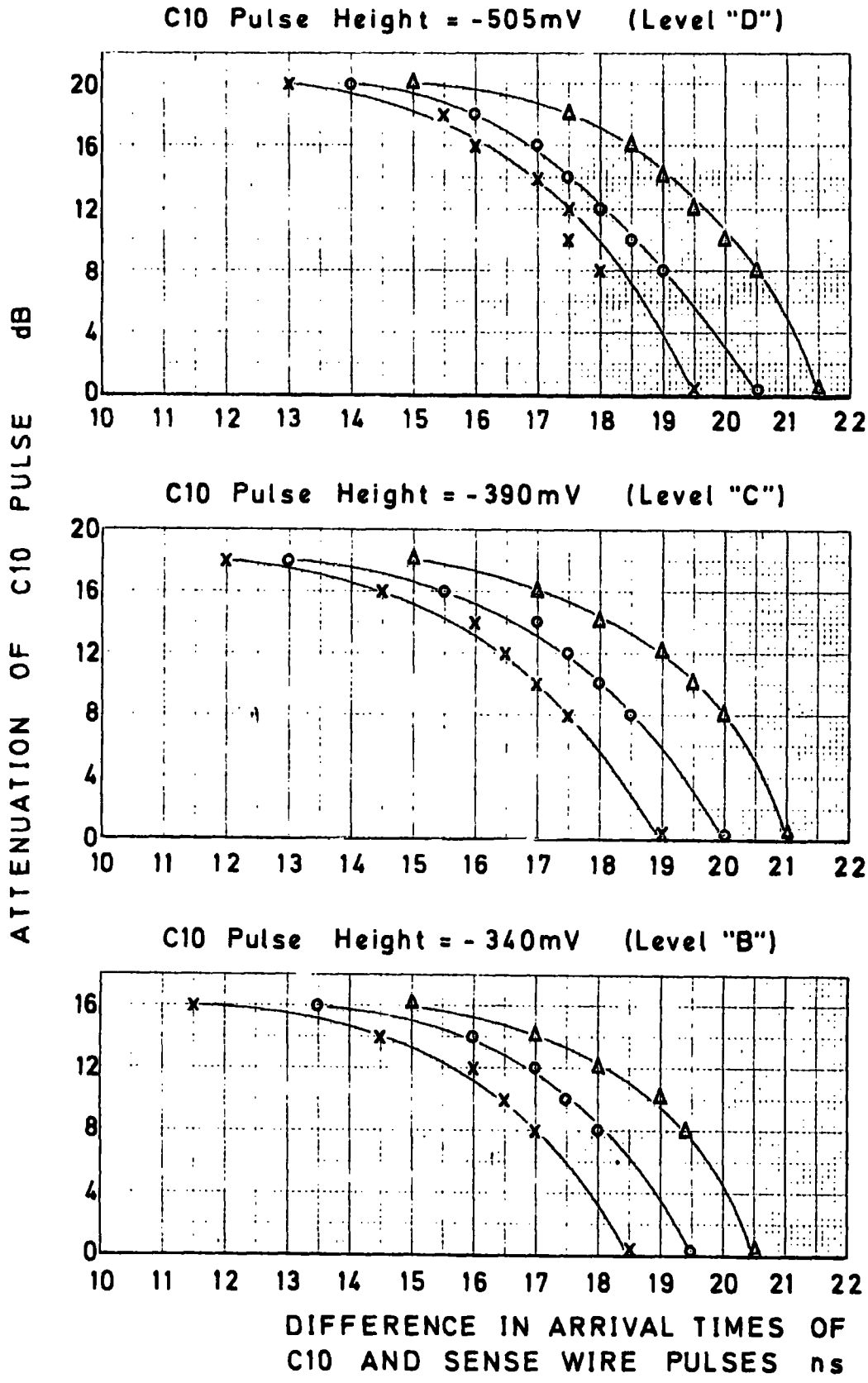

Sense Wire Pulse Heights :-

x = 13·5 mV o = 8 mV Δ = 3 mV Errors in timing = ±1ns

FIG. 4.18 : TIME SLEWING DUE TO ATTENUATION OF C10 PULSE

The coincidence pulse was fanned-out five ways to perform various functions:

The first was delayed by various methods and amounts, depending upon the system in use, and clipped to act as the DTD Controller "stop".

The second was input to a timing unit to produce a 1 ms long veto pulse to gate the coincidence unit. The end marker from this pulse supplied the external interrupt to the Crate Controller, via channel FD1 of the LAM Grader, that initiated readout of the CAMAC crates.

The third was used to "set" a Cable Timed Shaper in bistable mode. The "reset" was derived from a preset scaler in the (g-2) electronics which produced an end marker from a gated 100 MHz clock 855.36 μs after the proton pick-up pulse. The resulting output from the bistable produced a far more accurate inverse timing gate for the determination of the occurrence time of the event. A clipped 1 MHz clock train and a 50 MHz amplified clock train were used as inputs to the CAMAC μ-scaler to measure the gate length.

The fourth output was to a dual Borer scaler to act as an event counter that could be compared with the number of proton pick-up pulses recorded on the other channel which used the timing gate as its input.

The fifth output was delayed and widened to 80 ns to act as the Pattern B gate. As the coincidence unit was gated by the veto pulse the Pattern B Unit could only record the energy levels of the detected particle. The energy levels were timed into the gate using the LED pulser on the shower counter to adjust the delays. Hence no shaping of the pulses was now necessary.

Apart from the five energy levels three bits of EDM information were also included in the DTD system. The EDM counter, positioned between drift chamber H and shower counter C10, was in the form of two equally sized arms of thin scintillator mounted vertically above each other and filling the magnet pole gap with an active area similar to that of the shower counter. The dead space between the "up" and "down" counter was kept to a minimum after allowing for light exclusion. The least significant bit of information recorded whether a coincidence had occurred between the EDM counter and C10 and the other two bits recorded whether the "up" or "down" counters had detected a particle. It was also possible for either both or neither counters to detect the decay electron or secondaries[15]. Hence analysis of the eight bit binary word generated by the Pattern B unit in the software revealed both the energy and EDM status of the decay electron.

4.5.2. Modification of the Pre-amplifiers and Discriminators

Rudimentary analysis of the first DTD data revealed a large number of double or treble hits on a wire which appeared to be excessive. Such problems would never have been detected with the TDC system which only had single hit capability.

Inspection of the discriminator output pulses triggered by clean pulses from a pulse generator revealed a small after pulse of 80 - 100 mV 30 ns after the start of the discriminator output as shown in figure 4.19a. This appeared to be internally generated and indeed when the output pulse was adjusted from 10 to 18 ns

width, and the two unused outputs of the octal discriminators were terminated by 50Ω, the secondary pulse was reduced to less than 60 mV and the overshoot was eliminated as shown in figure 4.19b. The suppression of the secondary pulse was achieved by terminating the unused channels despite the Le Croy specification stating that all outputs were independent. Although the specification for the DTD modules quoted an input threshold of 350 mV it was found in practice to be in the 100 – 200 mV region with some channels as sensitive as 90 mV[16].

The pre-amplifier output also revealed an after pulse some 100 ns after the main pulse as shown in figure 4.20a. This had been noted by other workers[17] and was thought to result from mismatches between the sense wires, which were thought to have a typical impedance of 350Ω[18], and the 50Ω signal cable and, also, between the cable and pre-amplifier which had an input inpedance of 21Ω. By altering the pre-amplifier input resistor to 51Ω and changing an inter-stage resistor to 24Ω, to compensate for the resulting loss in gain, the cleaner pulse, without damped reflections at the back end, was produced as shown in figure 4.20b. The pre-amplifier circuit and modifications areshown in figure 4.21.

These modifications greatly reduced the number of false double hits recorded by the system.

4.5.3. Calibration of the DTD System

As with the TDC system the DTD modules were calibrated against

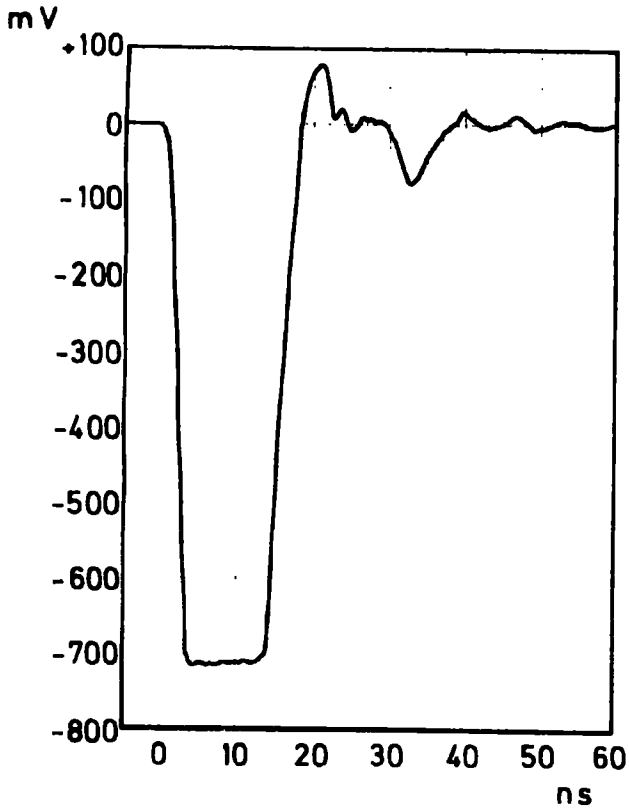

a BEFORE

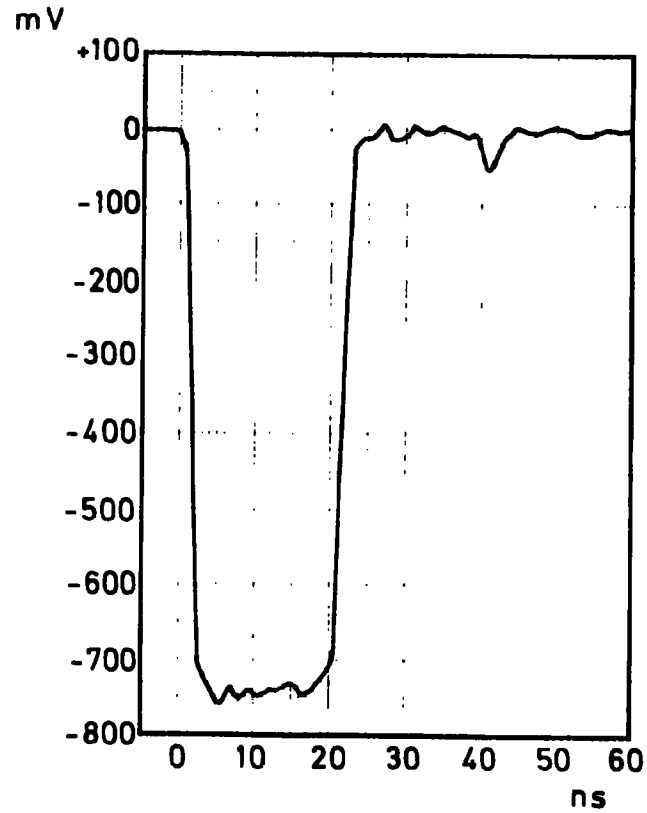

b AFTER

FIG. 4.19 : MODIFICATION OF DISCRIMINATOR OUTPUTS

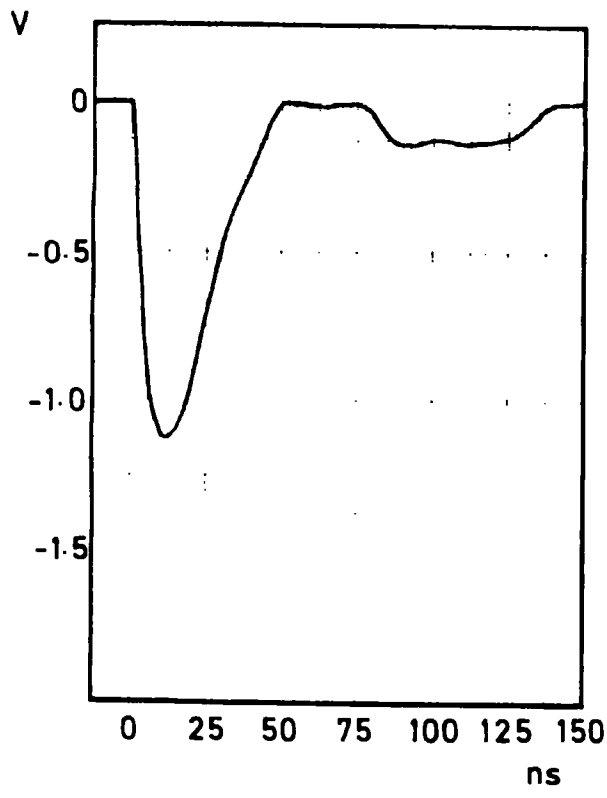

a BEFORE

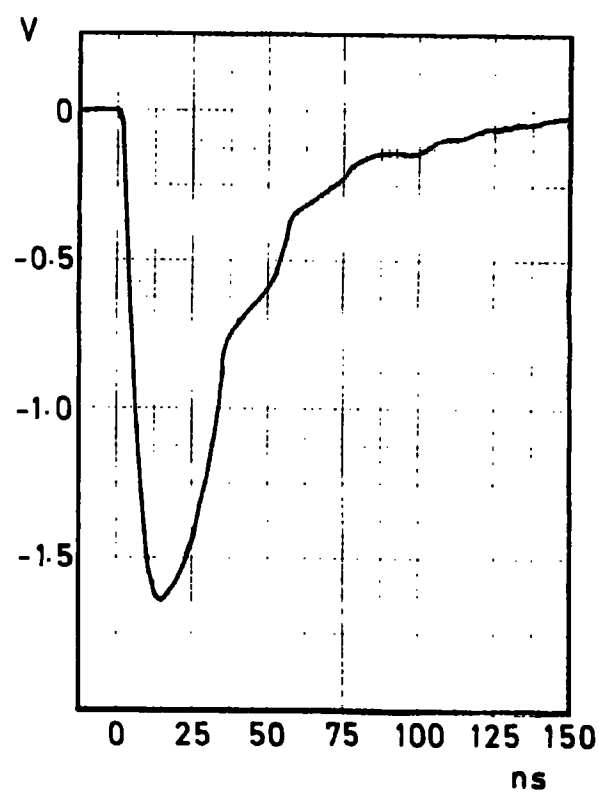

b AFTER

FIG. 4.20 : MODIFICATION OF PRE-AMPLIFLIERS

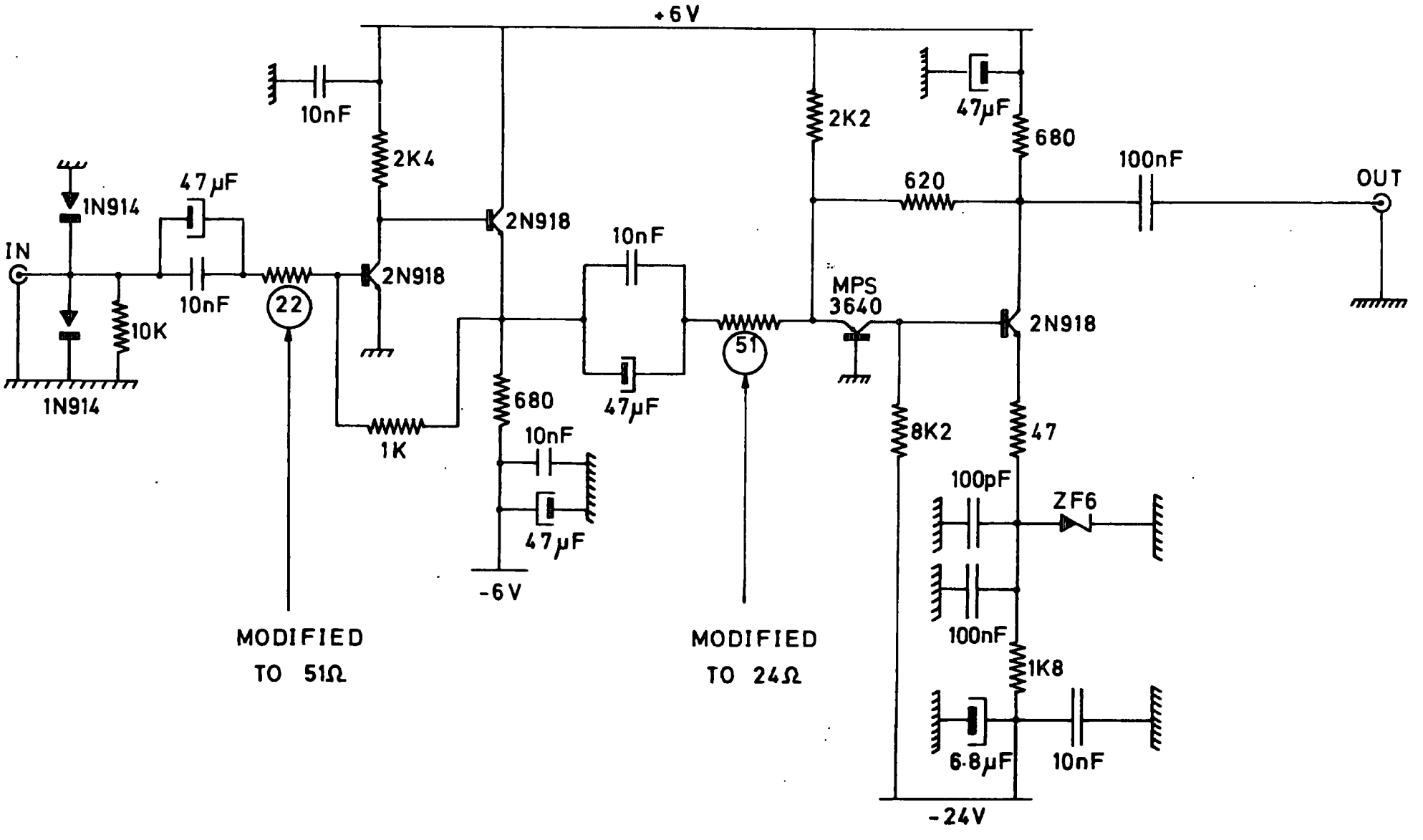

FIG. 4.21 : PRE-AMPLIFIER CIRCUIT AND MODIFICATIONS

a series of known delays at 10 ns intervals. It would be expected that as a master clock was used for all channels the calibrations would be identical except for statistical fluctuations in the interpolators. Due to an internal time delay in the Controller and the fact that the clock pulse was stopped on the following positive going edge after receipt of the "stop" pulse, at least one pulse reached the DTD modules. Hence a digitized time of 11 ns was recorded for a measured zero input start/stop delay. Assuming that this property was constant throughout the range, the calibration was made from 40 ns in 10 ns intervals. This would not only calibrate the DTD's but also check the randomizing of the interpolator as the 11 ns offset would cause the delay to fall midway between the 2 ns resolution of the timing bins. Figure 4.22 shows the calibration of a typical channel against linearity with allowance made for the 11 ns offset. As may be seen the linearity was far better than with the TDC's. Figure 4.23 shows the deviation from linearity of all eight channels in a module which indicates that at only two points, due to the statistics of the interpolator, does one channel vary from the other seven. The divergences from exact linearity could be attributed solely to the method of using a series of delay units to produce the set delays because these introduced errors due to faulty switches. A more stringent method for the calibration of the DTD's has been suggested following the calibration of the (g-2) Digitrons[19].

Calibrations were made of the length of the sense wire signal cables from the outputs of the pre-amplifiers to the patch panel in

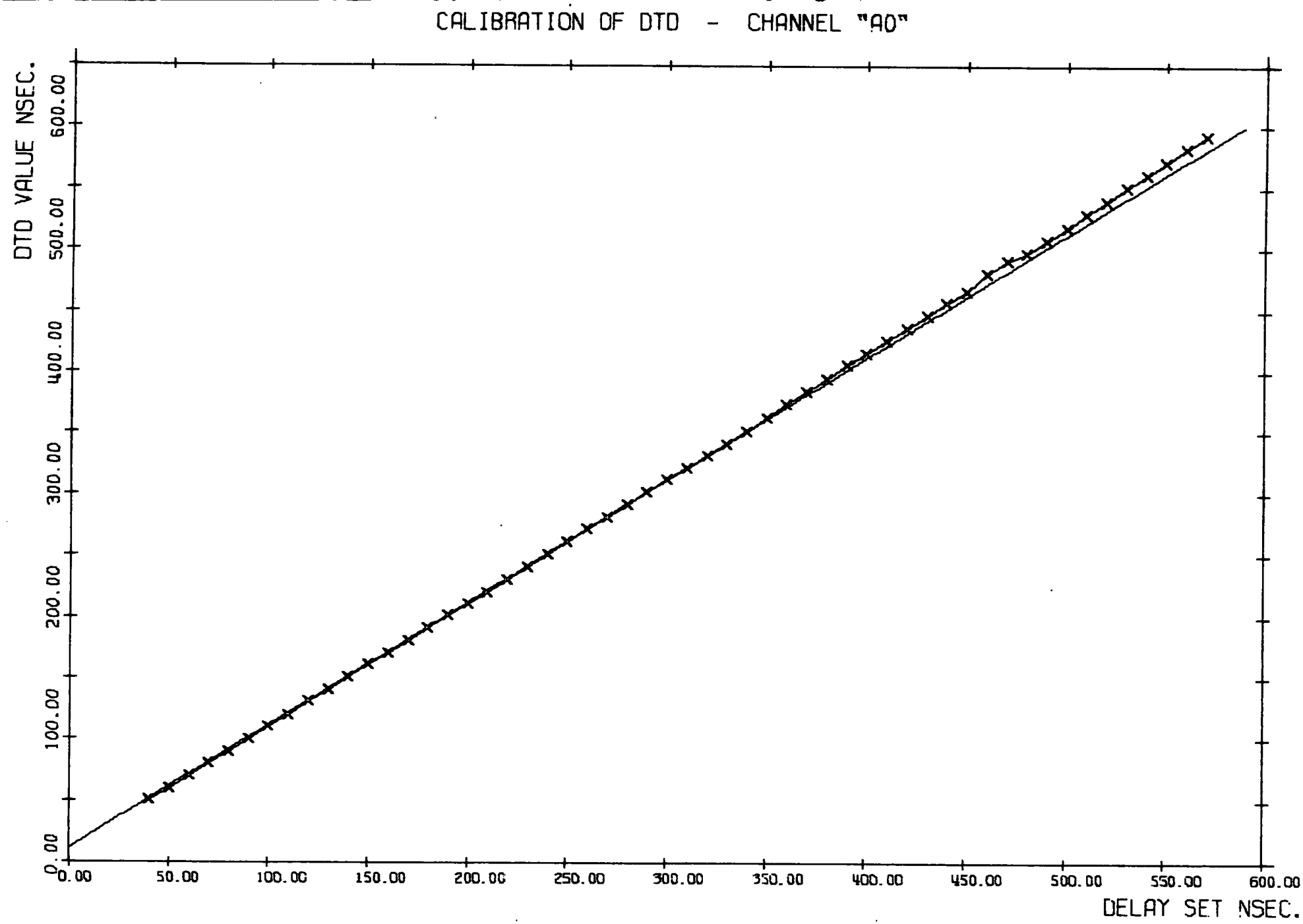

FIG. 4.22: TYPICAL CALIBRATION CURVE OF A DTD CHANNEL

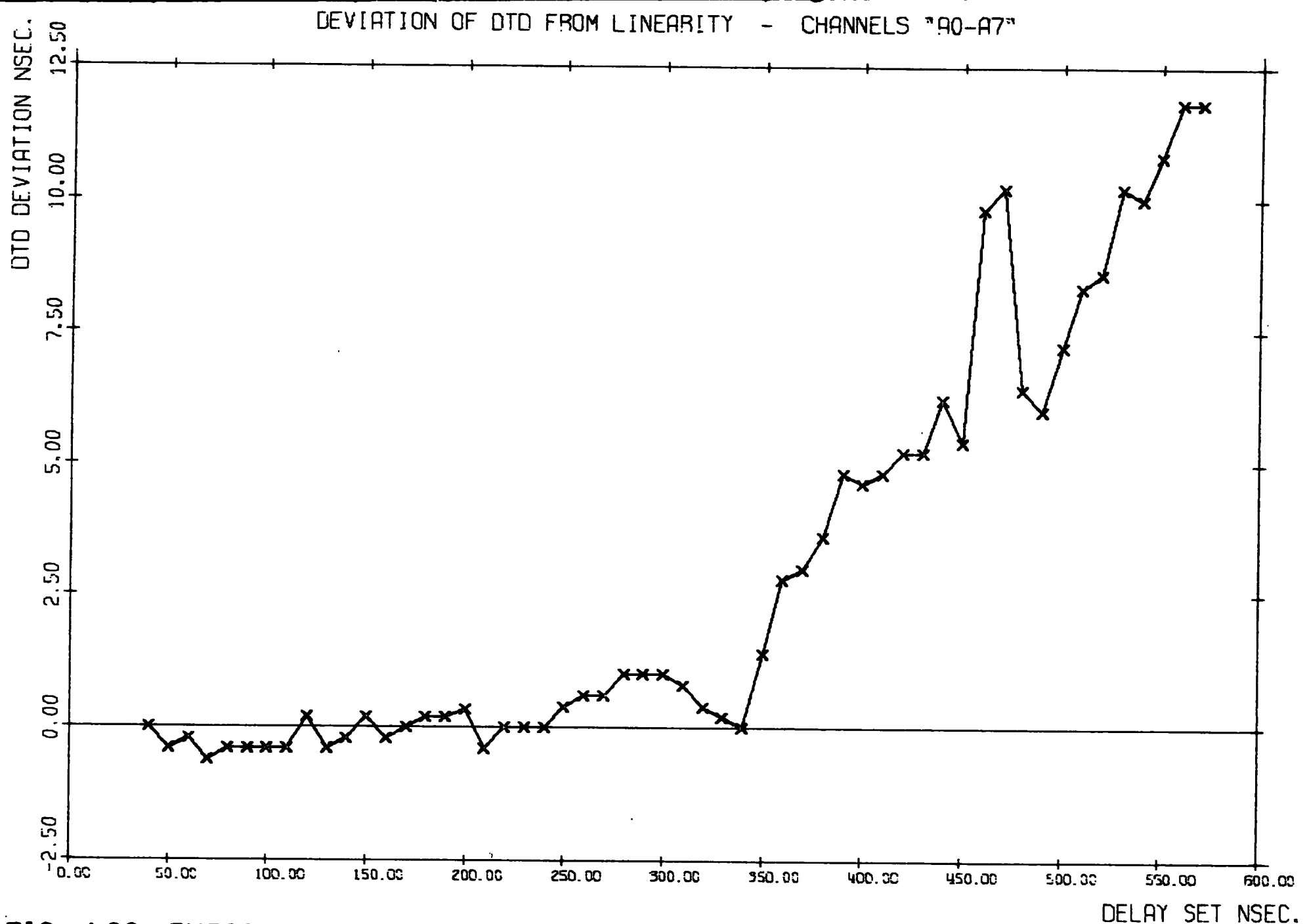

FIG. 4.23: TYPICAL DEVIATIONS OF AN OCTAL DTD FROM LINEARITY

the counting room. Channel A0 was taken as the absolute length. The cables were left open ended at the ring end and a pulse generator attached to A0 and the other channels in turn through a resistive split. The outgoing and reflected signals were viewed on a calibrated oscilloscope using LEMO T's after the resistive split outputs. The length of cable A0 was found to be 160.5 $\pm$ 0.5 ns and all other channels were found to be within $\pm$ 0.5 ns of this value.

A check was also made on the differences in arrival times of pulses input to the pre-amplifiers and passed to the counting room and discriminated, the discriminator outputs being measured relative to channel A0. All channels were within $\pm$ 1 ns of A0.

A final check was made on the time slewing caused by variable size inputs to the pre-amplifiers. Using a pulse generator and resistive split followed by attenuators the pulse on channel A0 was kept constant whilst the input to channel A1 was varied from 1 to 30 mV. The time slewing was less than 3 ns over the whole range, as shown in figure 4.24, but the maximum rate of slew occurred at the lower input values corresponding to likely chamber pulses. The time slewing caused by varying the attenuation of the pulse to one channel only, and not the other, was less than $\pm$ 0.2 ns over the range.

The difference in arrival times of the start pulses and the C10 pulses were measured at the entry points to the DTD's and DTD Controller but with the C10 delay (of various values throughout the runs) removed. The LED pulsing system was used once again to enable a study to be made of variable chamber pulse heights

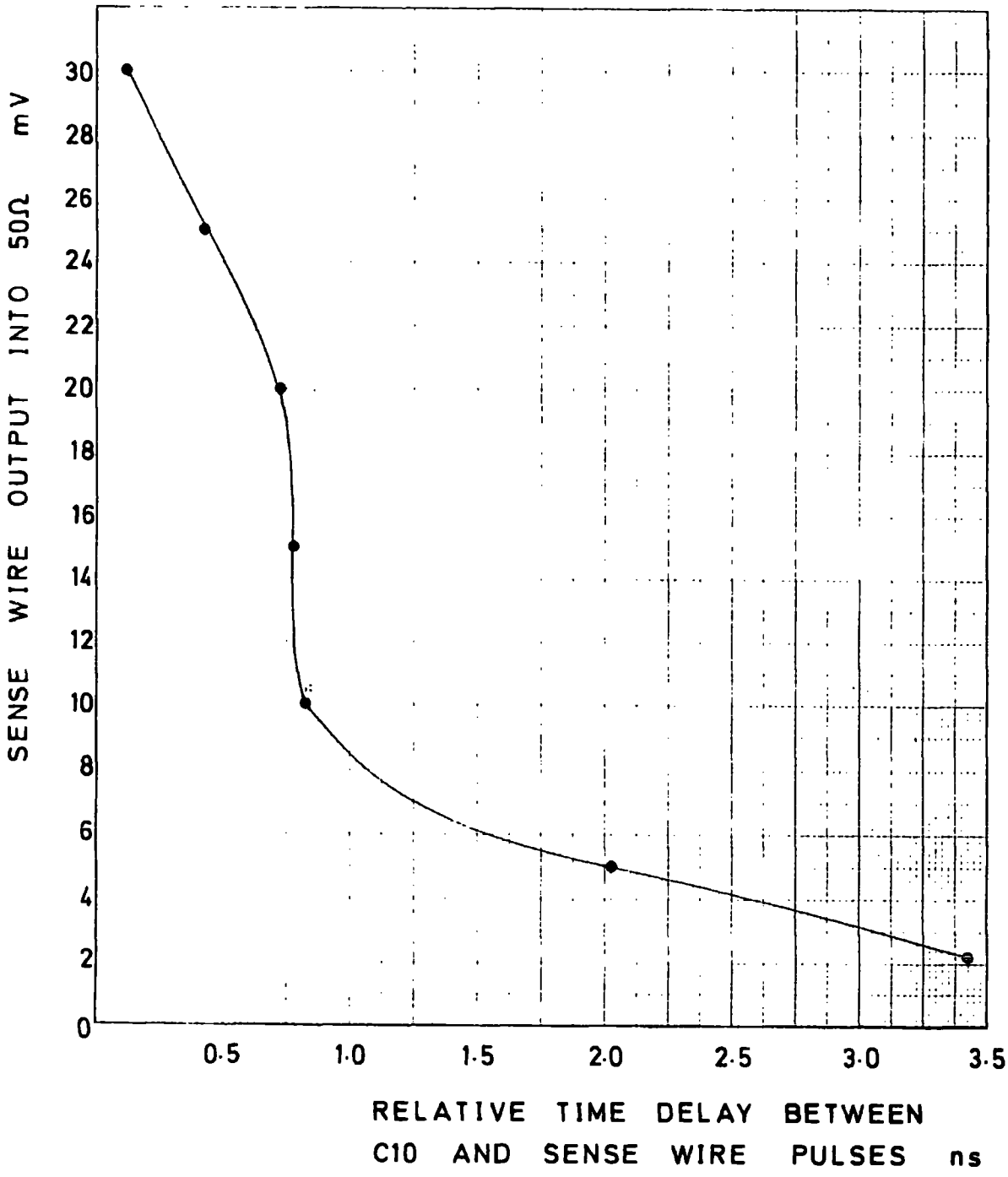

FIG. 4.24 : TIME JITTER DUE TO VARIATION OF SENSE WIRE PULSE HEIGHTS

and C10 pulse heights. Over all possible combinations of the two variables the sense wire starts were found to arrive 24 $\pm$ 2 ns before the C10 stops, account having been made for the 3 ns delay in the scintillator of the shower counter. To obtain the overall maximum digitizable drift time available with a particular system the 11 ns DTD offset and C10 delay cable length must be added to the above value. Remembering the inverse timing method the drift time then becomes equal to the maximum digitizable time minus the DTD time recorded plus the Controller vernier. All such calculations were performed in the software.

4.6 System Operation

Before each (g-2) experimental run the chamber potentials were checked and each cell tested for breakdown. Any bad chambers were removed from the system and cleaned. Often when gaseous or electrical breakdown occurred in one cell the resulting U.V. light produced photo-electrons in neighbouring cells thus producing apparent breakdown in those cells also. If the bad cell's input to its pre-amplifier was removed, i.e. the cell was "floated", then the sense wire potential rose to the local field value and the breakdown was prevented from occurring in that cell. Also the neighbouring cells were then found to operate normally.

The chambers operated better with age, a constant applied potential of 3.0 kV across the divider network being possible during the later cycles. This was probably due to any impurities in the chambers being totally outgassed and also that all defective

cells had been cleaned, or permanently floated if they were in non-important detection positions in the array.

Apart from periodic checks for breakdown and monitoring of the gas flow through the chambers it was found to be possible to run the chambers untouched for a period of several days.

4.7 Data Acquisition and Analysis Software

The HP2100 computer was a 16-bit machine and the data was written on to the magnetic tape using a standard CERN blocking technique[20,21] in order that off-line analysis could be performed using FORTRAN on any computer with the aid of dedicated unblocking routines.[22] The acquisition program was written at CERN in ASSEMBLER.

For the off-line analysis the standard event block had a variable length with the DTD data depending upon the number of hits recorded in the event. However the first fourteen elements were constant and are listed in table 4.1. All are either self-explanatory or have been described above. The possible values for energy and EDM status recorded by the element corresponding to the Pattern B unit are documented in table 4.2.

Knowledge of the above and the system calibrations allowed the off-line analysis to be performed to the accuracy of the data obtained.

TABLE 4.1

Array Element	Description
(1)	= 101 = number of elements in array.
(2)	= Number of words in event excluding self.
(3)	= LAM number. Always constant for this system - can be ignored.
(4)	= Event number generated by acquisition program.
(5)	= Pattern B register, gives energy and EDM information.
(6)	- - -
(7)	- - -
(8)	= 1 MHz clock scaler for event occurrence time.
(9)	= 50 MHz clock scaler for event occurrence time.
(10)	- - -
(11)	- - -
(12)	- - -
(13)	- - -
(14)	= DTD Controller vernier.
(15)	= DTD times.
	"
	"

Number of further elements depends upon number of hits in array.

TABLE 4.2

Pattern B inputs

2^7 = 128 EDM DOWN counter coincidence

2^6 = 64 EDM UP counter coincidence

2^5 = 32 EDM coincidence signal

2^4 = 16 D)
2^3 = 8 C)
2^2 = 4 B) (g-2) Energy level pulse heights
2^1 = 2 A)
2^0 = 1 T10)

Energy levels only		Energy levels + EDM information		
0	No signal. Energy fault.	0	No signal, energy fault.	
1	> 0 MeV	1	> 0 MeV	
3	> 900 MeV	3	> 900 MeV	NO
7	> 1800 MeV	7	> 1800 MeV	COINCIDENCE
15	> 2200 MeV	15	> 2200 MeV	
31	> 2800 MeV	31	> 2800 MeV	
		96	No signal, energy fault.	
		97	> 0 MeV	
		99	> 900 MeV	
		103	> 1800 MeV	COINCIDENCE
		111	> 2200 MeV	UP
		127	> 2800 MeV	
		160	No signal, energy fault.	
		161	> 0 MeV	
		163	> 900 MeV	
		167	> 1800 MeV	COINCIDENCE
		175	> 2200 MeV	DOWN
Any other values represent a pulse height bit error.		191	> 2800 MeV	
		224	No signal, energy fault.	
		225	> 0 MeV	
		227	> 900 MeV	
		231	> 1800 MeV	COINCIDENCE
		239	> 2200 MeV	UP AND DOWN
		255	> 2800 MeV	

REFERENCES

1) Bailey, J. M., Bassompierre, G., Borer, K., Combley, F., Hattersley, P., Lebee, G., Petrucci, G., Picasso, E., Pizer, H. I., Rinolfsson, O., Tinguely, R., CERN NP Internal Report 70 - 13

2) Cunningham, R. A., Taylor, D. G., Walker, R. P., Daresbury Laboratory Preprint DL/P 274 (Instrumentation) May 1977 submitted to Nucl. Instr. Meth.

3) Engster, C., Tarle, J. C., Verweij, H., CERN NP Internal Report October 1973

4) Verweij, H., Proc. of Inter. Conf. on Instr. for High-Energy Physics, Frascati (1973) 616

5) Sauli, F., CERN NP Internal Report 73 - 12

6) Cittolin, S., HAMBI CERN EP DHG Report 18/12/75

7) Scharff-Hansen, P., CERN EP Report HP/76-1/1 11/2/76

8) Cittolin, S., CERN EP Report HP/76-2/1 12/2/76

9) Bailey, J. M., Borer, K., Combley, F., Drumm, H., Krienen, F., Lange, F., Picasso, E., von Rüden, W., Farley F. J. M., Field, J. H., Flegel, W., Hattersley, P. M. Nature 268 (1977) 301

10) Comyn, M., Hedge, A. R., Durham University Internal Report NI 76 - 7

11) Comyn, M., Hedge, A. R., Durham University Internal Report NI 76 - 18

12) Engster, C., Verweij, H.,
Drift Time Digitizer Type DTD 164
Provisional Specification
CERN NP 20/6/75

13) van Koningsveld, L., Verweij, H.,
DTD Controller Type 211 Provisional Specification
CERN NP 20/6/75

14) van Koningsveld, L., Verweij, H.,
Fan-Out 12 Fold, N-4189 Provisional Specification
CERN NP 3/10/75

15) Lange, F., CERN EP Private Communication

16) Engster, C., CERN EP Private Communication

17) Breskin, A., Charpak, G., Sauli, F., Atkinson, M., Schultz, G.,
Nucl. Instr. Meth. 124 (1975) 189

18) Sauli, F., CERN NP Internal Report 75 - 13

19) Field, J.H., Lange, F., von Juden, W.,
Nucl. Instr. Meth. 143 (1977) 227

20) Ogilvie, J.,
Standard Format for Data Recording on Magnetic Tape
CERN EP Report HP/76-4/1 9/3/76

21) Rimmer, E.M.,
General Purpose HP-CAMAC Data Handling Facility
CERN NP DHG October 1973

22) Griffiths, L., Hopson, B.,
EVENT 360/44 Version
CERN NP DHG 14/11/74

CHAPTER 5

CALIBRATION OF THE (g-2) CHAMBER DRIFT VELOCITIES

5.1 Introduction

Before any track reconstruction may be attempted, using the data obtained, an accurate knowledge of the drift velocities in each of the chamber cells is required.

For more conventional drift chamber applications, either operating with no magnetic field present or in a homogeneous field, accurate scanning methods may by employed to determine the drift time - distance relationship across each cell. However with the unique form of the (g-2) fringe field no valid prior calibrations could be attempted before installation of the chambers in the Muon Storage Ring.

This chapter described the results obtained with prototype chambers using various systems and then discusses the most straightforward method available for calibrating the (g-2) chambers. This involved measuring the maximum drift time in each cell and comparing the results obtained with the expected theoretical results. The lack of anticipated accuracy is explained with reference to the choice of data used in the analysis and the magnetic and electric fields present over the active chamber volume. The fields calculated by the author are different from those originally used to choose the field compensation parameters used in the chambers. Contributions from the spurious double firing of digitization channels, as discussed in Chapter 4, were removed and the best overall estimates of the drift velocities are presented.

An effect was observed which was attributed to a splitting of the primary ionization at cell boundaries causing simultaneous drift of electron swarms from a single track towards two adjacent sense wires. The mechanisms involved are postulated and the results used to derive further estimates of individual cell drift velocities.

Finally an experimental system is suggested that could have provided an accurate calibration of the (g-2) chambers.

5.2 Calibration Techniques

The most accurate technique used in the calibration of drift chamber velocities is to precisely scan a chamber across a well collimated beam to determine the drift time - distance (space - time) relationship of a cell. The zero timing trigger and location of the incident beam is determined by a rigid scintillator telescope and, sometimes, also a pair of identical drift chambers to define a pencil beam. Such a system is outlined at the end of this chapter. Not only does this method provide a value for the maximum drift time in a cell, and thus the drift velocity from a knowledge of the drift distance, but also it indicates any non-linearity in the space - time relationship. Non-linearity may be caused by variations in a non-saturated drift field across a cell, causing variation of the drift velocity, or by local defects in the mechanical construction of the chamber. Thus the drift distance, x, covered in time t, whilst drifting with velocity w is given by:

$$x = \int_0^t w(t)\, dt \qquad (5.1)$$

For a constant drift velocity this reduces to $x = wt$ and a linear space - time relationship results. Obviously it is preferable to operate a chamber with a saturated drift velocity so that any local defects have no effect upon the space - time linearity and calibration is straightforward.

Another method which reveals the maximum drift time in a cell and the drift velocity, but not a detailed space - time relationship, involves the use of the integral spectrum of the drift times in a cell. A uniform flux is required across the cell and may be provided by cosmic rays, a radioactive source or preferably a diffuse high energy beam. A scintillator is used to determine the zero timing triggers and the drift times are binned from zero to the maximum drift time to produce the frequency distribution dN/dt defined by:

$$\frac{dN}{dt} = \frac{dN}{ds} \cdot \frac{ds}{dt} = \frac{dN}{ds} w(t) \qquad (5.2)$$

where s is the distance along the sense wire plane. If the flux is uniform throughout the cell the distribution is proportional to the drift velocity $w(t)$. Integration of the distribution reveals the $s = s(t)$ relationship. Figure 5.1 shows the theoretical distributions expected with ideal conditions. The slow rise to the flat-top in the dN/dt distribution is due to the reduction in pulse height around the sense wire introducing some inefficiency and also to the lower drift velocity in the high field region. By the nomenclature the particle traverses the chamber at time t_0 and is detected at time t. An initial peak in the distribution occurs for angled tracks which may erroneously be interpreted as a higher drift velocity around the sense wire. It is in fact due to the radial path taken by the electrons close to the sense

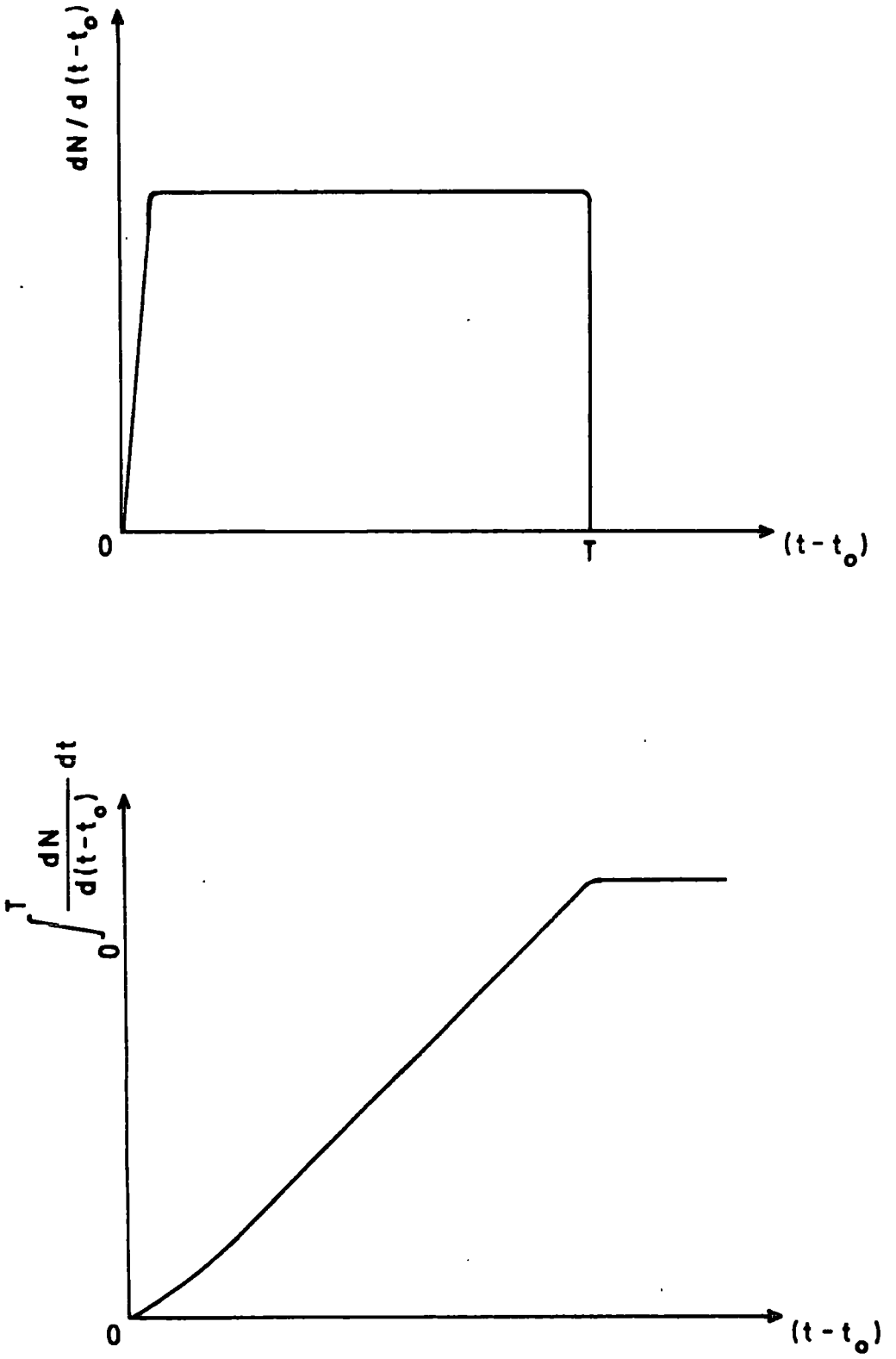

FIG. 5.1: THEORETICAL DIFFERENTIAL AND INTEGRAL DRIFT TIME SPECTRA

wire having initially drifted along the cathode plane, as discussed in Chapter 2. With a uniform flux across the chamber this geometrical effect causes an apparently higher flux around the sense wire as the electrons have a shorter distance to drift per unit distance in the sense wire plane when moving radially to the sense wire rather than parallel to the cathode plane. A similar effect occurs in a magnetic field for angled tracks and also with incorrect compensation which causes the electrons to travel in curved trajectories and nearly reach the cathode plane before moving radially inwards towards the sense wire.

This method has two severe limitations, however, which are especially prevalent in the (g-2) application where such a method was used. If the flux is not uniform across the cell the dN/dt distribution no longer has a flat-top and the integral spectrum does not produce a constant slope for a saturated drift velocity. Due to the left-right ambiguity of the cell the distributions are the sum of the two halves so the flux must be constant from potential wire to potential wire. Thus for a non-uniform flux the results indicate an apparent non-linearity in the space - time relationship and therefore a variable drift velocity, which may not be the actual case. For an ideal chamber with a saturated drift velocity, no magnetic field present and particles incident orthogonally to the sense wire plane the cut-off at time T, the maximum drift time, for the dN/dt distribution is rapid as shown in figure 5.1. This is due purely to geometrical considerations as indicated in figure 5.2a. However if the chamber is operated in a magnetic field, and electric field compensation is applied, a cell may be efficient over a length greater than the sense wire/potential wire spacing as shown in figure 5.2b. Thus the cut-off may not be quite as rapid as in the zero

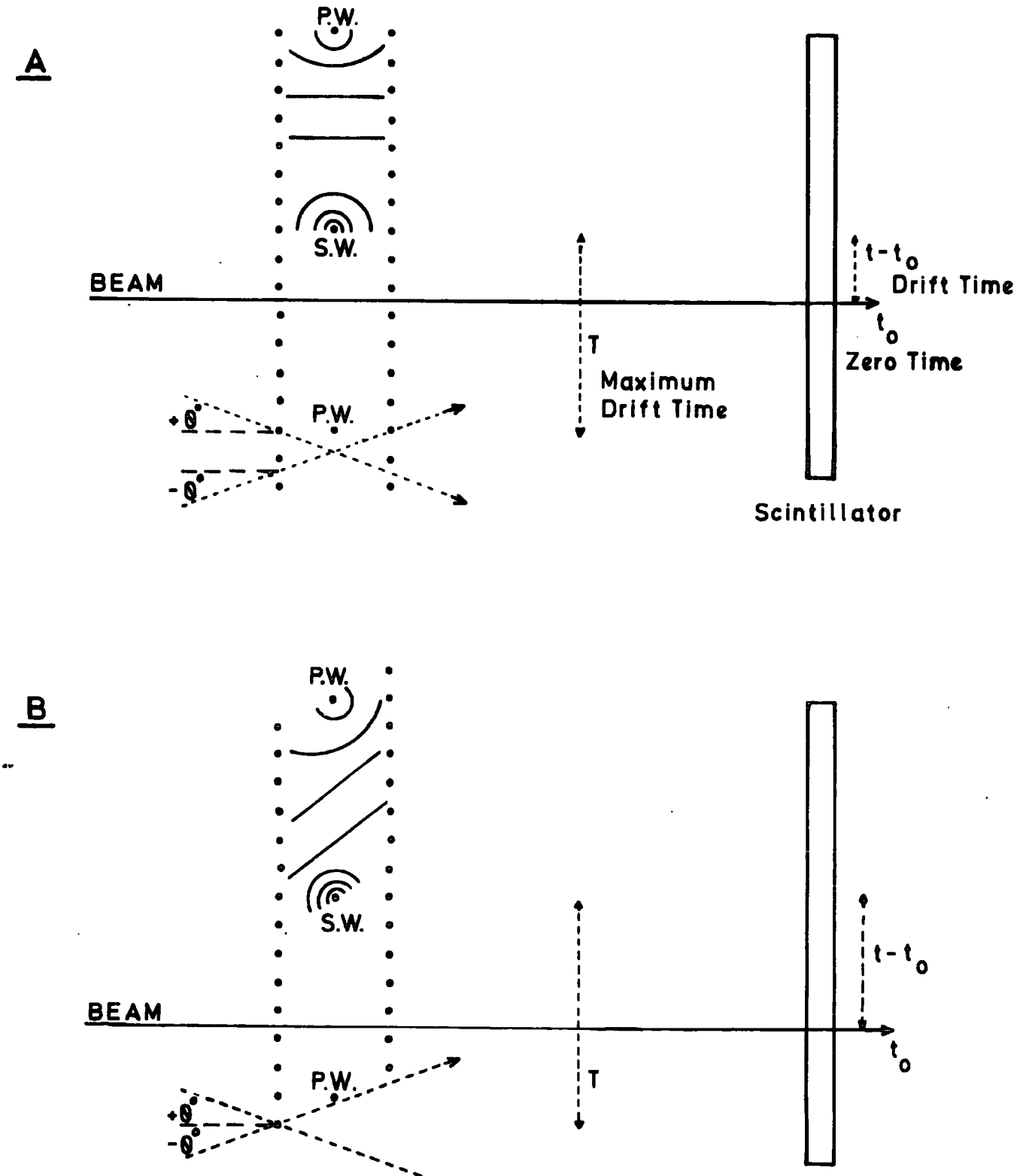

FIG. 5.2 : EFFICIENT CELL DETECTION REGIONS WITHOUT (A) AND WITH (B) ELECTRIC FIELD COMPENSATION FOR PARTICLES INCIDENT NORMALLY AND AT ANGLES $\pm\theta^{\circ}$

field case and the maximum drift time, T, now refers to a greater drift length.

A similar effect is present in both cases for particles incident non-orthogonally to the sense wire plane. Such tracks incident at $\pm\theta^{\circ}$ are represented by dotted lines in figures 5.2a and b. Using the precise scanning method the chambers would appear to be efficient over longer detection lengths in the sense wire plane due to the greater acceptance at the cell boundaries. This has been demonstrated by Breskin et al.;[1] figure 5.3 shows their results for the increase in the efficient detection region, measured along the sense wire plane, using a chamber operated in a magnetic field of 10 kG with exact electric field compensation. For particles incident at -42°, that is in the opposite direction to the electric field tilt of $+32^{\circ}$, the cell was 25% efficient over a 2 mm longer distance than for particles incident orthogonally. However, as described in Chapter 2, for inclined tracks the recorded drift times correspond to the electron swarms moving the shortest distance from the track to the sense wire along the field lines and not to the intercept of the track on the sense wire plane. Hence the maximum drift time recorded corresponds to the distance along the cathode plane to the track. Therefore the integral spectrum method must be used with care and a full understanding of the chamber geometry is required to accurately interpret the results.

Any localized inefficiencies in the chamber, especially at the cell boundaries, distort the dN/dt distribution and mask the true cut-off value.

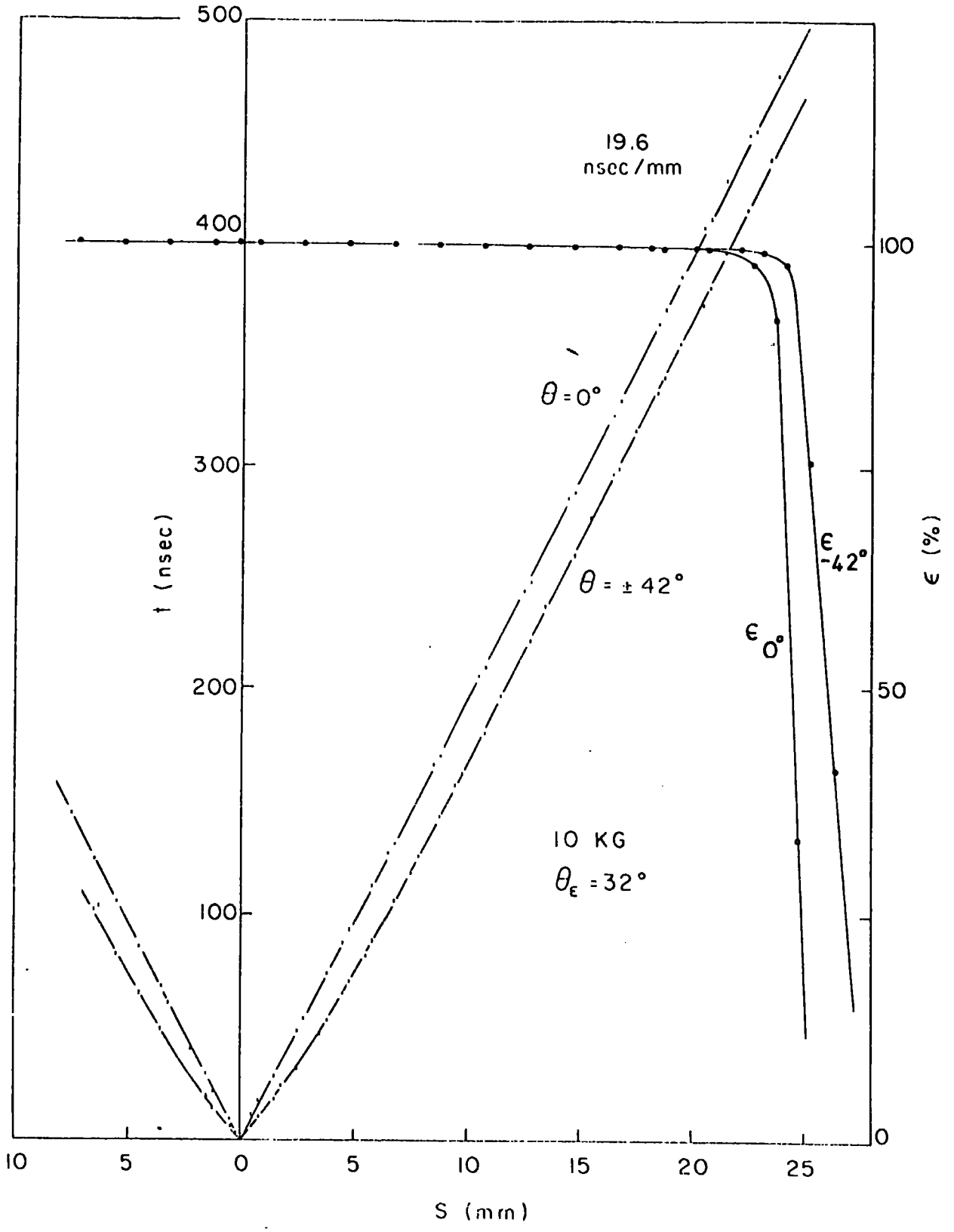

FIG. 5.3 : DEMONSTRATION OF INCREASE IN EFFICIENT DETECTION REGION OF A CELL FOR INCLINED TRACKS

5.3 Results of Chamber Calibrations

The calibrations derived from prototype and production chambers using various systems at the Daresbury Laboratory could only be used as a guide as the experimental conditions in no way represented the actual (g-2) fringe field. The method of binning whole cell drift times had to be used to calibrate the (g-2) chambers in the Muon Storage Ring as historically a precise scanning method could not be attempted. In the final section of this chapter a method is proposed which could have been used to calibrate the chambers accurately if a single (g-2) magnet had been available for use in a test beam system.

5.3.1 Initial Calibrations using Prototype Chambers

Several series of calibrations were performed at various stages of the (g-2) drift chamber development. Although of similar cell design to the final chambers, many of the prototypes had different operating parameters and were never calibrated in the (g-2) fringe field.

Most of the early work was performed in the absence of magnetic fields and thus no electric field compensation was applied. Using various drift fields and either collimated beta sources in the laboratory, or the positron Test Beam at the Daresbury Laboratory, the chambers were shown[2] to have reasonably linear space - time relationships with only small perturbations around the sense wires. The curved end also proved to have a reasonably linear relationship but with reduced spatial resolution. However an important point to note is that all chambers had clear mylar windows for ease of inspection and not the earthed aluminized mylar windows as in the final chambers. As shown in

section 5.4.2 the addition of the earthed planes had a dramatic effect upon the drift field in the curved end cell.

Tests using a 7.5 kG magnet and a prototype chamber suggested that an electric field tilt of two wire-spacings provided efficient compensation at such fields.[2] As all tests were performed at lower magnetic field values than those experienced in the majority of the (g-2) chamber cells, the results are not discussed in detail in this thesis. However they did suggest that a suitable compensation mechanism could be realised for the (g-2) chambers which would allow efficient detection and a linear space - time relationship across each cell.

The theoretical and experimental field parameters used to determine the final compensation mechanism, discussed in Chapter 3, led to estimates of the expected maximum drift times in each of the chamber cells. Figure 5.4 shows the physical cell layout in a chamber and the corresponding drift time values assuming linear drift time - distance relationships.

A set of three small drift chambers, of similar cell geometry to the (g-2) chambers, were operated[3] in magnetic fields of up to 13.5 kG in the Daresbury Laboratory Test Beam. Although the magnetic fields in no way represented the (g-2) case, the results suggested that the detection efficiency would be low for long drift lengths. The chambers were operated with a three wire-spacing field tilt and a drift field in the sense wire plane of 600 V cm^{-1}. As the magnetic field in the (g-2) chamber cells closest to the vacuum tank was higher than 13.5 kG the effect would be exacerbated. An increase of the electric field to 1000 V cm^{-1} improved the detection efficiency at longer drift lengths. However by this stage the (g-2) chambers were operational and as stated

in Chapter 3 the potentials opposite the sense wires had already been reduced to prevent spontaneous breakdown. Hence any increase in the field, although desirable, would have been difficult to implement without further distortion of the compensation mechanism. Figure 5.5 shows the expected maximum drift times in the (g-2) chambers derived from the drift velocities recorded in the small test chambers with extrapolation to the (g-2) fields. Note the longer drift times at high magnetic fields, probably indicating not only the expected decrease in drift velocity but also drift motion in a curved path rather than parallel to the sense wire plane. This is due to the incorrect electric field compensation which explains the lowering of detection efficiency at long drift lengths as the electron swarms are lost from the active chamber volume. However the errors in the quoted values are large due to the limited data recorded and the lack of a uniform flux across the chamber cells.

5.3.2 Calibrations Derived from the (g-2) Data

As stated the calibrations had to be performed in situ using the actual data recorded by track detection. Figure 5.6 demonstrates the variety of tracks that could produce a trigger in shower counter C10, the chamber cells being indicated in chamber II. The geometrical acceptance of the array for the expected range of electron energies is also shown. It is apparent that the cells closest to the vacuum tank received the highest number of hits.

The initial analysis was performed by binning all the recorded drift times, irrespective of whether they referred to genuine tracks. As the chambers were not staggered there was no resolution of the left-right

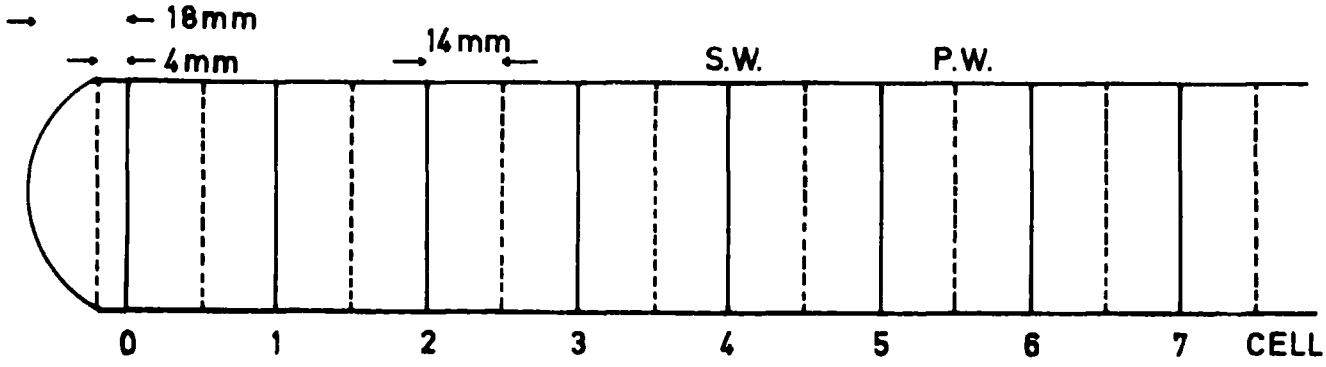

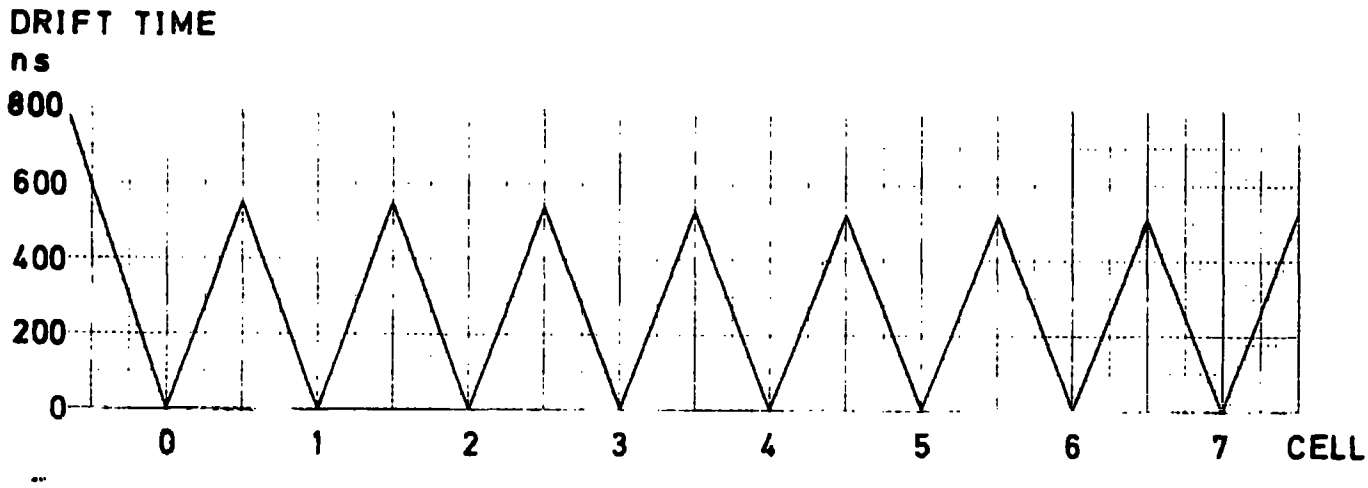

FIG. 5.4 : PHYSICAL LAYOUT OF CHAMBER CELLS AND THEORETICAL DRIFT TIMES

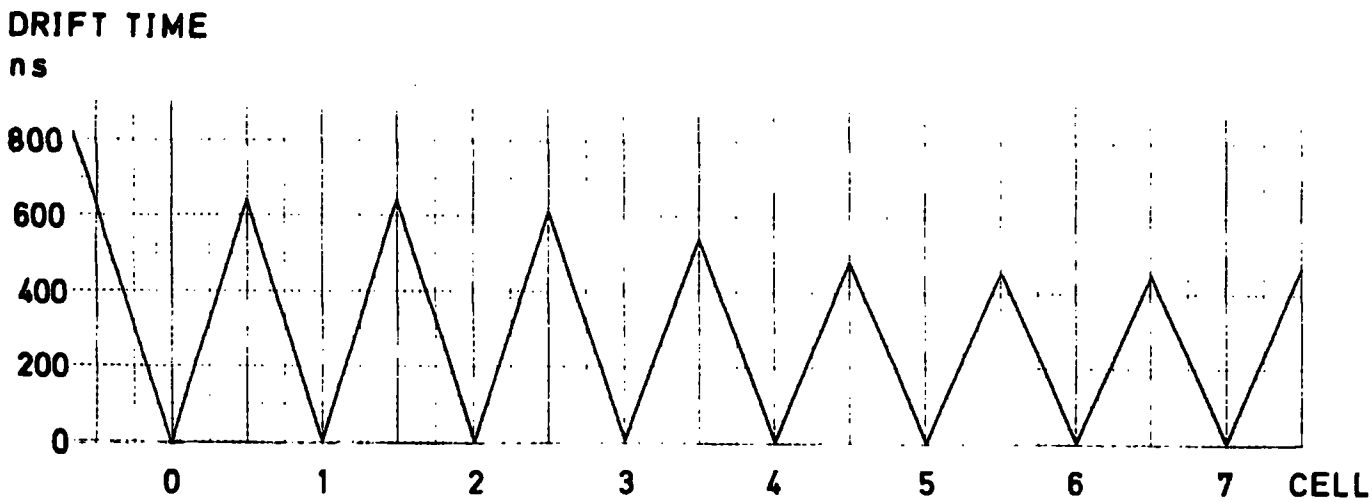

FIG. 5.5 : EXPERIMENTAL DRIFT TIMES DERIVED FROM SMALL EXPERIMENTAL CHAMBERS

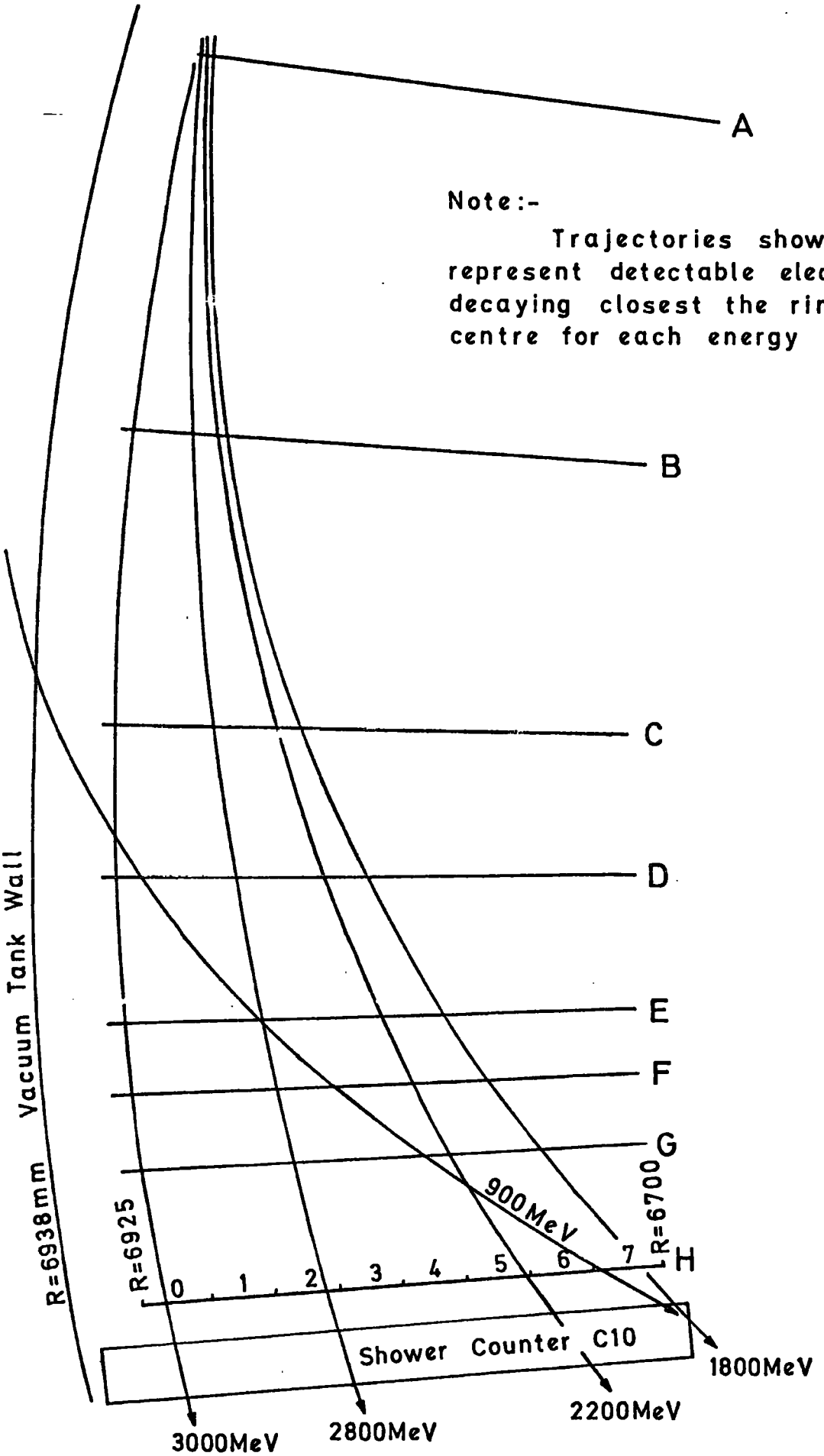

FIG. 5.6 : GEOMETRICAL ACCEPTANCE OF ARRAY FOR ALL DECAY ELECTRON ENERGIES

ambiguity and drift times from either side of the respective sense wires were summed. In addition the data from all chambers were summed as it was assumed that little variation in drift velocity occurred between corresponding cells in the eight chambers. Figure 5.7 presents the results of the analysis. Apart from the lack of the expected flat-tops to the distributions other points may be noted. Firstly the maximum digitizable drift time of the system in use was 676 ns which explains the sharp cut-offs in some of the distributions, which may otherwise have been interpreted as the maximum drift time cut-off. Also as the DTD's had a full digitizable range of 768 ns the negative drift times extending to -92 ns were valid due to spurious hits incident upon the array before the C10 timing trigger. This allowed an average background noise to be calculated and is displayed as a dotted line. The fall-off in particle flux from cell "0" to "7" is evident.

The total number of hits in each cell was calculated and a least squares fit using a third order polynomial was performed to deduce the form of the decrease in flux across the cells. The resultant curve is displayed in figure 5.8 with its four coefficients. In turn a third order polynomial was derived which when integrated over the respective cell co-ordinates, measured in millimetres from the curved end (all cells assumed to be 28 mm long), yielded the number of hits in that cell as given by the least squares fit. Figure 5.9 shows the plot of this function which, if divided into 1 mm bins, represented the expected number of hits across each cell assuming that the flux fell uniformly as described by figure 5.8. As described in section 5.2, the method of binning the drift time frequencies to derive the drift velocity relies upon a uniform flux across the chamber. As the left-right ambiguity was

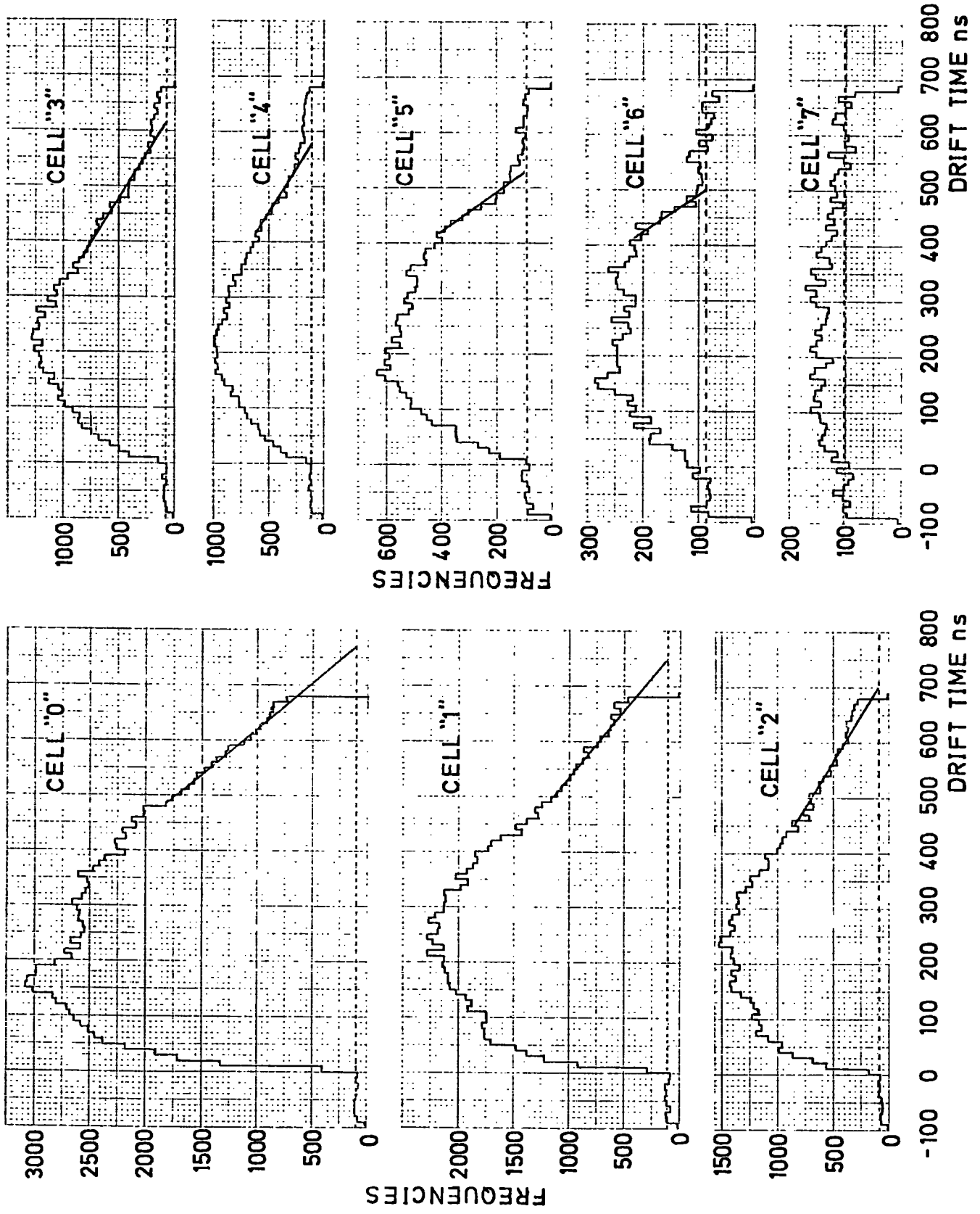

FIG. 5.7: DRIFT TIME DISTRIBUTIONS FOR EACH CELL SUMMED OVER ALL CHAMBERS FROM ANALYSIS OF ALL RECORDED HITS IN ARRAY

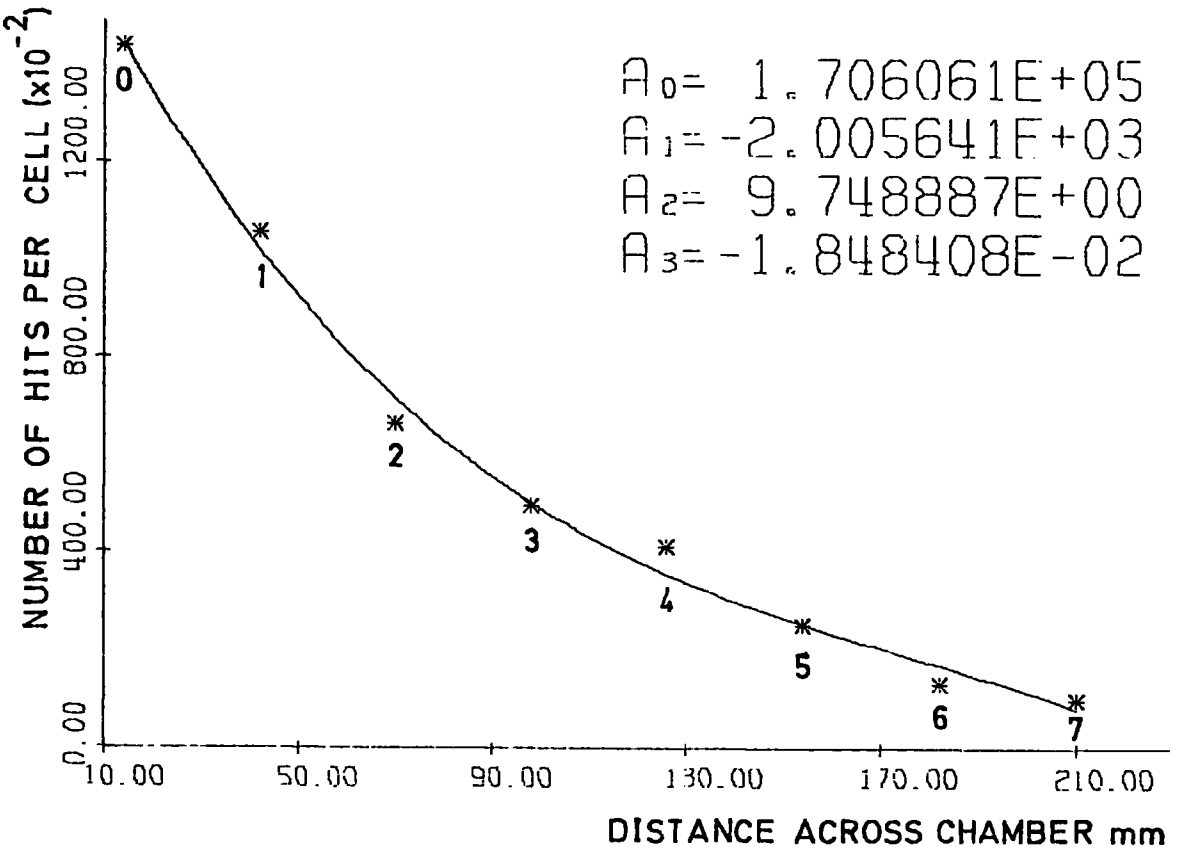

FIG. 5.8: THIRD ORDER POLYNOMIAL LEAST SQUARES FIT TO NUMBER OF HITS PER CELL

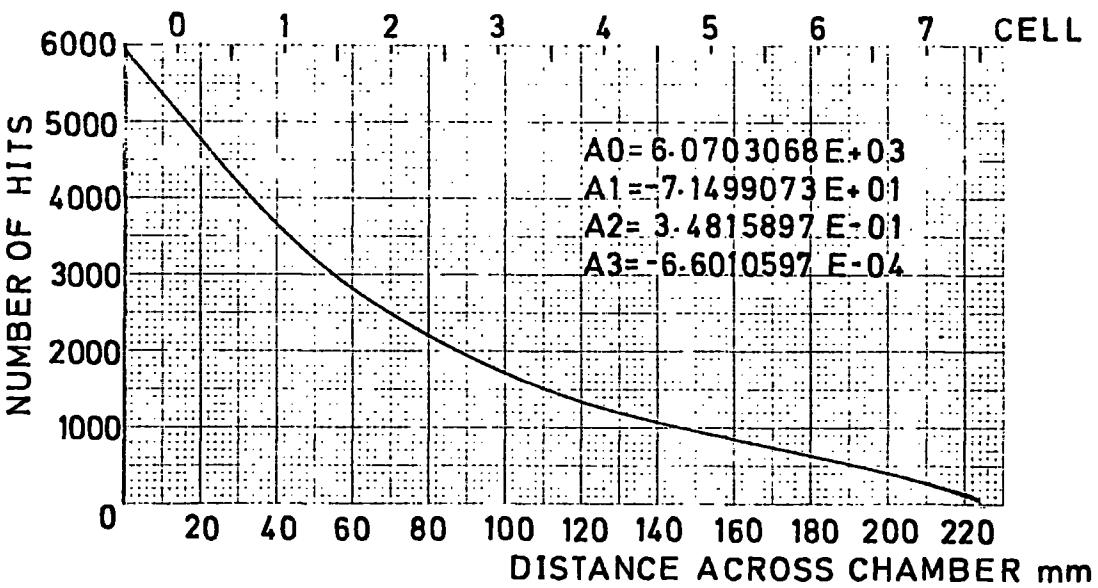

FIG. 5.9: THIRD ORDER POLYNOMIAL REPRESENTING TOTAL FLUX OF ELECTRONS ACROSS CELLS OF ARRAY

not resolved the flux across a cell would only appear uniform on summing the two halves if the slope of the flux function was constant. Figure 5.9 illustrates that a constant slope did not exist so the summed frequencies to the left and right of each sense wire were computed for each cell in 1 mm bins and are shown in figure 5.10. The maximum variation in bin frequency across a cell was less than 1.5% of the average bin frequency so a near uniform flux could be assumed. However it must be noted that the theoretical distributions must be compared to the experimental data with caution as several assumptions have necessarily been included in their determination. Their shapes may only be compared if constant drift velocities, 100% detection efficiencies across the cells and exact detection cut-offs at the cell boundaries are assumed. Any extension of efficient detection across the cell boundaries due to tilted electric fields or angled tracks is not included. Nevertheless the idealized distributions do indicate that if the chambers were fully efficient and the drift velocities in each cell were constant then the experimental distributions would have flat-tops. An initial peak and a slower fall-off at the maximum drift time would be expected due to the geometrical factors mentioned above.

Several conclusions may now be drawn from the distributions shown in figure 5.7. Firstly as flat-tops do not exist at any stage across the distributions it is obvious that the detection efficiency was not 100%. The expected inefficiency around the sense wires is observed and the detection efficiency appears to be high for about half the cell lengths. Beyond this the efficiency falls dramatically and for the cells in the highest magnetic field close to the vacuum tank the maximum drift time appears to be in excess of the 676 ns recordable. In cells 3, 4 and 5 the distributions fall and then plateau above the noise level at high

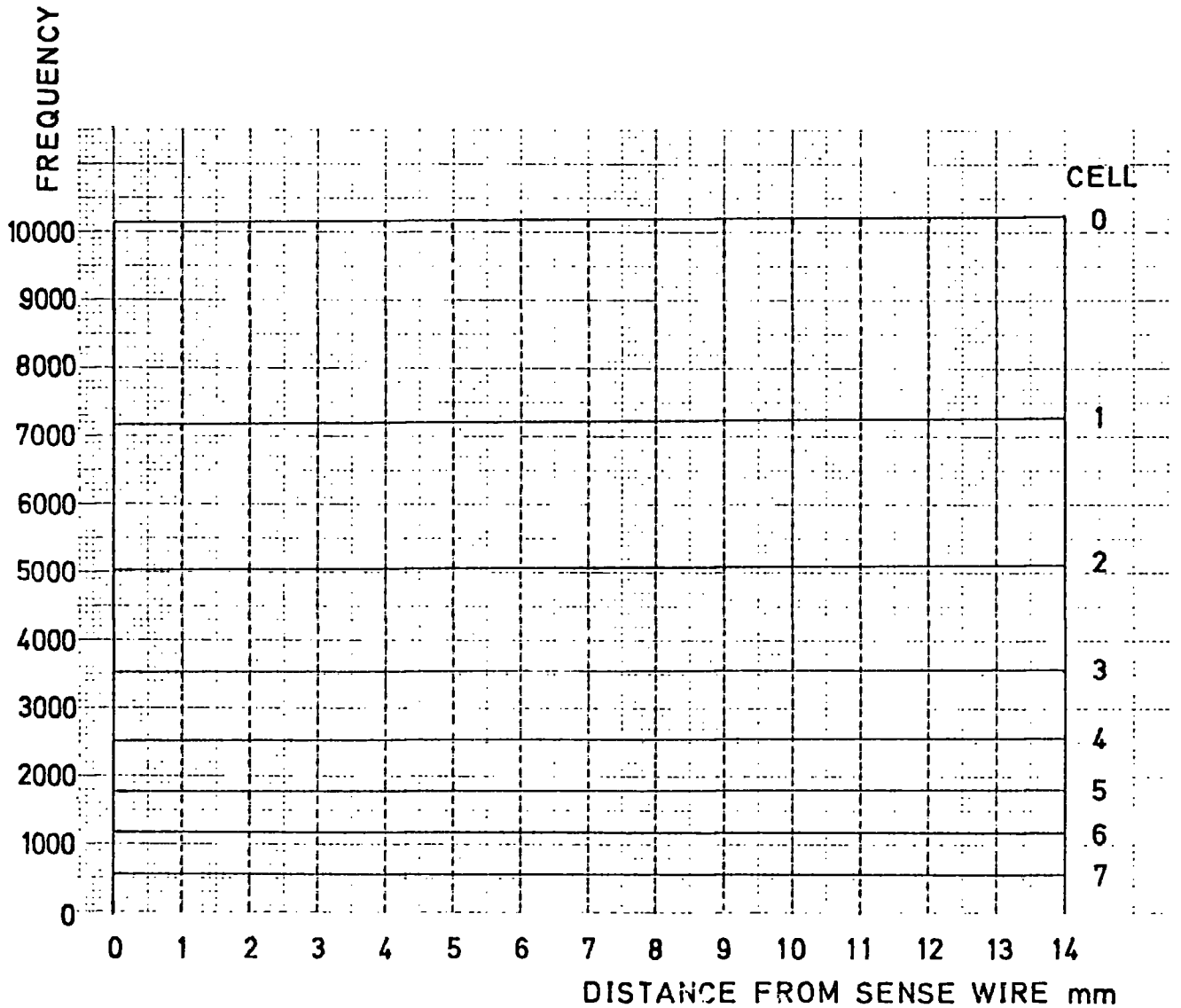

FIG. 5.10 : THEORETICAL DRIFT TIME FREQUENCY DISTRIBUTIONS IN 1mm BINS ACROSS EACH CELL DERIVED FROM TOTAL FLUX POLYNOMIAL

drift times indicating an extension of low efficiency detection beyond the potential wire. Other effects exist which have an unknown contribution to the form of the distributions. Probable non-saturation of the drift field alters the drift velocity in any localized low field regions. The observed inefficiencies are probably due to non-exact field compensation causing the electron swarms to travel in curved paths, rather than parallel to the sense wire plane, with subsequent loss of the swarms at longer drift distances. Also as the maximum drift times fall towards the ring centre it is likely that the drift velocities on the left and right-hand side of the sense wires are different. As indicated in figure 5.7, by extrapolating the fall-offs of the distributions to the noise levels the maximum drift times in each cell may be roughly assigned as 770, 750, 700, 615, 580, 530 and 500 ns for cells "0" to "6" respectively. The data in cell "7" is inadequate for firm conclusions to be drawn.

The shapes of the distributions demonstrate that the assumption of uniform particle flux reduction across the chambers and the use of the number of hits in each cell to deduce the theoretical distributions were incorrect. However an increase to 100% efficiency would have raised the number of hits in each cell by similar factors and the flux function would have had a similar form.

5.3.3 Study of Multiple Hits on a Wire

The distributions of figure 5.7 displayed all the data stored on tape which included not only spurious hits not associated with the timing trigger and breakdown noise but also multiple firings of the digitization channels due to the amplifier and discriminator outputs

as discussed in Chapter 4. These would lead to a false indication of the maximum drift time. A program written to analyse such occurrences revealed a hitherto unknown property of the DTD's. It was assumed that if the data block was analysed in order the resultant drift times on a wire would be increasing in value. However when the first hit drift time was subtracted from the second, if it occurred, a high incidence of negative values resulted. Inspection revealed that if a fifth hit occurred in a chamber - each chamber being associated with a DTD module having four timing channels - and the first timing channel had overflowed due to a spurious hit occurring before the timing trigger, then the drift time of the fifth hit was stored in the first channel. If the latest wire to be hit had also been hit previously then the longer drift time would be recorded first. Such events were discarded from the analysis and the property of the DTD's noted for future programming.

The difference between the first and second drift times on a wire were histogrammed and are displayed in figure 5.11 for runs performed before the amplifiers and discriminators were altered as detailed in Chapter 4. Figure 5.12 shows similar analysis for runs performed after the modifications. The results were summed over all chambers and cells, the results for individual cells being of similar form. The frequencies of 0 and 2 ns time differences were high in both data sets. Indeed the respective percentages in terms of the total number of data points were identical - 18% and 2% for each data set. This indicated some systematic double firing of the digitization channels which was difficult to explain. For the data taken before the modifications small peaks were seen at 32, 64 and 96 ns indicating multiple reflections between the sense wires and amplifiers, the cable length being 16 ns. Also a very broad peak

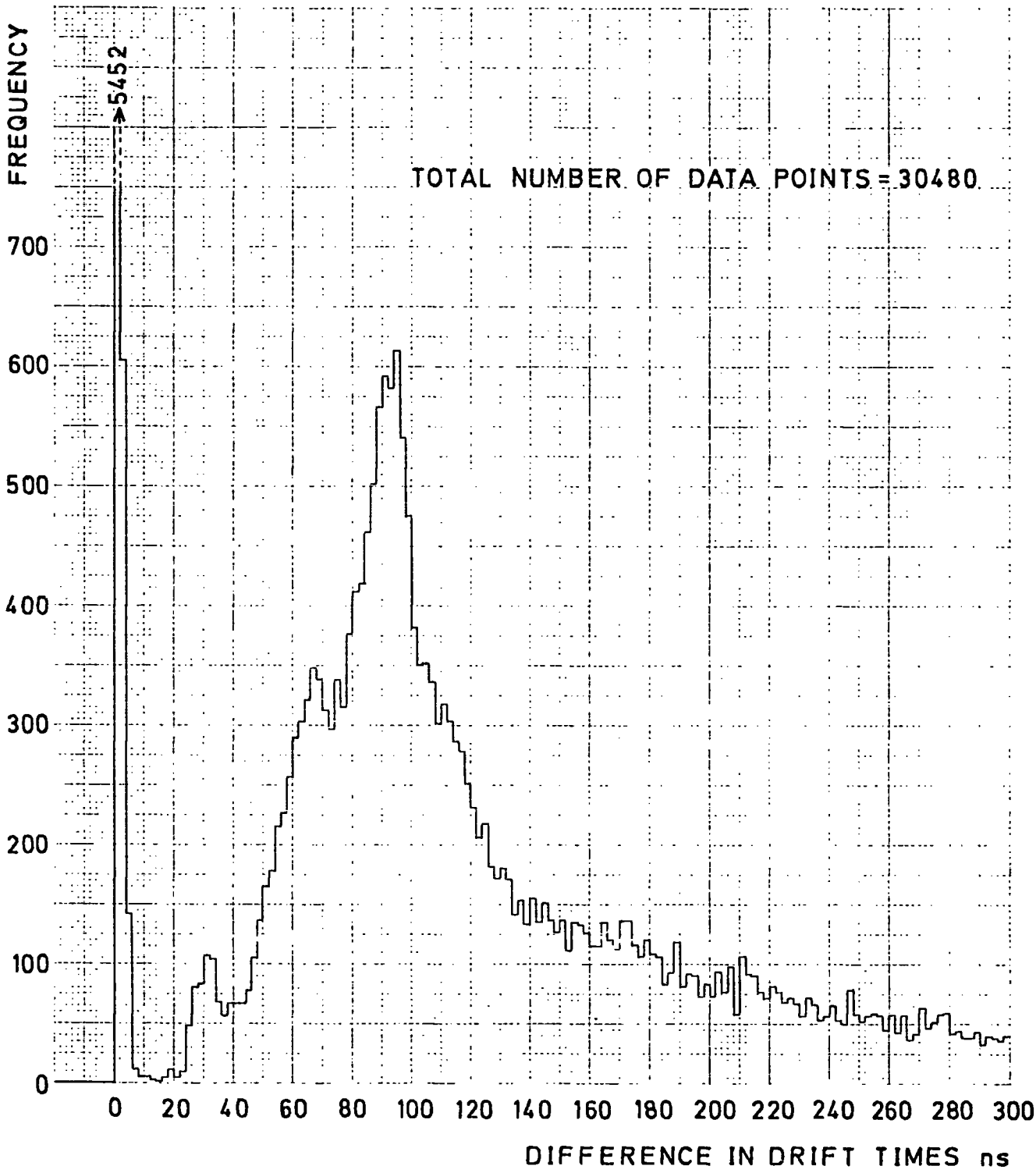

FIG. 5.11: DIFFERENCE IN DRIFT TIMES BETWEEN FIRST AND SECOND HITS ON A WIRE BEFORE MODIFICATIONS TO AMPLIFIERS AND DISCRIMINATORS

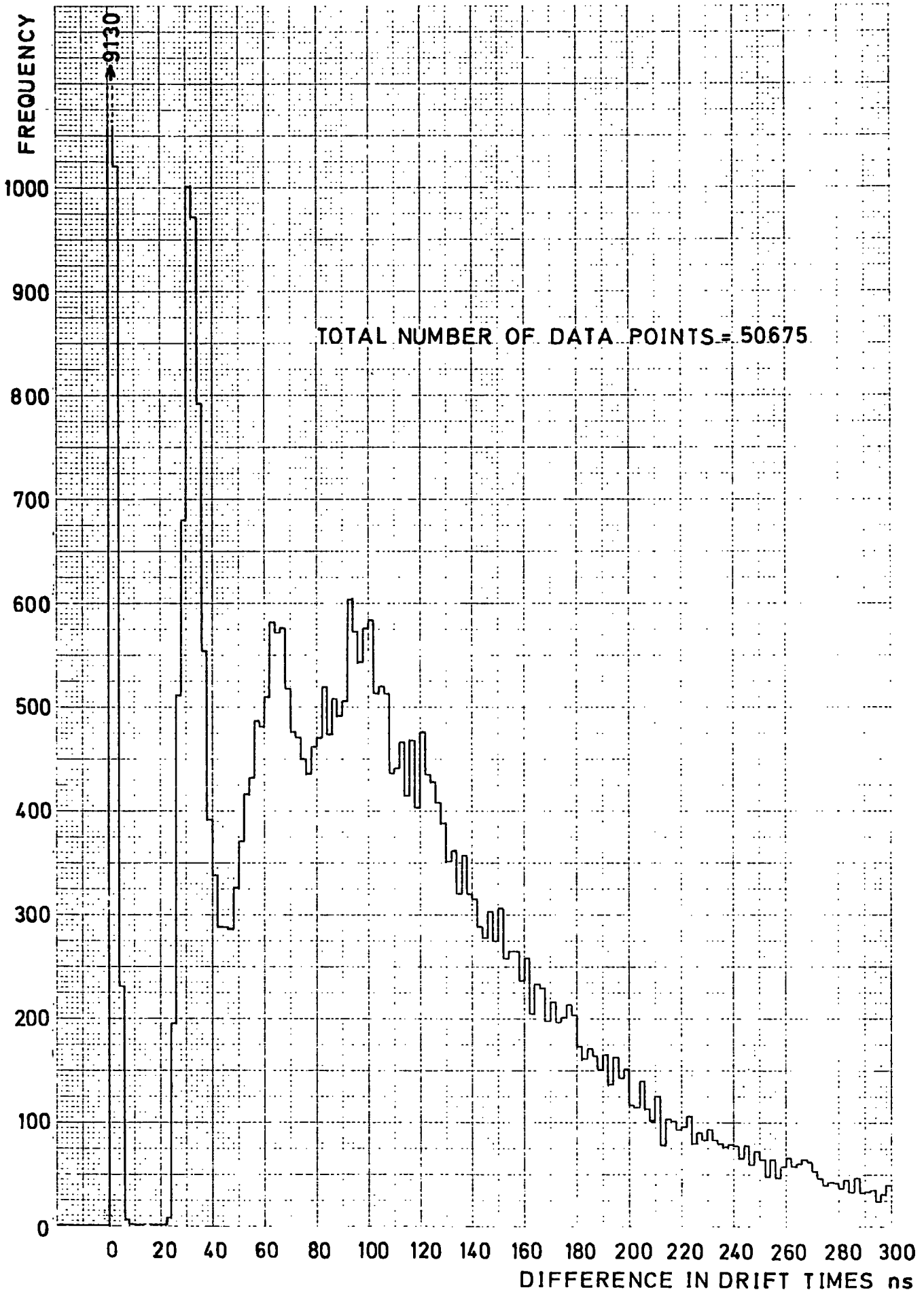

FIG. 5.12: DIFFERENCE IN DRIFT TIMES BETWEEN FIRST AND SECOND HITS ON A WIRE AFTER MODIFICATIONS TO AMPLIFIERS AND DISCRIMINATORS

around 90$\pm$ 10 ns indicated the deformation of the amplifier pulse, as noted in Chapter 4, causing double firing of the digitization channels. In comparison the data taken after the modifications indicated an enhancing of the first reflection at 32 ns, an identical percentage of the total data for the second reflection at 64 ns as in the pre-modification data, and the removal of the broad amplifier induced peak around 90 ns. The third and fourth reflections at 96 and 128 ns were more distinct. The tails in both data sets were due to genuine double hits in a cell caused by showering of the electrons in the vacuum tank wall or actual double decay tracks. Additional analysis, not presented in detail here, revealed that the time differences between the second and third or third and fourth hits on a wire, if they occurred, were predominantly 32 ns with the modified system. Before modification the 64 ns and 96 ns reflections were more dominant.

Correct analysis of the data would remove any longer drift times recorded on a wire. This would guarantee that only the true drift time was processed although in some instances two genuine tracks may have passed through the same cell. However it would be unlikely that they passed through the same cells throughout the array and in the tracking analysis if any chamber had two wires hits the event was rejected.

Allowance for the re-cycling of the timing channels after over-flows and the arrival of five or more hits did not remove all erroneous records. Many instances of incorrect drift time order were observed when only two hits occurred on a wire and no other hits were recorded in the module. Some malfunction of either the DTD input or readout system was indicated and any such events were rejected from all analysis.

5.3.4 Calibrations using Stringent Data Selection

Having noted that erroneous drift times could be recorded more stringent constraints were applied to the events histogrammed in attempts to derive more conclusive calibrations. Analysis was performed upon data taken for negative muons after modification to the amplifiers and discriminators.

Figure 5.13 displays the first, lowest drift times recorded on each wire in an event summed over all chambers for each cell. All reflections and longer drift times are removed and the longer drift time tails seen in figure 5.7 would be expected to decrease. This does indeed occur, but not to the expected degree. As before flat-topped distributions would be expected in ideal conditions. Better plateaus are observed with the latest analysis but still no definate conclusions may be derived about the maximum drift time cut-offs.

In an attempt to select irrefutably correct data a routine was written to select unambiguous single tracks in the array. The criteria were: a single wire hit in a chamber, no more than two hits on a wire - with associated choice of correct drift time - and correct curvature towards the centre of the ring for successive downstream chambers in the array. Without resolution of the left-right ambiguity the latter restriction was achieved by demanding that the wire hit was the same as in the previous upstream chamber or nearer to the ring centre. Successive chambers did not necessarily have to be hit, allowing for inefficiencies in detection. The results are presented in figure 5.14. They are not dissimilar to those of figure 5.13 but the peak around 170 ns in cell "0" is more prominent. This gave the first indication that the cell may have only been efficient for a short distance on the vacuum tank side of the sense wire. This would cause

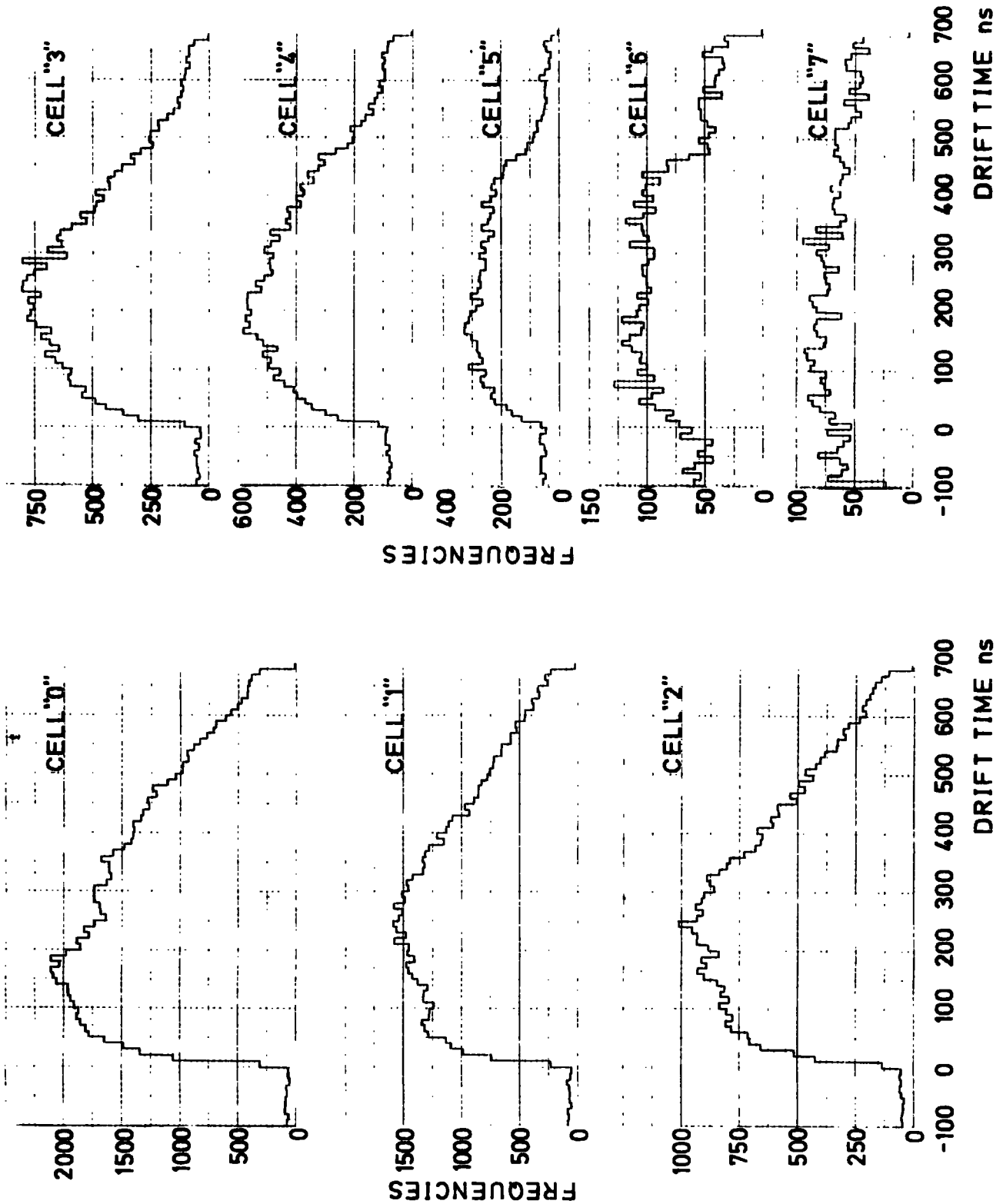

FIG. 5.13 : DRIFT TIME DISTRIBUTIONS FOR EACH CELL SUMMED OVER ALL CHAMBERS FROM ANALSIS OF FIRST HITS ON WIRES ONLY

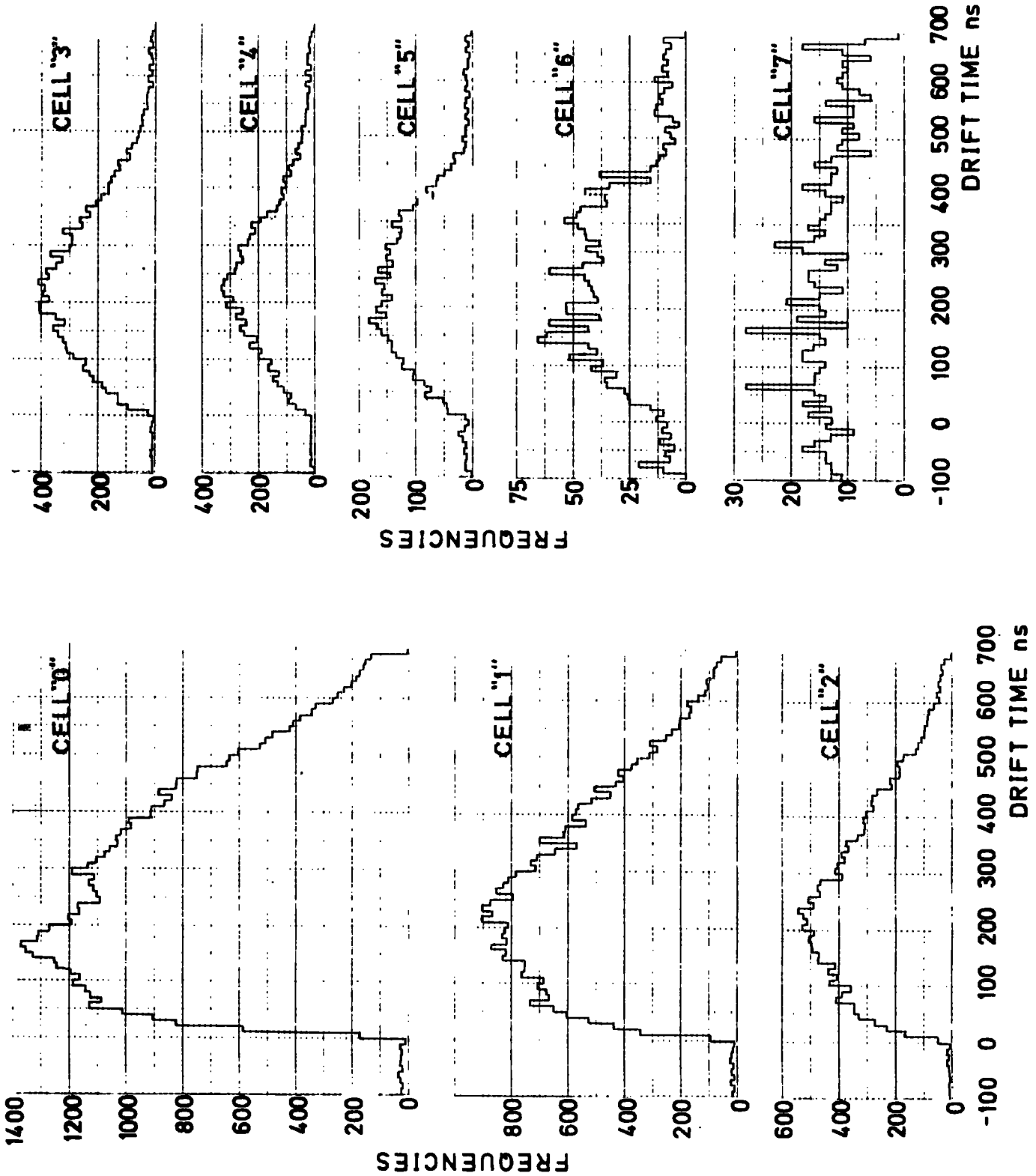

FIG. 5.14: DRIFT TIME DISTRIBUTIONS FOR EACH CELL SUMMED OVER ALL CHAMBERS FROM ANALYSIS OF CANDIDATE EVENTS ONLY

a peak and a rapid fall-off in the distribution if only one side of the cell was efficient beyond this distance.

It may be seen that reasonable flat-tops to the distributions only occur in cells "4" to "6", cell "7" having insufficient data to enable firm conclusions to be made. This suggests that the compensation mechanism was more exact for the lower magnetic fields present in these cells.

In all the distributions displayed no oscillations are observed due to the incidence of large angle tracks. Angles of up to 25° for 900 MeV electrons incident upon cell "7" may be expected, lower angles applying for cells closer to the vacuum tank and for higher energy electrons.

Further analysis, not presented here, split the data into the four (g-2) energy levels and did not reveal any difference in the form of the distributions with energy. Also histogramming of the data into each of the sixty-four cells revealed no discernible difference between corresponding cells in different chambers, except of course the number of data points.

Analysis of the limited data taken with the DTD system whilst detecting the decay of positive muons indicated slightly better plateaus to the distributions. As the electric field was a mirror image of the negative polarity field, and the magnetic field was merely reversed in direction, the distributions would naively be expected to be identical. One possible explanation is that the direction of field tilt for the positive polarity was in the same direction as the positron decay curvature, so the geometrical extension of the efficient detection area was less than in the negative case where the decay curvature was in the

opposite sense to the field tilt. Also the primary ionization was deposited in the same sense as the equipotential lines for the positive polarity rather than crossing them in the negative case. This implied that all the resultant electron swarms formed across the inter-cathode gap in the positive case experienced similar electric fields throughout their drift paths, and hence equal velocities. On the other hand any inhomogeneities in the electric field would have caused the electron swarms formed in the negative case to have varying drift velocities. Hence the pulse on the sense wire would have had a shorter time development in the positive case and thus a greater amplitude, leading to a higher detection efficiency at longer drift times and an extended flat-top to the drift time distribution.

5.4 Study of the Magnetic and Electric Fields

In order to explain the inconclusive drift time calibrations a closer study was made of the magnetic and electric fields present in the drift chambers.

The magnetic field plots were performed during two separate field mapping runs of the main (g-2) experiment whilst the vacuum tank was removed. The intention was to contruct an accurate set of mesh points over the chamber array volume for use in the final tracking analysis.

The electric field simulations were performed after data taking had been completed in an attempt to explain the poor calibrations.

5.4.1 Magnetic Field Plots

The measurements of the (g-2) fringe field were performed using a calibrated Hall Probe which enabled accuracies of 10 gauss to be achieved. The probe was attached to a traversing table which was accurately mounted horizontally in the region of magnet block 22. Positional errors of $\pm$ 0.5 mm are quoted for all the data presented in this section.

As no vertical co-ordinate was obtainable from the drift chamber system without the use of the MWPC's the assumption was made that the majority of the decay electrons originated from around the median plane. Data taken with the three MWPC's before installation of the complete drift chamber array indicated that the electrons decayed in a horizontal plane with a large percentage around the median plane.[4] Analysis of the EDM data suggested a semi-circular filling of phase-space in the vertical direction,[5] indicating that a large proportion would be expected to decay from within $\pm$ 20 mm of the median plane.

Figure 5.15 shows the variation in field radially at two points in azimuth corresponding to the boundary of two magnet blocks and a position offset 65 mm from the centre line of block 22. The radial distances measured from the centre of the ring and the cell boundaries are indicated. The values obtained are in agreement with those obtained whilst the magnets were under test before installation in the Muon Storage Ring.

Variations between the two azimuthal positions of up to 1.4 kG at certain radii indicate that drift velocity variations between corresponding cells in different chambers at varying azimuthal positions in a magnet block would be expected. However for cells 0, 1 and 2, which contain the majority of the data, the variations in field were not so great.

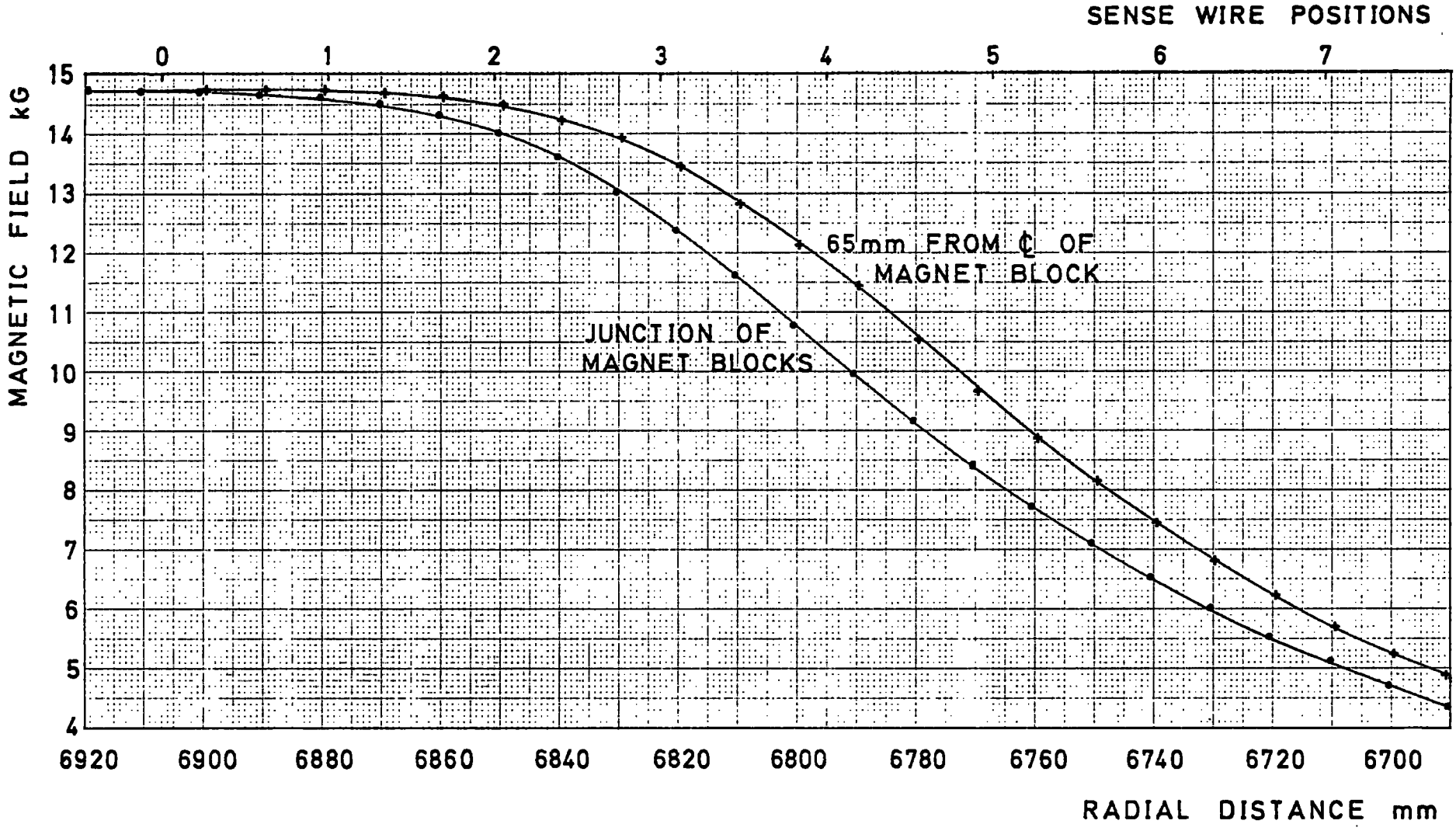

FIG. 5.15 : AZIMUTHAL VARIATION OF MEDIAN PLANE MAGNETIC FIELD

Figure 5.16 demonstrates the field plot derived from a set of measurements taken radially at various vertical positions at the boundary of two magnet blocks. Plots obtained at other azimuthal positions reflected the variation of field with azimuth shown in figure 5.15. However the overall form of the field plots were similar with the indication that the field was reasonably constant over a vertical distance $\pm$ 20 mm from the median plane. The homogeneous field present over the storage volume extended into the region covered by the first two drift chamber cells. Thus the majority of decay electrons traversed a near identical fringe field irrespective of their azimuthal birth position. Within $\pm$ 20 mm vertically of the median plane the magnetic field decreased towards the centre of the ring. For greater vertical displacements figure 5.16 illustrates that due to edge effects from the pole pieces the field rose from the homogeneous value of 14.75 kG to about 18 kG before falling in value towards the centre of the ring. Hence electrons decaying at large displacements from the median plane would have complex trajectories and the drift velocities in the extremities of the drift chamber cells would be different from the median plane values.

It is obvious that an indication of the vertical co-ordinate of the decay electron would have been desirable to enable a more accurate calibration of the drift velocities. However, as stated, no measurable variation in the drift time distributions of corresponding cells in various chambers was noted. Therefore either the magnetic field variation had only a small influence upon the drift velocities or the variations in the field vertically masked any variations in the radial field at different azimuths.

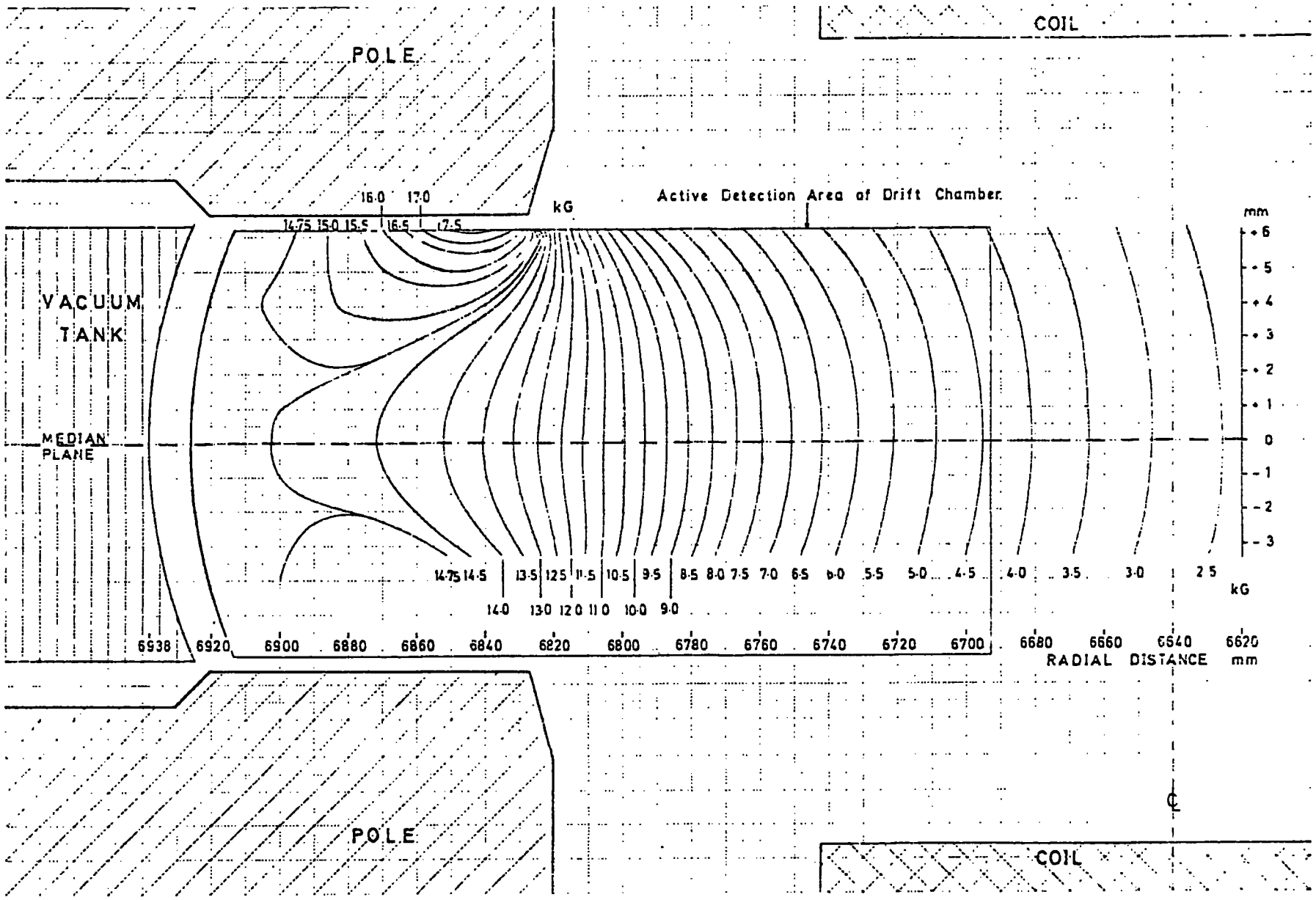

FIG. 5.16 : MAGNETIC FIELD MEASURED IN VERTICAL PLANE AT JUNCTION OF MAGNET BLOCKS

Any exact calibration method would have to study both vertical and radial drift velocity variations with azimuth.

5.4.2 Electric Field Plots

A more detailed evaluation than had previously been attempted was made of the electric fields present in the chambers. The values used by Browell and Short[2,3] were derived using a numerical relaxation method computed by hand. They also only extended the plot to the cathode planes, rather than the earthed windows, so incorrect boundary conditions resulted. As no suitable software was available the relaxation method was employed in a computer routine written to determine the fields with several cell geometries and wire potentials. Unfortunately the method proved to be rather time consuming.

The area to be studied was divided into a grid of square cross-section. The boundary could be of any rectangular shape and any boundary conditions and wire potentials could exist with suitable adaptation of the program. The third co-ordinate, parallel to the sense wires, was considered to be infinite. Figure 5.17 demonstrates the grid, the step size being at most half the H.T. wire spacing. From the nomenclature of figure 5.17 the residues at each of the mesh points, except the singularities at the boundary and wires, were systematically reduced until they were all below a fixed value. The residue was defined as:

$$R_{i,j} = V_{i,j+1} + V_{i+1,j} + V_{i,j-1} + V_{i-1,j} - 4V_{i,j} \qquad (5.3)$$

where V defines the potentials at the relevant mesh point co-ordinates. Initial arbitrary values were given to the potentials at non-singular mesh points.

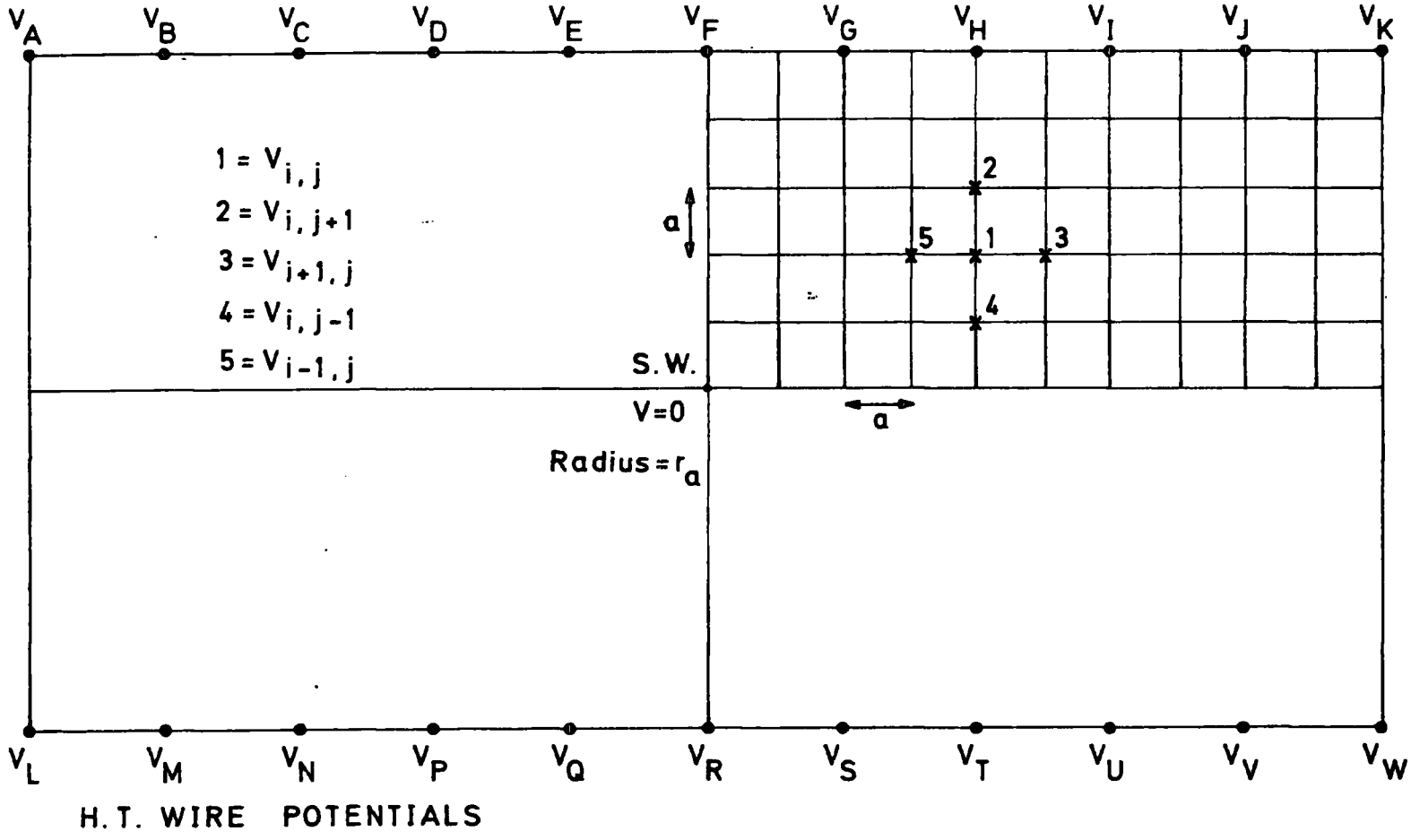

FIG. 5.17 : GRID USED IN NUMERICAL RELAXATION METHOD FOR COMPUTING EQUIPOTENTIALS

As the wires were at fixed potentials they formed local singularities. It has been shown[6] that the approximate solution derived by this method is related to the exact solution for wires of radius $r \approx ae^{-\frac{1}{2}\pi}$ at the singularities, where a is the step size. For all the potential maps displayed below the step size was 0.4 mm leading to an equivalent wire diameter of ≈80 μm. This was in good agreement with the 120 μm H.T. and potential wires but too large for the 20 μm sense wires. Thus the radial field computed around the sense wire was lower than the true value. However such a compromise step size produced the best overall potential map available using such a method.

The values obtained by Browell and Short were derived using the H.T. planes as the boundaries of the grid. As earthed windows were used in the (g-2) chambers and the distances between the windows and the upstream and downstream H.T. planes were different, it was necessary to compute the field for the entire volume between the windows. It had been noted[7] that the presence of earthed windows tended to decrease the expected angle of field compensation tilt. Electric field simulations performed by Wylie[8] indicated the alteration in field along the sense wire plane caused by varying the cathode plane to earthed window distance. These observations highlighted the need for the extended field plots.

Figure 5.18 shows the equipotentials present over the inter-cathode gap of two neighbouring half-cells. The equipotentials between the cathodes and earthed windows were computed but are not shown. The equipotentials are exhibited in this way as the cell boundaries are of most interest. The radial fields around the sense wires are soon distorted by the three wire-spacing field compensation slant.

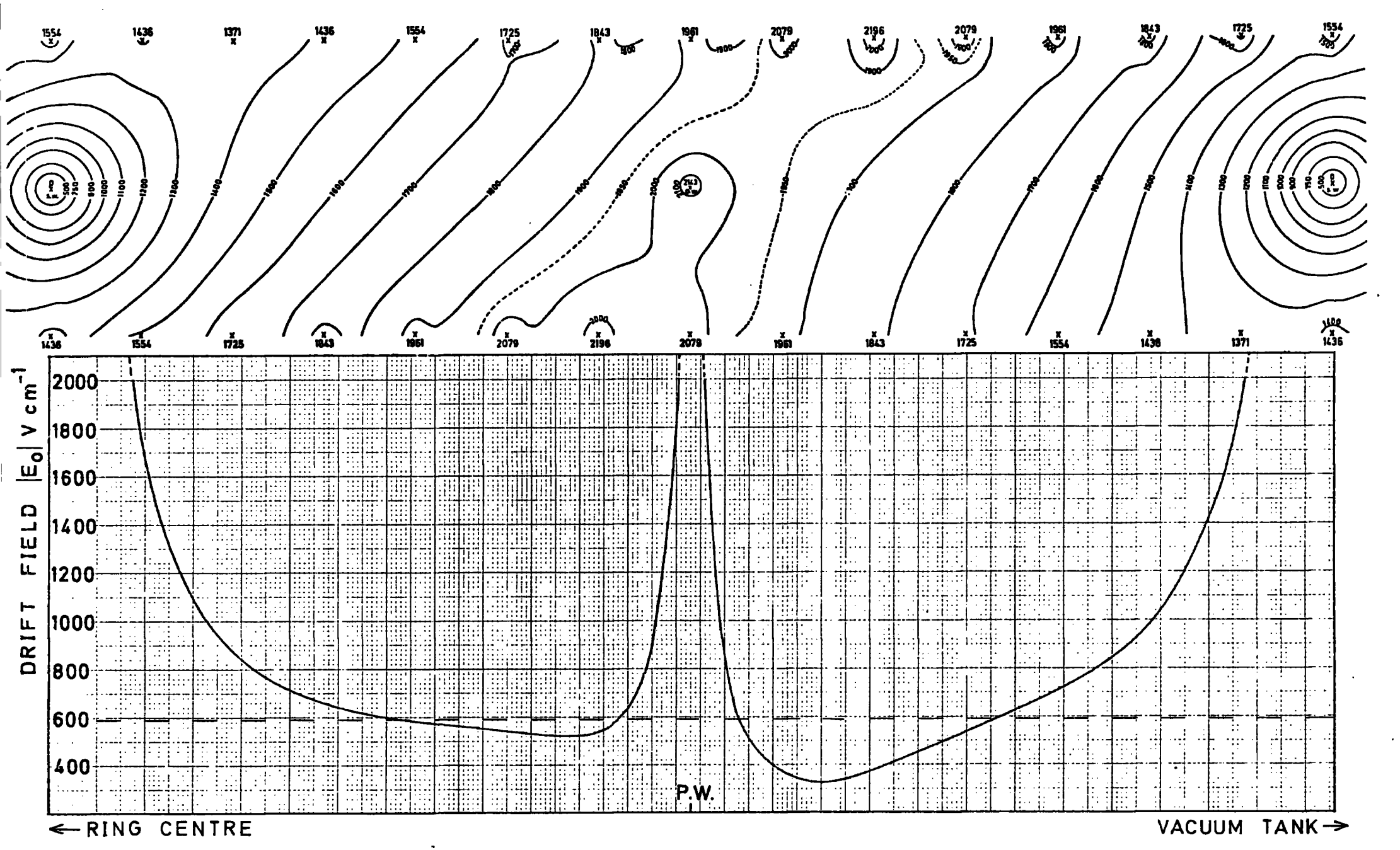

FIG. 5.18 : EQUIPOTENTIALS AND DRIFT FIELD $|E_0|$ IN A NORMAL UNIT CELL

The equipotentials of the drift space on the vacuum tank side of the sense wire are reasonably evenly spaced over the majority of the drift region and their tilts are almost constant but just below the design angle of 43^{o}. However around the potential wire the equipotentials are widely spaced, especially on the downstream side of the sense wire plane, and hence the field values are extremely low. This is a direct consequence of the compensation being equal to an odd number of wire-spacings. Had the tilt been equal to two or four wire-spacings, such an asymmetry would not have existed. The field plots of Browell and Short did not indicate the high fields around the higher potential cathode wires as the earth planes were not included in their calculations. Hence the model used to design the field compensation mechanism had artificially high potentials at the cell boundaries. Therefore the fields were greater and the boundary between the two drift spaces was more distinct.

The immediate consequence of the low field region was to drastically alter the drift velocities in the area. More importantly, however, as no discernible field tilt existed in the region, many of the electron swarms were swept out of the active chamber volume by the magnetic field and detection inefficiencies resulted.

Inspection of the drift space on the ring centre side of the sense wire reveals that not only was the field much lower over the majority of the drift space than on the vacuum chamber side of the sense wire, but also the equipotential tilt angles were smaller. Hence not only were the drift velocities different in this half of the cell but also, as the field compensation was too small, the detection efficiencies were lower.

Also displayed in figure 5.18 is the electric field measured along the sense wire plane. For comparison the value obtained from the formula $(V_{max} - V_{min})/1.4$ Vcm^{-1} is shown as a dotted line at 590 Vcm^{-1}. The fields over the entire inter-cathode gap were comparable to the sense wire plane values except near the cathode planes, where there were distortions due to the H.T. wires being poles of potential, and around the potential wire where severe field distortion existed.

As already mentioned the true radial fields around the sense wires were of higher values than shown. Therefore the equipotentials were more closely spaced around the sense wires and the perturbation of the tilting mechanism close to the sense wires was less than indicated. As a consequence lower fields existed in the remainder of the drift spaces and therefore higher drift velocities resulted if the fields were not above the saturation value.

The mechanical imperfections in chamber construction, noted in Chapter 3, led to intercathode gaps of 6.4 ± 0.6 mm. Hence the theoretical tilting angle was $43^{0} \pm 4^{0}$ and the fields around the sense wires could vary by over 10%. Also as the potential wires were not surveyed as accurately as the sense wires the half-cell lengths were not exactly equal. All these discrepancies led to variations in drift velocities between cells, although their effects were not discernible in the drift time distributions, as discussed above.

Equipotential maps were calculated for the curved end cell. Separate plots were performed for the equipotentials at the top and bottom of the chamber, where the sense wire to curved end distance was 8 mm, and in the

median plane of the chamber where the sense wire to curved end distance was 18 mm. The results are shown in figures 5.19 and 5.20. The detrimental effect of the addition of the earthed window on the curved end member is immediately apparent. Beyond the potential wire, positioned 4 mm from the sense wire, the drift field was directed towards the curved end rather than the sense wire. Hence tracks could only be detected over the first 4 mm of the drift space rather than the entire half-cell. If the earthed window had not been present on the curved end member the high fields around the strip electrodes would not have existed. The nearest earth plane would have been the vacuum tank situated approximately 15 mm from the curved end member. Therefore a low drift field, in the correct direction, would have existed throughout the cell. However the earthed chamber side windows would have affected the tilt angle of the equipotentials in the median plane due to the lack of potential wires over the 14 mm drift space allowing field penetration. Hence the detection efficiency at long drift lengths would have been low. It should be noted that as reported in Chapter 3 the curved end cells operated satisfactorily in a zero magnetic field environment with no earthed chamber windows.

As the dielectric constant of the G10 material is about 4, the thickness of the curved end wall was taken to be 1.6 mm, rather than 0.5 mm in reality, when the grid was constructed to calculate the potentials. This compensated for the difference between the dielectric constants of Ar/CH_4 and G10. In the displayed plots the true thickness of G10 is presented and the positions of the equipotentials between the strip electrodes and earthed window are estimated. The 1 mm wide strip electrodes were each represented by three adjacent equal valued singular points on the grid. As with the normal cell plot the equipotentials

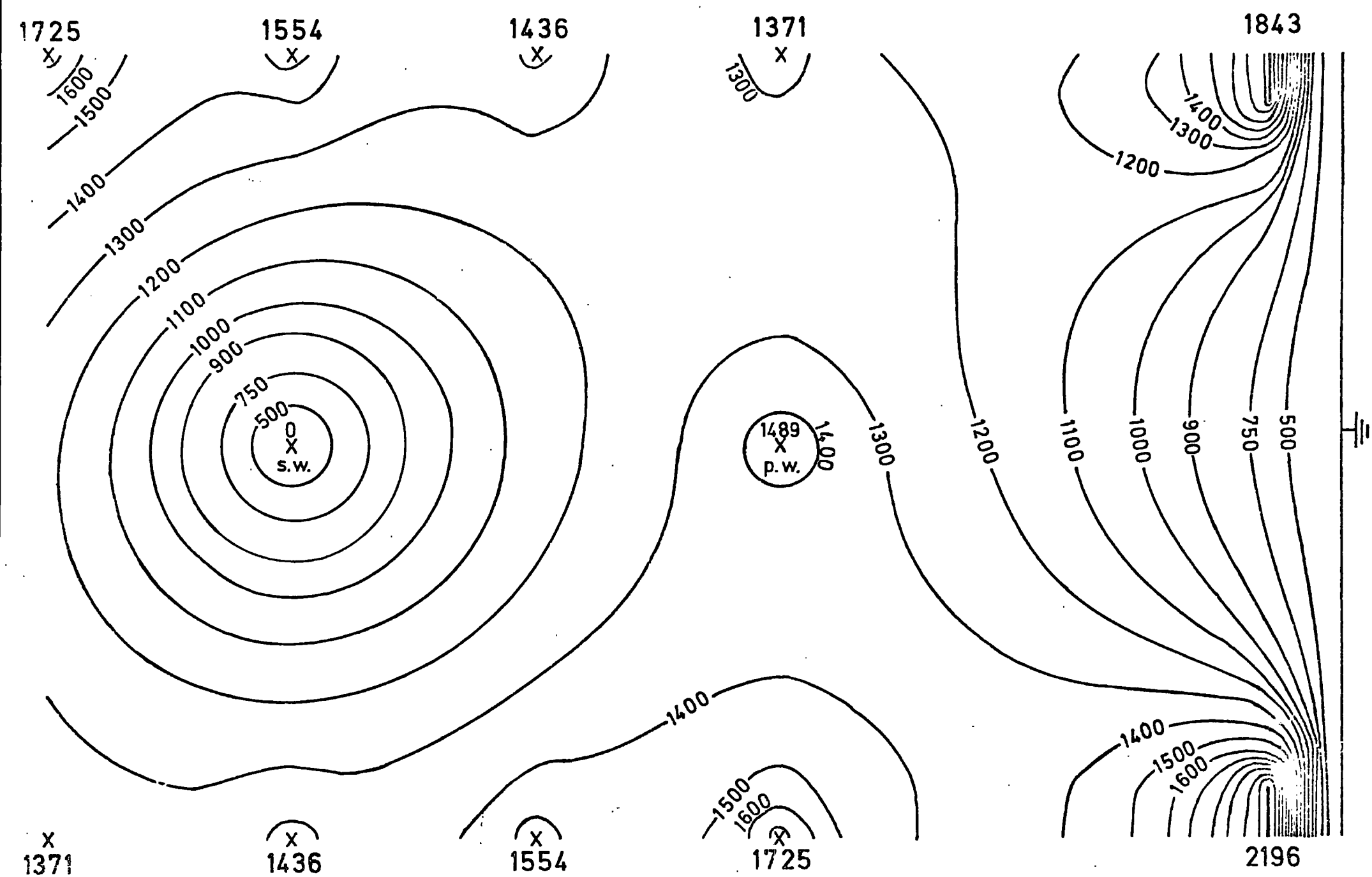

FIG. 5.19 : EQUIPOTENTIALS IN UPPER AND LOWER REGIONS OF CURVED END CELL

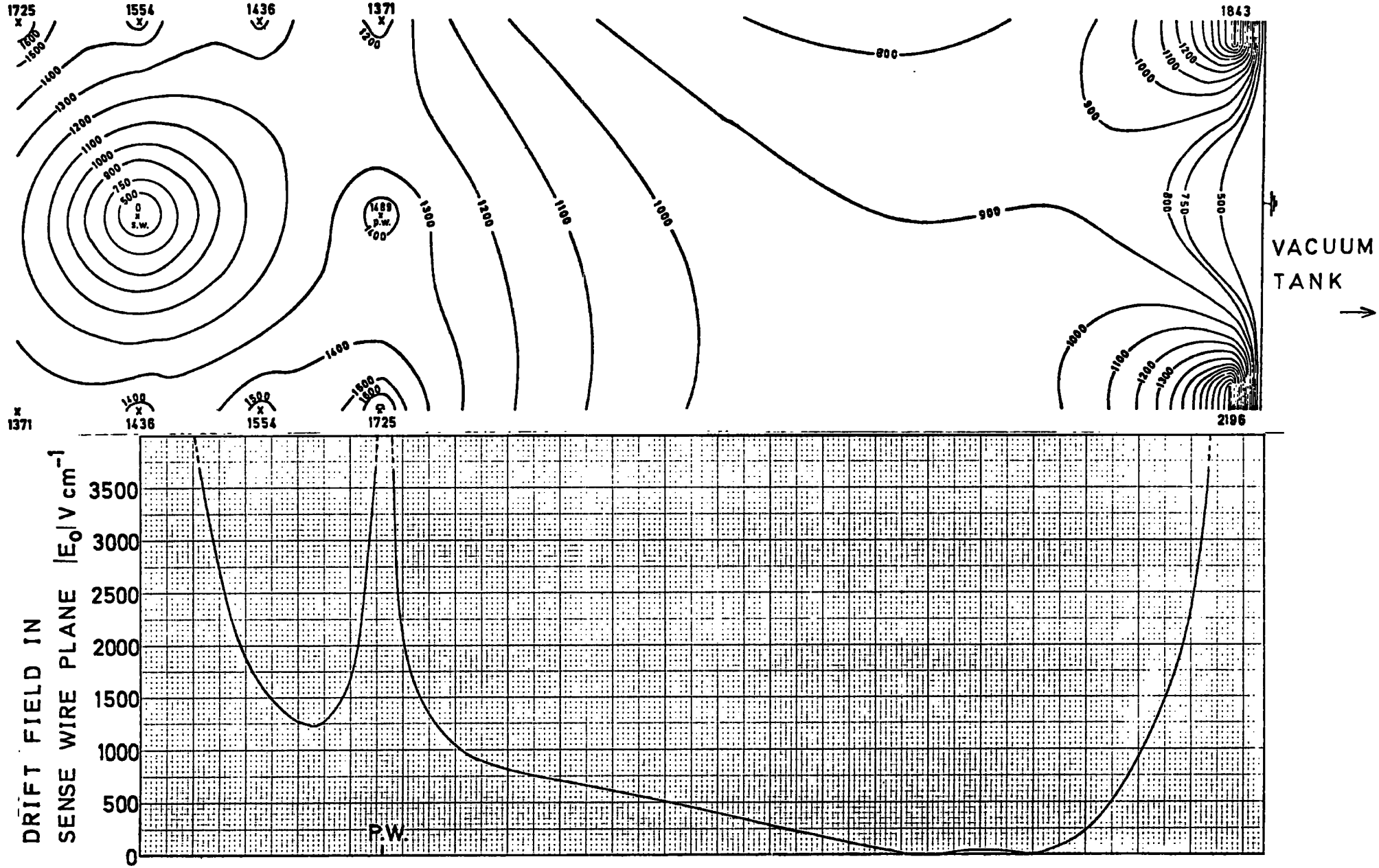

FIG. 5.20 : EQUIPOTENTIALS & DRIFT FIELD $|E_0|$ IN MEDIAN PLANE OF C.E. CELL

between the cathode planes and earthed chamber windows were computed but are not shown. In all plots the equipotential lines were constructed by hand using the potentials calculated at the grid points. After computation all non-singular residues were less than 0.1V and hence from equation (5.3) the grid potentials were more accurate.

The median plane plot of figure 5.20 also shows the field in the sense wire plane. Apart from the low field region on the downstream side of the potential wire, the equipotentials were almost circular and therefore a radial field existed, especially along the sense wire plane. The slight ellipticity seen in the 1200V equipotential would be removed if the true higher field around the sense wire could have been calculated using the relaxation method.

The normal cell plot displayed in figure 5.18, although not totally accurate in the sense wire regions, has indicated why the cells were inefficient at long drift lengths due to the poor field compensation in the potential wire regions. It also indicates that different drift velocities are to be expected in the two drift spaces on either side of a sense wire. Figures 5.19 and 5.20 show that the addition of the earthed chamber windows drastically altered the drift field in the curved end region and made the final 14 mm of the active volume in the median plane redundant. Adding the 15 mm spacing between the curved end member and the vacuum tank gives a total dead space of 30 mm in the available radial detection region. Hence very few high energy electrons could be detected unless they decayed a long way upstream of the chamber array. Only then could they be deflected 30 mm radially inwards by the magnetic field and be detected in the downstream chambers.

5.5 Theoretical Drift Velocity Calculations using the Field Plots

Using the magnetic and electric fields derived in the last two sections a theoretical assessment of the drift velocities across a chamber could be made. The magnetic and electric fields were calculated at 1 mm intervals from the potential wire in the curved end cell to the sense wire in cell "5". The tilt angles of the equipotentials, γ, were measured and hence the true electric field, E, could be derived from the electric field E_o in the sense wire plane:

$$E = E_o / \cos \gamma \qquad (5.4)$$

Using the equations presented in Chapter 2 the drift angles to the sense wire plane, θ, could be derived using:

$$\tan \theta = \omega\tau = \frac{Bw_o}{k\,E} \qquad (5.5)$$

where k = 0.75 for a Maxwellian velocity distribution and the zero magnetic field drift velocity values, w_o, were taken from figure 5.21. These values are due to Walenta[9] and are in good agreement with other published results.[10,11,12] Comparison with figure 3.10 shows that the drift velocities are much higher than those derived by Browell and Short[2,3] at low electric field values. This is probably due to the latters' methods of measurement and calculation of the electric field. Knowing the values of θ, and thus $\omega\tau$, the magnetic drift velocities w(E, B) could be calculated:

$$w(E,B) = w_o \left[1 + (\omega\tau)^2\right]^{-\frac{1}{2}} \qquad (5.6)$$

The non-exact compensation angle given by $(\gamma-\theta)$ was then used to convert w(E, B) into the measured drift velocity, w_s, along the sense wire plane:

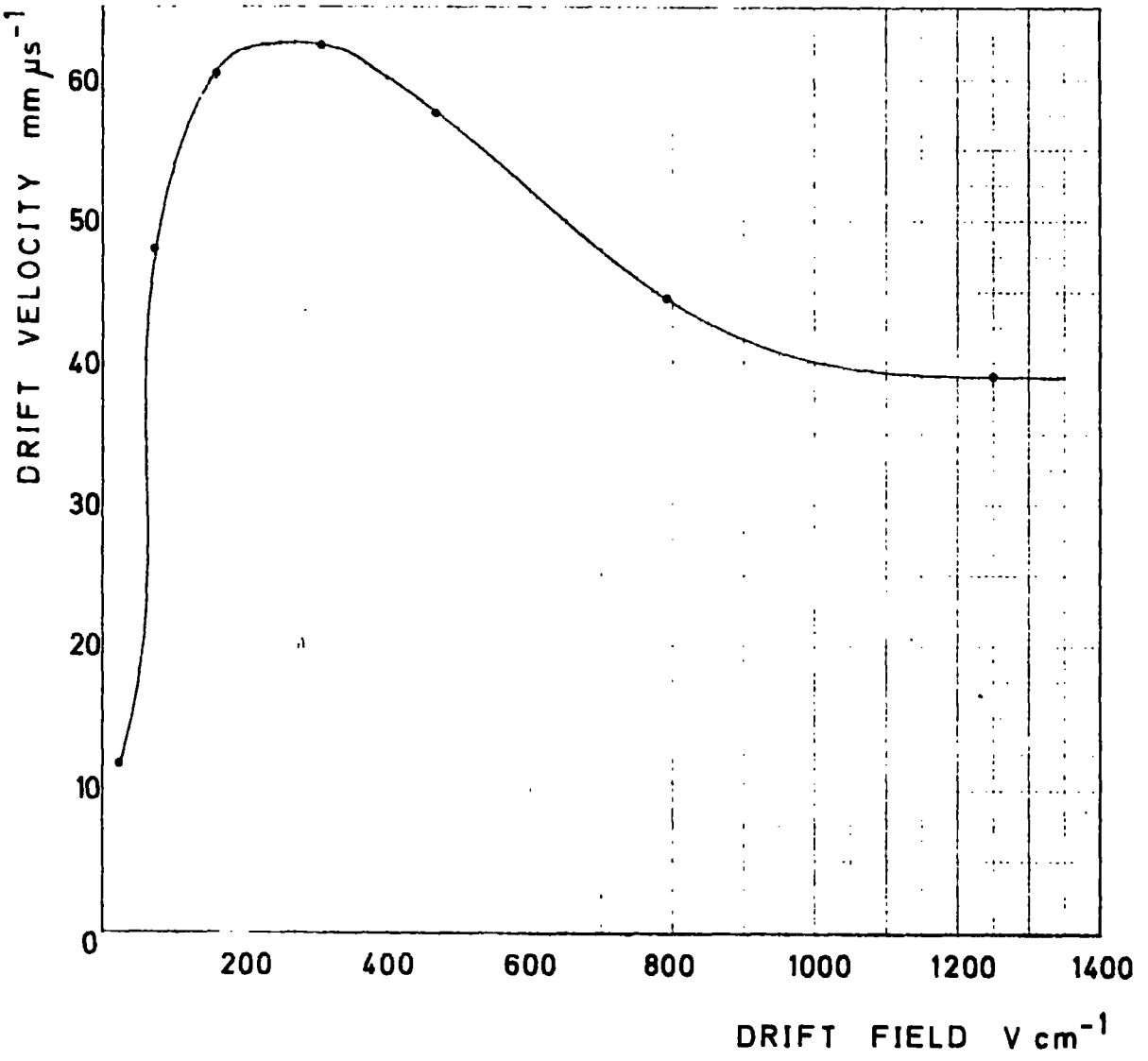

FIG. 5.21 : EXPERIMENTAL DRIFT VELOCITIES FOR $Ar-CH_4$ (90-10) DUE TO WALENTA

$$w_s = w(E,B) \cos (\gamma - \theta) \qquad (5.7)$$

The values of $(\gamma - \theta)$ calculated in 1 mm steps across a chamber are presented in figure 5.22. Only the five cells which contained the majority of the data are shown, the sense and potential wire positions being indicated. A larger scale diagram of cell "1" is given in figure 5.23. The most obvious features of the diagrams are the large values of $(\gamma - \theta)$ close to the potential wires in the half-cells on the ring centre side of the sense wires. These explain the low detection efficiencies at long drift times as the electron swarms drifted at the angle $(\gamma - \theta)$ to the sense wire plane. Over the first 6 mm of drift along the sense wire plane, starting from the potential wire, the average value of $(\gamma - \theta)$ was greater than 30^{o} and hence the swarms also moved about 4 mm perpendicularly to the sense wire plane. Therefore, assuming a uniform deposition of the primary and secondary electrons across the inter-cathode gap, two-thirds of the swarms were lost. Towards the sense wire the discrepancy was less and in the high field region the flow-lines followed by the electron swarms were almost radial. For the drift space on the vacuum tank side of the sense wire the values of $(\gamma - \theta)$ were lower and hence the detection efficiency was higher. Larger values of $(\gamma - \theta)$ occurred 3 mm from the sense wire, but in this region the electric field was radial so detection was not impaired.

Although the form of the variation in $(\gamma - \theta)$ was similar in each cell, the absolute values became smaller towards the centre of the ring. Indeed in cell "4" over-compensation occurred, denoted by positive values of $(\gamma - \theta)$, and loss of electron swarms on the vacuum tank side of the sense wire was unlikely. This explains the flatter tops

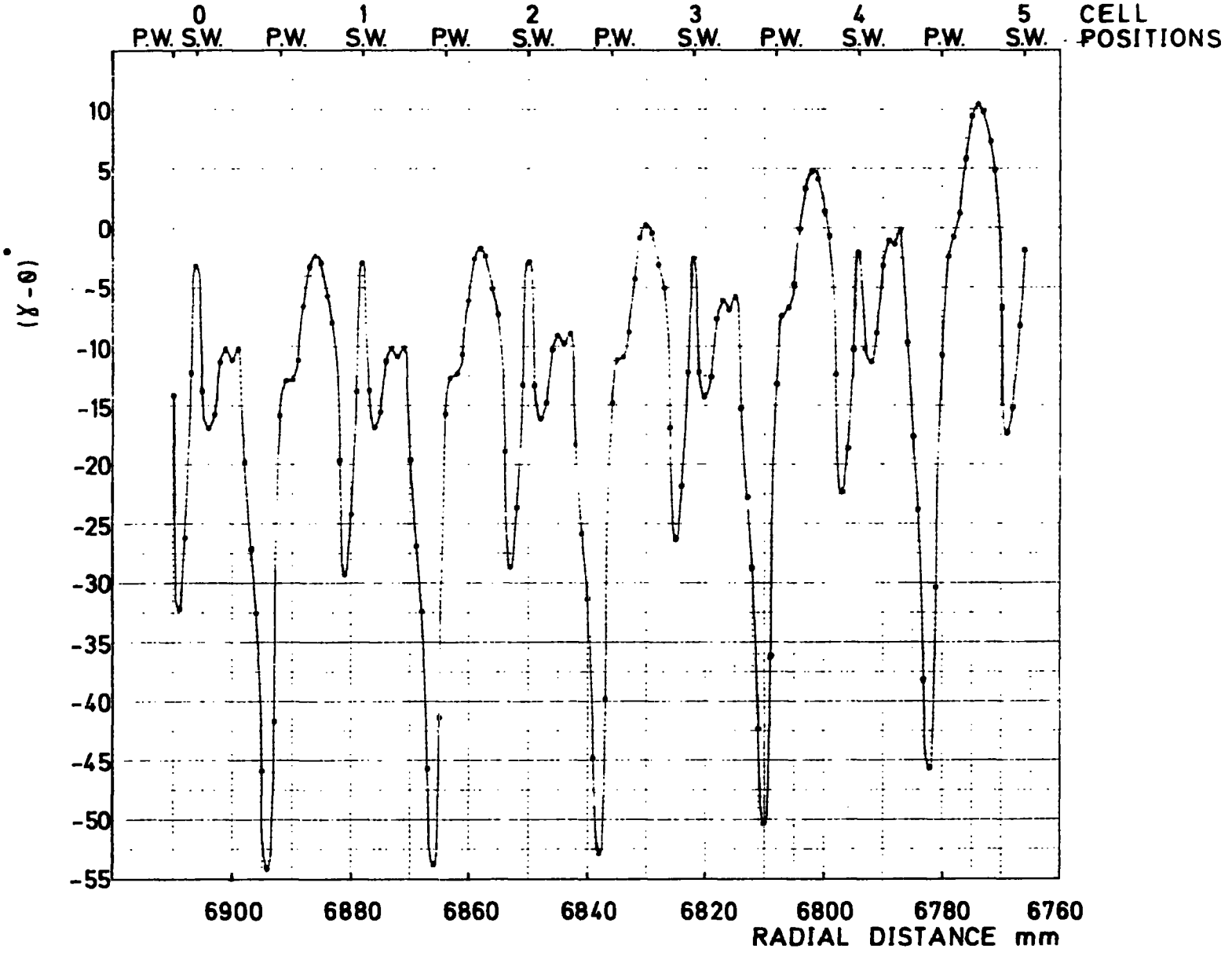

FIG. 5.22 : DIFFERENCE BETWEEN DRIFT AND FIELD COMPENSATION ANGLES

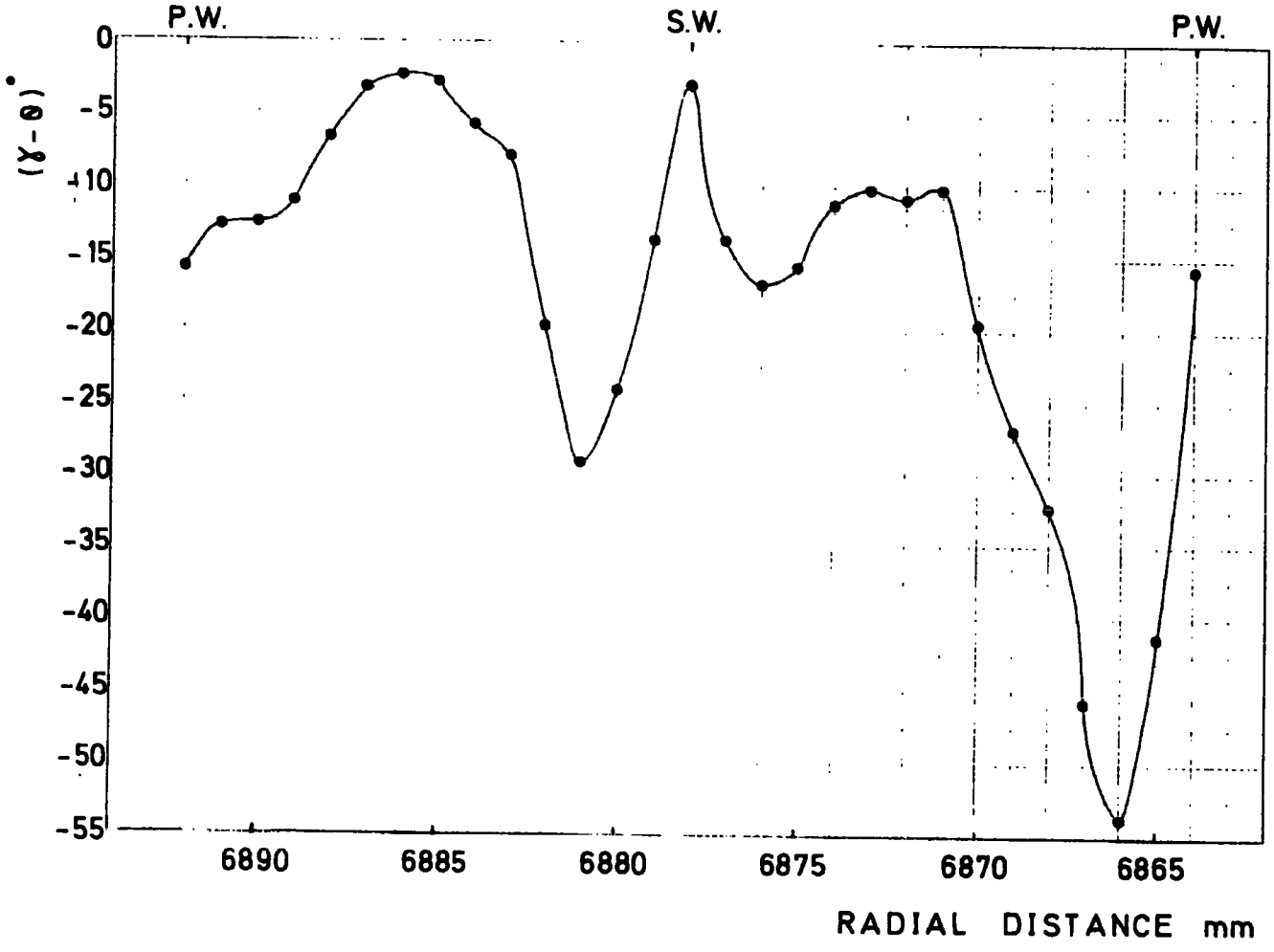

FIG. 5.23 : THEORETICAL DIFFERENCES BETWEEN ELECTRIC FIELD COMPENSATION AND DRIFT ANGLES (γ-θ) IN CELL "1"

observed in the drift time distributions for the cells closest the ring centre.

Figure 5.24 shows the computed values of w_s, the observed drift velocity parallel to the sense wire plane, across a chamber. Very low values are observed in the areas of incorrect field compensation. The values on the vacuum tank sides of the sense wires are more constant. This indicates that flatter drift time distributions would be expected in these half-cells. Corresponding values of w_s in successive cells towards the centre of the ring are seen to rise in value. This is due to both the decrease in magnetic field causing w(E,B) to increase, and also the decrease in $(\gamma - \theta)$ values which increase the magnitude of the cosine term in equation (5.7). The values of w_s in the two drift spaces of cell "1" are shown in more detail in figure 5.25.

The space-time relationships across each drift space were computed. The average values of w_s over the discrete 1 mm steps were used to calculate the step drift times and the summed values across each cell are shown in figure 5.26. A larger scale representation of the two cell "1" drift spaces are shown in figure 5.27. The space-time relationships of the vacuum tank side drift spaces are reasonably linear with only small deviations close to the sense and potential wires. However the relationships of the drift spaces on the ring centre sides of the sense wires are of complex form and cannot accurately be approximated by a linear relationship.

Certain comments must be made about the values presented in figure 5.26. As noted, the consequences of the true higher fields around the sense wires caused higher drift velocities than indicated over the remainder of the drift spaces. This was due to the chambers

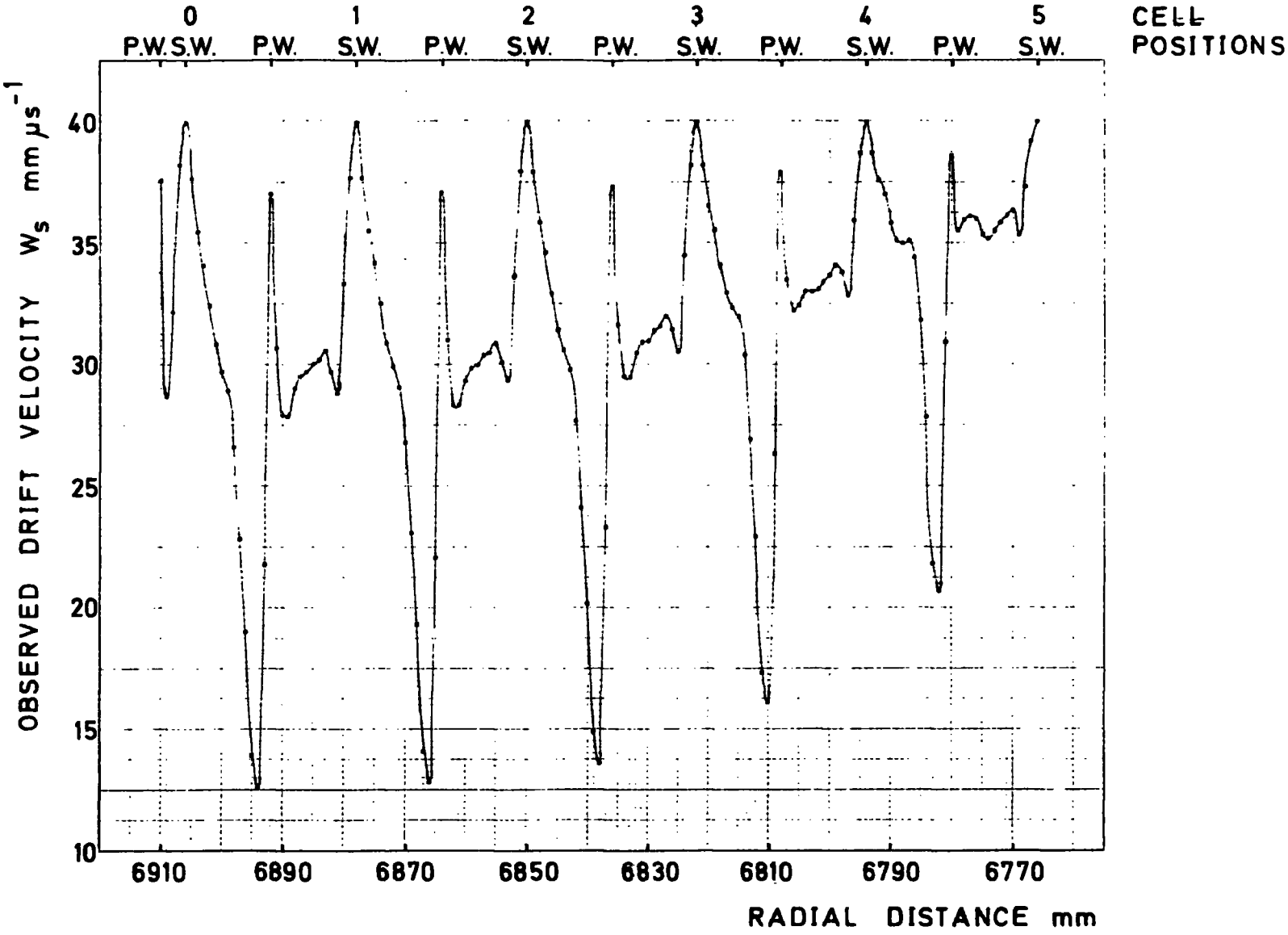

FIG. 5.24 : THEORETICAL OBSERVED DRIFT VELOCITIES W_s

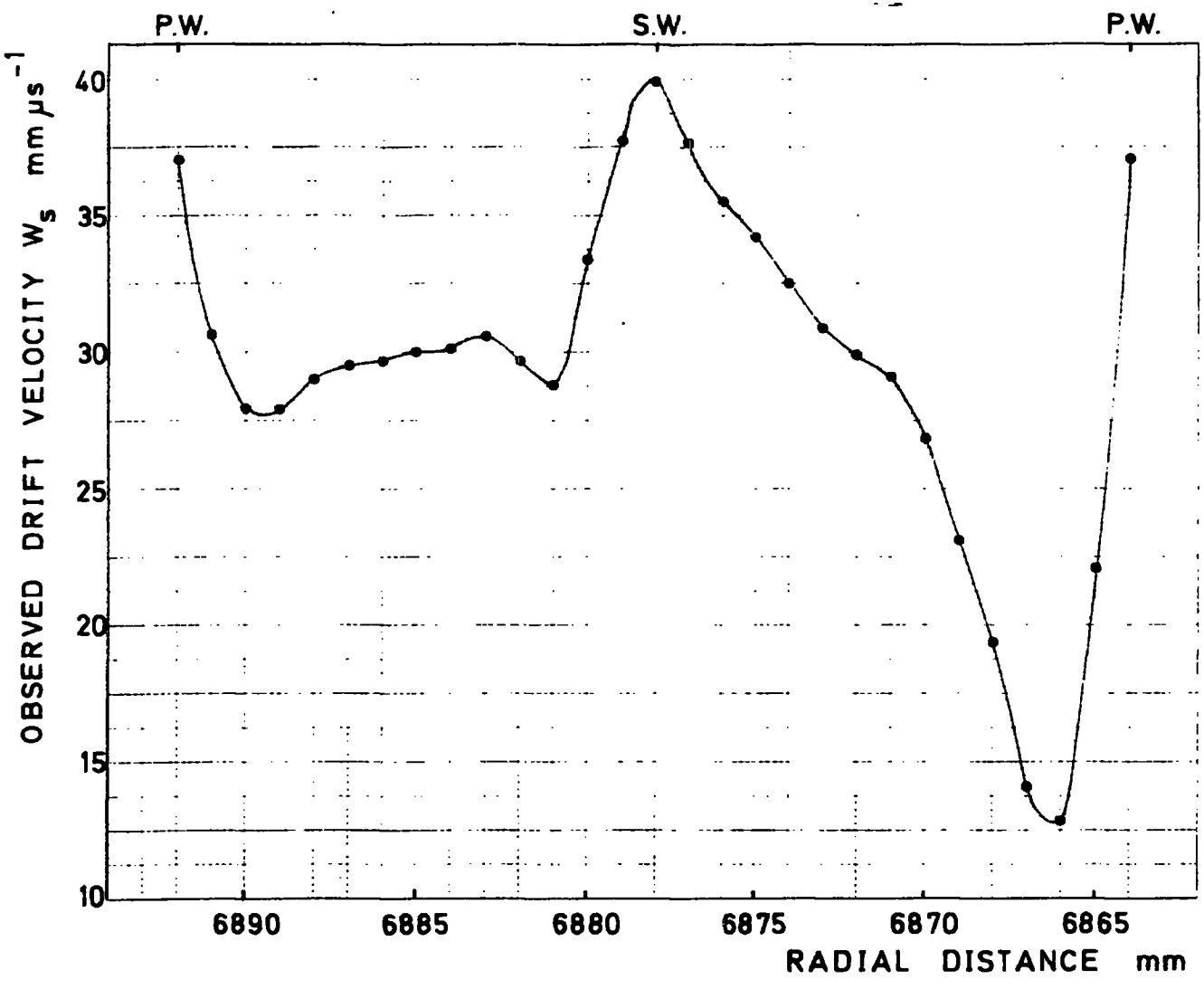

FIG. 5.25 : THEORETICAL OBSERVED DRIFT VELOCITIES IN CELL "1"

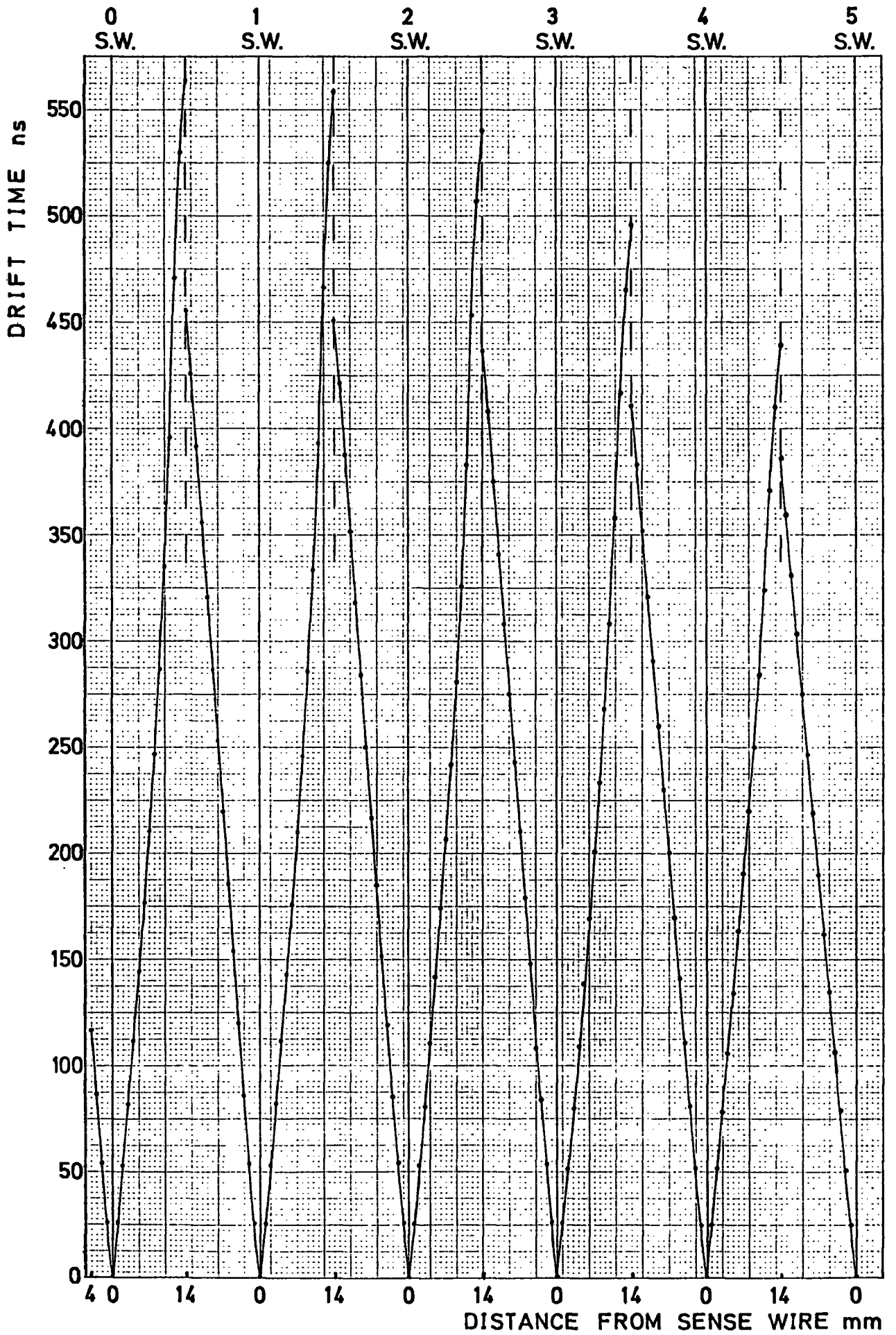

FIG. 5.26 : THEORETICAL SPACE-TIME RELATIONSHIPS

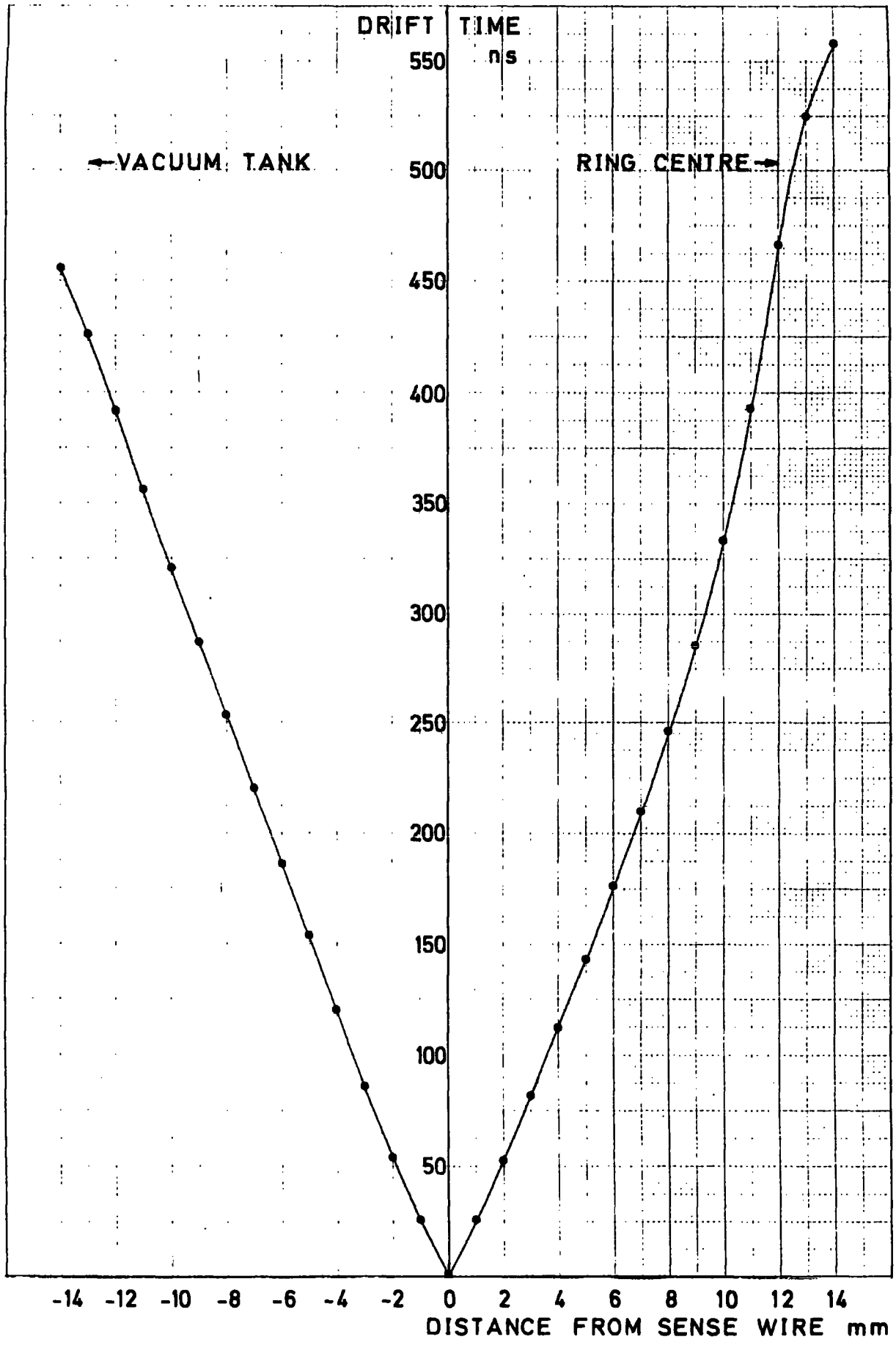

FIG. 5.27 : THEORETICAL SPACE-TIME RELATIONSHIP FOR CELL "1"

being operated below the saturation drift velocity and any lowering of the field caused the drift velocity to rise, as demonstrated in figure 5.21. The higher fields immediately around the sense wires caused the electron swarms to drift at the minimum-valued saturated drift velocity. However as the high field regions extended over shorter distances than indicated in the plots, the low drift velocities applied for a smaller fraction of the total drift time than in the above calculations. Therefore, assuming that all other parameters used in the calculations were correct, the maximum drift times calculated over 14 mm were too high. In consequence the precise form of the displayed space-time relationships may be slightly in error.

The drift time distributions for cell "0" indicated a peak and then a rapid fall-off around 170 ns. This was attributed to inefficiency on the curved end side of the cell at longer drift lengths. Figure 5.26 indicates a maximum drift time of 120 ns over the 4 mm to the potential wire. Either the wrong conclusion was drawn from the drift time distributions or the saturated drift velocity at high fields was less than the 40 mm μs^{-1} used in the calculations. Indeed the published data for Ar/CH_4, previously referenced, only applied to drift fields up to 1200 V cm^{-1}. The data derived by Browell and Short indicated a continued slow decline in drift velocity at higher fields with a minimum value as low as 25 mm μs^{-1}. Such a value would accurately produce the suggested maximum drift time of 170 ns if used in the calculations.

Referring to the detailed plots of w_s in figure 5.25, some conclusions may be drawn about the resulting form of the drift time distributions. The value of w_s falls steadily from the sense wire to the potential wire on the ring centre side of the cell, except in the

immediate vicinity of the potential wire where the value rises sharply. This would cause the distribution frequencies to decrease with increase in drift time until near the end of the distribution where a plateau would occur assuming a uniform incident flux of particles. Hence the fall-off in the distributions is partially explained without reference to the detection inefficiencies at long drift times. The vacuum tank side of the cell has more constant drift velocities over the majority of the drift space. Between four and eight millimetres from the sense wire the values of w_s are similar in each half of the cell and almost constant in value. In the other parts of the two drift spaces the values of w_s are either dissimilar or are rapidly varying, or at longer drift times only the ring centre half-cell is contributing to the drift time distribution. Therefore with a uniform flux of particles across the whole cell, the greatest number of particles per unit length in the sense wire plane that can be detected in the narrowest drift time band are incident between four and eight millimetres from the sense wire. This explains the extended peaks seen in the middle of all the distributions displayed in figures 5.13 and 5.14. Although higher frequencies would be expected at short drift times due to the high values of w_s around the sense wires, the lowering of the pulse height in these areas caused detection inefficiencies and the peak commenced at later times. Therefore from the theoretical calculations the drift time distributions would be expected to rise gradually to a maximum frequency, have a reasonably flat-top, corresponding to about a third of the drift length, and then fall rapidly due to the decrease in drift velocity on one side of the cell and the decrease in detection efficiency. At long drift times a low frequency plateau occurs due to only one half-cell contri-

buting to the distribution. Any extension of the low frequency detection region beyond the potential wires would increase the length of this plateau. This description closely resembles the experimental distributions displayed in figures 5.13 and 5.14.

Comparison between figures 5.22 and 5.24 for the values of $(\gamma-\theta)$ and w_s calculated across the chamber with the corresponding values obtained by Short in deriving the compensation mechanism, previously shown in figures 3.15 and 3.16, highlights the poor field compensation that actually existed. The idealized calculations due to Short used a constant electric field value across the chamber which produced a constant value for $(\gamma-\theta)$ in the cells closest the vacuum tank and a maximum value of 30^{o} in cell "7" after a steady rise from cell "3" onwards. In comparison figure 5.22 shows variations of up to 55^{o} in a half-cell. Similarly in Shorts' calculations w_s was constant close to the vacuum tank and rose towards the ring centre, varying by 8% overall. The computed values of figure 5.24 show variation by a factor of three in a half-cell.

The above theoretical results, although not precise, have given an insight to the true space-time relationships in the individual half-cells and have explained the poor shapes of the drift time distributions used for calibration purposes.

5.6 Observed Splitting of the Trail of Primary Ionization at the Cell Boundaries

The study of the electric drift fields and subsequent calculation of the theoretical space-time relationships was instigated not only to

explain the shapes of the drift time distributions, but also to confirm the results of other analysis. A high frequency of hits on adjacent sense wires in a chamber was noted during preliminary data analysis. It was too high for genuine double tracks or showering so the data were studied to see if the two recorded drift times could have originated from a single traversing particle. It was postulated that at the cell boundaries the trail of primary ionization could be split by the field tilting mechanism and be detected independently at the two neighbouring sense wires. With perfect field compensation the three wire-spacing tilt would exactly define drift directions in the two half-cells and splitting would occur along the 6 mm boundary measured in the sense wire plane - or more for angled tracks. However to produce a detectable number of electron swarms in each drift space the particle would have to cross a certain depth of chamber associated with each drift direction, as demonstrated in figure 5.28. Therefore a 4 mm overlap appears to allow a finite detection efficiency at both sense wires. If such a process could occur a resolution of the left-right ambiguity in each cell is inherent. This would present the only direct solution realisable in the (g-2) array.

A program was written to scan the data to find any events with just two adjacent wire hits in a chamber. The two drift times of such events were histogrammed in the respective arrays associated with the vacuum tank or ring centre drift spaces of each cell. The sums of the two drift times were also histogrammed. The values for the ring centre side of cell "0", the vacuum tank side of cell "1" and the sum are shown in figure 5.29 with the corresponding values for cells "4" and "5". The results are summed over all chambers in the array. Only the relevant

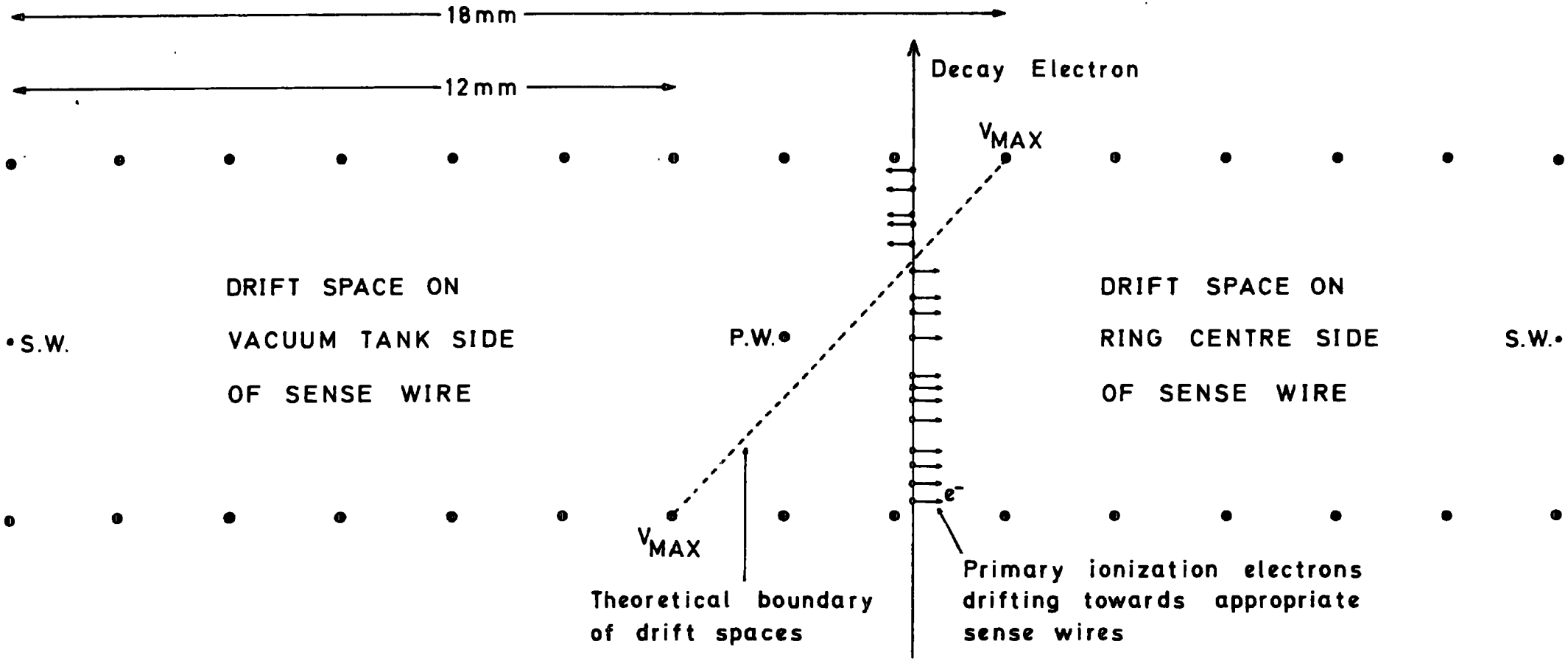

FIG. 5.28 : SPLITTING OF TRAIL OF PRIMARY IONIZATION AT CELL BOUNDARY

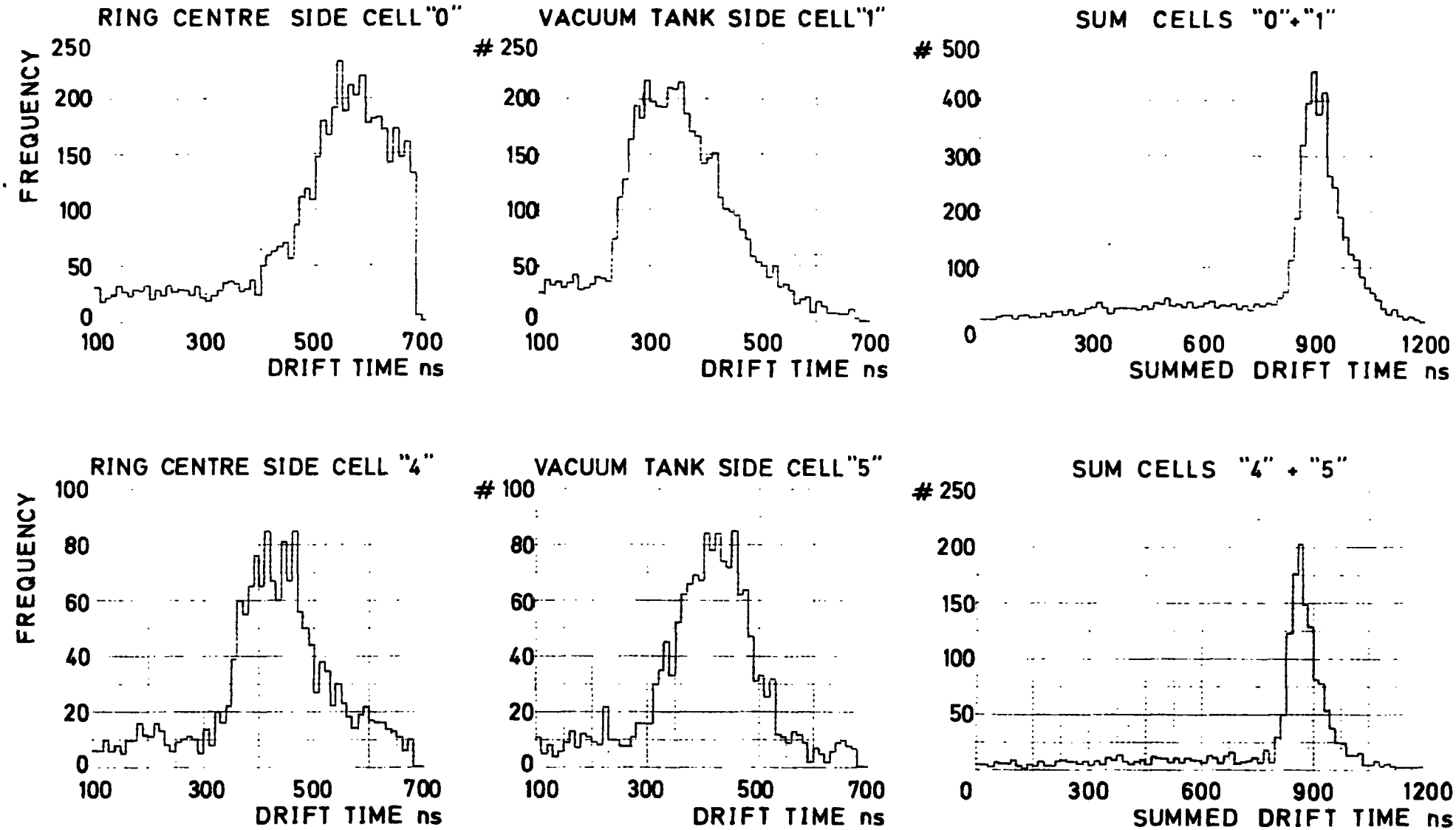

FIG. 5.29 : ANALYSIS OF DRIFT TIMES OCCURRING IN NEIGHBOURING CELLS

parts of the histograms are displayed. The drift times in the ring centre and vacuum tank sides of the sense wires are markedly different, as expected from the theoretical results. The cut-off on the ring centre side of cell "0" is due to the 676 ns digitizing limit of the system.

Table 5.1 summarizes the theoretical and experimental values obtained for the distributions of drift times at the cell boundaries. The theoretical drift times derived in the previous section were used to calculate the sum in neighbouring drift spaces, measured in the sense wire plane, and also the expected ranges of values over the entire inter-cell boundaries. The boundaries were defined by the theoretical maximum equipotential describing the three wire-spacing field tilt shown in figure 5.28. Detection efficiency was assumed to exist along the whole length of the boundary. Indeed non-orthogonally incident decay electrons would extend this overlap region, as measured in the sense wire plane, so such an assumption was valid. The theoretical potential wire to sense wire drift times were multiplied by the relevant geometrical factors to obtain the theoretical range of drift times in the boundary regions. This approximation was valid as similar field and compensation angle values existed in the boundary regions as in the main parts of the associated drift spaces. These drift time values in neighbouring half-cells were added to give the summed drift time ranges across the boundaries. Corresponding values derived from the computer analysis of the experimental data are shown. The peak values of the drift time distributions in the half-cells are taken to represent the values in the sense wire plane for particles traversing the potential wire, where detection efficiencies in both cells are greatest.

TABLE 5.1

Cell	Theoretical half-cell drift times P.W. – S.W.	Sum	Theoretical range of half-cell drift times at boundary	Theoretical range of sum	Experimental peak drift times in half-cells	Sum	Experimental range of half-cell drift times at boundary	Experimental range of sum	Experimental peak value of sum
0									
R	564	1020	403–645	989–1036	570	910	480–680	825–1065	910
V	456		586–391		340		430–250		
1									
R	558	1009	399–638	979–1025	570	900	500–680	825–1050	915
V	451		580–387		330		430–260		
2									
R	540	977	386–617	948–992	560	870	490–680	810–1035	900
V	437		562–375		310		410–260		
3									
R	496	907	354–567	882–919	460	840	380–610	795–1005	880
V	411		528–352		380		510–280		
4									
R	439	825	314–502	810–833	430	850	360–520	795–975	870
V	386		496–331		420		490–340		
5									

V = Vacuum Tank side of sense wire
R = Ring Centre

All drift times in nanoseconds

Errors: Theoretical values correct to approximations made

Experimental values ± 15 ns

Comparison of the two sets of values indicates that the theoretical model was accurate for the half-cells on the ring centre side of the sense wires, where field compensation was poor, but underestimated the drift velocities on the vacuum tank side. These discrepancies may be understood with reference to figure 5.18 and the comments of section 5.5 where it was stated that the true field around the sense wires was higher than calculated and hence lower throughout the rest of the drift spaces. In the ring centre half-cells the lowering of the drift field, which would raise the drift velocities, would be accompanied by a worsening of the field compensation angles due to the dominant role played by the low field region around the potential wire. Hence the observed drift velocity, w_s, would remain almost constant. However on the vacuum tank side the drift field would be lowered, the compensation improved and hence w_s raised. It should be noted that agreement between experiment and theory was better in the lower magnetic field regions towards cell "5". This indicates that the approximations included in the equations to derive the theoretical results are more exact at fields of 10 kG.

Summation of the drift time pairs gave the experimental distributions whose ranges and peak values are tabulated. Note the range in values compared to the addition of the experimental half-cell drift times at the boundaries, which would produce ranges in the sum of only 0-40 ns. Comparison of the peak values with the theoretical values indicate agreement at lower magnetic fields but much higher drift velocities towards the vacuum tank. Also the variation in summed drift times across the chambers is much lower than theoretically predicted. This is due to the increase in observed drift velocity in the vacuum tank side drift spaces from cells "0" to "3", followed by a decrease in drift velocity. This

was not predicted in the theoretical calculations. A probable explanation is that the field compensation in half-cells "0" to "3" was good and the increase in observed drift velocity was mainly due to the increase in w(E,B) with gradually decreasing magnetic field. Beyond cell "3", however, the magnetic field fell more rapidly and although the value of w(E,B) rose, the field tilt overcompensated the drift angle and the observed drift velocity consequently fell. The increase in observed drift velocity in the ring centre half-cells was due to a similar rise in the value of w(E,B) and, more importantly, to the lower field tilt angles providing more exact compensation in the lower magnetic fields experienced beyond the boundary of cells "2" and "3".

The trend towards near correlation of drift velocities in both the drift spaces of cells closest the ring centre presents a better explanation of the flatter tops to the drift time distributions of these cells displayed in figures 5.13 and 5.14. The experimental peak values presented in table 5.1 agree well with fall-off positions noted in the drift time distributions.

It must be noted that although the peaks of the experimental distributions have indicated the most likely drift velocities, and have been related to the theoretical results, the widths of the distributions are large and necessarily introduce uncertainties. Although limited, the experimental data probably indicate the true variations in drift velocities throughout the chamber volumes. The distributions are so significant above the background of genuine two track events and noise that the postulated splitting of the trail of primary ionization must have occurred. The width of the distributions may be explained with reference to several factors. The distributions associated with the

individual half-cells naturally have a range due to the variation in drift distances along the cell boundary. Secondary effects are due to the fields experienced by the majority of electron swarms forming the observed sense wire pulses. In cases where all the electron swarms associated with a drift space are formed close to a cathode plane, the fields experienced over the initial part of their drift length are much lower than those in the sense wire plane, as shown in figure 5.18. Hence the space-time relationships vary across the inter-cathode gap. The effect of the variation in magnetic field parallel to the sense wires has already been discussed. Variations of over 10% in field value occur in cells close to the vacuum tank, resulting in theoretical variations of drift velocity of almost the same order. The azimuthal variation in magnetic field plays a minor role in comparison.

The values for the sum of the associated pairs of drift times would only be single valued if constant drift velocities existed throughout the entire chamber volumes. In each distribution the sums of the drift times vary by over $\pm$ 11% of the mean value. This gives an indication of the variation in drift velocities throughout the entire volumes at the inter-cell boundaries. The tails to the distributions at high drift times reflect the very low field values between the potential wire and cathodes. The peak values are taken to represent the drift velocities in the sense wire planes of the chambers and the median plane of the magnet poles, where detection efficiencies and incident particle fluxes are greatest.

The analysis associated with the study of the splitting phenomenon has not only clarified the mean chamber drift velocities but also

highlighted the variation in drift velocities, especially at the cell boundaries. The long tails and imprecise shape of the whole-cell drift time distributions are also more readily understood.

5.7 Proposed System for Precise Chamber Calibration

The results presented in the previous sections have highlighted the poor drift velocity calibrations attainable without an accurate scanning system. Using the drift chamber array in situ the only accurate scanning that may have been performed would have required a complex scintillator collimator system and cosmic rays moving in a horizontal plane to trigger the timing channels. Such an arrangement would have taken a long time to accumulate sufficient data and also necessitated operation outside the normal (g-2) experiment running time. Economic and operational considerations ruled out such an approach. Historically no chambers were built at the time (g-2) magnet blocks were available for use in a testbeam calibration system. Also the need for such accurate calibrations was not evident until operation in the (g-2) experiment had commenced. Therefore, with hindsight, the following system is proposed to provide accurate calibration of the (g-2) drift chambers.

For a full calibration the drift velocities at all radial, vertical and azimuthal positions in the chambers need to be determined. Due to the unique form of the (g-2) fringe field the chamber would have to be mounted between the magnet poles in the experimental position and the incident beam and collimator system moved in relation to it. To provide an accurate series of scans at different azimuthal positions, it is probable that at least two (g-2) magnet blocks would be required to

accurately reproduce the fringe field of the total ring. Hence the full system would consist of two (g-2) magnet blocks and the baseplate to allow chamber mounting in the various experimental azimuthal positions. The collimator system would have to be firmly mounted on a traversing table which allowed independent adjustment in vertical and radial directions. The beam would be steerable and probably diffuse to allow coverage of the entire chamber volume with variation of incident angle. Such a system is presented in figure 5.30.

As low energy electrons have a high curvature in the (g-2) field it is necessary to use higher energy particles such as protons or pions. The collimator system must accurately define the trajectory of the particle, giving the position of traversal in the sense wire plane of the chamber and the angle of incidence. The most accurate system would include a combination of thin scintillators and drift chambers. The vertical (SV 1-4) and horizontal (SH 1-4) thin fingers of scintillator would be positioned upstream and downstream of the (g-2) drift chamber to define a beam of small cross-section and provide the timing trigger. The pairs of single cell drift chambers, positioned as close as possible to the (g-2) chamber, provide more precise vertical and radial co-ordinates. They need to be small but do not require calibration. The pairs of horizontally and vertically aligned sense wires are accurately surveyed so that their intersections occur at identical radial and vertical co-ordinates.

The recorded drift times in all five drift chambers, triggered by the scintillator collimator, are analysed. Only drift times within a very narrow time band are accepted from the collimator chambers, all other events being rejected. As the chambers are not calibrated the

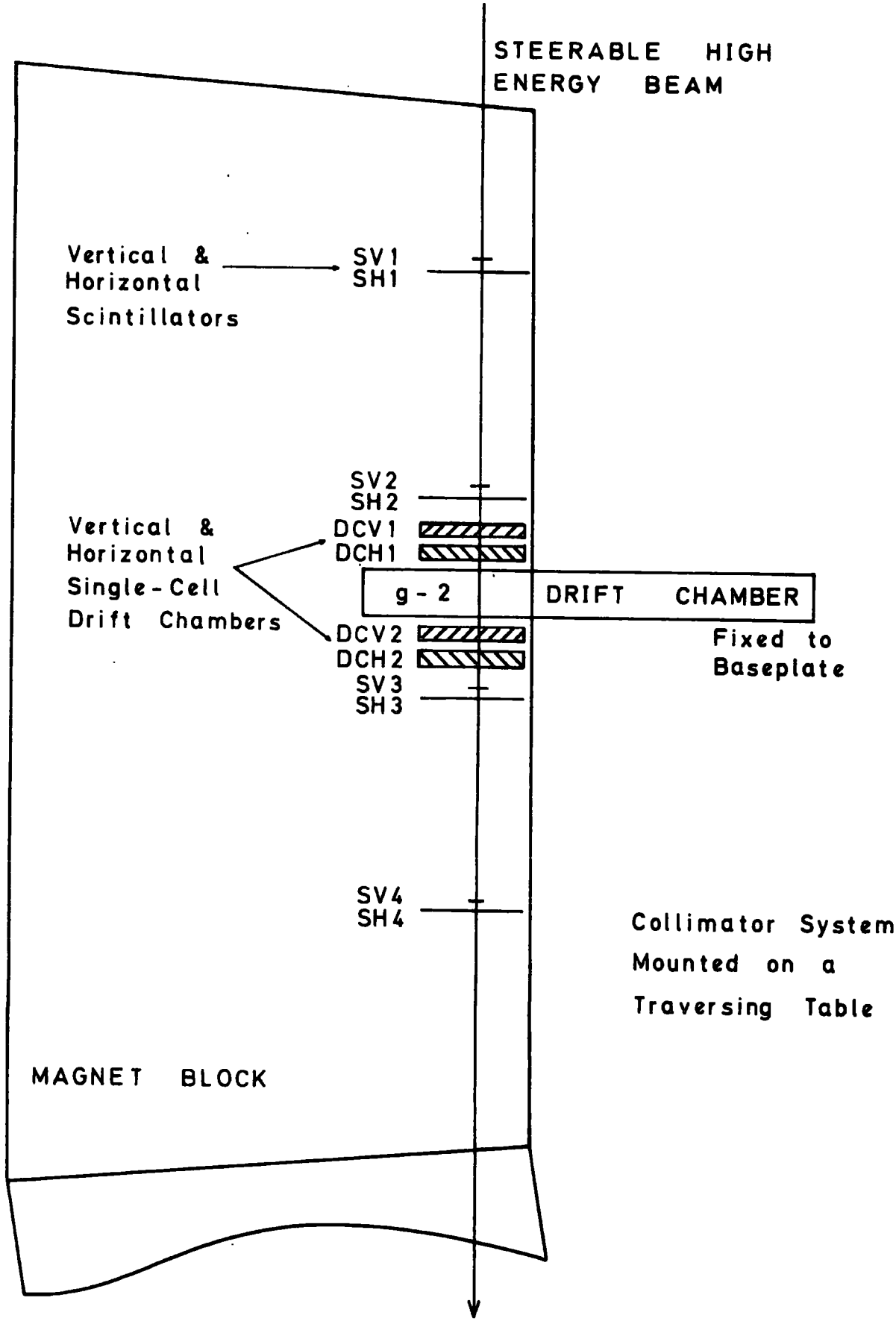

FIG. 5.30 : PROPOSED CALIBRATION SYSTEM

drift times must correspond to particles traversing very close to the sense wires, where field compensation and calibration is not required. A suitable range would be 0 - 3 ns, defining a pencil beam of square cross-section with dimensions of a few hundred microns. Such a "software collimator" has been successfully used by other workers in chamber calibrations.[1] An accurate knowledge of the collimator co-ordinates allows the exact trajectories of the incident particles to be calculated and therefore their points of intersection in the sense wire plane of the (g-2) chamber. Series of drift time distributions are recorded in radial scans across the (g-2) chamber at various vertical displacements. From the resulting space-time relationships the drift velocities may be determined throughout the chamber volume. The minima in the space-time relationships denote the sense wire positions, so checks may be made upon the alignment of the collimator system. Also from the widths of the drift time distributions the spatial resolutions may be computed. Sets of calibrations may be performed at each of the azimuthal positions in the magnet blocks normally occupied by the (g-2) chambers. Additional studies may also be made of the variation in drift times with angle of incidence of the particles. The beam would have to be realigned and the collimator system manoeuvred accordingly. Such measurements would indicate any variation in the space-time relationships for decay electrons of different energies.

The calibration system described above would necessarily involve a complex, non-magnetic scanning table to mount the collimator. In addition it would have to be surveyed precisely to produce the required accuracy. The number of sets of readings required to determine the drift velocities over the entire chamber volume is high and would be

time consuming. However due to the form of the (g-2) fringe field and the non-uniformity of the drift velocities, such a complex system is required to provide a complete and accurate calibration. If such a calibration had been performed the vertical co-ordinates of the decay electrons detected by the array would also have been required to determine the exact drift velocities in each case.

REFERENCES

1) Breskin, A., Charpak, G., Gabioud, B., Sauli, F., Trautner, N., Duinker, W., Schultz, G.,
Nucl. Inst. Meth. 119 (1974) 9

2) Short, K. A.,
Ph.D. Thesis, University of Durham (1975)

3) Browell, R.,
Ph.D. Thesis, University of Durham (1976)

4) Bailey, J. M.,
Daresbury Laboratory, Private Communication

5) Combley, F. H.,
University of Sheffield, Private Communication

6) Waligorski, M. P. R.,
Nucl. Instr. Meth. 109 (1973) 403

7) Breskin, A., Charpak, G., Sauli, F., Atkinson, M., Schultz, G.,
Nucl. Instr. Meth. 124 (1975) 189

8) Wylie, A.,
CERN NP Internal Report 74-7 6 September 1974

9) Walenta, A. H., Ph.D. Thesis, Heidelberg (1972)
data presented in
Charpak, G., Workshop on Research Goals for Cosmic-Ray Astrophysics in the 1980's.
ESRIN Frascati, 24-25 Oct 1974

10) English, W. N., Hanna, G. C.,
Canadian Journal of Physics, 31 (1953) 768

11) Fulbright, H. W.,
Ionization Chambers in Nuclear Physics,
in Encyclopedia of Physics (ed. S. Flugge)
(Springer-Verlag, Berlin, 1958), p.1.
data presented in
Sauli, F., Principle of Operation of Multiwire
Proportional and Drift Chambers
CERN 77-09 3rd May 1977

12) Bortner, T.E., Hurst, G. S., Stone, W.G.,
Rev. Sci. Instr. 28 (1957) 103
data presented in
Palladino, V., Sadoulet, B.,
Nucl. Instr. Meth. 128 (1975) 323

CHAPTER 6

DETERMINATION OF THE DECAY ELECTRON TRAJECTORIES

6.1 Introduction

The main purpose of the drift chamber array was to reconstruct the circulating muon beam profile by extrapolating the decay electron trajectories back into the storage volume. Ideally the tracking programs would be developed with calibrated data. Knowing the general bounds of the expected distribution, any errors in the programs would be immediately apparent. However, as recorded in Chapter 5, the calibrations were very imprecise. The more accurate theoretical calculations were only completed during the writing of this thesis and unfortunately time did not allow program modification to test the most probable space-time relationships. Indeed in the early stages of program development the results of the tracking analysis were used to test the drift velocity calibrations. Other members of the Nuclear Instrumentation Group had attempted to analyse the data but had derived muon radii that were too small, indicating the impossible condition of a circulating beam outside the storage volume. Therefore a new cartesian co-ordinate system was devised by the author to act as a check of the previous results.

This chapter initially evaluates the array in terms of detection efficiency and then presents additional information obtained from the data. The co-ordinate system and an outline of the method of track reconstruction follows. The results of the analysis, including several manipulations of the array geometry performed in the programs, are presented. A manual check of the methods of determining the trajectories was performed to ensure that computational errors were not

producing the low muon radii values.

The muon radii distributions obtained are discusssed and further approaches to the analysis are suggested. Finally more complex tracking methods are outlined. These could be used on exactly calibrated data in conjunction with a grid of magnetic field values over the array volume, which had been produced.

6.2 Evaluation of the Array Performance

The performance of the chambers, as regards drift times and their validity, has already been discussed. Also the data acquisition systems used have been compared. However the overall efficiency of the system in recording decay electrons of both polarities, after the initial 75 μs detection dead-time, has not yet been presented.

6.2.1 Chamber Efficiencies

The overall data taking rate of the array depended ultimately upon the number of muons stored with each injection. As the chambers were only fully efficient 75 μs after injection and could only detect one decay electron each cycle, detection was dependent upon an electron decaying at later times in the correct section of the ring. A trigger from the downstream shower counter C10, in coincidence with the timing gate, was recorded in up to 60% of all cycles with good beam conditions when operating with negative polarity muons. With bad beam the proportion fell as low as 20%. The cleaner injection associated with storing positive polarity muons allowed detection at earlier times

in the cycle and trigger rates of up to 70% were recorded.

5-10% of the shower counter triggers had no associated drift times. This was due to the region extending 30 mm radially from the potential wires in the curved end half-cells to the vacuum tank, where detection was not possible. The trajectories of some high energy decay electrons would be confined to this region over the sector defined by the drift chamber array. They would trigger the shower counter but not be detected by the array. Detection inefficiencies in the curved end cells of the downstream chambers would also be included in this figure.

The data were analysed for single track events. These were defined rudimentarily as those events which had only one wire hit in a chamber and no more than two drift times recorded on that wire, the correct choice of time being made as previously described. In addition the cells hit in successive downstream chambers had to trend towards the ring centre, thereby assuring correct curvature of the decay electron. These constraints removed events containing spurious hits due to chamber noise, showering or genuine multiple tracks. However events with adjacent cells hit in a chamber, due to the splitting of the primary ionization, were also rejected. Single track events were obtained for 50% of the shower counter triggers with the final data acquisition system and negative polarity muons. However before the modifications to the amplifier/discriminator circuits only 25% of the triggers produced single track events.

The results of a long run taken with negative polarity muons are presented in figure 6.1. The single track events are sub-divided into the four (g-2) energy levels and also into the number of chambers hit on each track. These are presented as percentages of the total in each classification. It will be noted that the higher energy electrons

TOTAL NUMBER OF TRIGGERS = 40,360
NUMBER WITH NO DRIFT TIMES = 4,497 = 11·14 %
NUMBER OF SINGLE TRACKS 1-8 HITS = 20,529 = 50·86%
NUMBER OF SINGLE TRACKS 3-8 HITS = 10,032 = 24·86%

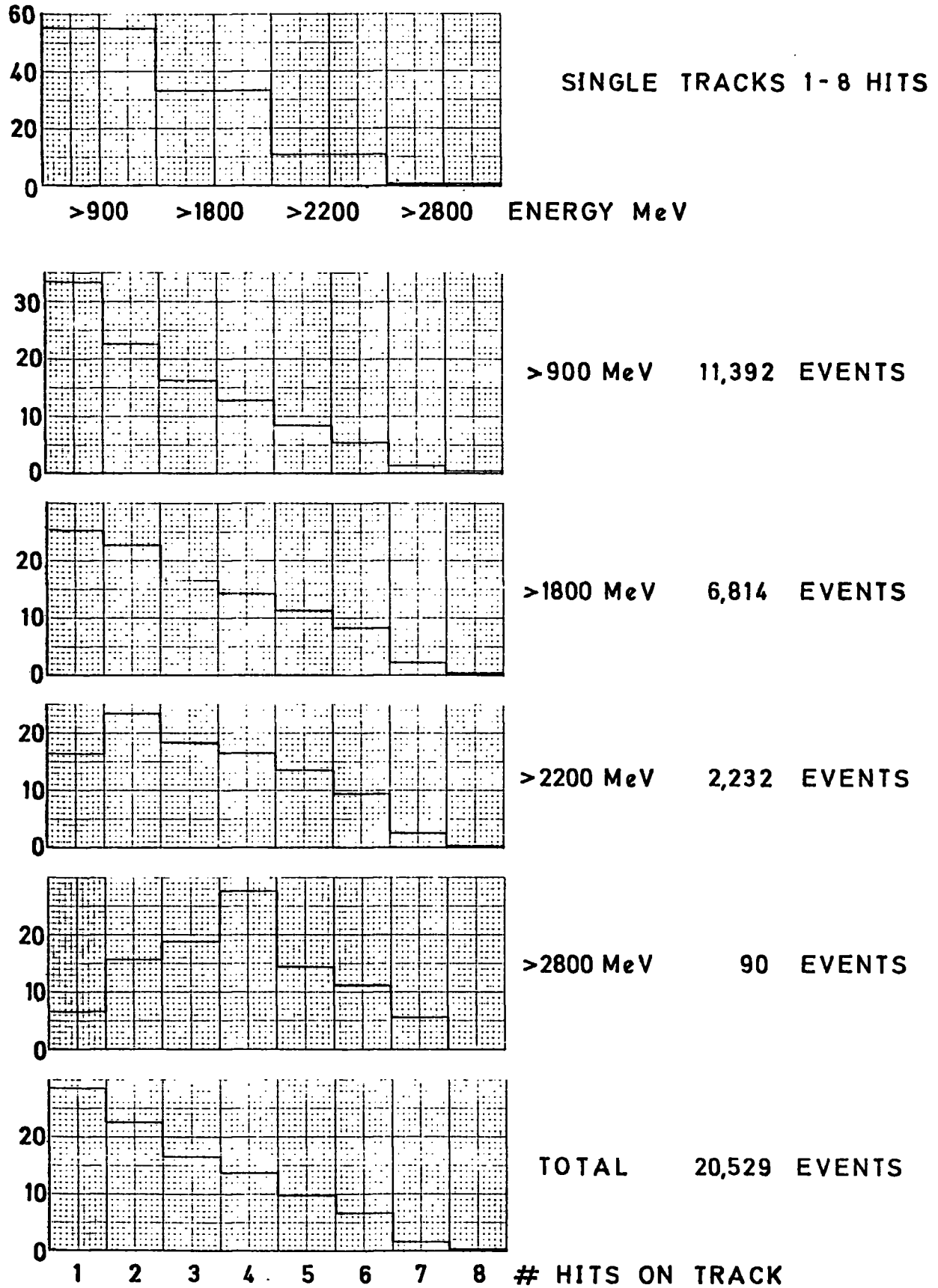

FIG. 6.1 : BREAKDOWN OF SINGLE TRACK EVENTS

traversed a greater number of chambers due to the smaller radius of curvature of their trajectories. However 50% of the events had only one or two points defined on the trajectories and hence reconstruction was impossible, a minimum of three being required. Hence with the data presented only 25% of the original triggers produced candidates for tracking analysis. Before modifications to the acquisition system this figure was as low as 10%.

The individual cell efficiencies are more difficult to define. During trials at the Daresbury Laboratory cell efficiencies of 99% had been achieved in the absence of magnetic fields.[1] No specific measurements were performed in the (g-2) array and off-line analysis would be rather subjective. The two outer chambers of an adjacent triplet could be used as a collimator and the cell efficiencies in the middle chamber calculated. However the existence of a genuine traversing particle may be defined in many ways and the removal of spurious hits presents a problem. The fact that all three hits need not occur in corresponding cells in each chamber also introduced problems. Therefore a more realistic estimate was derived for the array as a whole. Obviously some cells may be more inefficient than others, normally due to mechanicial imperfections, but an average value would give an indication of the lower limit of chamber performance.

From the data presented in figure 6.1 may be calculated the number of cells hit in all single tracks with at least three data points recorded. Further analysis indicated whether the track was first detected in cell "0" and whether it was detected in successive chambers until the end of the array. The number of exceptions indicated the inefficiency of the cells. However from geometrical considerations the

track would not always be detected in cell "0" due to the large azimuthal spacing of the upstream chambers. Also some sense wires were disconnected due to breakdown problems. Therefore the average efficiency of 82% derived from the data represents an underestimate of the true value.

6.2.2. Results from the EDM Counter

The function of the twin-armed scintillator counter positioned between chamber "H" and shower counter C10 has been described in Chapter 1. As stated, either the "up" or "down" counter could be in coincidence with the shower counter, or both, or neither. The ratio of counts in the up and down counters indicated the position of the split between the two scintillator arms in relation to the median plane of the vertical muon distribution. Figure 6.2 shows the average distribution of coincidences over a twenty-two day period recording the decay of negative polarity muons. The percentages varied by only $\pm$ 0.8%, even when the scintillators were inverted but maintained at the same vertical position. This demonstrated the equal efficiencies of the two independent scintillators and also the stability of the stored circulating muon beam.

Also shown in figure 6.2 is a breakdown of the "no coincidence" events into the four (g-2) energy levels. The high percentage of low energy events suggested that the decay electrons, although detected in the chambers and shower counter, passed on the ring centre side of the active area of the EDM counter. A check of the cells traversed by the particles confirmed that the trajectories were of high curvature and

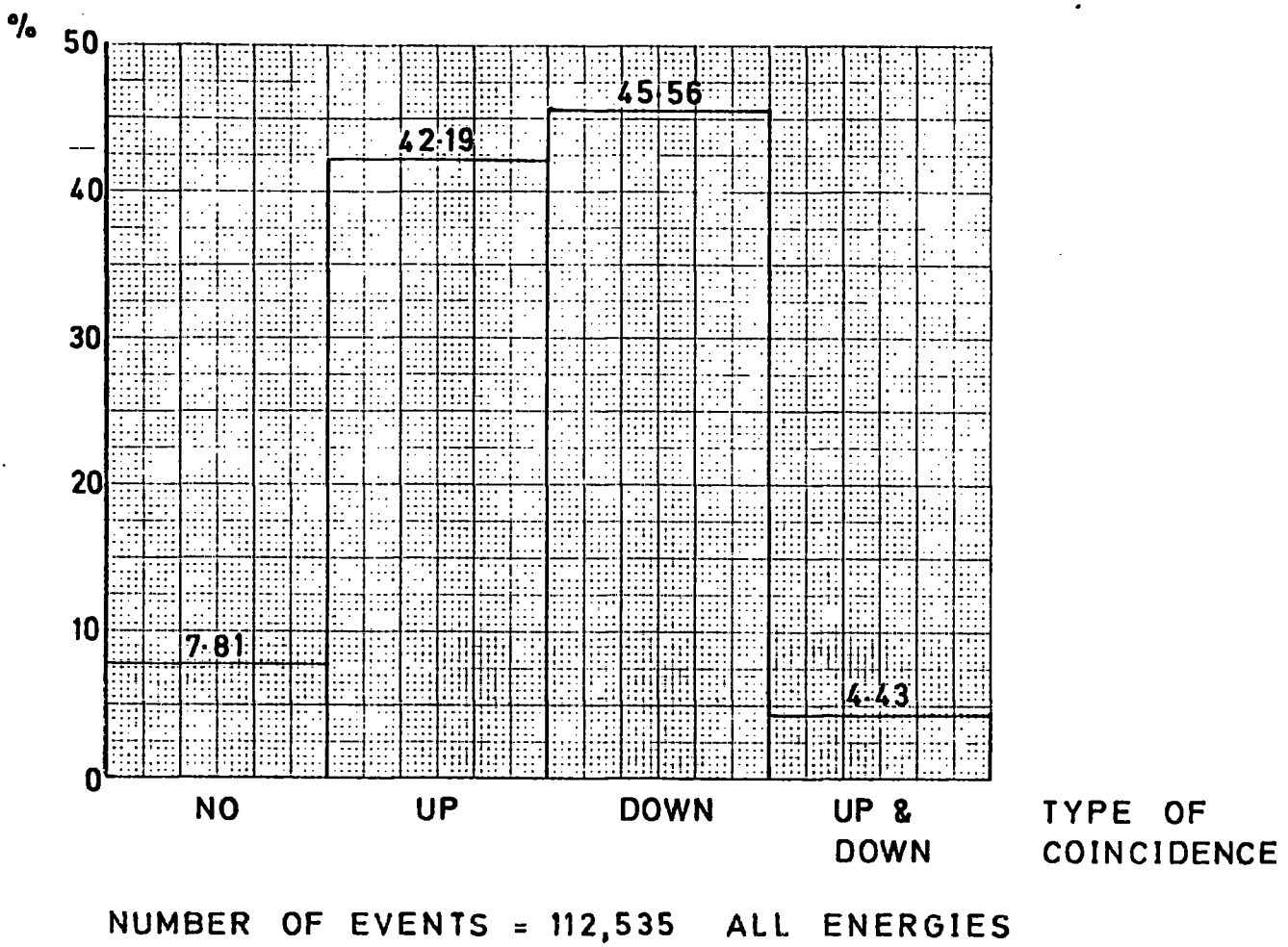

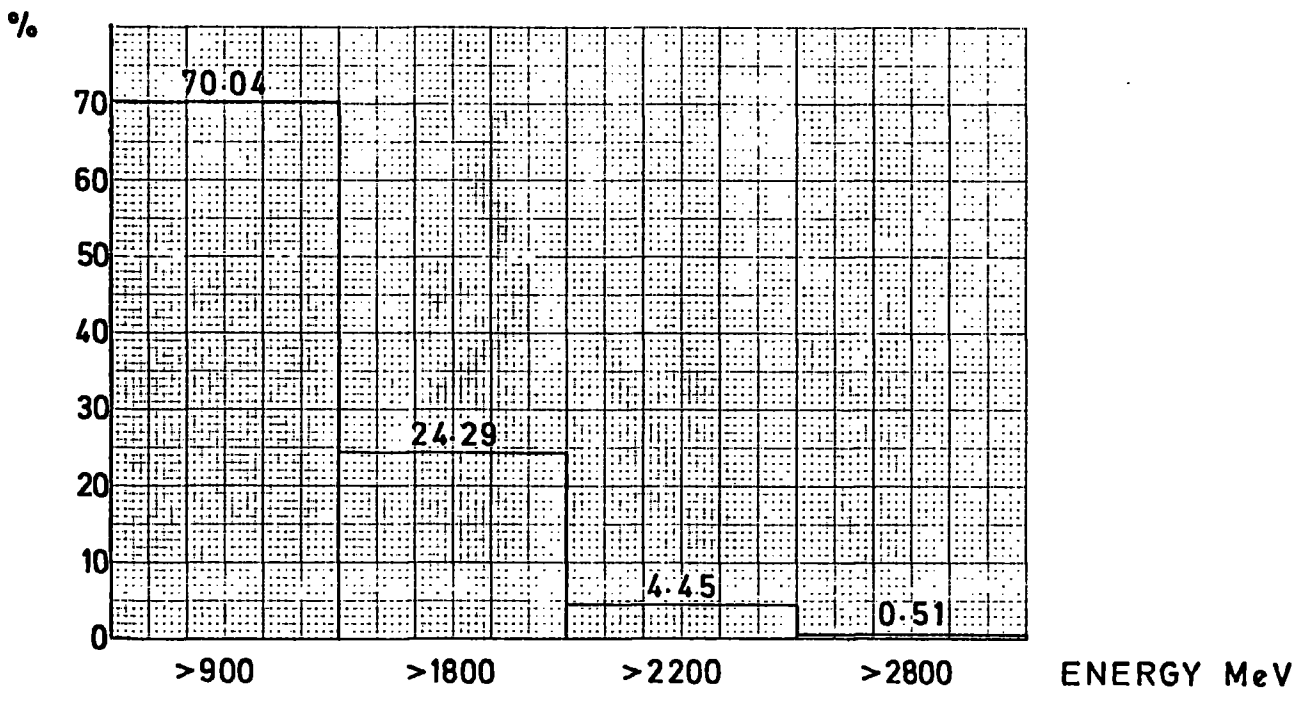

FIG. 6.2 : BREAKDOWN OF EDM COINCIDENCES

that the electrons traversed cell "6" or "7" in the most downstream drift chamber adjacent to the EDM counter. This indicated that the efficient detection area of the EDM counter did not extend as far towards the ring centre as that of the shower counter.

6.2.3. Calculation of the (g-2) Precession Frequency

The occurrence times of the detected decay electrons, in relation to the injection of the pion beam, were recorded using 50 MHz and 1 MHz clocks as described in Chapter 4. The times were histogrammed for all single track events with agreement between the two timing channels. The resultant distribution is shown in figure 6.3 for a series of runs recording negative polarity muon decays. The characteristic exponential decay with superimposed (g-2) precession frequency is observed. The distribution begins at 75 μs due to the delay set in the system timing gate to ensure full chamber efficiency. The average precession period over the twenty-eight oscillations recorded is 4.31 $\pm$ 0.04 μs, which agrees with the computed (g-2) value of 4.29655 μs. This confirms that the analysis program successfully selected single decay electron tracks and not noise associated with a non-rotating background.

6.3 Tracking Analysis

As previous attempts at track reconstruction by other authors had produced horizontal muon distributions outside the vacuum tank volume a totally new cartesian co-ordinate system was devised. This

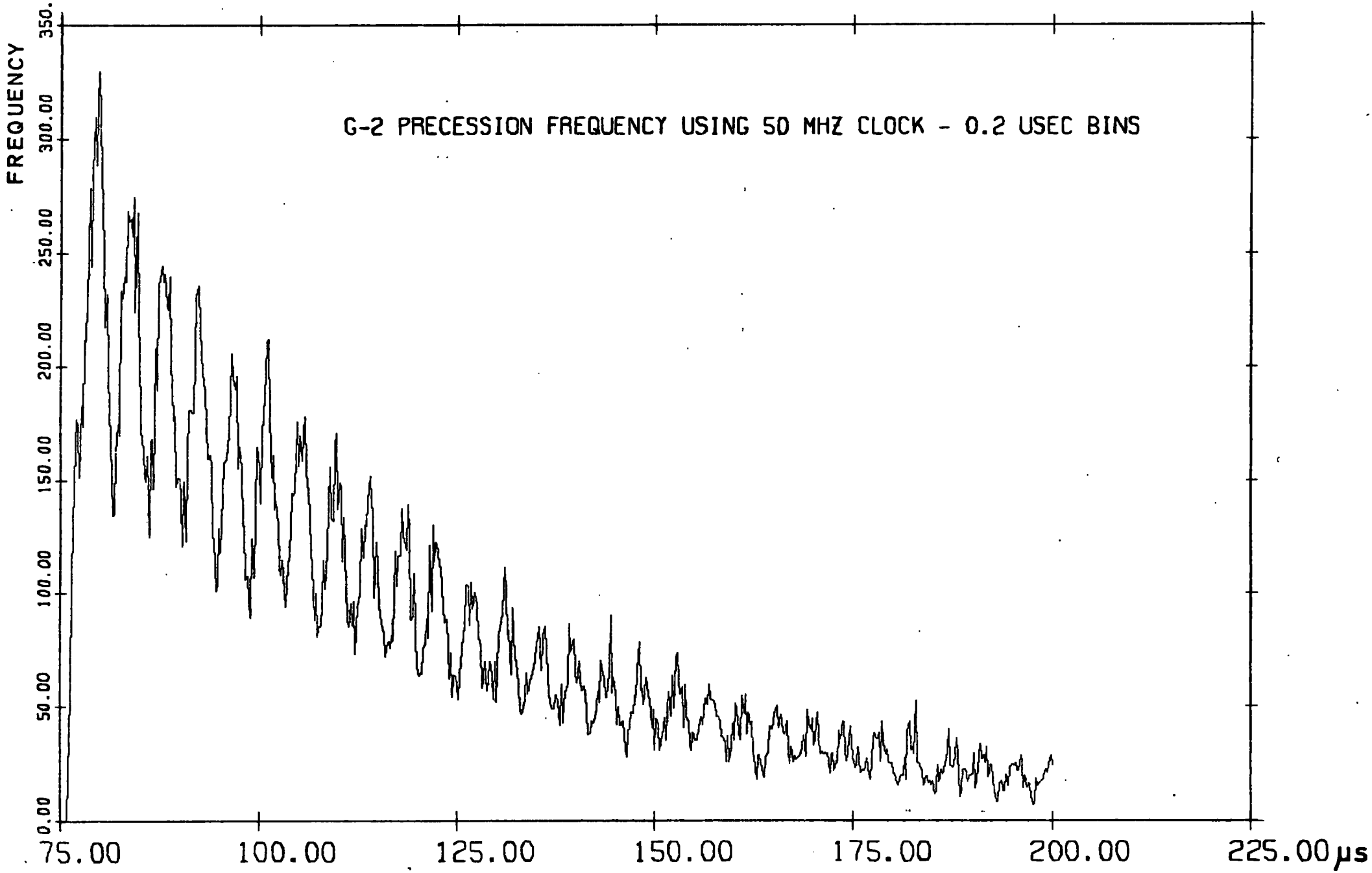

FIG. 6.3 : OCCURRENCE TIMES OF DETECTED DECAY ELECTRONS

not only defined the sense wire positions more accurately but used the baseplate datum line as the ordinate axis and the centre of the ring as the origin of the co-ordinate system. Therefore the computed sense wire positions could be directly checked with the physical measurements described in Chapter 3.

The principles of the analysis programs are explained and the results presented. A detailed study of computer round-off errors was made to ensure that the low muon radii values were not the result of truncation errors. The effects of varying the array geometry by modification of the computer programs are discussed.

6.3.1 The Co-ordinate System

Each drift time recorded represented a pair of possible chamber positions corresponding to drift lengths on either side of the sense wire. A knowledge of the (X,Y) co-ordinates of the appropriate sense wire, the chamber azimuthal angle θ and the drift length, x, allowed the exact co-ordinates of the two possible traversal positions in the sense wire plane to be calculated. Figure 6.4 shows that the method of co-ordinate determination was identical to the chamber mounting procedure described in section 3.7. The sense wire (X,Y) co-ordinates were calculated from the measured radial distances, R, and the correction factors, ΔR, used to compensate for the non-radial mounting of the sense wire planes. The chamber angles, θ, were positive for chambers mounted upstream of the datum line and negative for downstream chambers. The correction angles, $\Delta\theta$, calculated for each sense wire, were always directed downstream. The drift length, x, calculated from the recorded drift time and the calibrated drift velocity, was measured along the sense wire

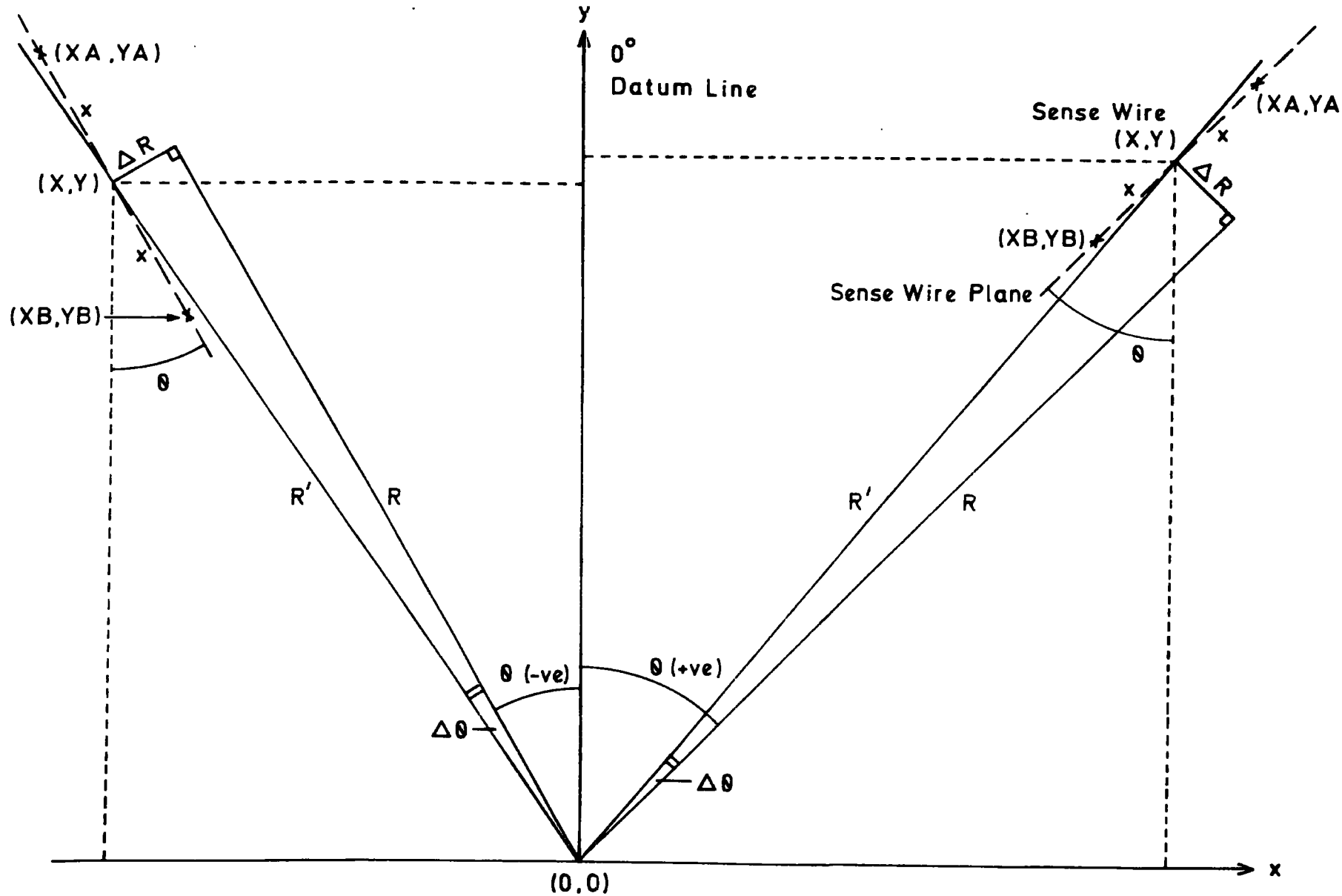

FIG. 6.4 : DETERMINATION OF TRAVERSAL POSITION CO-ORDINATES

plane. The two possible pairs of co-ordinates for the traversal positions were given by:

$$\begin{aligned} XA &= X + x \sin \theta \\ YA &= Y + x \cos \theta \end{aligned}$$

$$\begin{aligned} XB &= X - x \sin \theta \\ YB &= Y - x \cos \theta \end{aligned} \qquad (6.1)$$

where suffix "A" denotes the vacuum tank side of the sense wire and "B" the ring centre side. The sign of the angle θ ensures that equations (6.1) hold for solutions in chambers on both the upstream and downstream side of the datum line.

An uncertainty of $\pm$ 0.1 mm in the value of R typically produces uncertainties of $\pm$ 0.01 mm in X and $\pm$ 0.099 mm in Y.

If the sense wire planes had been mounted radially the use of a polar co-ordinate system would have been adopted in preference to the cartesian system used.

6.3.2 Curve Fitting Procedures

Decay electrons traversing the (g-2) fringe field had trajectories of complex form. However, as demonstrated in figure 5.15, the magnetic field fell less than 1 kG over cells "0" to "2". Therefore a circle fit would represent a good approximation in these three cells which contained the majority of the data. Figure 6.5 indicates the method of determining the radius of the muon orbit from the assumed circular trajectory of the decay electron. The electron decayed tangentially in the forward direction from the muon orbit in the laboratory reference frame as only decay energies above 900 MeV were selected.

A circle could only be fitted to single tracks with at least three

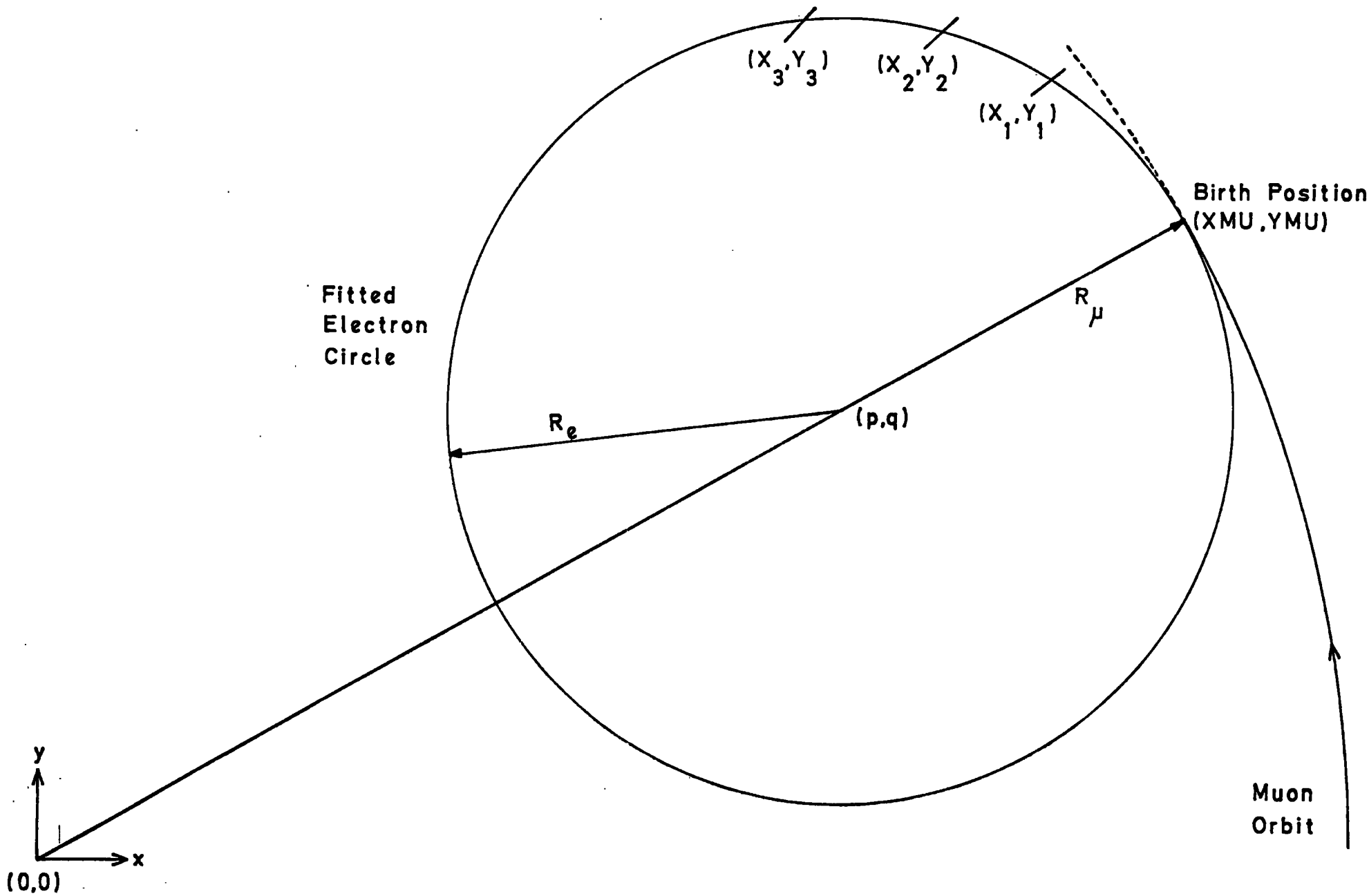

FIG. 6.5 : DETERMINATION OF THE MUON ORBIT RADIUS

recorded drift times. Taking one of the pair of possible co-ordinates in each of the three chambers, represented in figure 6.5 by the points (X_1, Y_1), (X_2, Y_2), and (X_3, Y_3), a circle of radius R_e and centre co-ordinates (p, q) could be fitted in the following manner. The basic equation of such a circle, including the point (X, Y), is:

$$X^2 + Y^2 + p^2 + q^2 - 2Xp - 2Yq = R_e^2 \qquad (6.2)$$

Substituting for each of the three known points in turn, three equations in three unknowns may be derived:

$$X_1^2 + Y_1^2 + p^2 + q^2 - 2X_1p - 2Y_1q = R_e^2 \qquad (6.3)$$

$$X_2^2 + Y_2^2 + p^2 + q^2 - 2X_2p - 2Y_2q = R_e^2 \qquad (6.4)$$

$$X_3^2 + Y_3^2 + p^2 + q^2 - 2X_3p - 2Y_3q = R_e^2 \qquad (6.5)$$

The following parameters were computed, each of which were always positive valued:

$$A = X_1 - X_2 \qquad D = Y_1 - Y_2 \qquad G = X_1^2 + Y_1^2$$

$$B = X_1 - X_3 \qquad E = Y_1 - Y_3 \qquad H = X_2^2 + Y_2^2$$

$$C = X_2 - X_3 \qquad F = Y_2 - Y_3 \qquad I = X_3^2 + Y_3^2 \qquad (6.6)$$

From equation (6.3)

$$R_e = \left[G + p^2 + q^2 - 2(X_1p + Y_1q) \right]^{\frac{1}{2}} \qquad (6.7)$$

Subtracting equation (6.4) from (6.3) gives:

$$q = (G - H - 2pA)/2D \qquad (6.8)$$

Similarly by subtracting equation (6.5) from (6.3) and substituting the derived expression for q in equation (6.8) and re-arranging, an equation for p solely in terms of the known parameters of (6.6) is derived:

$$p = \frac{G - H - \left[D(G - I)/E \right]}{2 \left[A - (BD/E) \right]} \qquad (6.9)$$

It may be seen that three expressions exist for R_e depending upon which of equations (6.3, 4, 5) is chosen as the source. Similarly three pairings are available to derive q and six combinations to derive p. Hence the value of R_e may be deduced fifty-four ways. Each uses different combinations of the parameters listed in (6.6) and therefore different truncation errors may be expected. Using double precision arithmetic in the FORTRAN programs the values of R_e, p and q agreed to the fourteenth significant figure in all cases. The parameters used in equations (6.7, 8, 9) gave results close to the mean values of all combinations and therefore were used in the analysis programs.

Tangentiality between the muon orbit, centred on the origin, and the extrapolated electron decay circle occurred at the point (XMU,YMU). This was defined by the outer intersection of the line joining the origin and the point (p, q) with the electron circle. The equationof the line is simply:

$$Y = q\,X/p \qquad (6.10)$$

and the equation of the electron circle which includes the birth position (XMU,YMU) is:

$$(XMU - p)^2 + (YMU - q)^2 = R_e^{\,2} \qquad (6.11)$$

Hence substitution from equation (6.10) for XMU and calculation of the positive root of the quadratic equation gives the value of YMU as:

$$YMU = q + \left[R_e^{\,2} / (1 + p^2/q^2) \right]^{\frac{1}{2}} \qquad (6.12)$$

and hence $XMU = p\ YMU/q$ (6.13)

leading finally to the radius of the muon orbit:

$$R_\mu = (XMU^2 + YMU^2)^{\frac{1}{2}} \quad (6.14)$$

It must be noted that a parabolic or higher order polynomial fit to the data points would produce a smaller value for R_μ than the simple circle fit. Therefore if the muon radii distribution is undervalued with a circle fit, the adoption of a more accurate fitting procedure would exacerbate the problem. For this reason the circle fit was persued at length in the analysis.

6.3.3. Description of the Tracking Programs

All the programs had a similar structure, any detailed variations are described in the next section with the presentation of the results.

Initially the sense wire co-ordinates, chamber angles, maximum drift times and cell drift velocities were read from permanent files and all counters, flags and histogram arrays were zeroed. The tapes were positioned at the beginning of the required runs using the standard tape reading subroutines and the individual events read in turn. Each event was tested for correct tape format, number of drift times recorded and the (g-2) energy level and EDM coincidence values deduced. The drift times, cell and chamber numbers were unblocked and tested to see if a single track with correct curvature had been recorded. Candidate tracks had to have at least three data points. If the track was not first recorded in cell "0" or not recorded in successive chambers until the end of the array a counter was incremented but the event still

accepted. If all three hits occurred in cells "0", "1" or "2" the chamber and cell numbers plus drift times were put into arrays for transfer to the fitting subroutines. The drift times were checked to confirm that they fell in the expected range. Any events not fulfilling all these conditions were rejected, appropriate error counters being incremented.

The first fitting subroutine calculated the pairs of possible traversal co-ordinates as described in section 6.3.1. The circle fitting routine was then called eight times for each possible combination of three points from the three pairs of traversal positions. This subroutine calculated the radial distances from the origin of the three points and if the values did not decrease in successive downstream chambers then the fit was rejected as the curvature was incorrect. The parameters of equation (6.6) were computed and the values of p and q derived for the co-ordinates of the centre of the electron circle. A negative ordinate value, q, would imply either an electron radius greater than the parent muon radius, or a small electron radius occurring on the opposite side of the ring to the drift chamber array. Such solutions were not permissible so the fits were rejected. The radial distance of the point (p,q) was calculated and compared with the known range of possible radii for 900 - 3100 MeV electrons decaying in a 14.7 kG field from any point in the storage volume. Any solution outside these bounds was rejected. A further check was made knowing the possible ranges of electron radii for each of the four (g-2) energy levels. Allowing some latitude in these ranges, the computed value of R_e was compared and the fit rejected if it did not fall within the appropriate range. The birth position

(XMU,YMU) and the muon radius R_μ were calculated for correct fits. Also the decay electron energy could be calculated from the value of R_e. Using the expression for an electron describing a circular trajectory in a magnetic field:

$$Bev = \gamma m_e v^2 / R_e \qquad (6.15)$$

and ignoring the small rest mass energy of the electron, the energy in MeV is calculated from R_e, measured in millimetres, for an average magnetic field of 14.4 kG, by the formula:

$$E = \gamma m_e vc = ecBR_e = 0.432\ R_e \qquad (6.16)$$

The computed variables, or error flags, were returned for each of the eight fits. The calling subroutine checked all the results and incremented the counters. The muon radius was checked to see if it was in the range 6700 - 7100 mm, a much greater range than expected.

If no correct fits were obtained for an event, an error flag was set and a return made to the main program.

If a single good fit was obtained all the parameters were returned to the main program. With later tracking programs, if a fourth hit was recorded a further subroutine was called to calculate the deviation of this fourth point from the fitted circle. In turn the co-ordinates of the two possible traversal positions in the fourth chamber were substituted in the circle equation, with known values of p and q, to calculate the radius, R. The two values of R were compared with R_e and the smaller of the differences taken as the deviation. The deviations were histogrammed according to (g-2) energy level and cell number.

If more than one good fit was obtained for an event the computed

electron energy was compared with the range of the appropriate recorded (g-2) energy level. If only one fit fell within the range, then it was taken as the correct fit and, if applicable, the deviation of the fourth point computed before returning all parameters to the main program. Otherwise ambiguity still existed and an error flag was returned.

In the main program the counters were incremented and the returned parameters scaled for inclusion in the histogram arrays. The contents of the counters were displayed at the end of each run to illustrate the number of tracks selected and a breakdown of the types of fits and rejections made. The counters were also summed over a series of runs on an entire tape and a summary printed. The histograms were displayed using a general purpose routine written by the author. In the later programs the values of p, q, R_e, XMU and YMU were displayed for all fits with a counter for all error flags returned. Similar parameters were displayed for single good fits only. The effects of varying the array geometry and drift velocities could be studied closely with these histograms. The deviations of the fourth points, if computed, were displayed next, followed by the calculated electron energies sub-divided into the (g-2) energy levels recorded for each event. Finally the muon radii were presented, initially divided into the four energy levels and then totalled over all energies.

6.3.4 Results of the Track Analysis

The axis of the storage tank had a radius of 7000 mm and the tank walls had radii of 6914 mm and 7086 mm. However the active storage volume was limited in most sections of the ring by the electrostatic

field electrodes which were only ± 60,8 mm from the axis in the horizontal plane. Therefore the expected distribution of muon radii would extend from 6940 mm to 7060 mm, with a peak around 7000 mm as the optimum storage conditions applied for the axis. As the vertical co-ordinates of the decay electrons were not recorded, the computed distributions included electrons decaying from the entire vertical dimension of the active storage volume, which extended ± 40 mm from the median plane. This would accentuate the peak around the axis value.

When the first tracking program was developed the drift velocities were very uncertain. Therefore a series of fits were made over a range of values. A rigorous track selection demanded at least three hits on a track and the first recorded hit had to be in cell "0" with consecutive chambers hit until the end of the array. Constant drift velocities were assumed throughout each cell; the maximum drift times in cells "0", "1" and "2" ranged from 850, 810 and 780 ns respectively, down to 610, 590 and 570 ns in nine equal steps. A typical distribution for the muon radii, summed over all energies, is shown in figure 6.6 for the lowest maximum drift time values. Over the entire range of drift velocities the peak of the distribution shifted from 6914 mm to 6921 mm, maintaining a similar shape throughout. Also the number of fits obtained with the same data rose by 25% over the range. Thus the lower maximum drift times, and hence maximum drift velocities, gave the best results. However the majority of the distribution still lay outside the actual storage region and a further lowering of the maximum drift times would not move the distribution an appreciable amount. It was noted that the fits for higher energy decay electrons did produce higher muon radii, the

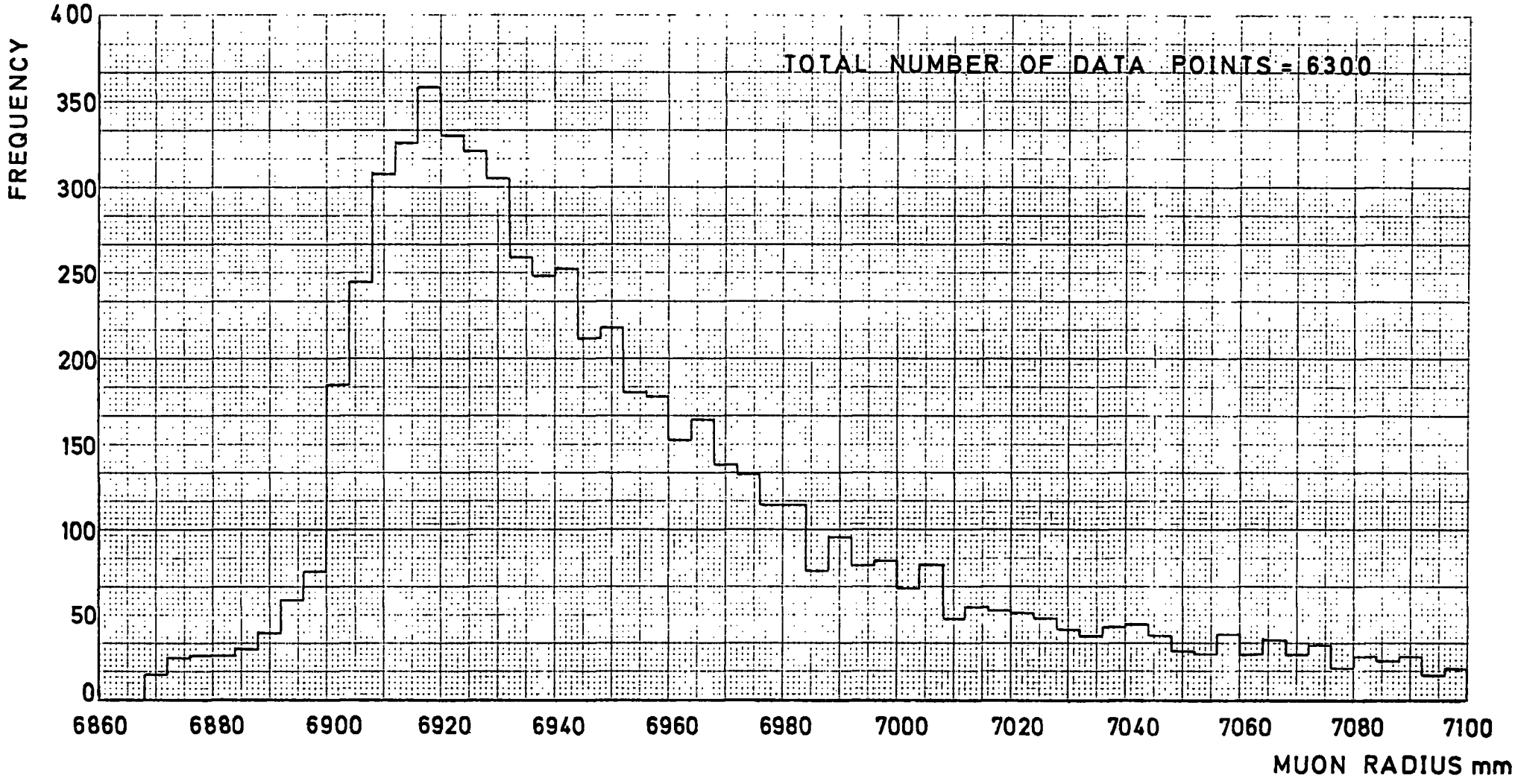

FIG. 6.6 : TYPICAL MUON RADII DISTRIBUTION SUMMED OVER ALL ENERGIES

peaks of these distributions approaching 6940 mm. However the majority of the data were for lower energy decays and the higher radii fits only formed the tail of the total distribution. The better fits were probably due to the higher energy decay electrons having low curvature and therefore the hits occurred mainly in the vacuum tank half-cells of wires "0" and "1", where the linear space-time relationships were more valid.

Another series of programs had modified input parameters to represent distortions in the positions of the drift chamber array. Tracks with at least three hits were chosen, but they did not necessarily have to be detected first in cell "0" or in consecutive chambers.

Initially the azimuthal chamber angles were altered by $\pm 1^{0}$, far more than any possible error in the mounting of the baseplate. As the fitting procedure was azimuthally symmetric the distributions should be unaltered. This was indeed the case with identical distributions for all histogrammed parameters. Not only did this confirm the correctness of the fitting procedure but it also demonstrated that truncation errors did not occur in the computation.

The second series of tests compared the normal distribution with those obtained when increasing and decreasing the sense wire radii by 10 mm. The effect was to slightly alter the forms of the distributions and to move the peaks slightly less than 10 mm in the appropriate directions. Although small errors were quoted for the measured sense wire positions, they could not explain the errors in the muon radii distributions.

Finally the correction angles $\Delta\theta$, to allow for the non-radial mounting of the sense wire planes, were altered by $\pm 0.1^{0}$. This

corresponded to an error in the mounting of the chamber cradles on the baseplate and also to a non-parallel alignment of the sense wire plane with the cradle axis. No discernible shifts in the peak values were noted and the distribution shapes were only slightly altered.

As the baseplate was shaped to fit closely to the faces of the magnet blocks it was thought unlikely that any mis-alignment of the whole array occurred. From the results presented above it was clear that any possible chamber mis-alignment could not account for the total error in the muon radii distribution. Therefore further studies concentrated on the drift velocities used in the determination of the drift distances.

The whole cell drift time distributions obtained during the initial data analysis had long tails at high drift times, which indicated lower drift velocities in the potential wire regions. A series of corrections were applied to the recorded drift times to compensate for the resultant non-linearity of the space-time relationships. Figure 6.7 demonstrates three assumed forms of the space-time relationship which could be reduced to linearity by the formula:

$$DT_{corr} = DT - \left[(DT/MAX)^{n} \times CORR\right] \qquad (6.17)$$

The corrected drift time, DT_{corr}, was calculated from the recorded drift time, DT, by subtracting a term derived from the maximum recorded drift time in the cell, MAX, and its difference from the maximum linear relationship value, CORR. The exponentiation factor, n, determined the precise form of departure from linearity, as shown in figure 6.7. The fourth power produced the least departure from linearity at shorter drift times. The values of MAX and CORR used in cells "0", "1" and "2" for all fits are shown, the displayed curves applying to cell "0". The

$$DT_{corr} = DT - \left[\left(\frac{DT}{MAX}\right)^{n} \times CORR\right]$$

Cell	MAX	CORR
0	800	160
1	770	140
2	740	130

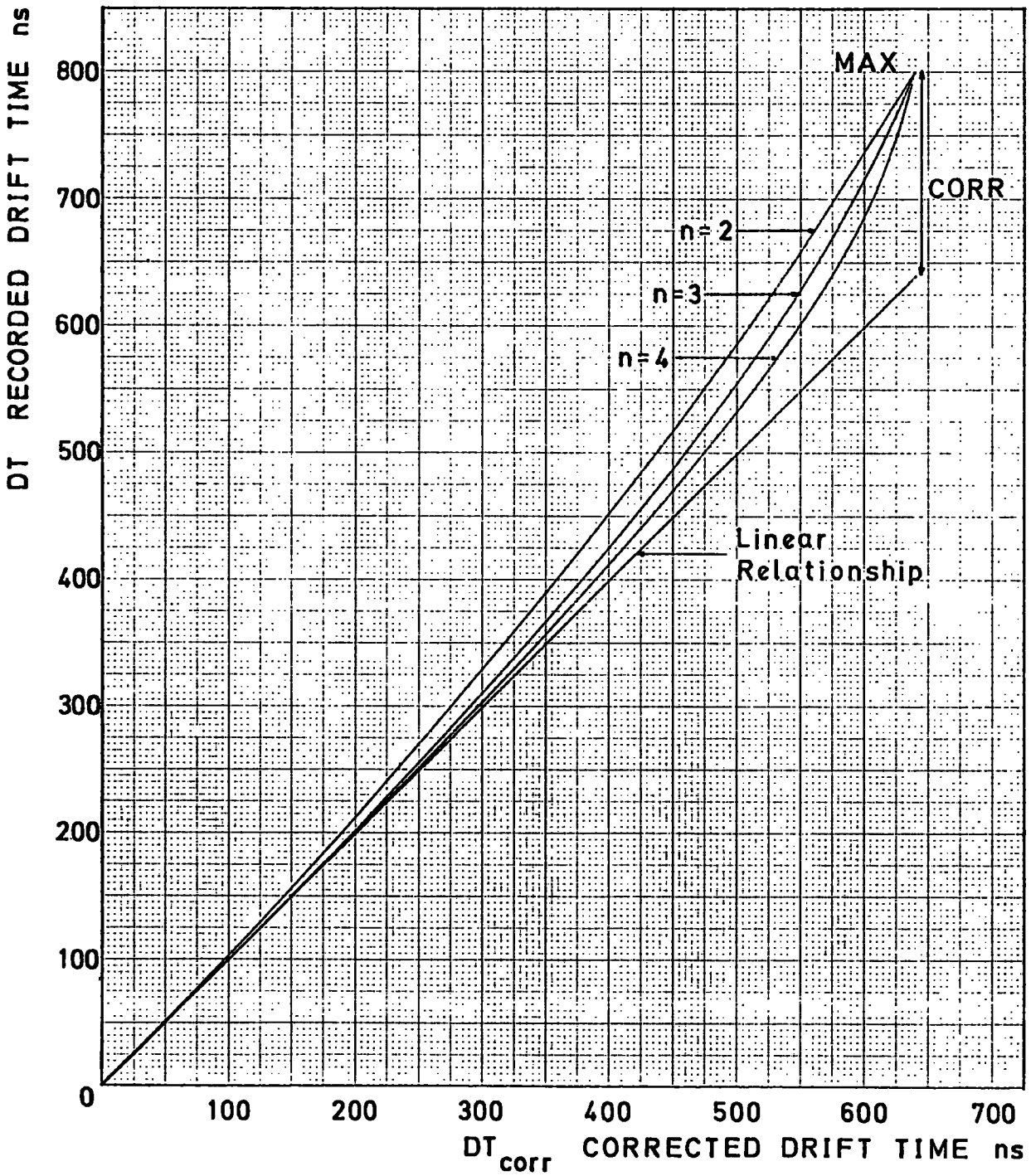

FIG. 6.7 : ASSUMED SPACE-TIME RELATIONSHIPS REDUCED TO LINEARITY BY FORMULA

space-time relationships were assumed to be valid for the drift spaces on either side of the sense wires.

Comparison of the results obtained with n = 2,3 and 4 revealed higher muon radii with increasing values of n, and also an increased number of single good fits achieved with the same data. This indicated that the space-time relationships described by n = 4 most closely resembled the experimental values. As before, better fits were obtained for higher energy decay electrons. However a lower proportion of the single track events produced single good fits compared to lower energy electrons. Also more ambiguous fits remained for the lowest energy electrons. Figure 6.8 provides a breakdown of the success of the fitting procedures for each (g-2) energy level with n = 4. Figure 6.9 presents the muon radii distributions obtained from the same analysis. The shift towards higher radii is observed with increasing energy but, as the low energy data dominate, the total distribution still peaks at low values. As the lower energy particles traverse cells closer to the ring centre more often than the higher energy particles, it appeared probable that the postulated space-time relationships applied more accurately to cells "0" and "1". Indeed the theoretical space-time relationships derived in Chapter 5 showed close agreement between the ring centre side half-cell values, shown in figure 5.27, and the n = 4 fit. However the vacuum tank side half-cells appeared to have more linear relationships and therefore the n = 4 fits did not represent either the form or higher values of the drift velocities in these half-cells. Hence the lower energy decay electrons, which traversed closer to the ring centre, would tend to include more data points in the vacuum tank half-cells and therefore introduce a systematic distortion of the

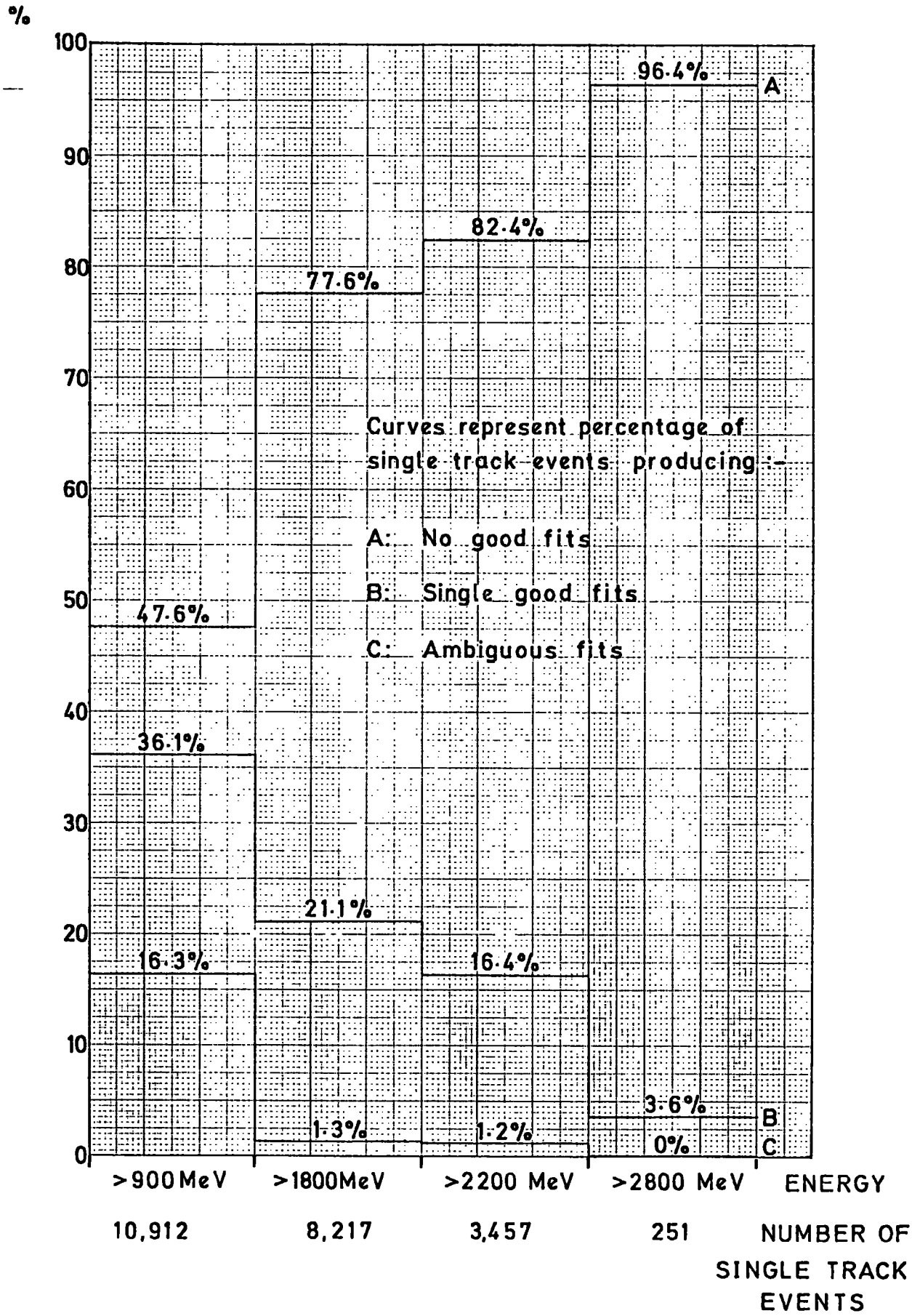

FIG. 6.8 : BREAKDOWN OF FITTING SUCCESSES AT EACH (g-2) ENERGY LEVEL

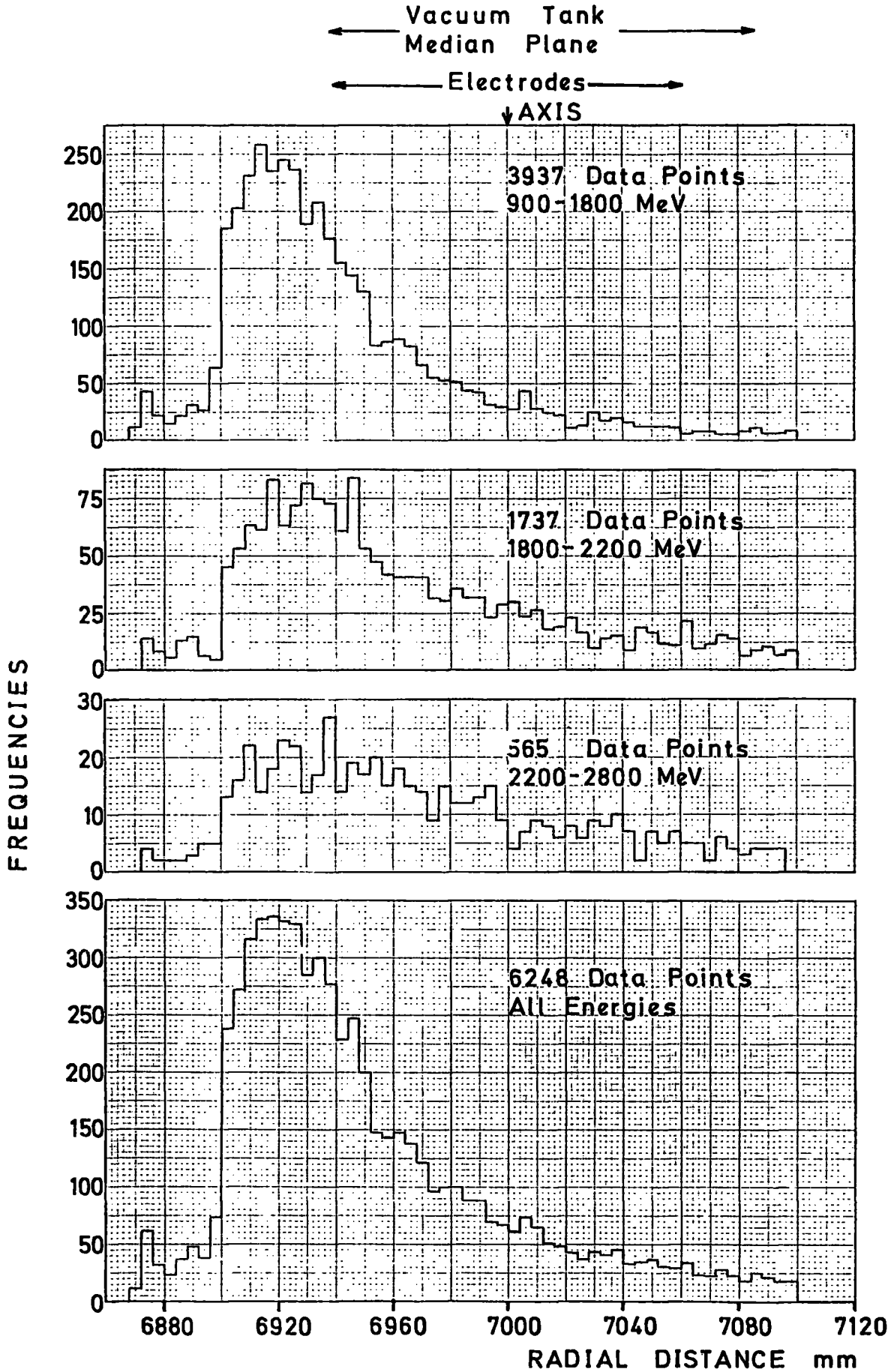

FIG. 6.9 : MUON RADII DISTRIBUTIONS

true drift lengths and hence decay trajectories. Such a distortion is more likely to explain the low muon radii values than an undetected geometrical misalignment of the array.

Further analysis allowed the inclusion of different drift velocities in the vacuum tank and ring centre side half-cells. Only constant drift velocities were used in the programs as the thorough theoretical analysis had not been performed at that stage. However indications from the analysis of the splitting of the primary ionization track data and initial calculations of the electric fields in the chambers allowed more accurate drift velocities to be used. Also the maximum drift time on the vacuum tank side of the curved end cell was limited to 170 ns over the 4 mm active length. Fits which included drift times beyond this value were rejected by substituting false co-ordinates in the fitting routine.

Analysis using sense wire to potential wire drift times of 170, 320 and 320 ns in the vacuum tank side drift spaces of cells "0", "1" and "2", and 590, 580 and 560 ns in the ring centre side drift spaces gave a close resemblance to the values presented in Table 5.1. The peak of the muon radii distribution, totalled over all energies, occurred at 6912 $\pm$ 4 mm. However the data were limited as only tracks with at least four hits were selected. The circle fits were performed upon the second, third and fourth hits on a track and the deviation of the first hit from the computed circle was calculated. The analysis was repeated with the fits made to the first, second and third hits and the deviations to the fourth. The peak value was shifted to 6920 $\pm$ 4 mm and all muon radii increased. As the latter analysis included more data points in cell "0" and the vacuum tank side of cell "1", a further

indication of the better approximation to linear space-time relationships in these half-cells was given.

The distribution of deviations of the fourth point on tracks in the lowest (g-2) energy level, which occurred in cell "2", is given in figure 6.10 with a schematic of the derivation of the deviation values. If the drift velocities were fully calibrated and the circle fit afforded an exact solution in cells "0" to "2", the deviations would represent a measure of the spatial resolutions of the chambers, say $\pm$ 0.5 mm. However figure 6.10 shows the majority of the data lying within $\pm$ 7 mm of the peak at + 2 mm with many larger deviations. As the distribution only contains values from the events with single correct fits, it implies that the other seven possible fits produced worse results. Therefore single track events satisfying the selection conditions, but still containing spurious drift times, probably produced the larger deviations - especially those over 14 mm which indicate a traversal position in an adjacent cell. The lack of rigid constraints in the fitting routine allowed the inclusion of such events and produced the long tail in the muon radii distributions. The width of the peak of the distribution is due to the incorrect assumption of constant drift velocities in the half-cells. The positive displacement of the distribution from zero indicates that the fit to the first three points produced a systematic lowering of the true electron radius, and hence of the muon radius also. Deviation distributions in cells closer to the vacuum tank, and for higher energy electrons, do not have such marked displacements, indicating once more the effect of the drift velocity approximations in the ring centre half-cells. This also explains the higher muon radii values obtained for the higher energy electrons which do not traverse so close to the ring centre.

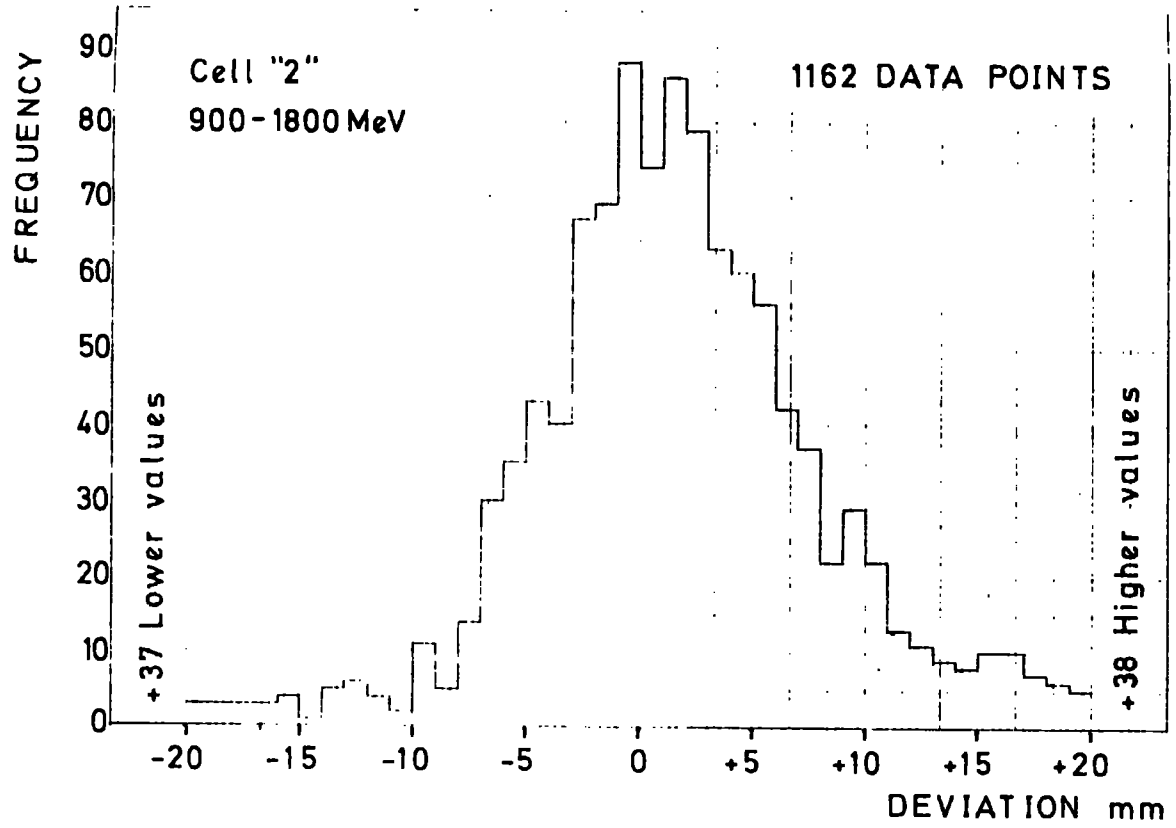

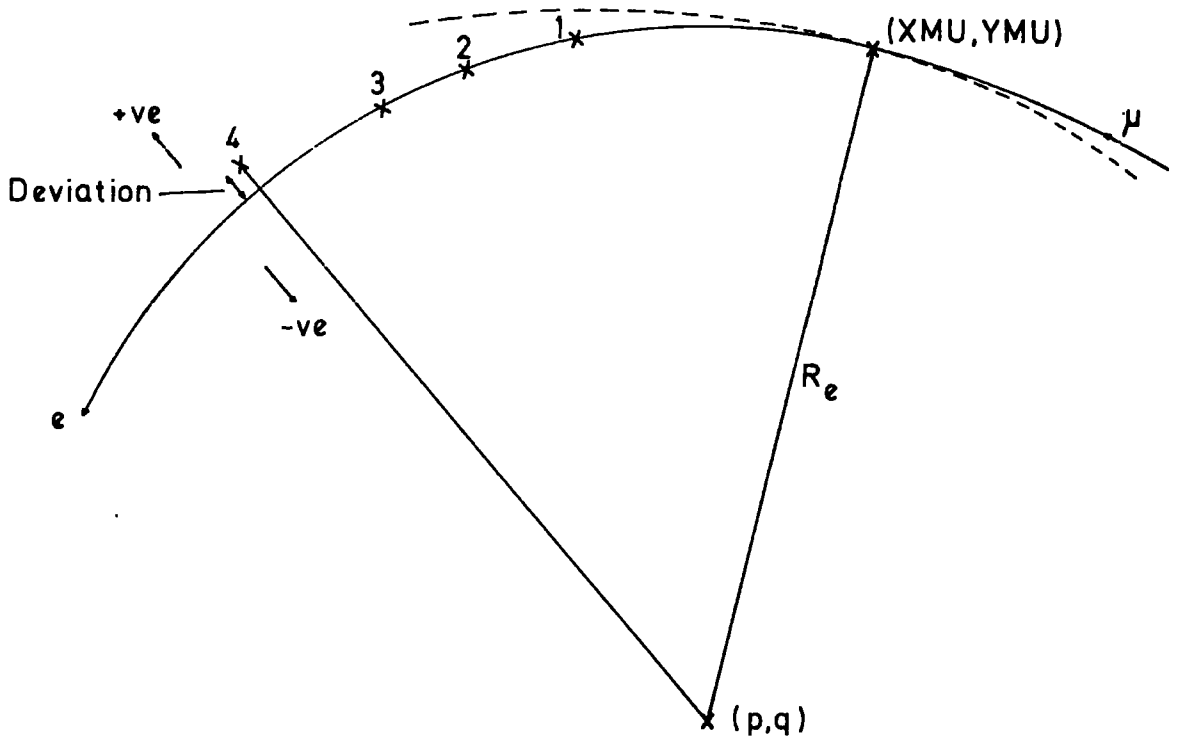

FIG. 6.10 : DISTRIBUTION OF DEVIATIONS OF FOURTH HITS FROM TRACKS AND SCHEMATIC OF DERIVATION

The later analysis programs displayed the recorded drift times in the appropriate half-cells for events producing single good fits. This resolved the left-right ambiguity in cells "0" to "2" and the maximum drift time values closely resembled the experimental values recorded in Table 5.1. However the number of data points in the ring centre half-cells exceeded those in the vacuum tank half-cells; the opposite would be expected considering that the flux of decay electrons fell towards the ring centre. This indicated that the incorrect drift velocities forced the wrong triplets of track co-ordinates to be chosen to produce the best fits.

The decay electron energies were computed from the electron circle radii using equation 6.16. The values were histogrammed for each (g-2) energy level to check the calibration of the shower counters. However as the computed electron radii were known to be undervalued, the derived energies were also automatically low. Figure 6.11 displays the values for (g-2) energy levels A, B and C taken from the above analysis. The cut-offs are due to limits imposed in the track fitting routine. The majority of the data lies at lower values in each range, as expected, with the long tails at higher energies reflecting similar tails in the muon radii distributions. Hence no firm confirmation of the shower counter energy calibration may be drawn from the results.

6.4 Manual Check of the Track Fitting Routines.

In order to check the accuracy of the fitting routines, and also to

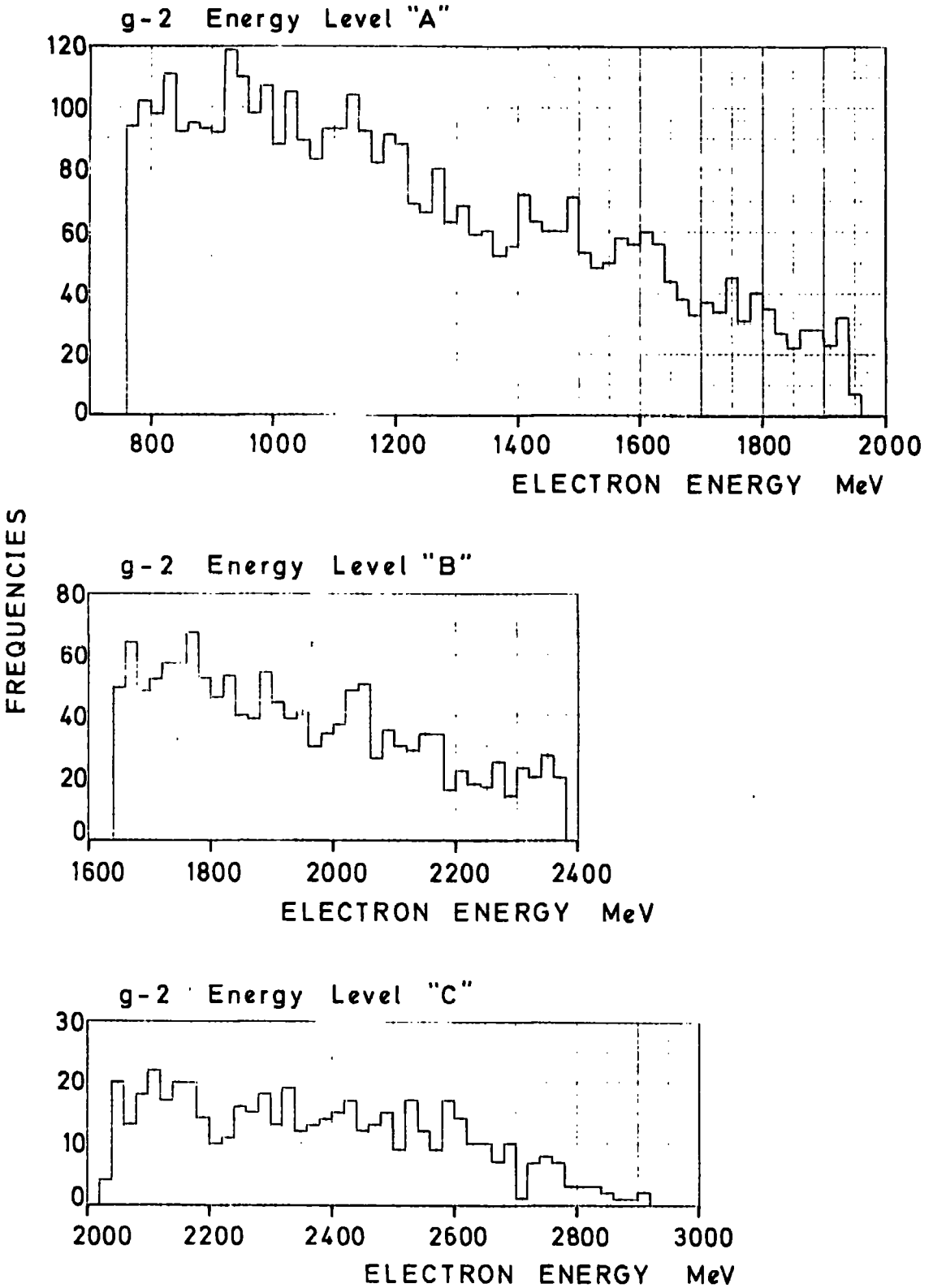

FIG. 6.11 : COMPUTED DECAY ELECTRON ENERGY DISTRIBUTIONS

confirm that the correct fit was selected, a manual reconstruction of a decay electron track was made. An accurate half scale drawing of the drift chamber array was used to enable the construction of a theoretical track. The birth position lay on a radius at + 1.6° to the datum line and corresponded to a muon radius of 6960 mm, as shown in figure 6.12. The circular trajectory had a radius of 2500 mm and traversed cell "0" in chambers E, F and G and cell "1" in chamber H, all on the vacuum tank side. The chamber co-ordinates measured on the drawing were compared with the theoretical values. The X co-ordinates were accurate to 0.1 mm and the Y co-ordinates to 1 mm; acceptable results considering the difficulty of drawing a 1250 mm radius circle by hand. Suitable constant drift velocities were assumed and the drift times calculated in each cell. The track analysis program was modified to allow input of just the drift times for a single event. Otherwise the program was identical to the main analysis program with a circle fit made to the first three points and the deviation of the fourth point calculated.

The effect of the small distortion in the drawing of the electron circle was immediately apparent when the track parameters were calculated. R_μ equalled 6961.7 mm, R_e was 2515.2 mm and the theoretical value of (124.5,4458.3) for the centre of the electron circle (p,q) became (138.4, 4444.3). The birth position (XMU,YMU) moved from the theoretical position of (194.3,6957.3) to (216.7,6958.3). Rather than manipulate the drift times to reproduce a true circular trajectory the above computed values were taken as absolute and all other sets of results compared with them. However the results immediately demonstrated

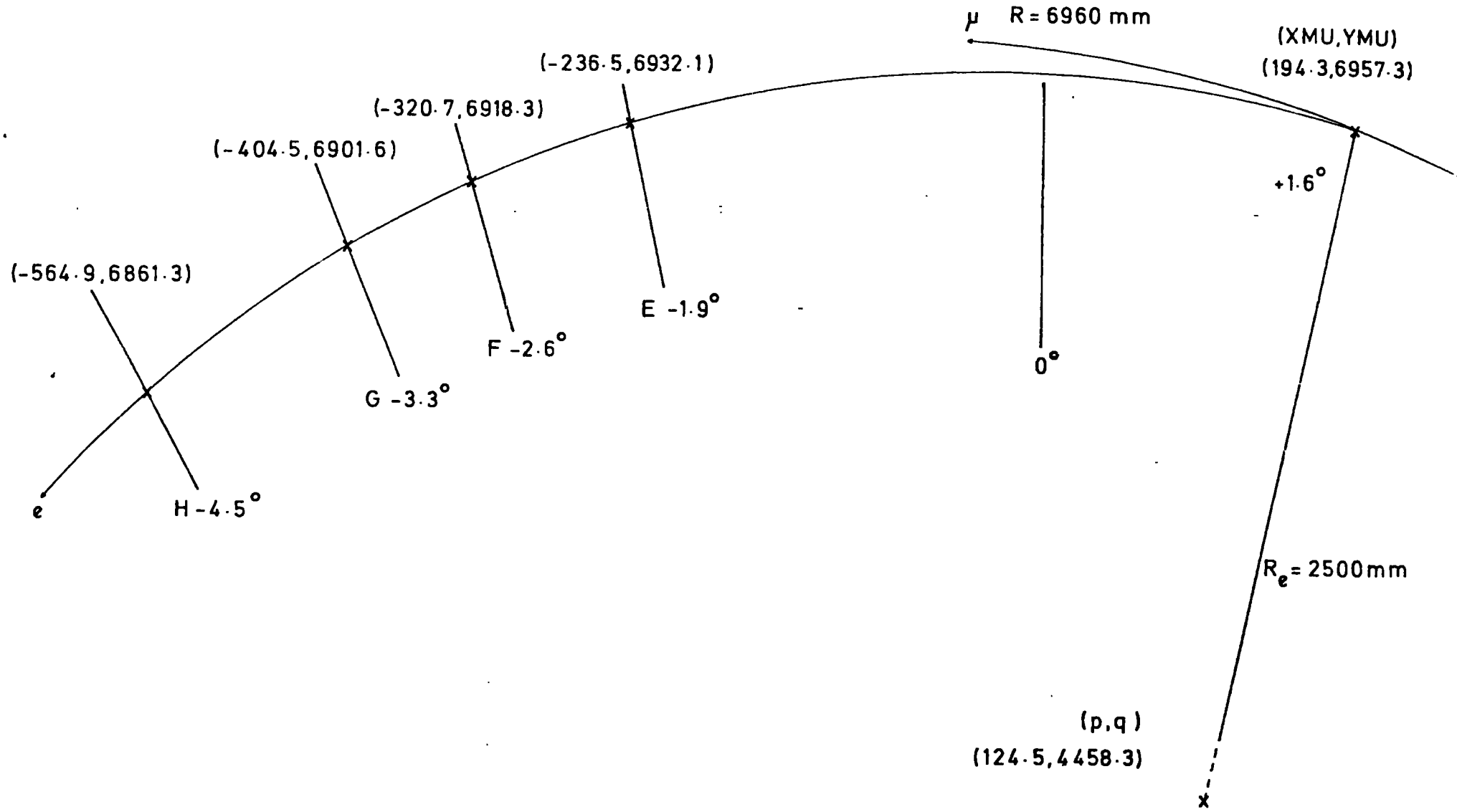

FIG. 6.12 : SCHEMATIC OF MANUAL TRACK RECONSTRUCTION

the effect of small errors in the track co-ordinates upon the resultant electron and muon radii. The computed electron energy was 1086.5 MeV and the deviation of the fourth point + 0.83 mm.

Of the eight possible fits to the data, six were rejected as the radial displacements from the ring centre of the three track co-ordinates did not decrease in successive downstream chambers. A seventh was rejected as the centre of the electron circle was too far from the ring centre to produce a valid decay electron, and therefore the eighth fit produced the only correct, unambiguous track.

Tests similar to the ones applied to the experimental data were performed. The chamber angles relative to the datum line were altered by $\pm 10^{0}$ and the value of R_{μ} was unaltered. The sense wire radii were increased and decreased by 10 mm, resulting in variations of $\pm$ 9.999 mm in the value of R_{μ}, $\pm$ 5.8 mm in R_{e} and hence a corresponding variation in computed energy of $\pm$ 2.5 MeV.

A tilt was applied to the whole array by moving chamber A 3 mm closer to the vacuum tank and leaving chamber H unaltered. Such a deformation of the baseplate orientation would have been detected during the measurement of the sense wire positions. The value of R_{μ} increased by only + 1.65 mm so such a perturbation would not explain the low muon radii values.

The drift times were altered to simulate variations in the spatial resolutions of the chambers and the incorrect drift velocity calibrations. An alteration of 10 ns represented a drift distance of 0.18 mm, which was an underestimate of the uncertainty in the half-cell space-time relationships. Initial variations of $\pm$ 10 ns to all drift times repeated the sense wire radii variations, the value of R_{μ} varying

by ± 0.18 mm. A more important test was to vary the drift time in the second chamber only by ± 10 ns. The positive displacement towards the vacuum tank caused the value of R_μ to decrease by 5.7 mm, and the negative displacement towards the ring centre caused an increase of 8.5 mm. The non-linear theoretical space-time relationship of the ring centre side half-cell, shown in figure 5.27, indicates that an approximation to a linear relationship with the same maximum drift time would underestimate the drift length by up to 2 mm at intermediate drift times. Hence the exact solution would displace the track co-ordinate towards the ring centre in these half-cells. The large increase in the value of R_μ for the negative displacement was due to the electron radius increasing from 2515.2 mm to 2861.4 mm with a subsequent movement of the centre of the electron circle and a rise of 150 MeV in the computed energy. Also the birth position was moved 125 mm upstream. The positive and negative displacements altered the deviation of the fourth point by ± 1.33 mm.

A displacement of 0.5 mm towards the ring centre for the second point increased the values of R_μ to 7018.9 mm and R_e to 3718.1 mm, with the energy equalling 1606.2 MeV and the deviation of the fourth point - 23.7 mm.

These manipulations of the second hit position obviously have the greatest effect upon the electron radius. By comparison a variation of ± 10 ns in the drift time of the third hit only altered the value of R_μ by - 2.5 mm and + 3.1 mm, with the deviation of the fourth point altering by ± 0.8 mm. However the calculations have demonstrated the inherently large variations in the value of R_μ due to small errors in

the determination of the track co-ordinates. This is due to the co-ordinates defining such a small arc of the fitted electron circle. Although all track fits would not necessarily have a systematic displacement of the second point towards the ring centre if exact drift velocity calibrations were available, the errors due to the values used may explain the resultant low muon radii values.

6.5 Discussion of Results and Suggestions for Further Analysis

The low valued muon radii distributions derived by previous authors have been improved upon, especially for higher energy decay electrons, but not to the required extent. The best distribution ranged from 6900 to 7100 mm with a peak at 6940 mm, as against the expected values of 6940 to 7060 mm with the peak at the optimum storage radius of 7000 mm.

The previous section has demonstrated the necessity for extremely accurate drift velocity calibrations. Distortions of the array geometry have been discounted as possible reasons for the low values. It would be expected that the theoretical space-time relationships derived in Chapter 5, scaled to the appropriate experimental potential wire to sense wire drift times, would produce improved distributions. However such calibrations would still not exactly define the true experimental relationships. As previously mentioned, the electron swarms associated with particles traversing cells in the potential wire regions drifted close to the cathode planes due to the poor electric field compensation. Field distortion around the cathode wires would perturb the space-time relationships at these long drift times. Also, due to the non-saturated drift

velocities, the overall spatial resolution of the chambers was lower than if they had been operated in a fully saturated mode.

Despite the increased confidence in the results that would have existed if fully calibrated data had been available, it must be noted that extreme variations of the constant drift velocities employed in the analysis programs had remarkably little effect upon the shape and values of the muon radii distributions. Analyses not reported in this thesis relaxed the constraints applied in the fitting routines and included extreme variations in the drift velocities. The number of successful fits obtained with the same data was not substantially increased for any combination of parameters. However the correct fits obtained with different parameters were not always necessarily associated with the same events or the same triplet of possible track co-ordinates. Therefore comparison of the results may not always have indicated the true effect of the variation in parameters.

Throughout the analysis the lack of direct solution to the left-right ambiguity presented problems. As the space-time relationships have been shown to be markedly different in the two drift spaces on either side of the sense wire, a direct knowledge of which drift space was traversed by the electron would have allowed more accurate determination of the relationships. Suggested further analysis employing the theoretical space-time relationships could also divide the deviation histograms into values calculated in the vacuum tank and ring centre side of each cell, as well as the distinction between decay energies already included. Any difference between the two distributions obtained for a cell would indicate which half-cell space-time relationship used in the fitting routines was more inaccurate. The effects of varying the relationships

could then be studied more closely.

Another problem was the low number of points recorded on each track. The analysis concentrated on fitting circles to only three points in the cells where the magnetic field was almost constant. Further analysis with calibrated data would have included least squares fits to a circle with four or more data points. This would have allowed more rigorous constraints to be applied in the fitting routines, but the data were limited for tracks with more than three hits recorded. The inefficient region of the curved end cell drastically reduced the number of data points recorded, especially for higher energy decay electrons. If efficient detection with constant drift velocities had existed throughout this region it is probable that the basic circle fit would have produced satisfactory results. Ultimately more complex tracking methods, such as those discussed in the following section, could have been used to track the electrons towards the ring centre through the inhomogeneous magnetic field where a circle fit would no longer be valid.

All the track analyses performed and suggested have used the anticipated results to gauge the accuracy of the drift velocities employed. Obviously this is the converse to correct procedure and there can be no substitute for an accurate calibration of the space-time relationships.

The above discussion has considered errors in the calculated drift lengths and the methods of analysis. However no consideration has been given to the validity of the assumed circular electron trajectory. The detected electrons decayed from one of the two electric field-free sections of the storage tank. These two regions imparted a systematic distortion to the horizontal and vertical betatron motions which were associated with muons not stored at the optimum momentum corresponding to circular orbit at 7000 mm radius, where exact focusing occurred.[2] This tended to

increase the radii of the muon orbits in the field-free regions. However the muons would no longer be describing circular orbits about the ring centre; an assumption used in the calculation of the electron birth position. It may be shown that in such cases the computed displacement of the birth position from the ring centre was always less than the true value. Therefore errors occur for electrons decaying from muons not in the optimum orbit, although they are less than 1 mm.

No account has been taken of possible scattering in the 0.8 mm thick titanium wall of the storage vessel. As such scattering would be directed throughout a cone around the forward decay trajectory of the electron, as viewed in the laboratory, its effect would be to widen the muon radii distribution rather than systematically increase its value.

The radial magnetic field plots displayed for various azimuthal positions in the median plane have indicated decreasing field values towards the ring centre. As stated, a circle fit to three points on a trajectory decreasing in curvature would produce an overestimate of the muon radius value. However for trajectories displaced more than $\pm$ 3 mm vertically from the median plane the magnetic field rose from the homogeneous field value, due to edge effects from the magnet poles, before decreasing more rapidly than in the median plane case, as shown in figure 5.16. Thus the decay electron trajectory would have constant curvature in the homogeneous field region, increased curvature in the higher field region and decreasing curvature towards the ring centre. Cells "0" to "2" cover the higher field region with the maximum values occurring around the boundary of cells "1" and "2". The circles fitted to data recorded in these cells would have lower radii than the true decay curvatures in the homogeneous field and therefore low muon radii would result. No direct measurement of the vertical decay co-ordinate was

recorded but, as already discussed, the proportion of the total data occurring at such large displacements from the median plane was small. Therefore the reduction in the muon radii values only occurred in a minority of the recorded events.

Hence any possible departures in the recorded data from the assumed circular electron trajectories, formed tangentially to circular muon orbits about the ring centre, would not have had any profound effects upon the computed muon radii distributions. Therefore the low muon radii values obtained and the moderate percentage of single track events which produced good fits were due to the approximate drift velocity calibrations available.

6.6 Discussion of Accurate Tracking Methods

Accurate track reconstruction of particles traversing an inhomogeneous magnetic field is necessarily complex. The (g-2) fringe field varied in radial, vertical and azimuthal directions, although it was symmetric about the horizontal median plane. As reported, a series of measurements were performed to allow the determination of a mesh of field values throughout the volume described by the drift chamber array.

The vertical co-ordinates of the decay electrons would be required in accurate tracking procedures, but trajectories in a horizontal plane could be accurately assumed. Initial values for the momenta and approximate birth positions of the electrons could be obtained from the basic circle fit to the data. These would be used as the first iteration values in the accurate tracking routines.

Several approaches have been made to the problem of accurately reconstructing trajectories in such complex magnetic fields.[3,4] All

rely upon a precise knowledge of the magnetic field at regular intervals and use numerical integration methods to solve the equations of motion for the particles. The step by step reconstruction of the trajectories involves iterative approaches to the correct track, often employing Runge-Kutta-Simpson techniques. The precise approach used normally depends upon the complexity of the field, the required accuracy and the consequent computation time involved.[5]

An approach used for a polarized target experiment at CERN[6] could have been modified to the (g-2) case if the approximation to azimuthal symmetry had been acceptable. The particular magnetic field was axially symmetric with a mirror symmetry about the horizontal median plane. Parametrization of the magnetic field led to the development of an algorithm to allow track reconstruction, and hence momentum determination, from the recorded track co-ordinates. The azimuthal symmetry allowed a vector potential to be defined in terms of the radial and vertical field values and the radius from the axis of symmetry.

An extremely complex program has been developed for the Split Field Magnet facility of the ISR at CERN.[7] This program tracked particles through the inhomogeneous field using co-ordinates derived from MWPC data. In addition it allowed uncertainties in the recorded track co-ordinates. Provision was made for the spatial resolution of the chambers, multiple scattering in the chamber array and scattering in the wall of the ISR vacuum tank.

The uncertainties in the calibration of the (g-2) data did not warrant the utilization of more complex tracking routines and certainly the time scale did not allow the development of such complex programs as those discussed above.

REFERENCES

1) Short, K. A., Ph.D. Thesis, University of Durham (1975)

2) Combley, F., Picasso, E., Phys. Reports 14C (1974) 1

3) Peters, M. W., Nucl. Instr. Meth. 113 (1973) 371

4) McKee, R. J., Nucl. Instr. Meth. 114 (1974) 321

5) Bock, R. K., Louis, F., CERN NP-DHG Report 75-3 10/6/75

6) Birsa, R., Bradamante, F., Daum, C., Fidecaro, G., Fidecaro, M., Giorgi, M., Lanceri, L., Penzo, A., Piemontese, L., Schiavon, P., Vascotto, A., Villari, A., Nucl. Inst. Meth. 146 (1977) 357

7) Metcalf, M., Regler, M., Brott, C., CERN 73-2, Laboratory 1. Data Handling Division, 7/2/73

CHAPTER 7

APPRAISAL OF THE (g-2) DRIFT CHAMBER ARRAY AND CONCLUSIONS

7.1 Summary of the Drift Chamber Array Performance

The (g-2) drift chamber array was an ambitious project from its inception. The use of drift chambers was in its infancy and their employment in such an inhomogeneous magnetic field is still rare. At the design stage a suitable chamber gas and operating parameters had to be found. The chambers themselves were of novel design due to the physical constraints of the detection region. In particular the curved end cell was of unusual configuration to allow efficient detection close to the thin-walled vacuum tank section of the (g-2) storage ring. The baseplate and chamber cradles allowed accurate, reproducible mounting of the drift chamber array.

Having cured initial breakdown problems by modification of the cathode wire potentials in the sense wire regions, the chambers proved to be reliable and were operated for long periods without attention. Chamber efficiencies of over 99% and spatial resolutions of 150 μm in the normal cells, and 300 μm in the curved end cell, were obtained during commissioning trials in magnetic field free conditions.

The chambers were of the adjustable field type and the required electric field compensation was determined theoretically, a three-wire spacing throughout the chamber finally being used. The sense of the field tilt was reversed when the stored muon polarity was reversed.

Data acquisition systems using TDC modules to digitize the drift times were used during trials at the Daresbury Laboratory and initially at CERN. Their inherent non-linearity was a disadvantage. Therefore a

recently designed Drift Time Digitizer system was employed which used a master oscillator to digitize all timing channels. This not only ensured linearity but also correlation between all channels. Also multiple hits could be recorded on a wire with this system. However several inherent design faults were encountered with the new system and modifications of the pre-amplifier discriminator circuits proved necessary. Ultimately the data acquisition system was developed and fully calibrated, allowing timing resolutions of $\pm$ 2 ns under all detection conditions. However only one trigger could be processed during each (g-2) injection cycle.

The chambers were not fully efficient until 75 μs after injection. This was due to space charge effects around the sense wires induced by the high flux of particles traversing the chambers during injection. A blanking system using a thyratron circuit was contemplated. This would reduce the applied chamber voltages at the time of injection and thereby limit charge amplification around the sense wires. However as the chambers had such a narrow operating plateau - in the region of 50 V - any overshoot in the applied blanking pulse would induce breakdown to occur. As the pulse would be applied at the H.T. distribution box in the (g-2) counting room, signal attenuation and deformation would occur in the cables running to the ring. Also the sensing circuits on the output of the Brandenburg power supply would attempt to compensate the change in applied voltage. For these reasons the blanking system was not pursued. With good beam conditions 70% of the injections produced triggers in the drift chamber array. Therefore the lack of detection efficiency at early times, when the majority of the muons decayed, was not critical.

50% of the system triggers produced clean single track events suitable for analysis. However as no accurate calibration of the chamber space-time relationships was performed in the (g-2) fringe field the drift

velocities could not be determined to the necessary accuracy. As no on-line or off line analysis programs had been developed during the data-taking period, the consequencies of the poor calibrations were not appreciated. The whole cell drift time distributions indicated the maximum drift times in each cell, but the precise forms of the space-time relationships were not revealed. Detection inefficiencies were apparent at long drift lengths and immediately around the sense wires.

The chamber electric fields were determined theoretically and, in conjunction with the measured median plane magnetic field values, the theoretical space-time relationships were computed. The electic field plots also indicated the inefficient detection region in the curved end cells. Particles traversing chambers in the potential wire regions were frequently observed to produce drift times recorded at both adjacent sense wires. Analysis of this data provided further drift velocity information which was in good agreement with the theoretical results. However accurate calibration would only be provided by an experimental system scanning across a chamber in the (g-2) fringe field, as proposed in Chapter 5.

The argon-methane (90:10) gas mixture has been used successfully by other workers. Although the use of other mixtures such as argon-ethylene has become fashionable, there is no reason to suppose that satisfactory results cannot be obtained in magnetic fields with such a mixture.

Despite modifications to the measured array geometry and extreme variations in the drift velocities used, all attempts at track reconstruction using a circle fit failed to produce muon radii distributions in the anticipated range. Confirmation of the computational accuracy of the fitting routines was provided by a manual reconstruction of a decay electron track. This analysis also revealed the inherently large variations in the

computed value of the muon radius when small variations were made to the recorded track co-ordinates. One important point to note is that the appropriate constraints applied in the fitting routines ensured that in the majority of cases unambiguous single fits were obtained without direct knowledge of the left-right ambiguity solutions in each cell.

Having discounted all other possible sources of error, it was concluded that the low muon radii values were due to systematic errors in the drift velocities used in the calculations. Further analysis employing more accurate space-time relationships was likely to improve the distributions. Unfortunately time did not permit the implementation of the necessary modifications to the tracking routines.

As a direct consequence of the undervalued electron and muon radii, the computed decay electron energies were also lower than expected.

Other data recorded allowed the occurrence times of all correct track fits to be histogrammed. The resultant distribution revealed the characteristic (g-2) precession frequency to good accuracy. Inclusion of data from an EDM counter sandwiched between drift chamber H and shower counter C10 indicated that many decay electrons failed to be recorded in either scintillator arm of the counter. These electrons traversed chamber H in the cells closest the ring centre, indicating that the radial detection region of the EDM counter was not as great as the shower counter.

7.2 Suggested Improvements to the Drift Chamber Design

With the advantage of hindsight many improvements may be suggested that would have ensured more accurate operation of the (g-2) drift chambers.

It has been shown that the basic problem was the non-uniformity of the drift velocities. This was due to the drift field being too low and the

field compensation non-exact. However as the cathode wire potentials had already been lowered in the sense wire regions to prevent breakdown, the required increase would not have been possible. A drift field in the region of 1500-2000 V cm^{-1} would be required to ensure saturated drift velocities at all magnetic field values. The observed drift velocity, w_s, would then only depend upon the magnetic field which altered the drift angle. A constant field compensation angle throughout the chamber would produce satisfactory results, but an accurate calibration of the space-time relationships would still be necessary. If a variation in the electric field tilt angle was required, it would be preferable to make the transition in the sense wire region, where the electric field is radial and high valued, rather than in the potential wire region. The subsequent distortion of the drift velocities would be much lower.

The inter-cell boundary in the (g-2) chambers was poorly defined due to the odd number wire-spacing tilt. Re-designed chambers would have a larger inter-cathode gap so that a four wire-spacing tilt could provide the necessary field compensation angle, and also allow the application of higher drift fields.

The inefficiency of the curved end cell severely reduced the number of data points recorded. Present day construction techniques would probably include printed circuit cathode planes, shaped to the chamber geometry in this region, in order to provide a continuous drift field throughout the cell. Inspection of the chambers over two years after their construction revealed a slackening of the wires in the curved end region. This was almost certainly due to a weakening of the glass side members which were under extreme tension from the wire planes, with no support from the curved end member. For this reason chambers constructed in the future to similar design criteria will probably employ printed

circuit cathodes etched on thin copper coated mylar. Only the sense wire plane would be constructed with wires attached to a frame under tension. The printed circuit cathodes would be made planar by adhering them to lightweight frames under vacuum.

Although the tracking routines successfully resolved the left-right ambigiities, a direct chamber signal would have been advantageous and would have significantly reduced the track analysis computation times.

Chambers built with the above improvements would have undoubtedly produced superior results to those obtained. However considering the period when the (g-2) chambers were designed, all the difficulties could not have been foreseen.

7.3 Conclusions

The track analysis has demonstrated that the co-ordinates needed to be defined to an accuracy of at least 200 μm. This represents the upper limit of chamber resolution when operating in such inhomogeneous magnetic fields. The consequent need for saturated drift velocities throughout the chambers, plus accurate calibration, has been emphasised.

The methods of data analysis and theoretical drift velocity determination have produced the best possible calibrations of the data. Although improved muon radii distributions may be achieved with other space-time relationships, the results could not be regarded with complete confidence as they would not be derived from direct calibrations.

The use of drift chambers in the array was the logical choice as they could provide the highest spatial resolution of any detector. Increased understanding of drift chamber operation in magnetic fields since the construction of the (g-2) chambers allows improved operating

parameters to be suggested. These would improve the resolution to the required accuracy. In all other respects the (g-2) array operated successfully. In particular an extremely accurate data acquisition system was evolved, incorporating new hardware.

The results of the main (g-2) experiment did not rely ultimately upon the drift chamber data. The experiment produced several results of unequalled accuracy for both muon polarities, as reported in Chapter 1. In particular the anomalous magnetic moments and muon lifetimes were determined to great precision. The anomalies were accurate to ten parts per million (ppm), the combined value yielding a result accurate to 8 ppm. This was in remarkable agreement with the theoretical value, known to 9 ppm, and indicated the correlation between experiment and the most precise quantum electro-dynamical calculations for the muon.

The continued use of drift chambers as precise position detectors is assured. Not only do they provide cheap large area detectors in the field of high energy physics but, as demonstrated in Chapter 2, the principle has also been extended to the development of hybrid detectors for use in many fields. The ultimate spatial resolution attainable with certain chambers is in excess of 100 μm. Much of the present research is directed towards the development of such accurate detectors and the associated hardware for data acquisition.

ACKNOWLEDGEMENTS

The author would like to thank Professor A. W. Wolfendale for his support of this work and the use of laboratory facilities. The S.R.C. is acknowledged for its provision of a C.A.S.E. award in association with the International Research and Development Company Limited, Newcastle. The author is further indebted to the S.R.C. and C.E.R.N. for the allocation of additional expenses and the use of laboratory facilities.

The author's supervisor, Dr. J. M. Breare, in warmly thanked for his guidance, assistance and encouragement throughout the work. The skills of the Nuclear Instrumentation Group's technician, Mr. J. Webster, are noted and he is thanked for the cheerful way in which he actively aided the project throughout. Mr. R. McDermott is thanked for producing many excellently machined pieces of equipment for use in the early development of the drift chambers. Mr. A. Robertshaw and his colleagues at I.R.D. are acknowledged for producing the final drift chambers.

Dr. R. Browell and Dr. K. A. Short are thanked for introducing the author to the art of drift chamber operation in the accelerator environment. Dr. B. Sitar and Mr. A. R. Hedge provided invaluable assistance and provoked enlightening discussions during two cycles at CERN. Along with all other members of the N. I. group, past and present, they are thanked for their assistance, encouragement and friendship throughout the author's stay.

Dr. P. A. Ridley and Dr. F. Golding are thanked for their help with the on-line computing facility during runs at the Daresbury Laboratory, and Mr. M. D. Rousseau is acknowledged for his support.

Dr. J. M. Bailey is thanked for his advice and support throughout the various stages of the project at Daresbury and CERN.

The author is indebted to Professor E. Picasso for his permission to work on the (g-2) experiment at CERN and his interest and encouragement during the author's many visits. Dr. F. Krienen and all other members of the (g-2) team, too numerous to mention by name, are remembered for their advice, encouragement and stimulating discussions which made the author's visits so enlightening and enjoyable. Mr. W. Glessing and his technicians are acknowledged for their assistance on all mechanical aspects of the (g-2) drift chamber array. Dr. P. Sharff-Hansen and all other members of the Experimental Physics Data Handling Group are gratefully acknowledged for their ceaseless efforts to provide an excellent on-line computing facility.

Everybody at both the Daresbury Laboratory and CERN who assisted in any way towards the everyday running of the experiment, transportation of equipment or administration is thanked wholeheartedly for their co-operation. Without them the whole project could not have run so smoothly. All technical and secretarial staff at the University of Durham are similarly acknowledged.

The author's mother is thanked for her accurate typing of the thesis and Mr. A. Walker for his excellent printing.

The author's fiancee, Margaret, has been unfaltering in her encouragement and patience, especially during the author's periods at CERN and during the writing of this thesis. All friends and relatives are also thanked for their support.

Finally the author would like to express his gratitude towards his mother for her guidance, encouragement and sacrifice throughout his education. Without such devotion he would have been unable to achieve the completion of his thesis.